Mathematical Models for Optimisation of Drug Administration in Intensive Care Units

Thesis

Mathematical Models for Optimisation of Drug Administration in Intensive Care Units

Stefano Finazzi, MSci, PhD

Degree of Doctor of Philosophy

The Open University

Affiliated Research Centre

Istituto di Ricerche Farmacologiche Mario Negri IRCCS

Director of Studies
Dr. Guido Bertolini

Supervisor
Prof. Mervyn Singer

September 2018

Abstract

Clinical status of critically ill patients is often extreme and rapidly evolving. Hence, pharmacological therapies must be tailored to patients' characteristics and adapted according to the evolution of their clinical pictures. To identify optimal personalized treatments, possible scenarios produced by different therapeutic choices must be predicted and compared. This process requires complex analyses involving the development of appropriate mathematical models.

In this Thesis, I focused on two important aspects of the pharmacological treatment of critically ill patients: the administration of antimicrobial drugs and the control of their glycaemic level. Although these problems are clinically very different, the modelling of their pathophysiological mechanisms can be addressed with similar tools.

I performed analyses based on retrospective clinical data collected with *MargheritaTre*, an electronic health record developed by GiViTI. The software to synchronize databases from hospitals to our laboratory and to preprocess data for analyses was written for the purpose of this Thesis.

Starting from the study of the physiological mechanisms at the basis of vancomycin pharmacokinetics I constructed a model to describe the evolution of the plasma concentration of this drug in critically ill patients. Compartment models were fitted on a sample of 141 patients, testing about 30 patient covariates and several functional dependencies for each variable.

Glucose dynamics were described through a system of delay differential equations reproducing intake, uptake and endogenous production of glucose, and organ-organ interactions mediated by hormones. Existing models, describing only the dynamics of glucose and insulin, fail to reproduce the correct evolution when glucose concentrations vary too rapidly. I improved these models, by introducing an equation describing glucagon dynamics and taking into account its effect on glucose metabolism. I investigated the dynamical properties of my model with analytical analyses, numerical simulations and fitting it to observed data.

A Donata e ai miei genitori

ACKNOWLEDGEMENTS

> Questa tesi è dedicata ai miei genitori e a Donata, le persone che più mi sono state vicine in questi quattro anni, in cui sono stati realizzati i lavori presentati in questa tesi. Con loro ho condiviso gioie e difficoltà. Grazie al loro appoggio è stato più facile affrontare dubbi e incertezze.

These were the first lines of the acknowledgement section of my first Thesis at SISSA–ISAS. With the very same lines I want to thank again Donata and my parents. Seven years ago, it continued like this:

> Per varie ragioni è stato molto difficile scegliere di continuare a fare questo lavoro: i loro consigli mi hanno aiutato a capire quello che volevo per il mio futuro. In particolare voglio ringraziare Donata per aver compreso e condiviso questa scelta e per il coraggio di aver accettato, per qualche anno, il rischio di spostamenti in luoghi non ancora definiti.

This is precisely what happened in the last seven years, which, at the beginning, were characterised by the uncertainty of not knowing where to live, year by year, first in Trento, then in Paris and eventually here, in Bergamo. And so, today, I thank again Donata for having followed me.

> Un aiuto fondamentale per chiarirmi le idee è venuto da Stefano, che ho annoiato con lunghe discussioni, e da Guido, che mi ha offerto la possibilità di utilizzare le mie competenze al di fuori della fisica e con cui spero di continuare a collaborare, insieme a tutti i ragazzi del GiViTI. Li ringrazio entrambi per il loro grande entusiasmo nella ricerca, anche se in campi diversi. Ringrazio anche Daniele per la sua capacità di tradurre, interpretare e analizzare dati clinici con strumenti matematici e statistici. Da lui ho imparato a cogliere molteplici aspetti di un problema e a leggerli con linguaggi

diversi. E infine ringrazio Iacopo, con cui lavorerò per i prossimi due anni, che ha sicuramente contribuito alla mia decisione.

Finally, four years ago, that hope become reality. I am now working in the Mario Negri Institute, in the Laboratory of Clinical Epidemiology. I want to thank prof. Garattini for trusting me and my supervisor, Guido, for offering me the possibility to work in this lab and supporting me during these years. I thank him and my English supervisor, Mervyn, for their evaluable pieces of advice about the work of this Thesis. Thanks also to Roberto, my third-party monitor.

I thank all the colleagues I have been working with during these last four years. First, many many thanks to the guys of our brand-new unit of Medical Statistics and Mathematical Physiology, better known as the *pink room*, Carlotta, Giovanni, Giulia, and Greta, for their help with the analyses, for several stimulating discussions, and above all, for their sincere friendship and the time spent together, both at work and outside of work. I also thank Giulia for contributing in the last year of this project to improve the software to export data from *MargheritaTre* (M3), and to develop the glycaemic models.

I thank our project managers, Elena, Gaia, Giulia, the new-entry Valentina, and our extraordinary secretary Luana. Elena, in particular, has provided a fundamental contribution to the work of this Thesis. We joined the lab almost altogether and everything begun with the first pharmacokinetic model we built for her Master Thesis. Those preliminary analyses were the basis of this work and of the AbioKin project, that is coordinated by Elena and myself.

Thanks also to the IT guys, Carlo, Claudio, Daniele, Giampi, Matteo, Michele, Michelez, Obou, and Befe, that has just joined the group. A special thank to Giampi, who has been developing M3, Michele, for his essential and tireless support with the installation of M3, and Claudio and Matteo, for helping me with data synchronisation. Without their contribution nothing of what was done for this Thesis would have never been possible.

Thanks to all the guys of the lab who do not work in Ranica, Liliane, for her truly infectious enthusiasm, Alessia, Davide, and Joanne.

Thanks also to the undergrad students who have been working with me in the last semester, Giorgia, who helped me with the review of pharmacokinetic models, Irene, who worked on the Compact project, and Michela, who has written the protocol of the GluDyPS project.

Thanks to Carlotta, Elena, Gaia, Giulia, Greta, and Luana for packaging the kits for the AbioKin project.

I thank all the clinicians of the GiViTI, especially Mario, who coordinates the M3 project, Sergio for providing the data for the farmacokinetic model, Giuseppe, who is the clinical PI of the AbioKin project, Clara for her essential support in the organisation of the AbioKin protocol, and Bruno for his boundless knowledge on all the aspects of infections in Intensive Care Medicine.

ACKNOWLEDGEMENTS

Thanks to Antonello, who introduced me to the pharmacokinetics and pharmacodynamics of antibiotics, helped Elena and me with our first pharmacokinetic models. In the following months, he will also measure drug concentrations for the AbioKin project. I thank Danilo and Gianni for their suggestions about glycaemic metabolism and models. I thank Luigi for stimulating discussions about pathophysiology and for helping me with the interpretation of the results of my models.

I want to thank Deborah and Roberto for hosting the AbioKin samples in the bio-bank of the Mario Negri Institute.

Thanks also to Livio, who has been the only person I met at any time in the Institute while writing up my Thesis during the last summer.

I want to thank Fondazione Cariplo for supporting this research through Grant no. 2014-1962, Associazione Menuccia Grosso, and Maria for her donation.

Finally, many thanks to Guido, Joanne, and Mervyn for carefully reading and correcting the manuscript of this Thesis and to the members of the examination panel (Prof. Della Pasqua, Dr. Gobbi, and Dr. Bonati) for their valuable suggestions.

CONTENTS

Abstract **3**

Acknowledgments **7**

Contents **11**

Introduction **15**

1 Data collection: MargheritaTre **22**

1.1 The electronic health record 23

1.1.1 Data structure 23

1.1.2 Real time analyses 24

1.1.3 Support to clinical studies 24

1.1.4 Architecture 25

1.2 ICU and patient characteristics 25

1.3 Data management 26

1.4 Data extraction for research purposes 30

I Antimicrobial Pharmacokinetics **33**

2 Physiology of Pharmacokinetics **34**

2.1 Physico-chemical mechanisms 36

2.1.1 Movement through membranes 36

2.1.2 Perfusion 39

2.1.3 pH 39

2.1.4 Protein binding . . . 41
2.2 Macroscopic pharmacokinetic processes . . . 41
2.2.1 Distribution . . . 42
2.2.2 Elimination . . . 46
2.3 Secondary PK parameters and PK/PD indices . . . 55
2.4 Compartment models . . . 58
2.5 Pharmacokinetics in critically ill patients . . . 60
2.5.1 Effect of organ dysfunctions on pharmacokinetics . . . 61
2.5.2 Sepsis . . . 64

3 Antimicrobials in critically ill patients 66
3.1 Basic concepts . . . 66
3.1.1 Pharmacokinetics . . . 66
3.1.2 Mechanisms of action . . . 68
3.1.3 Kill characteristics . . . 70
3.2 Vancomycin . . . 71
3.2.1 Pharmacokinetic/pharmacodynamic analysis of vancomycin in ICU patients 73
3.2.2 Population pharmacokinetic parameters of vancomycin in critically ill patients 74
3.2.3 Vancomycin dosing assessment in intensive care unit patients based on a population pharmacokinetic/pharmacodynamic simulation . . . 76
3.2.4 Vancomycin dosing in critically ill patients: robust methods for improved continuous-infusion regimens . . . 78
3.2.5 A new regimen for continuous infusion of vancomycin during continuous renal replacement therapy . . . 79

4 Compartment Pharmacokinetics 82
4.1 One-compartment model . . . 82
4.2 Two-compartment model . . . 85
4.2.1 Homogeneous solution . . . 86
4.2.2 Non-homogeneous solutions . . . 89
4.3 Population models of kinetics . . . 95
4.3.1 Single-subject model . . . 98
4.3.2 Several subjects . . . 100
4.3.3 Population model . . . 100

5 Pharmacokinetic models of vancomycin 108
5.1 Methods . . . 108

5.1.1 Development sample . . . 108
5.1.2 Covariates . . . 109
5.1.3 Data management . . . 111
5.1.4 Model construction and variable selection . . . 115
5.2 One-compartment model . . . 117
5.2.1 Model development . . . 117
5.2.2 Goodness of fit . . . 123
5.2.3 External validation . . . 125
5.2.4 Clinical interpretation . . . 129
5.3 Two-compartment model . . . 131
5.3.1 Model development . . . 131
5.3.2 Goodness of fit . . . 138
5.3.3 External validation . . . 140
5.3.4 Clinical interpretation . . . 143
5.4 Single-patient predictions . . . 146
5.4.1 Simulated concentrations and graphical representation . . . 146
5.4.2 Clinical relevance . . . 149
5.5 Discussion . . . 152
5.6 Future perspectives . . . 153

II Glucose Dynamics 157

6 Physiology of glucose dynamics and mathematical models 158

6.1 Physiology of glucose homoeostasis . . . 159
6.1.1 Pancreas . . . 160
6.1.2 Liver . . . 162
6.1.3 Kidneys . . . 162
6.1.4 Muscles and adipose tissue . . . 163
6.1.5 Central nervous system . . . 164
6.2 Intravenous glucose-tolerance test . . . 165
6.3 Ultradian oscillations of insulin and glucose . . . 169
6.3.1 Multicompartmental ODE system . . . 170
6.3.2 DDE systems with explicit delays . . . 173
6.4 Models for critically ill patients . . . 179
6.4.1 Glucose and insulin subsystems . . . 179
6.4.2 Model for estimation of time-dependent parameters . . . 181

6.4.3 Adaptive model with endogenous insulin production 181

7 Glucose–Insulin–Glucagon dynamics **183**

7.1 Glucose–insulin dynamics 184

7.2 The glucose-insulin-glucagon model 189

7.3 Stability analysis 190

7.4 Numerical simulations 200

7.5 Model fitting 202

7.6 Conclusions and future perspectives 213

Conclusions **217**

A Effective delay from ordinary linear equations **221**

B Delay differential equations **225**

C Code structure **227**

C.1 Database synchronisation and restoring 227

C.2 Creation of views 228

D List of abbreviations and symbols **230**

Bibliography **241**

INTRODUCTION

Patients admitted to Intensive Care Units (ICUs) often manifest very atypical, extreme and rapidly evolving conditions. In these settings, the choice of appropriate pharmacological therapy can be extremely complex to determine and must take into account the effects of the combination of several variables. In particular, treatments tailored to the specific conditions of each patient must be adopted, often beyond standardized protocols. The identification of such a personalized therapy requires the analysis of a large amount of clinical and pharmacological data and of the possible scenarios produced by different therapeutic choices. Thus, it is of paramount importance to provide clinicians with efficient tools to handle all these variables.

In particular, when two or more factors interact in a nontrivial way, simple clinical reasoning is not sufficient and must be supported by more sophisticated analyses. For instance, the effect of a drug can be modified by the simultaneous administration of a second drug [78, 132, 147] or by the presence of an organ failure [167, 135] (e.g. renal failure can seriously affect the plasma concentration of many drugs [110]). A proper analysis is even more complex when patient conditions evolve rapidly and dynamic effects must be taken into account.

In this Thesis I shall focus on two specific aspects of the pharmacological treatment of critically ill patients. First, I shall consider the administration of antimicrobial drugs, whose effectiveness strongly depends on the achievement of minimum concentrations for a sufficient time [97]. Second, I shall investigate the physiological aspects at the bases of regulation of the glycaemic level [17, 34], whose time evolution is generally quite complex and difficult to predict. Although these problems are very different from a clinical perspective, the modelling of their pathophysiological mechanisms can be addressed using similar tools.

All the work done for this Thesis proceeds along five steps

1. development of informatics tools to load, manage, and process data;

2. study of the physiological aspects of the investigated clinical problem;

3. formulation in mathematical language of the relevant physiological mechanisms;

4. application of statistical tools to estimate the parameters of the mathematical models;

5. clincal interpretation of the results.

Data collection

Since the first step is common to all the subsequent analyses, I have devoted the first chapter of this Thesis to the presentation of *MargheritaTre* (M3), the electronic health record used to collect data, and the software I have written to preprocess those data.

M3 is an electronic health record dedicated to ICUs developed by GiViTI (Italian Group for the Evaluation of Interventions in Intensive Care Medicine), thanks to a research grant cofounded by the Italian Ministry of Health, four Italian Regions, and private companies. GiViTI is a collaborative research group, founded in 1991 to evaluate and improve the quality of care in the ICU [3]. Overall, GiViTI involves about 450 ICUs. Among them, about 250 units regularly collect epidemiological data (comorbidities, clinical conditions at admission, complications during stay, some data about treatments, and outcomes) of all admitted patients through the Prosafe software [8]. However, epidemiological data do not allow to study single clinical processes or trace the evolution of the patient's clinical picture over time. M3 was developed precisely to collect information with the necessary granularity to assess such phenomena.

The objective of the M3 project is to integrate clinical research and clinical practice through an electronic health record that both supports everyday practice in ICU and provides high-quality data for research purposes. To accomplish this purpose, M3 was designed by a multidisciplinary team involving clinicians, nurses, IT specialists, and epidemiologists. The ultimate aim of the project is to return the results of our research to clinicians, through the same software. In this direction, two modules were developed to generate alarms in the case of allergies to prescribed drugs and to support, through a step-by-step procedure, the evaluation of brain-death patients for organ donations.

The development and the maintenance of the software and the analyses of the data collected with both Prosafe and M3 were performed by the GiViTI coordinating centre, which is hosted by the Laboratory of Clinical Epidemiology of the Mario Negri Institute of Clinical Research IRCCS.

At the beginning of this Thesis project, four years ago, the M3 software was stable, and had already been used for six years in more than 20 ICUs. Overall the databases of all the ICUs contained records of more than 20 000 patients. However, databases had not yet been synchronised with our with servers and no tool was available to extract data and to process them. Thus, a

significant part of the work of this Thesis was devoted to developing the tools needed to make this huge amount of data ready to be analysed, as illustrated in Chap. 1.

Research with MargheritaTre

This work has allowed to exploit M3 data for several research projects. Our research efforts have been devoted mainly to the study of the management of infections from different perspectives and with different levels of details.

Along this line, we first performed an observational study to portray the strategies adopted in our ICUs for the utilization of antibiotic drugs. The specific aims of this project were to understand what molecules are adopted in prophylaxis, empirical, and target therapies in relation to infection sites and microorganisms, measuring the length of antibiotic treatments and describing the administration strategies. This analysis showed a large variability between ICUs with strategies which were not always optimal.

The results of this investigation has stimulated further questions. We have started a program of antimicrobial stewardship involving seven general ICUs with the objectives of: (1) understanding what are the motivations and the causes of the observed clinical decisions, (2) spotting problems and identifying solutions to improve strategies related to the management of infections, (3) measuring the effect of this stewardship program with rigorous performance indicators evaluated before and after the interventions. The project is conducted in collaboration with clinical experts (infectious disease specialist, clinical microbiologist, intensivist).

In parallel, having observed suboptimal choices of the dosage regimens, we decided to study the pharmacokinetic properties of some of the most used antimicrobial molecules in critically ill patients with the ultimate objective of implementing pharmacokinetic real-time simulators in M3 to directly support clinical decisions. The work realised for this Thesis and presented in its first part represents the first step of this long-term project.

We started also two projects that are not related with the management of infection. One is focused on a systematic review of databases containing drug-drug interactions with the objective of implementing in M3 a system of automatic alerts to signal life-threatening drug interactions in critically ill patients. The latter project is focused on the study of glucose metabolism. Being the subject of the second part of this Thesis, further details about this project will be provided below.

Antimicrobial Kinetics

Designing an appropriate antimicrobial treatment in ICU is very complex, as attested by the recurrence of cases of inappropriate or suboptimal therapies, as described in the literature [13, 94], often resulting from an incorrect estimate of drug pharmacokinetics and pharmacodynamics [188].

To properly choose the antimicrobial molecule, its dosage, and the manner of administration, several variables must be taken into account. For instance, the presence of various comorbidities or organ failures, hyperdynamic conditions associated with sepsis [55], or the adoption of treatments such as haemodialysis or haemofiltration [134, 48] can alter the plasma concentration of many drugs. Furthermore the effectiveness of a drug can be modified by the simultaneous administration of several other drugs with which it can interact [78, 132, 147]. This can result in either underexposure, which may reduce the therapeutic effect and favour the development of resistant bacterial strains, or overexposure, with possible increase of drug toxicity.

Pharmacokinetics and pharmacodynamics have been extensively investigated [97, 129] using in-vitro models [76] and from a clinical standpoint (e.g., see [56]). Mathematical models of pharmacokinetics and pharmacodynamics have also been constructed analytically [52] or using Monte Carlo simulations [66]. In particular, stress has been laid on the important role in the design of effective antimicrobial therapies played by parameters such as the minimum inhibitory concentration (MIC), the maximum plasma concentration ($C_{\max}$), and their ratio $C_{\max}$/MIC, the area under the time/concentration curve, and the time above MIC T_{MIC}. Furthermore, specific pharmacokinetic software (i.e. NONMEM, MWPharm, ADAPT II) has been developed to help clinicians achieve the desired values of the above parameters. However, translating the many advances of research into clinical practice is often problematic [115], both for cultural reasons and because available software is difficult to use in everyday life, partly considering that the parameters need to be constantly updated to yield appropriate estimates of drug doses, timing, and route of administration.

In Part I of this Thesis I investigate the pharmacokinetic properties of antibiotic kinetics focusing on vancomycin, a molecule widely used in ICU with a very narrow range between the minimum therapeutic concentration and the maximum concentration above which it becomes toxic. For this reason its concentration is measured in clinical practice when therapeutic drug monitoring (TDM) is required according to clinical judgement.

Preliminary analyses from *MargheritaTre* database showed that the concentration of vancomycin in patients admitted to the Italian ICUs participating in the project is often lower than the minimum therapeutic concentration or higher than the toxicity threshold. We observed that, by adopting standard dosage regimens, it is difficult to attain a correct plasma concentration when patients conditions are extreme (e.g., large distribution volumes, or renal failure). In those situations personalised dosage regimens should be designed. Predictive algorithms must be developed on the basis of pharmacokinetic models which take into account several clinical factors. The development of these models is possible only through large datasets with sufficient inter-individual variability.

As briefly introduced in the above section, the work presented in this Thesis represents the first

step of a larger long-term project based on our electronic health record. The specific aims of this Thesis are: (1) the development of tools to extract data from *MargheritaTre*, preprocess and make them available for analyses, (2) the construction of a population pharmacokinetic compartment model of vancomycin, (3) the external validation of this model.

My analysis was performed on retrospective data collected with *MargheritaTre* from 141 patients admitted to *MargheritaTre* in the ICU of the San Giovanni Bosco Hospital, Torino, Italy. This was one of the first ICU that joined the project and its database contains the largest set of patient records including measured values of plasma vancomycin concentration. External validation was performed on data collected from other five ICUs.

In Chap. 2, I review the most relevant aspects of pharmacokinetics, starting from physiologically principles and showing how compartment models can be mathematically interpreted as the coarse-grained approximation of physiological mechanisms. In Chap. 3, I review the mechanisms that can modify the kinetic properties of antibiotics in critically ill patients focusing on vancomycin kinetics and present a few important population models for this drug developed on critically ill patients. In Chap. 4, I illustrate the mathematical structure of the pharmacokinetic models and present the techniques used to construct a population model. In Chap. 5, I construct one-compartment and two-compartment population pharmacokinetic models to describe the evolution of the concentration of vancomycin in critically ill patients. I determine the clinical parameters that affect the evolution of plasma drug concentration, compare the performance of the two models, and test the reliability of their prediction with both internal and external validation. Finally, I discuss the limits of these models and briefly present AbioKin, an ongoing project designed to collect *ad hoc* data to study the pharmacokinetics of some of the antibiotic molecules most widely used in ICUs.

Glycaemic control

Critically ill patients often show high glycaemic peaks due to the development of insulin resistance. Since large amounts of blood glucose are highly toxic, it is considered good practice to adopt a tight glycaemic control by means of insulin, glucose and nutrition administration [126, 190]. However it is still unclear what real benefit is obtained by applying strict control [75, 123, 191, 124, 204] and what is the optimal target of blood glucose in critically ill patients [62, 202, 59].

Maintaining glycaemic values within the desired range is very difficult [17, 34]. On the one hand, in critically ill patients the glycaemic level often reaches very high values due to insulin resistance. On the other hand, patients under strict glycaemic control often experience glycaemic values below the desired range [119, 108], thus running the risk of a dangerous hypoglycaemic complications, as demonstrated in experimental studies [64].

Both hyperglycaemia and hypoglycaemia are associated with increased mortality. For these

reasons, reliable algorithms would be very useful to identify the most appropriate insulin therapy [14, 120].

Several existing models allow the simulation of the metabolism of glucose. Unfortunately, they all suffer from several drawbacks. Although models developed to describe glucose dynamics in healthy subjects or in patients affected by chronic diabetes are quite sophisticated [185, 118, 112, 107] from both physiological and mathematical standpoints [60, 113], they fail to reproduce the complex and rapidly changing dynamics observed in critically ill patients.

These models include several free parameters that must be estimated by a fitting procedure from patient data. To this aim, blood glucose concentration must be measured several times over a time interval where patient conditions are almost constant. Since critically ill patients are very unstable, this requires the collection of a large number of blood samples over a very short time (a few hours) [28]. However such a frequent sampling is generally impractical with standard diagnostic techniques (blood gas analysis) [193].

To overcome this drawback, simplified models with fewer parameters have been proposed to fit data from critically ill patients [44, 207, 82]. However, these models are too simplistic to reproduce the complex physio-pathological mechanisms at the basis of glucose dynamics on time scales longer than a few hours [192, 45]. Furthermore those models are not robust against rapid variations of the system parameters (e.g. in case of fast intravenous doses of glucose).

To support clinicians in the design of glucose- and insulin-administration regimens it would be important to implement in electronic health records simulators of glucose dynamic based on these models. However, the realization of such a tool represent a complex problem requiring to first identify a suitable model and then fit it to a wide dataset containing frequent measurements of blood glucose concentration. The objective of this Thesis is to identify a model appropriate from a theoretical physiological perspective, studying the feasibility of the construction of a reliable algorithm.

These questions are addressed by achieving the following specific aims (Part II): (1) study of the robustness of existing models in realistic conditions through numerical simulations, (2) proposal of a more robust and physiologically sensible model that can be adapted to extreme conditions of low or high blood glucose concentrations, (3) study of the mathematical properties of this model through a semi-analytical phase-space analysis of the stability of its solutions.

In Chap. 6, I review the main physiological processes at the basis of glucose homoeostasis and present several models describing the evolution of blood glucose concentrations under very different conditions. In Chap. 7, I first study the performance of one of the most complete models describing the coupled dynamics of glucose and insulin through numerical simulations. To overcome the drawbacks of this model I introduce a new system of equations to take into account the role of

counter-regulatory hormones, such as glucagon, in maintaining glucose levels within their normal range. I study the performance of my model with both semi-analytical analyses and numerical simulations. I also fit the model to real data, critically discussing my results.

A list of abbreviations and symbols is provided in Appendix D.

Chapter 1

DATA COLLECTION: MARGHERITATRE

New information technologies have allowed to more rapidly and efficiently manage, store, and share the amount of data generated during the health care process. Particularly, the introduction of electronic health records (EHR) has transformed the way information is documented and used in clinical practice.

Initially, EHRs were enthusiastically expected to improve the quality of care and increase the overall efficiency of the care processes [83]. However, some barriers hindered the diffusion of EHRs [11] and their expected benefits were confirmed only by a few studies [46, 137]. Nevertheless, EHR diffusion has now become widespread [81] and a recent meta-analysis reviewing 47 articles concluded that, while EHRs may reduce documentation time, improve guideline adherence, lower the number of medication errors and adverse drug effects, no associations with mortality were detected [39].

Diffusion of EHRs has generated huge amounts of data that can be mined to address countless research questions [100]. In the ICU in particular, a lot of information is collected per single patient: vital signs are recorded very frequently, several laboratory tests are performed every day, multiple drugs are administered at the same time, and sophisticated medical devices are employed in everyday clinical practice. The simultaneous availability of several parameters, which track the functionality of almost all organs, in large databases, provides an essential tool to the emerging field of network physiology, which aims to describe the structural and functional connectivity of physiological networks underlying both individual organs and the global behaviour at the organism level [19, 95, 18, 96]. In this framework, quite common conditions in critically ill patients such as coma or multiple organ failure can be described as a failure of communication and dynamic coordination among organs [38, 127, 15].

An example of the huge amount of clinical data collected in ICU is provided by MIMIC-

III (Medical Information Mart for Intensive Care), a freely accessible database, created to share data of over 50,000 patient admissions to the ICUs of Beth Israel Deaconess Medical Center in Boston [103]. This database has made it possible to investigate different aspects of the health care process from critical care, e.g. the validation of algorithms to identify septic patients [121] or the proposal of a new score for renal failure [178], to other related fields, such as laboratory medicine [91].

Although the potential of EHRs for clinical research is evident and universally recognized, ensuring high quality data [41] and guaranteeing homogeneous data collection and reproducibility of results is not straightforward [102, 16]. To overcome these concerns, the Italian Group for the Evaluation of Interventions in Intensive Care Medicine (GiViTI - Gruppo italiano per la Valutazione degli interventi in Terapia Intensiva) has developed *MargheritaTre* (M3), an EHR for ICU that serves a double purpose: to be a valid tool to support everyday clinical practice and to provide reliable and mostly structured data for clinical research [4, 63]. It is currently adopted by 40 units in Italy. Special attention was devoted to the development of the software interface. A good interface is indeed the *sine qua non* condition to facilitate data input, reduce documentation time, and guarantee the quality of collected data [10].

In this chapter I present the structure of M3 and the types of available data, describe the patient epidemiology, and illustrate how this database can be exploited to conduct research projects.

1.1 The electronic health record

1.1.1 Data structure

Compared to commercial EHRs, M3 does not allow for ICU-specific customisation in order to ensure quality and uniformity of data. Accordingly, modifications to the software proposed by clinicians must be evaluated by the coordinating centre before implementation in M3. Approved changes are then released to all ICUs.

Most information is stored by M3 in structured form (see Table 1.1): vital signs from ICU monitors, results of blood gas analyses and laboratory tests, pharmacological therapies, procedures and treatments (e.g. ventilation, haemodialysis, etc...), nursing activities, infections, organ failures, injuries.

Clinical notes, anamneses, and epicrises are usually recorded as free text in EHRs. However, to facilitate data analysis, M3 records this information in a partially structured form: clinicians can compose notes by selecting tags from a list of about 500 keywords.

Table	Type	Content	Rows
admissions	S	one row per patient, admission date and time	10^5
anamnesis	PS	medical history, comorbidities, allergies (free text and keywords)	10^6
diagnosis	PS	clinical conditions, surgical interventions, diagnosis, admission reasons (free text and keywords)	10^6
clinical notes	PS	note date, time, user, and content (free text and keywords)	10^8
vital signs	S	variable, date, time, value, units	10^8
laboratory tests	S	test name, date, time, value, units	10^7
microbiological tests	S	date, time, microorganism, antimicrobial susceptibility	10^6
drug administration	S	drug, start and end times, rate of infusion, drug amount, route	10^7
nutrition	S	nutritional bag, start and end times, rate of infusion, route	10^6
blood purification treatments	S	techniques, start and end times, parameters	10^5
procedures	S	type of procedure (e.g., ventilation), start and end times	10^7
nursing activities	S	type of activity, start and end times	10^6
pathologies	S	infections, failures, injuries, onset and resolution time	10^6

Table 1.1: Type of information stored in M3 tables (S = structured data, PS = partially structured data) and table dimension (number of rows).

Every piece of information is either input by doctors or nurses or imported from monitors, devices, or the hospital information system. For legal requirements, M3 traces date, time, and the user that inputs each item of data.

1.1.2 Real time analyses

Clinicians can analyse their data through graphical tools included in M3. These tools offer the possibility to plot time evolutions of the value of any clinical parameter or laboratory test and to create synoptic tables. They are routinely used by doctors and nurses to discuss patients' clinical picture in daily briefings. For more sophisticated analyses, data can be directly exported to xlsx files.

1.1.3 Support to clinical studies

M3 is designed to implement modules to support nurses and physicians in all phases of a clinical study. For each patient admitted to ICU, M3 checks the eligibility criteria to the study and guides the clinician in the enrolment phase. From such a module investigators can directly access the protocol of the study and print the form to obtain patient or next-of-kin informed consent. A

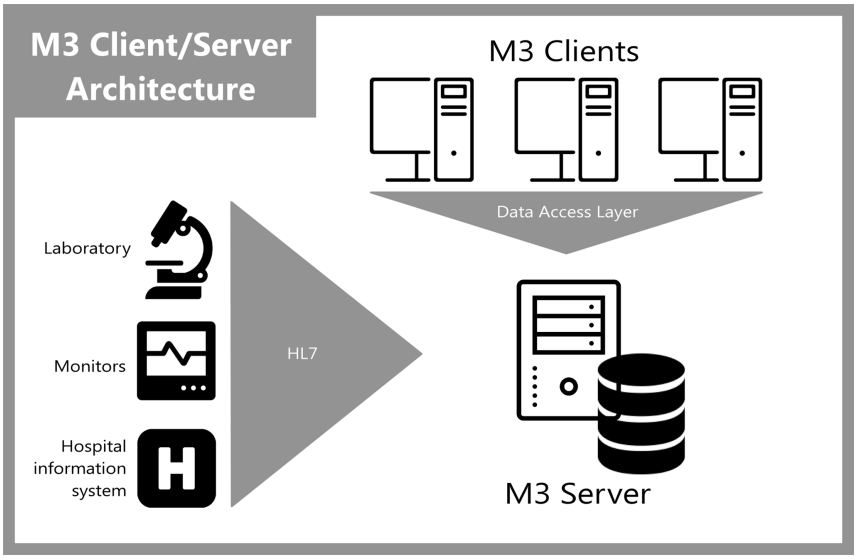

Figure 1.1: Architecture of M3.

series of automatic notes reminds physicians to withdraw biologic samples or perform laboratory tests, and the completeness of all required information is automatically checked.

1.1.4 Architecture

M3 has a client/server architecture (see Fig. 1.1), with one server per ICU. Clients are typically installed on bedside computers and at control desks. They have a modular graphical interface that allows doctors and nurses to input and visualize data for diagnosis, therapies, laboratory tests, etc...

Each module can load and store data independently from the other modules by communicating with the server, through a data access layer (DAL). The DAL manages all read and write operations on a relational database [7], where all data are stored in more than a hundred tables.

Automatic services import data from monitors, devices, and from the hospital information system and save them in the database through the server.

M3 implements a *safe crash* utility that periodically saves to pdf files the full records of patients present in the ICU (every 4 hours by default). This ensures that clinical activities are not stopped in case of a software crash.

1.2 ICU and patient characteristics

M3 contains data from 40 Italian ICUs: 34 general ICUs (GICU), 2 surgical ICUs (SICU), 1 cardiosurgical ICU (CICU), 2 neurosurgical ICUs (NSICU), and 1 high dependency unit (HDU).

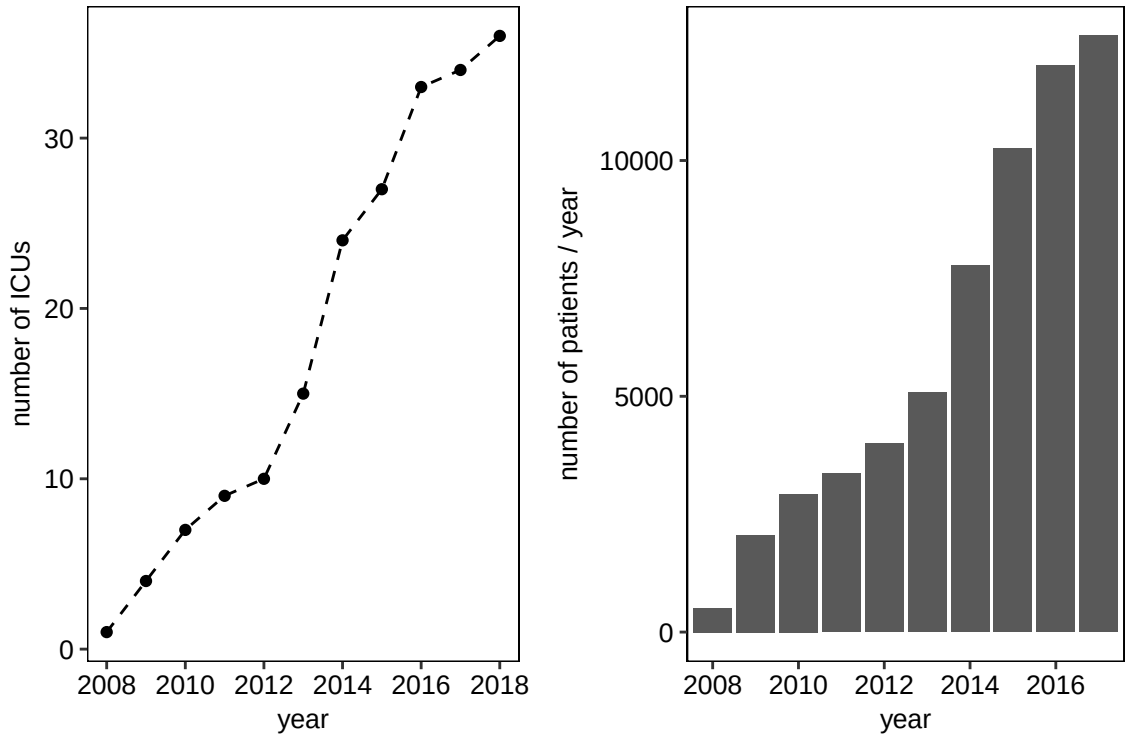

Figure 1.2: Number of ICUs participating in the M3 project (left panel) and number of recruited patients per year (Data from M3 database, February 1st, 2018 [63]).

After anonymisation, data are daily synchronized with a database at GiViTI coordinating centre, which coordinates all the projects based on M3 data.

In Fig. 1.2, I report the number of ICUs participating in the M3 project since the first M3 release in 2008 (left panel) and the number of recruited patients per year (right panel), which has grown over time. More than 12 000 patients per year were recruited in 2016 and 2017. The M3 database contained 65 987 patients on February 1st, 2018 [63].

The median age of patients is 69 years, 60% patients are male and 49% patients are non-surgical. The median length of stay in ICU is 2.2 days with an average ICU mortality of 17%. Table 1.2 provides a breakdown of the population by care unit, the occurrence of disease types at ICU admission and the frequency of three of the most common treatments in intensive care.

1.3 Data management

A rather complex process of data management is required to make *MargheritaTre* data available for the analyses. The code needed to synchronise data with our servers and to pre-process them was written in the first years of this PhD work and subsequently improved according to the needs of each analysis. In this section I shall briefly illustrate the architecture of this code. Further

	GICU	SICU	CICU	NSICU	HDU	Total
Number of ICUs	34	2	1	2	1	40
ICU admissions	58,752 (89%)	2,303 (3.5%)	2,133 (3.2%)	1,573 (2.4%)	1,226 (1.9%)	65,987 (100%)
Elective surgical	13,251 (23%)	1,198 (52%)	1,626 (76%)	404 (26%)	439 (36%)	16,918 (26%)
Emergency surgical	13,248 (23%)	665 (29%)	268 (13%)	546 (35%)	252 (21%)	14,979 (23%)
Non surgical	30,711 (52%)	440 (19%)	239 (11%)	539 (34%)	535 (44%)	32,464 (49%)
Not available	1,542 (2.6%)	0 (0%)	0 (0%)	84 (5.3%)	0 (0%)	1,626 (2.6%)
Age, years, median (Q1–Q3)	69 (55-78)	72 (61-81)	71 (62-78)	59 (43-72)	74 (63-82)	69 (55-78)
Gender, male	35,005 (60%)	1,358 (59%)	1,390 (65%)	896 (57%)	712 (58%)	39,361 (60%)
Cardiovascular disease	11,552 (20%)	189 (8.2%)	1,754 (82%)	36 (2.3%)	211 (17%)	13,742 (21%)
Gastrointestinal disease	9,480 (16%)	933 (41%)	40 (1.9%)	26 (1.7%)	274 (22%)	10,753 (16%)
Neurological disease	11,542 (20%)	69(3.0%)	71 (3.3%)	939 (60%)	142 (12%)	12,763 (19%)
Respiratory disease	11,949 (20%)	316 (14%)	81 (3.8%)	86 (5.5%)	215 (18%)	12,647 (19%)
Trauma	6,287 (11%)	138 (6.0%)	35 (1.6%)	411 (26%)	124 (10%)	6,995 (11%)
Infections	8,491 (14%)	148 (6.4%)	42 (2.0%)	22 (1.4%)	136 (11%)	8,839 (13%)
Lung	3,791 (45%)	65 (44%)	8 (19%)	5 (23%)	43 (32%)	3,912 (44%)
Abdomen	1,478 (17%)	39 (26%)	2 (4.8%)	7 (32%)	22 (16%)	1,548 (18%)
Urine	665 (7.8%)	2 (1.4%)	1 (2.4%)	0 (0%)	18 (13%)	686 (7.8%)
Skin	478 (5.6%)	5 (3.4%)	4 (9.5%)	1 (4.5%)	7 (5.1%)	495 (5.6%)
Brain	380 (4.5%)	0 (0%)	0 (0%)	7 (32%)	8 (5.9%)	395 (4.5%)
Blood	310 (3.7%)	0 (0%)	19 (45%)	0 (0%)	5 (3.7%)	334 (3.8%)
Bones	103 (1.2%)	0 (0%)	0 (0%)	2 (9.1%)	2 (1.5%)	107 (1.2%)
Other	2,390 (28%)	52 (35%)	8 (19%)	5 (23%)	54 (40%)	2,509 (28%)
Ventilation	44,407 (76%)	1,581 (69%)	1,836 (86%)	1,102 (70%)	412 (34%)	49,338 (75%)
CVC	39,119 (67%)	1,426 (62%)	1,845 (86%)	967 (61%)	463 (38%)	43,820 (66%)
Urinary catheter	51,197 (87%)	2,048 (89%)	1,967 (92%)	1,374 (87%)	1,121 (91%)	57,707 (87%)
ICU mortality	10,645 (18%)	183 (8.0%)	36 (1.7%)	161 (10%)	62 (5.0%)	11,087 (17%)
ICU length of stay, median days (Q1–Q3)	2.5 (0.9-7)	1.1 (0.8-2.2)	0.9 (0.8-1.5)	2.6 (1-9.8)	2.2 (1-4.3)	2.2 (0.9-6.6)

Table 1.2: Details of M3 patient population, occurrence of disease types at admission, treatments received, and ICU outcome by care unit: general ICU (GICU), surgical ICU (SICU), cardiosurgical ICU (CICU), neurosurgical ICU (NSICU), and high dependency unit (HDU). Percentages are computed out of the total number of admissions in the M3 database for the number of ICU admissions (second row), out of the number infected patients admitted to an ICU of the same type for the detail of the anatomic location of the infection, and out of the total number of patients admitted to an ICU of the same type for any other variable. (Data from M3 database, February 1st, 2018 [63])

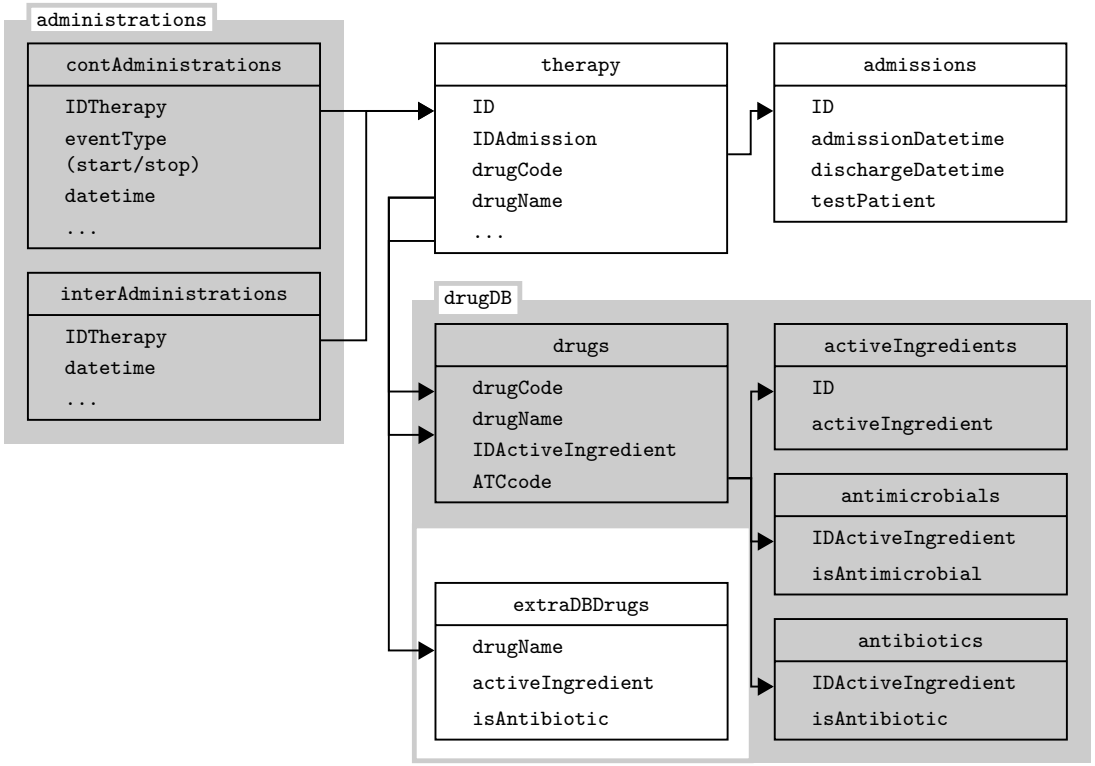

Figure 1.3: Structure of tables storing information of drug administration. Solid arrows denote join operations between tables.

details can be found in Appendix C.

Data from each ICU are automatically synchronized every day with our servers after de-identification. A daemon running on a Linux server checks every minute for database updates. Each database is then restored on a PostgreSQL Server version 10.3. This daemon is written in Python v.2.7.6 and is launched by a init.d script.

After restoration, data are transformed in a more structured and analysable form by means of several views (see Table 1.1). Data from all ICUs are finally stored in a single database. This part of the code is based on a Python script that calls bash scripts and is executed every night by crontab.

The structure of the PostgreSQL queries used to create data views for analysis is quite sophisticated. Each *MargheritaTre* database contains 146 tables that cannot be analysed in their original form. To gather all the information referring to the same clinical aspect (demographic information, drug administrations, laboratory tests, etc...), up to ten tables (or sometimes even more) must be joined together. To illustrate how this complexity is managed, Fig. 1.3 schematically represents the reconstruction process of the complete information on drug administrations starting from M3 tables.

Finally, I wrote several tools to make data available for analyses in R from the PostgreSQL

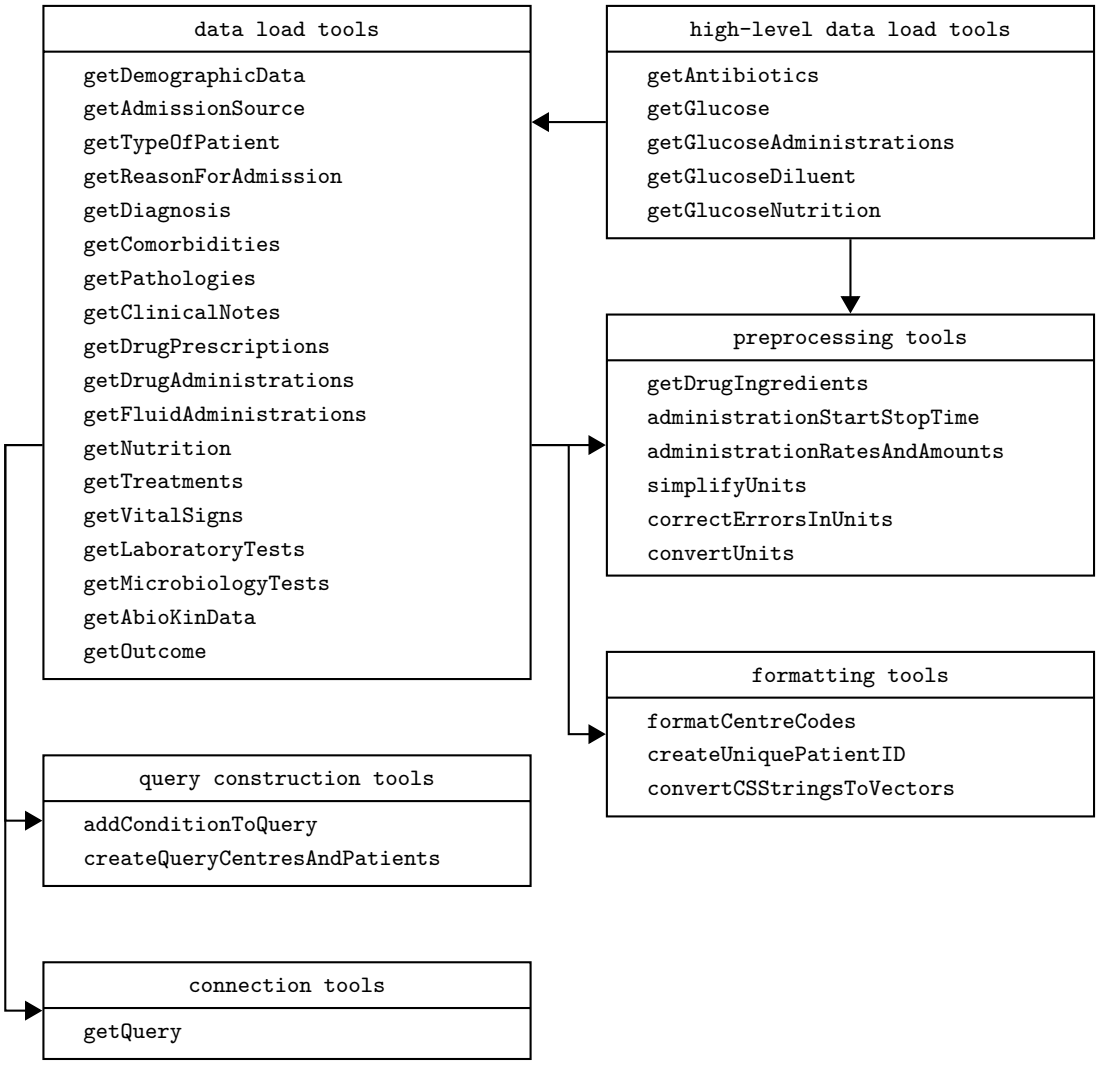

Figure 1.4: Structure of the R code that loads data from the PostgreSQL server and preprocesses them.

database. Tables of any type of data can be easily loaded by typing a single R command, possibly specifying selection conditions (e.g., ICU code, patient ID, type of drugs, etc...) in PostgreSQL language. A query is automatically created and passed to the PostgreSQL server. Data resulting from the query execution are loaded into R data frames and preprocessed. The structure of this R code is schematically illustrated in Fig. 1.4. There is a low level function (`getQuery`) that interacts with the PostgreSQL server, creating a connection, executing a query, and closing the connection. A set of high-level functions (data load tools) create a different query for each type of data, possibly appending selection conditions. Such queries are constructed with the help of the query construction tools and then executed on the server through `getQuery`. The result of the query is then processed by each data load function through a set of preprocessing tools and the final dataset is eventually returned ready to be analysed.

Higher level functions are written to manipulate data for any specific analysis. To load data relevant to the topics of this Thesis I wrote a set of functions to filter antibiotic administrations and

to retrieve any type of glucose administration. The latter task is quite complex because glucose is ubiquitous. Only a small amount of this molecule is administered directly as an active ingredient. In fact, glucose is generally administered through bags for enteral or parenteral nutritions, bags of fluid (e.g. glucose Ringer's solution), or even through glucose solutions used as a diluent for the intravenous administration of other drugs.

The functions `getGlucoseAdministrations`, `getGlucoseDiluent`, and `getGlucoseNutrition` load all data relative to drug administrations (active ingredient and diluent), nutrition, and continuous infusions of fluid solutions using the appropriate data load tools (`getDrugAdministrations`, getFluidAdministrations, and `getNutrition`). After data are loaded, these functions also read the composition of each drug and bag from the drug database and compute the rate and the total amount of administered glucose.

1.4 Data extraction for research purposes

To illustrate the potential of M3 to conduct research and clinical projects, I will discuss what kind of information can be derived from the M3 database. To this purpose I will present three examples related to the management of infections, one of the complex clinical problems that GiViTI is investigating from different perspectives and with different levels of detail.

At the epidemiological level, one can extract from M3 information on the usage of antimicrobial drugs in term of molecules, dosage, and routes of administration and study correlations with the epidemiology of the micro-organisms or with the reason for administration. Care processes can be investigated by analysing single clinical cases, relating the evolution of their condition to diagnostic results and therapeutic decisions. Finally, the analysis of series of vital signs, results of laboratory tests, and other clinical parameters allows the study of several pathophysiological aspects of critically ill patients.

These different levels of analysis are illustrated through two examples. In Fig. 1.5, I present the number of patients treated with antibiotics in 2017 by molecule and reasons for administration: empirical therapy, targeted therapy, and prophylaxis. This simple analysis provides an overall picture of the molecules used in the ICUs participating in the M3 project and reveals that the choice of the antibiotics is not always optimal. For instance, piperacillin/tazobactam is used in prophylaxis even if it should be reserved only for the treatment of infections [33]. Results of this kind are necessary to identify widespread problems and suggest how to design projects of antibiotic stewardship to improve the management of infections.

In Fig. 1.6, I study the typical evolution of the clinical picture of a 76 year-old male patient with

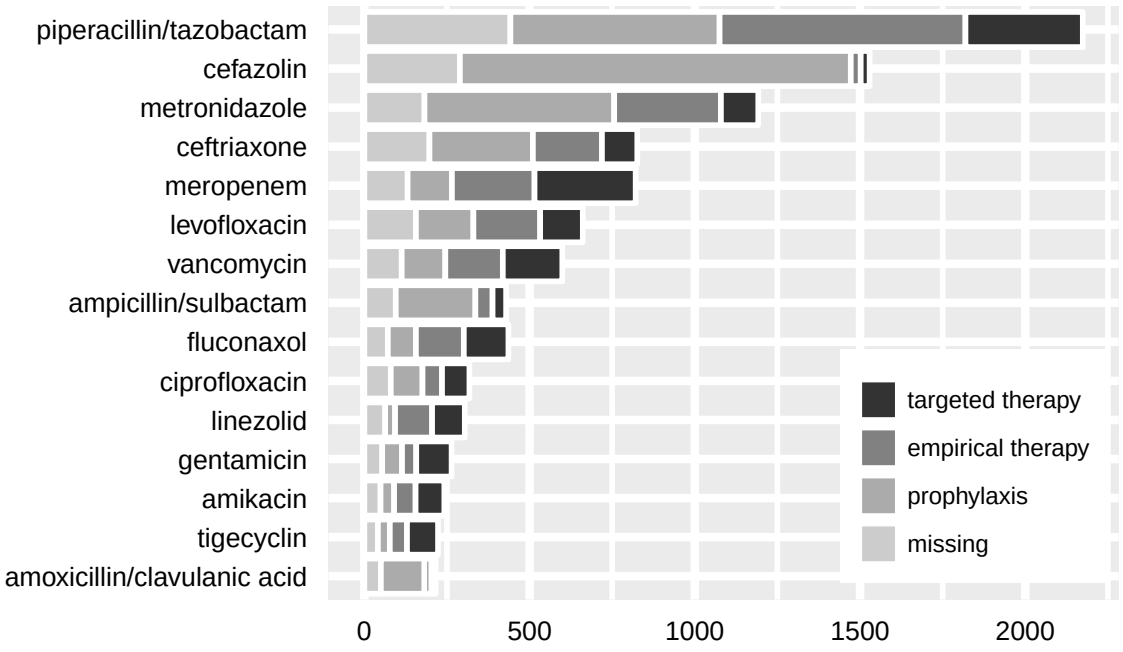

Figure 1.5: Number of patients treated with the 15 most administered antibiotics in 2017 by molecule and reason for administration.

a non-surgical infection of the urinary tract by integrating different pieces of information from his record. The horizontal bars in the upper part of the plot represent administrations of antimicrobial drugs in empirical (light grey) and targeted therapy (dark grey). Solid and dashed vertical lines indicate dates of isolations and results of antibiotic sensitivity tests, respectively. The lower panels report the evolution of temperature, heart rate, respiratory rate, arterial oxygen saturation, lactate plasma concentrations, white blood cell count and procalcitonin.

The patient's condition on ICU admission are critical: the values of heart and respiratory rates, lactate, white blood cell count, and procalcitonin are high. A urine sample is collected for microbiological culture and an aggressive empirical antibiotic therapy is started with meropenem and vancomycin. All clinical parameters rapidly improve. After three days the microbiological culture is available and the antibiotic therapy is de-escalated to a targeted therapy with ciprofloxacin. This treatment is suspended after three days when the clinical picture is stable. However, the white blood cell count increases again and a *Stenotrophomonas maltophilia* susceptible to co-trimoxazole is isolated in a bronchoscopic aspirate. Targeted therapy with co-trimoxazole is started. The following day the patient is transferred to the infectious disease unit, since his condition is no longer critical. This complete picture allows one to describe the full process of care, to study the clinical effects of the adopted therapeutic strategies, and to possibly identify interventions to improve the quality of care.

Starting from data collected with M3 we have recently started a program of antimicrobial stewardship involving seven general ICUs, where the analyses and the graphical tools presented in

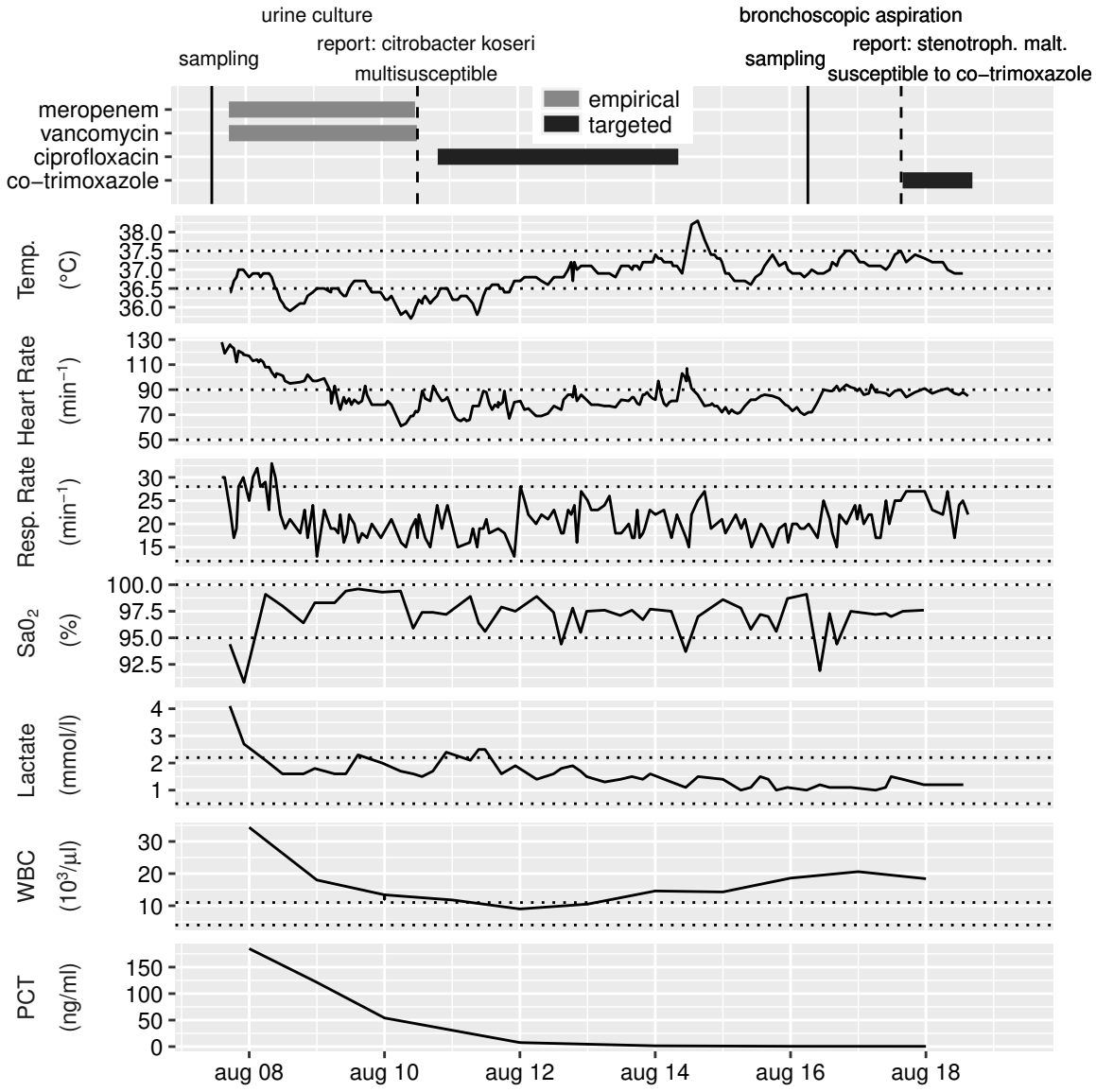

Figure 1.6: Antibiotic administrations, dates of microbiological cultures, antibiotic sensitivity report, and evolution of temperature, heart rate, respiratory rate, arterial oxygen saturation, plasma lactate concentration, white blood cell count (WBC), and procalcitonin (PCT) for a 76 year-old male patient with non-surgical infection of the urinary tract and hypovolaemic shock at admission. Temperature, heart rate, and respiratory rate were collected about 15 times a day, oxygen saturation and lactate 5 times a day, WBC twice a day, and PCT once a day. Reference ranges are indicated by dotted lines. The reference range of PCT is not reported since variations in PCT are more informative than its absolute value, interpretation of which may depend on patient conditions, site of infection, and causative microorganism [198]. The reference range for respiratory rate (12–28 min^{-1}) has been adapted to elderly patients (65–80 years old) [158].

this section, both at epidemiological and single-patient level, are used in clinical audits by experts to spot problems and identify solutions to improve antimicrobial administration strategies.

Part I

ANTIMICROBIAL PHARMACOKINETICS

Chapter 2

PHYSIOLOGY OF PHARMACOKINETICS

The success of a pharmacological therapy strongly depends on the selected dosage regimen. A drug may be ineffective when its concentration at the required site of action is too low. Conversely, a drug becomes toxic if its concentration exceeds a specific threshold. Thus, dosage, route, frequency, and duration of administration must be appropriately set to achieve the optimal drug efficacy.

The choice of these parameters is particularly crucial in critically ill patients. Their atypical and extreme conditions require the design of personalised dosage regimens. Furthermore, it is often important to reach the therapeutic target in a timely manner as the clinical picture may evolve very rapidly.

To answer the question how, how much, when, and for how long a drug should be administered, the kinetics of several processes must be taken into account. A drug must move from the site of administration to the site of action. When a drug is administered, the absorption process starts, it diffuses to tissues, also reaching those organs (liver and kidneys) that eliminate it. As soon as a drug is administered, the rate at which it enters the body exceeds the elimination rate. During this phase, drug concentration increases in both blood and tissues. Eventually, the elimination rate will overcome the absorption rate and drug concentration will decrease. If a drug is administered at a constant rate, absorption and elimination balance each other. In this scenario the drug concentration reaches a constant stationary level [162].

Figure 2.1 provides a graphical picture of all phases of drug kinetics, from administration to elimination. A drug can be administered through several sites (indicated by circles), that can be classified as either intravascular or extravascular. By intravascular routes, the drug is directly introduced into the bloodstream. Extravascular administration routes may be topic (e.g. dermal, pulmonary) or systemic (e.g. oral, sublingual, buccal, intramuscular, subcutaneous, rectal). When a drug is administered through one of the latter routes, it must be absorbed in order to enter the

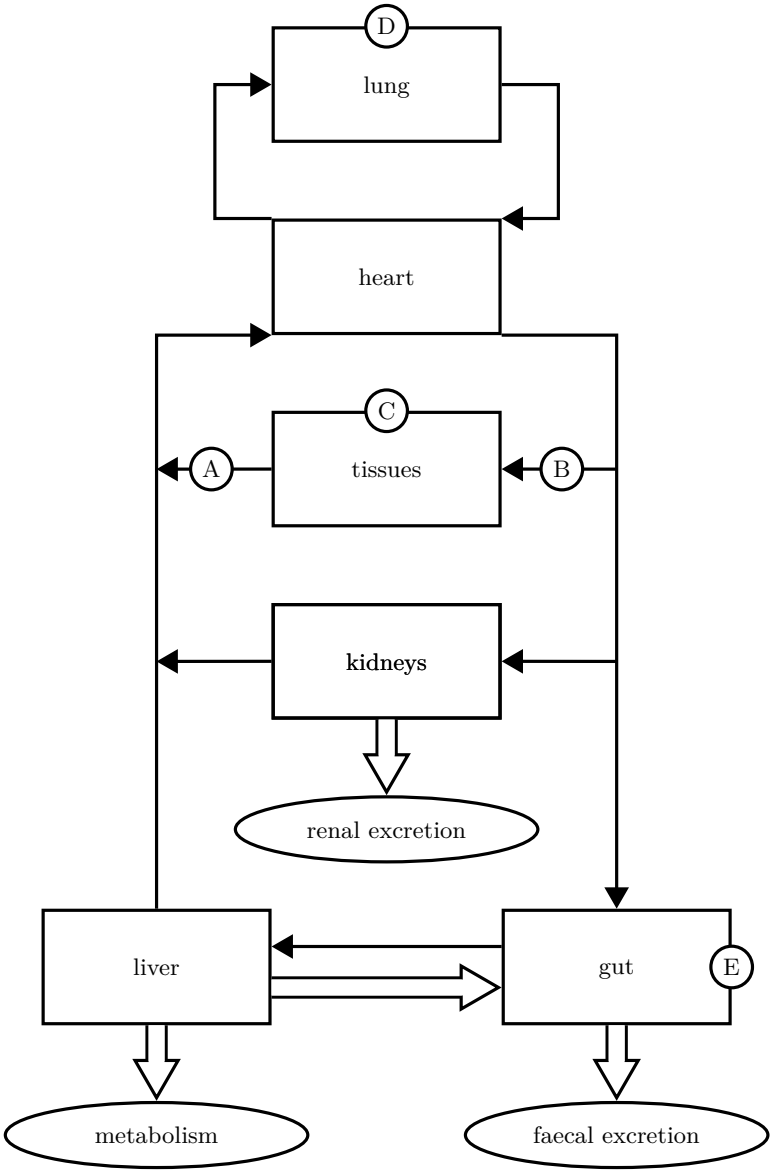

Figure 2.1: Schematic picture of the complex path followed by a drug. Possible sites of administration (circles) are: (A) veins, (B) arteries, (C) muscle and subcutaneous tissue, (D) lung, (E) gastrointestinal tract. Lines with arrows represent drug movements, thick arrows route of eliminations (adapted from Ref. [162]).

blood flow. The time scale of the absorption process strongly depends on the administration site and may require sophisticated mathematical modelling.

In this Thesis I shall focus only on drugs administered intravascularly, for which the absorption step is not required. This route is routinely used in the ICU as all patients have vascular accesses (arterial, venous peripheral, and/or venous central) and infusion pumps are used to precisely control rates and amounts of administered drugs.

From mathematical and statistical perspectives, the absence of the absorption process strongly simplifies pharmacokinetic analyses and makes results more reliable. When a drug directly enters the blood, there is no uncertainty associated with the duration and the rate of the absorption

process, which may show important between-patient variability.

Once the pharmacokinetic properties of a drug are understood, one must consider its pharmacodynamic characteristics, i.e., determine how a given concentration in the site of action correlates with the magnitude of the produced effect. The knowledge of both kinetic and dynamic aspects allow to design an effective dosage regimen to achieve the therapeutic objective. For instance, to design an effective antimicrobial therapy, one must take into account that the optimal therapeutic concentration of antimicrobial drug at the site of an infection depends on both site and causative microorganism [166].

The main physiological mechanisms at the basis of these processes are briefly described in this Chapter at the general level and specific pharmacokinetic properties of antimicrobials are reviewed in Chap. 3. This Chapter is organized to provide a review of pharmacokinetics principles with a bottom-up approach. First, in Sec. 2.1 I briefly present the main features of microscopic physico-chemical principles governing drug kinetics (membrane crossing, perfusion, protein binding). Second, in Sec. 2.2 I describe the macroscopic processes (distribution, elimination) resulting from this microscopic mechanisms. Processes which are not relevant to the following analyses are not discussed (e.g., absorption). Third, Sec. 2.4 is devoted to introduce the basic concepts of compartmental models, which naturally approximate the complex pharmacokinetic processes presented in Sec.2.2. In compartmental models, the evolution of drug concentration is described by simplified systems of differential equations where the contribution of the physiological processes is summarized into few parameters. The analyses of this Thesis are conducted at this corse-grained level of approximation. A more detailed review of the methodological aspects at the basis of the construction of this models and the estimation of their parameters is presented in Chap. 4.

Finally, in the last section of this Chapter, I review how pharmacokinetic processes are affected by pathological conditions in critically ill patients. The physiological variables tested as covariates in the construction of the models presented in Chap. 5 are chosen as markers of those conditions.

2.1 Physico-chemical mechanisms

2.1.1 Movement through membranes

The microscopic processes at the basis of all pharmacokinetic aspects (absorption, distribution, and elimination) ultimately consist of the movement of molecules through membranes. To construct a realistic mathematical model describing pharmacokinetics it is therefore important to understand the physical and chemical mechanisms according to which drugs move through membranes.

Cellular membranes are composed by a lipid bilayer with embedded proteins. The hydrophobic portion of lipid molecules is oriented towards the centre of the membrane while the hydrophilic end is directed toward the surrounding aqueous environment. Furthermore, between some cells (e.g., in capillary membranes and intestinal epithelium) there are channels filled by aqueous liquid. The aggregate of several layers of cells and interstitial spaces form macroscopic functional membranes (e.g., cells and interstitial space between the gastric lumen and capillary blood), which, depending on their composition, determine how and how fast molecules move from one body compartment to the other, facilitating or impeding drug movement to different extents.

Diffusion and Convection

The simplest process by which drugs cross membranes is diffusion, which is a passive mechanism driven by concentration gradient. In this process the rate at which molecules cross the membrane is symmetric in both directions. The net flux F of molecules crossing the membrane from side 1 to side 2 is proportional to the difference between the concentrations C_1 and C_2 on the two sides of the membrane

$$F = d\,S\,(C_1 - C_2)\,, \tag{2.1}$$

where d is a diffusion coefficient expressing the permeability of the membrane and S is its surface area. Note that $d\,S$ has the units of flow (volume/time), and consequently, d has units of velocity (space/time). The diffusion rate depends on geometric features (the membrane surface S) and physical-chemical properties of the membrane, and of the considered drug which are parametrised by d. The permeability d is mainly affected by molecular size, lipophilicity, charge, and membrane thickness. For instance, water-soluble molecules can move through narrow channels between cells and diffusion is boosted by water convection. Small lipid-soluble non-ionised drugs tend to penetrate lipid membranes more easily. Conversely, large, polar, and charged molecules move slowly across membranes.

When drug transport is governed by diffusion processes, the net flux is maximum if there is no drug on one side of the membrane, while it vanishes when drug concentration is the same on both sides. Thus, the stationary solution of such a system consists of a dynamic equilibrium with $C_1 = C_2$.

Carrier-Mediated Transport

Certain types of molecules (e.g., hydrophobic polar molecules) are not able to cross the cell-membrane through free diffusion. The passage across the membrane of such molecules is then mediated by membrane transport proteins, through two processes: passive facilitated diffusion and active transport.

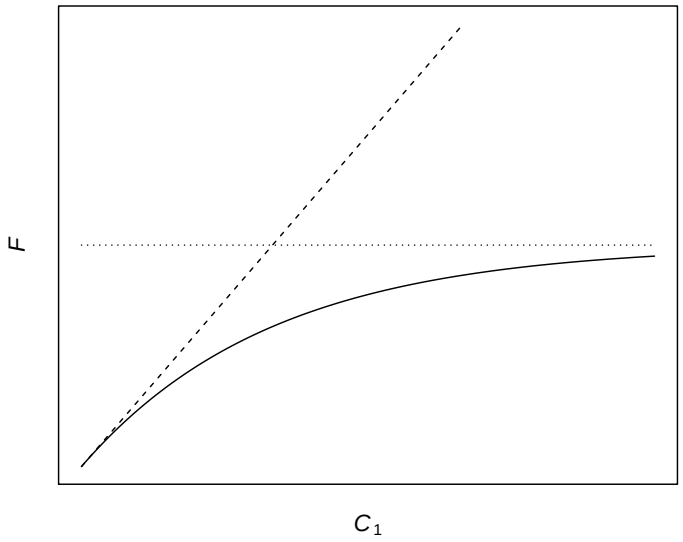

Figure 2.2: Initial flux (internal concentration $C_2 = 0$) of molecule transport for passive (dashed) and facilitated (continuous) diffusion as a function of the external concentration C_1. The dotted line represents the limiting rate of F for facilitated diffusion at large C_1.

Facilitated diffusion is a passive mechanism that does not require utilisation of chemical energy and the passage of molecules is driven by the concentration gradient. However, there are several differences with respect to the simple diffusion illustrated above. Since this mechanism is based on the binding between the carrier and the transported molecule, the rate of transport may depend on temperature in a stronger way than simple diffusion. Whereas the transport rate of simple diffusion is linear in the concentration gradient between the two sides of the membrane [see Eq. (2.1)], the facilitated-transport rate may have a concentration-dependent saturation threshold. This behaviour is illustrated in Fig. 2.2, where the transport rate F for facilitated (solid line) and simple (dashed lines) diffusion are compared as functions of the external concentration C_1, for $C_2 = 0$. The flux F of facilitated diffusion saturates at a limiting value (dotted line) when C_1 becomes large.

Active transport requires energy consumption to forcedly move molecules from one side to the other of the membrane against their concentration gradient. Primary active transport uses ATP as the source of energy. This mechanism is typically used to transport metal ions through ion pumps or ion channels. In secondary active transport cotransporters exploits electrochemical potential difference as the source of energy. These carriers use energy from the favorable movement of one molecule down to its concentration gradient to move another molecule against its concentration gradient.

2.1.2 Perfusion

To describe and quantify how drugs move within the body, it is not sufficient to simply understand how molecules are transferred through membranes separating one tissue from another. It is also necessary to estimate how drugs are delivered to those tissues by blood. In other words, it is not possible to disentangle permeability and perfusion considerations.

When membranes have a high resistance to the drug, the rate of transport is limited by low permeability. Conversely, for highly permeable membranes, the step limiting the rate of drug transfer is perfusion. As shown in Eq. (2.1), molecules can only be transported if a concentration gradient is maintained. When membrane crossing is fast, identical concentrations on both sides are rapidly reached. The flux of molecules ceases until the concentration gradient is restored by new molecules delivered by the bloodstream.

Thus, the transfer rate of small lipophilic molecules is limited by perfusion, while the transport of large polar molecules is less sensitive to changes in perfusion but is limited by membrane permeability.

2.1.3 pH

If a drug is an acid or a base, its degree of ionisation may affect its transport rate. Ions are hardly able to diffuse across membranes, as illustrated in Sec. 2.1.1. For weak acids and bases it depends on the drug dissociation constant K_a and on the pH of the environment. Taking the non-ionised form of an acid drug to be HA, the relation for acid-base dissociation in the Brønsted–Lory model is

$$\mathrm{HA} + \mathrm{H_2O} \overset{K_a}{\rightleftharpoons} \mathrm{A^-} + \mathrm{H_3O^+}. \tag{2.2}$$

The equilibrium condition is fixed by

$$K_a = \frac{\left[\mathrm{A^-}\right]\left[\mathrm{H_3O^+}\right]}{\left[\mathrm{HA}\right]}, \tag{2.3}$$

which may be written using the linear operator p $[\mathrm{p}x = -\log_{10}(x)]$ as

$$\log_{10}\left(\frac{\left[\mathrm{HA}\right]}{\left[\mathrm{A^-}\right]}\right) = \mathrm{p}K_a - \mathrm{pH}. \tag{2.4}$$

where $\mathrm{pH} = \mathrm{pH_3O^+}$. Defining the non-ionised fraction of the acid HA as

$$f_{ua} = \frac{\left[\mathrm{HA}\right]}{\left[\mathrm{A^-}\right] + \left[\mathrm{HA}\right]}, \tag{2.5}$$

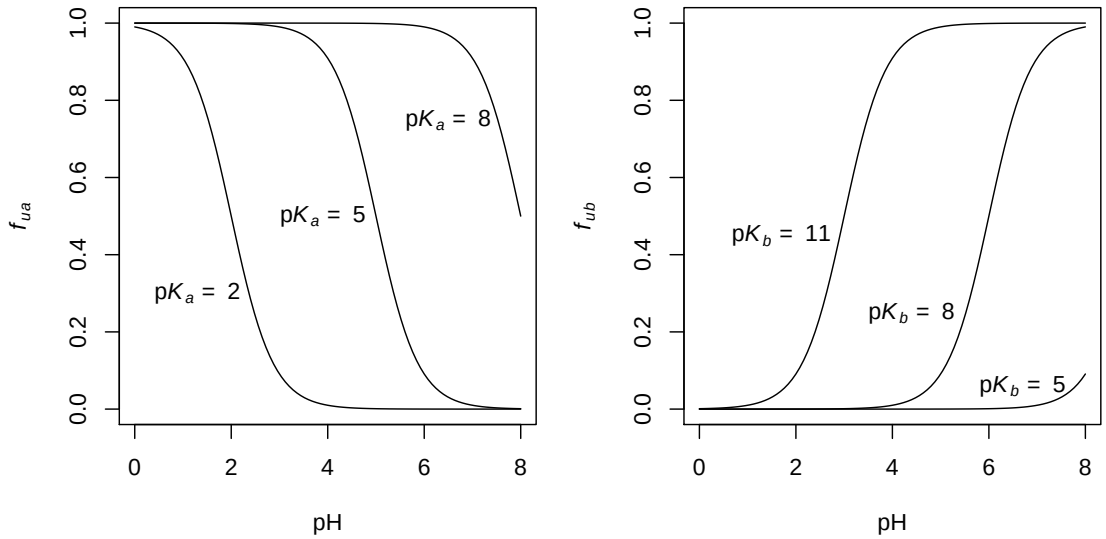

Figure 2.3: Non-ionised fraction f_{ua} (left panel) and f_{ub} (right panel) for different acids ($\mathrm{p}K_a$ = 2, 5, 8) and bases ($\mathrm{p}K_b$ = 5, 8, 11, corresponding to $\mathrm{p}K_a$ = 9, 6, 3 of the conjugate acid), respectively. Very weak acids ($\mathrm{p}K_a = 8$) are mostly non-ionised in all physiological environments. Only extremely weak basis are non-ionised in environments with physiological values of the pH.

one obtains

$$f_{ua} = \frac{1}{10^{\mathrm{pH}-\mathrm{p}K_a} + 1}. \tag{2.6}$$

According to this equation (see Fig. 2.3, left panel), drug is completely non-ionised if $\mathrm{pH} \ll \mathrm{p}K_a$ and ionised when $\mathrm{pH} \gg \mathrm{p}K_a$. Very weak acids ($\mathrm{p}K_a > 8$) are predominantly non-ionised in all physiological environments ($\mathrm{pH} < 8$).

For a basic drug B,

$$\mathrm{B} + \mathrm{H_2O} \overset{K_b}{\rightleftharpoons} \mathrm{BH^+} + \mathrm{OH^-}, \tag{2.7}$$

with

$$K_b = \frac{\left[\mathrm{BH^+}\right]\left[\mathrm{OH^-}\right]}{\left[\mathrm{B}\right]}. \tag{2.8}$$

Since $\mathrm{pH} + \mathrm{pOH} = \mathrm{p}K_w$, where K_w is the constant of water self-ionisation, with $\mathrm{p}K_w \approx 14$, the ratio between non-ionised and ionised forms of the basic drug B can be written as

$$\log_{10}\left(\frac{[\mathrm{B}]}{\left[\mathrm{BH^+}\right]}\right) = \mathrm{p}K_b - \mathrm{pOH} = \mathrm{p}K_b - \mathrm{p}K_w + \mathrm{pH} = \mathrm{pH} - \mathrm{p}K_a, \tag{2.9}$$

where K_a is the acid dissociation constant of the conjugate acid $\mathrm{BH^+}$, which satisfies $\mathrm{p}K_a + \mathrm{p}K_b = \mathrm{p}K_w$. Consequently, the non-ionised drug fraction for the basis B is

$$f_{ub} = \frac{1}{10^{\mathrm{p}K_w - \mathrm{p}K_b - \mathrm{pH}} + 1}. \tag{2.10}$$

This relation shows that for physiological values of pH, which are less than 9 in all body fluids, basic drugs are almost completely ionised $f_{ub} \ll 1$ (see Fig. 2.3, right panel), except for very weak bases with $\mathrm{p}K_b > 8$.

As an example, let me consider the passage of drugs through a membrane separating a first region with acid environment ($\mathrm{pH}_1 < 7$) from a second region with $\mathrm{pH}_2 = 7$. The above analysis suggests that the transport of very weak acids is independent of the pH of the first region, since these drugs are completely non-ionised on both sides of the membrane. Conversely, the transport of drugs with a $\mathrm{p}K_a < 7$ strongly depends on the pH of the environment of the first region. For these drugs the transport rate is rapid when $\mathrm{pH}_1 < \mathrm{p}K_a$, since in such an environment most of the acid drug is still non-ionised. When the pH of the environment of the first region is larger than $\mathrm{p}K_a$, the acid drug is instead ionised and the transport rate becomes small. Analogous considerations show that only extremely weak ($\mathrm{p}K_b > 11$) bases are transported independently of the environmental pH of the first region. The passage of stronger bases across this barrier is instead very slow, since those bases exist almost exclusively in an ionised form.

2.1.4 Protein binding

Several drugs bind to plasma proteins (mainly albumin). Protein binding and dissociations are reversible and quasi-instantaneous processes so that an equilibrium is established between bound and unbound forms. Since proteins cannot easily cross membranes, only the unbound form is transferred. Thus, protein binding can affect the rate of drug transport when the transfer rate is limited by permeability. In this case only a small part of the drug delivered to the tissue can cross the membrane. Altered protein binding will thus influence the transport rate.

Conversely, if the rate-limiting factor is perfusion, both dissociation and diffusion of the unbound molecule through the membrane are so rapid that the rates of delivery and transport are equal. In this case an alteration in the protein content is not expected to influence the transfer rate.

2.2 Macroscopic pharmacokinetic processes

In this Section I discuss the macroscopic pharmacokinetic processes focusing on those aspects which are more relevant for the construction of the pharmacokinetic models presented in the following Chapters. I present the physiological mechanisms on which these processes are based, discussing how they depend on physiological parameters and modelling this dependence in mathematical formalism.

2.2.1 Distribution

Distribution refers to the transfer of a drug from one location to another within the body, from the administration site to the sites of action and elimination. This complex process results from the interplay of the microscopic mechanisms outlined in the previous section. A complete description of those processes would require drug concentration to be measured in several tissues. However it is not possible to obtain all the desired measurements in humans. Information on distribution rates must be derived from observation of drug concentrations in plasma, combined with good physiological models.

Two quantities characterise how drug distributes within the body: the volume where a drug can diffuse and the time taken to fill this volume.

Distribution volume

From blood a drug may move to several tissues, each of them having its own volume and a different affinity with the drug. Thus, drug concentrations may differ from one tissue to another. Accordingly, the total amount of drug present in the body is

$$Q = V_p\, C_p + \sum_i V_{t,i}\, C_{t,i}, \tag{2.11}$$

where V_p, C_p are plasma volume and drug concentration, and $V_{t,i}$ and $C_{t,i}$ are the volume and the concentration reached by the drug in each tissue. To construct a mathematical formulation of the distribution process it is convenient to simplify this picture. To reduce the number of variables several tissues are grouped in few *compartments* (see Chap. 4), each with effective volume V_i and concentration C_i.

Similarly one can define a total apparent volume, as the volume required to store the total amount of drug Q with the plasma concentration C_p, namely

$$V_a = \frac{Q}{C_p}. \tag{2.12}$$

The apparent volume may differ from the total physical volume $V_{\text{tot}} = V_p + V_t$, where V_t is the tissue volume, if drug concentration in tissues and plasma differ. Defining the ratio

$$r_c = C_t/C_p \tag{2.13}$$

between tissue and plasma concentrations C_t and C_p, the total drug amount is

$$Q = (V_p + r_c\, V_t)\, C_p. \tag{2.14}$$

From this expression, $r_c\,V_t$ is the apparent tissue volume and the total apparent volume reads

$$V_a = V_p + r_c\,V_t. \tag{2.15}$$

For some drugs r_c is very large. In this case, the apparent volume may be much larger than the total body volume.

Drug distribution is strongly affected by protein binding since only unbound drug can generally cross membranes and pass from blood to tissues and *vice versa*. Thus, if a drug is bound to proteins to a different extent in plasma and tissues, then r_c may be different from 1.

I define the fraction of drug unbound and bound to plasma proteins as

$$f_u = \frac{C_u}{C_p}, \qquad f_b = \frac{C_b}{C_p}, \tag{2.16}$$

where C_u and C_b are the concentrations of unbound and bound drug, respectively. These fractions depend on drug-protein affinity, characterised by an association constant K_a, which defines the equilibrium of the reaction

$$\text{drug} + \text{protein} \overset{K}{\rightleftharpoons} \text{drug-protein complex}. \tag{2.17}$$

By defining the unbound and bound protein concentrations as P_u and P_b, the concentration of the drug-protein complex is $P_b = C_b$ (assuming that each protein has only one binding site) and

$$K = \frac{C_b}{C_u\,P_u}. \tag{2.18}$$

The fraction of bound and unbound drugs can be computed by solving the above equation, imposing $C_u + C_b = C_p$ and $P_u + P_b = P_p$, where P_p is the total plasma concentration of proteins. A straightforward calculation yields

$$K\,C_p\,f_u^2 + [K\,(P_p - C_p) + 1]\,f_u - 1 = 0, \tag{2.19}$$

In the limit where the protein concentration is much larger than drug concentration ($P_p \gg C_p$)

$$f_u \approx \frac{1}{1 + K\,P_p}. \tag{2.20}$$

All drug molecules are trivially unbound if $P_b \ll K^{-1}$, whereas the unbound fraction vanishes when $P_b \gg K^{-1}$. Since only unbound drug is transported from blood to tissues, this relation suggests that the total apparent volume is strongly affected by plasma protein concentrations. If

drug appears in bound and unbound forms also in tissues, the fraction of unbound drug in tissues is

$$f_{tu} \approx \frac{1}{1 + K_t\, P_t}. \tag{2.21}$$

where P_t is the protein concentration in tissue and K_t is the association constant in tissue, which may be different from K. For a passive membrane, the equilibrium drug concentration is reached when the unbound concentrations in plasma and tissues are equal $C_u = C_{tu}$, namely

$$f_u\, C_p = f_{tu}\, C_t. \tag{2.22}$$

The concentration ratio between tissue and plasma is

$$r_c = \frac{f_u}{f_{tu}} = \frac{1 + K_t\, P_t}{1 + K\, P_p}. \tag{2.23}$$

The apparent distribution volume of Eq. (2.15)

$$V_a = V_p + \frac{f_u}{f_{tu}}\, V_t. \tag{2.24}$$

This relation shows that the apparent distribution volume is large when drugs are highly bound in tissues and almost unbound in plasma. If the concentration of plasma proteins increases (e.g. by administration of albumin), the fraction of unbound drug in plasma f_u decreases, drug concentration in tissues decreases and so does the apparent distribution volume. For instance, if an antimicrobial drug which binds to albumin is administered when the level of plasma albumin is high, it will rapidly reach a high concentration in plasma (because of the reduced total apparent volume) but the concentration in tissue may be lower. The dosage regimen must then be adapted according to the site of the infection (bloodstream or tissues).

Rate of distribution

The time required to achieve the therapeutic target of drug concentration at the site of action strongly depends on blood perfusion in tissues and membrane permeability to the administered drug.

Perfusion. Drug penetration at the site of infection is limited by perfusion when membranes oppose no barrier to drug transport. In this case the flux of drug from blood to the tissue depends solely on the drug's *presentation* and *leaving* rate to/from the tissue. The former is $F_B\, C_A$, where F_B is the blood flow and C_A is the arterial drug concentration, the latter is $F_B\, C_V$, where C_V is

the venous drug concentration. In this case the net drug uptake is

$$F = F_B\, f_u\, (C_A - C_V) \tag{2.25}$$

To compute the time to fill the tissue with drug, assuming that the arterial drug concentration remains constant, it is enough to solve a simple linear first-order differential equation describing the variation of the amount of drug in the tissue:

$$\frac{\mathrm{d}Q_t}{\mathrm{d}t} = F. \tag{2.26}$$

Using Eq. (2.25), $Q_t = V_t\, C_t$, and the equilibrium condition between venous and tissue drug concentrations [Eq. (2.13)], $C_t = r_c\, C_V$, with $r_c = f_u/f_{tu}$ [Eq. (2.23)] which holds if there is no impedance to drug movement in the tissue, the above equation becomes

$$\frac{\mathrm{d}C_t}{\mathrm{d}t} + \kappa_e^{\mathrm{perf}}\, C_t = \kappa_p\, f_u\, C_A \tag{2.27}$$

where I have defined the perfusion rate κ_p

$$\kappa_p = \frac{F_B}{V_t} \tag{2.28}$$

as the amount of blood reaching the tissue per unit time and unit tissue volume, and the perfusion exit rate κ_e^{perf} as

$$\kappa_e^{\mathrm{perf}} = \frac{F_B\, f_{tu}}{V_t} = \kappa_p\, f_{tu}. \tag{2.29}$$

The solution of the above equation is

$$C_t(t) = r_c\, C_A \left[1 - e^{-\kappa_e^{\mathrm{perf}}\, t}\right]. \tag{2.30}$$

assuming that at time $t = 0$ there is no drug in the tissue. The half-life time to fill the tissue is therefore

$$\tau_{\mathrm{perf}} = \frac{\log(2)}{\kappa_e^{\mathrm{perf}}} = \frac{\log(2)}{\kappa_p\, f_{tu}}. \tag{2.31}$$

The time to fill the tissue is shorter if the perfusion rate is higher. Furthermore it takes longer when the drug affinity with the tissue is greater (f_{tu} small), since a larger amount of drugs can be stored in the tissue.

Permeability. Drug distribution is limited by permeability when the permeability constant d or the contact surface S [see Eq. (2.1)] are small and when the perfusion rate κ_p is large. In this case

the uptake of drug by tissue is small compared with the amount of drug presented by blood to the tissue and the venous and arterial concentration are almost the same $C_A = C_V$. The differential equation expressing the time variation of the total amount of drug in the tissue now reads

$$\frac{\mathrm{d}Q_t}{\mathrm{d}t} = d\,S\,(f_u\,C_A - f_{tu}\,C_t)\,, \tag{2.32}$$

whose solution is identical to Eq. (2.30), provided that the exit rate for perfusion is replaced with the new permeability-limited exit rate

$$\kappa_e^{\mathrm{perm}} = \frac{d\,S\,f_{tu}}{r_c\,V_t}. \tag{2.33}$$

The corresponding half-life time is $\tau_{\mathrm{perm}} = \log(2)\,V_t/d\,S\,f_{tu}$.

2.2.2 Elimination

Drugs are eliminated from the body through two mechanisms: excretion and metabolism. Excretion occurs via the bile, through the breath, but mainly via the kidneys. Metabolic elimination generally occurs in the liver through several possible pathways based on a few common chemical mechanisms: oxidation, reduction, hydrolysis, and conjugation.

In this Thesis I shall not enter into the details of the chemical reactions at the basis of metabolic processes. Rather I shall provide a phenomenological description of the kinetic parameters relevant to the analysis of the evolution of drug concentrations in plasma and tissues.

Indeed, for the purposes of a pharmacokinetic description, a single parameter, drug clearance, is enough to model both excretion and metabolisms. The elimination rate $\mathrm{d}Q/\mathrm{d}t$ is in general proportional to drug concentration. Accordingly, drug clearance k_{drug} is defined as the relative proportionality constant:

$$\frac{\mathrm{d}Q}{\mathrm{d}t} = k_{\mathrm{drug}}\,C_p. \tag{2.34}$$

The constant k_{drug} has the units of flow, that is volume over time. The rate of presentation of a drug to a site of elimination is given by the product of blood flow and arterial drug concentration $F_B\,C_A$. If elimination is not complete, blood still carries some drug after leaving the elimination organ. The leaving rate is $F_B\,C_V$, with C_V being the venous concentration. The corresponding elimination rate is $F_B\,(C_A - C_V)$ and the extraction ratio r_e, the amount of eliminated over presented drug, is

$$r_e = 1 - \frac{C_V}{C_A}. \tag{2.35}$$

Using this relation in Eq. (2.34),

$$k_{\text{drug}} = r_e \, F_B, \tag{2.36}$$

drug clearance is the product of blood flow and the fraction of eliminated drug. Thus, it is possible to interpret it as the flow of blood that is completely cleared of drug. For $r_e \leq 1$ drug clearance cannot exceed the blood flow in the elimination organ, i.e. about 1.1 and 1.35 l/min in kidneys and liver, respectively.

When several mechanisms contribute to drug elimination, the total elimination rate is the sum of the elimination rates of the single processes. Hence the total clearance k_{drug} is the sum of the clearances associated with these processes. Since drug is cleared almost completely by liver and kidneys,

$$k_{\text{drug}} = k_{\text{liver}} + k_{\text{kidneys}}. \tag{2.37}$$

Hepatic clearance

From Eq. (2.36), hepatic metabolic clearance depends on liver perfusion and liver extraction rate. If extraction is complete, hepatic clearance is the sum of the flow of portal and hepatic arterial blood flows, 1050 ml/min and 300 ml/min, respectively.

If drug with low extraction ratio is bound with plasma proteins, its hepatic clearance will be reduced because only unbound molecules are metabolised, thus the effective hepatic clearance is

$$k_{\text{liver}} = k_u \, f_u, \tag{2.38}$$

where k_u is the clearance calculated according to unbound concentration $k_u = r_e \, F_B$.

Another factor limiting metabolic clearance is the availability of the enzymes responsible for the metabolic process. If drug concentration exceeds the concentration of metabolic enzymes, the rate at which drug is eliminated saturates. The Michaelis–Menten formula provides a simple phenomenological way to quantify the elimination rate for a process with saturation:

$$\frac{\mathrm{d}Q}{\mathrm{d}t} = -\frac{k_{\text{drug}}}{1 + C_u/C_s} \, C_u. \tag{2.39}$$

When the unbound drug concentration is much lower than the saturation concentration C_s, the elimination rate is proportional to drug concentration, and it is still possible to define a clearance constant. [Eq. (2.34)]. Conversely, when C_i is much larger than the saturation concentration C_s, the elimination rate becomes constant and equal to V_m. In this limit the clearance is no longer constant but becomes a decreasing function of drug concentration, eventually vanishing for very

large concentrations

$$k_{\text{liver}} = \frac{k_{\text{drug}}}{1 + C_u/C_s}. \tag{2.40}$$

The liver can remove drug not only via metabolism but also by biliary excretion. Biliary clearance is proportional to bile flow F_{bile} and depends on the ratio between drug concentration in bile C_{bile} and in plasma according to

$$k_{\text{bile}} = \frac{C_{\text{bile}}}{C_p} F_{\text{bile}}. \tag{2.41}$$

Bile is not a product of filtration but of active secretion. For this reason the ratio between bile and plasma concentration can be very large, approaching 1000. However, only some classes of molecules may show high biliary clearance. The molecule must have a mechanism for active secretion, it must be polar and its molecular weight must be greater than 250 g/mole. Because of the lipophilic and porous nature of bile cannaliculae, small non-polar molecules are reabsorbed.

Renal clearance

Every minute kidneys filter about 120 ml of plasma water, i.e. about 10% of total blood flow ($\sim$ 1.1 l/min) passing through these organs. This flow is called glomerular filtration rate k_{GFR} and represents the maximum theoretical value of renal clearance due to passive filtration mechanisms (see Eq. (2.36)).

For certain drugs renal clearance may be effectively larger than k_{GFR}, because two other mechanisms contribute to renal elimination: secretion, and reabsorption. Hence, the total renal elimination rate can be expressed as

$$\frac{\mathrm{d}Q}{\mathrm{d}t} = (1 - f_{\text{reabsorption}}) \left[\left.\frac{\mathrm{d}Q}{\mathrm{d}t}\right|_{\text{filtration}} + \left.\frac{\mathrm{d}Q}{\mathrm{d}t}\right|_{\text{secretion}} \right], \tag{2.42}$$

where $f_{\text{reabsorption}}$ is the fraction of reabsorbed drug and $\mathrm{d}Q/\mathrm{d}t|_{\text{filtration}}$ and $\mathrm{d}Q/\mathrm{d}t|_{\text{secretion}}$ are the rate of filtration and secretion, respectively.

The renal clearance of a molecule can be easily estimated by measuring the urine flow F_U and the molecule concentration in plasma (C_p) and in urine C_U. Since $F_U\, C_U$ is the elimination rate, by definition [Eq. (2.34)], renal clearance is

$$k_{\text{kidneys}} = \frac{F_U\, C_U}{C_p}. \tag{2.43}$$

Filtration. When blood enters a nephron, the basic anatomic unit of renal function, it is first filtered by the glomerulus. Here, molecules smaller than about 2000 g/mole easily pass through the sieve, larger molecules hardly pass and molecules larger than 20 000 g/mole are blocked. For

instance, proteins like albumin are not found in the urine. As a consequence, only the fraction of unbound molecules is eliminated with a filtration rate

$$\left.\frac{\mathrm{d}Q}{\mathrm{d}t}\right|_{\text{filtration}} = f_u\, k_{\text{GFR}}\, C_p. \tag{2.44}$$

It is possible to define a clearance associated with the filtration process as

$$k_{\text{filtration}} = f_u\, k_{\text{GFR}}. \tag{2.45}$$

Secretion. Blood then passes through the proximal tube, where drug is actively removed by secretion. Molecules undergoing massive secretion may show a clearance greater than the glomerular filtration rate. The efficiency of secretion is affected by protein binding and perfusion. If a drug is poorly secreted, its concentration at the secretion site is identical to its plasma concentration and only the unbound fraction is secreted. Accordingly, the clearance associated with secretion is proportional to f_u. Conversely, when secretion of a drug is very fast, drug is almost completely removed from blood and the secretion rate does not depend on the unbound fraction. Since the dissociation of the protein-drug complex is practically instantaneous, the total amount of drug dissociates from proteins and is secreted during the time drug remains in contact with the secretion site.

Reabsorption. The third process influencing renal clearance is reabsorption. Through this mechanism, which can be either active (in the proximal tube) or passive (all along the nephron), several molecules re-enter the bloodstream. Similarly to what happens in other membranes, the lipoidal membranes of the cells forming the tubule acts as a barrier against polar and charged molecules. For this reason lipophilic molecules are more easily reabsorbed than polar molecules.

Furthermore, 80%–90% of the filtered water is reabsorbed in the proximal tubule thanks to sodium transport from the lumen into the blood by Na^+/K^+ATPase in the basolateral membrane of the epithelial cells. Most of the remaining water is reabsorbed in the distal tubule. Consequently, drugs concentrate in the filtrate. If a drug is filtered but not secreted or reabsorbed, it may reach a concentration about 100 times as great as the unbound concentration in plasma when about 99% of water is reabsorbed. As an example, about 2 g of creatinine are excreted every day with a normal volume output of about 2 l/day. The order of magnitude of urine creatinine concentration is about 1 g/l, about hundred times as great as the order of magnitude of plasma creatinine concentration ($\sim$ 10 mg/l).

If a drug is mostly reabsorbed its renal clearance strongly depends on urine flow. In the limit when reabsorption approaches equilibrium, urine drug concentration and unbound plasma

concentration are equal $C_U = C_u$, with $C_u = f_u\, C_p$. From Eq. (2.43),

$$k_{\text{kidneys}} = f_u\, F_U. \tag{2.46}$$

Since F_U is normally from 1 to 2 ml/min, renal drug removal is extremely low when the drug is reabsorbed, especially when protein binding is strong.

Another factor affecting reabsorption of weak acids and bases is urine pH. While blood pH is almost constant, around 7.4 (although it may become lower than 7 or higher than 7.6 in severe pathological conditions [130, 12]), urine pH has an average value of 6.2 but may vary over a much wider range, between 4.5 and 7.5, under forced acidification and alkalinisation, respectively [20, 160]. Again assuming that reabsorption approaches equilibrium, the concentration of non-ionised drug in plasma and in urine will be the same. For an acid drug, using the notation introduced in Sec. 2.1.3,

$$C_p\, f_{ua,p} = C_U\, f_{ua,U}, \tag{2.47}$$

where $f_{ua,p}$ and $f_{ua,U}$ denotes the non-ionised fraction of the considered drug in plasma and in urine, respectively. Using Eqs. (2.43) and (2.6),

$$k_{\text{kidneys}} = \frac{10^{\text{pH}_U - \text{p}K_a} + 1}{10^{\text{pH}_B - \text{p}K_a} + 1}\, F_U, \tag{2.48}$$

where pH_U and pH_B are urine and blood pH, respectively. In Fig. 2.4, left panel, I plot the ratio between renal clearance k_{kidneys} and urine output F_U as a function of urinary pH, for different acids ($K_a = 2$, 5, 8, 11). For very weak acids, $K_a \gtrsim 8$, the acid is completely non-ionised in both plasma and urine (Fig. 2.3, left panel). Hence renal clearance does not depend on urinary pH and coincides with the volume of the urine output. For stronger acids k_{kidneys} is very sensitive to urinary pH. Those acids are almost completely ionised in blood, whereas their degree of ionisation varies in urine depending on urinary pH. As a consequence, their clearance is generally very low and decreases with urinary pH. The clearance of those acids may exceed urine output if urine is more alkaline than blood.

Similarly, I compute the renal clearance for weak bases. Assuming reabsorption at equilibrium, the concentrations of non-ionised basic drug in blood and urine are the same. Using Eqs. (2.43) and (2.10),

$$k_{\text{kidneys}} = \frac{10^{\text{p}K_w - \text{p}K_b - \text{pH}_U} + 1}{10^{\text{p}K_w - \text{p}K_b - \text{pH}_B} + 1}\, F_U. \tag{2.49}$$

In the right panel of Fig. 2.4, renal clearance is plotted for various basic drugs ($K_b = 2$, 5, 8, 11, corresponding to $K_a = 3$, 6, 9, 12 for the conjugated acid). Drug clearance does not depend on urinary pH and equals the urine output for very weak bases which are completely non-ionised in

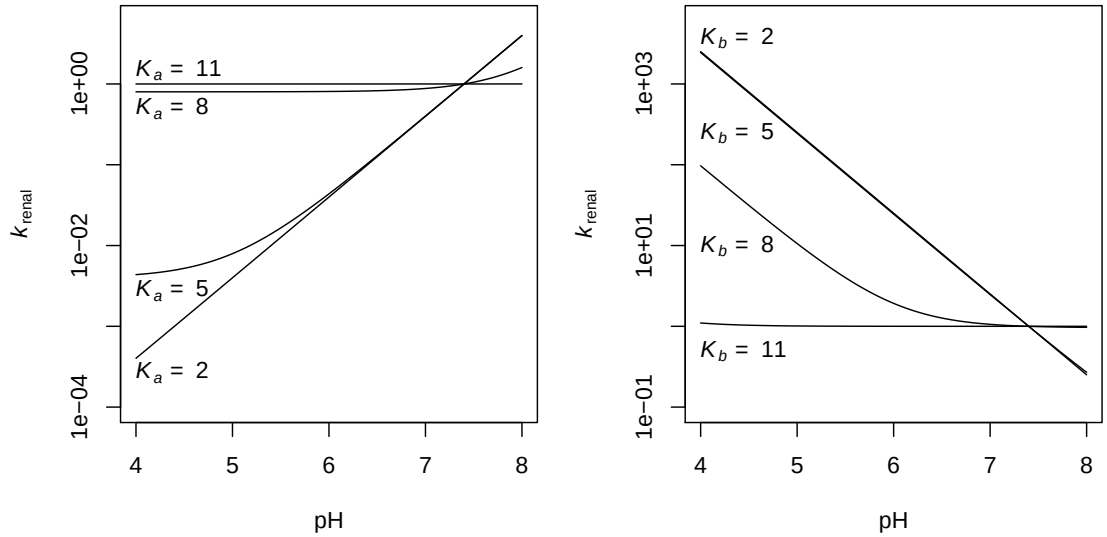

Figure 2.4: Ratio between renal clearance and urine output k_{kidneys}/F_U for acids (left panels) and bases (right panel) with different K_a and K_b as functions of urinary pH, for blood pH equal to 7.4, assuming that reabsorption approaches equilibrium.

both plasma and urine (Fig. 2.3, right panel). For stronger bases, renal clearance strongly depends on urinary pH. Renal clearance is less than the urine output if urinary pH is higher than blood pH. Instead, k_{kidneys} becomes much larger than the urinary output when urine is acid. In this case, drug is non-ionised in blood, while it is ionised in urine if $\text{pH}_U < \text{p}K_w - \text{p}K_b$. As a consequence re-absorption is blocked by the pH gradient and diffusion from plasma to urine is enhanced.

Renal replacement therapy

Renal replacement therapy (RRT) contributes to different extents to the total effective clearance of certain drugs. RRT clearance is influenced by physico-chemical drug properties, by specific RRT technology and by its operating characteristics [134]. RRT clearance is high for drugs with high renal clearance. Thus, drug removal by RRT is significant for drugs that are weakly bound to proteins and with small distribution volumes. In particular, hydrophilic molecules which distribute in plasma and in the extracellular space are removed by RRT and may require a correction of the dosage regimen to ensure a therapeutic effect. Conversely, lipophilic drugs, which show consistent intracellular accumulation, have a large distribution volume. Hence, their concentration in the tissues is not significantly affected by RRT (despite undergoing complete RRT removal) since only a small fraction of drug is located within the plasma.

Solute removal by RRT may occur by means of diffusion, in haemodialysis, and convection, in haemofiltration. In the former mechanism, solutes pass from blood to a counter-flowing fluid separated by a porous membrane, by passive diffusion. Clearance efficacy of haemodialysis is larger for small molecules. Thus, depending on filter type, drugs with high molecular weight

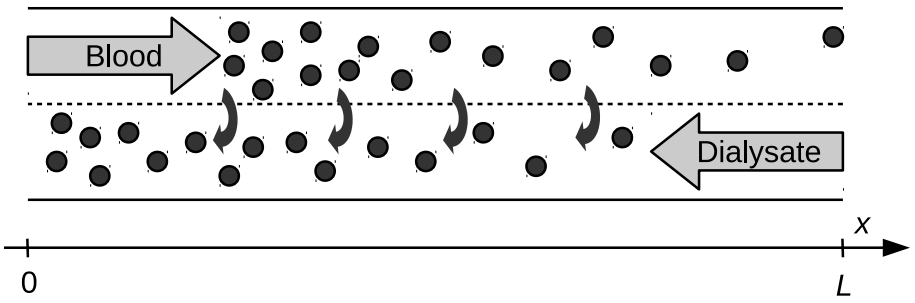

Figure 2.5: Schematic representation of haemodialysis. Molecules diffuse from dialysate to blood which are counter flowing.

($> 1000 - 10\,000$ Da) are protected from removal. In haemofiltration drugs are removed primarily by convection. Molecules smaller than filter pores (molecular weight smaller than $30\,000 - 50\,000$ Da) pass through the filter and are eliminated. Since water is also removed, replacement fluids must be administered to maintain an adequate circulatory volumes before or after filtration. Finally, haemodialysis and haemofiltration may be combined in haemodiafiltration.

Haemodialysis. Figure 2.5 shows a schematic representation of haemodialysis. Molecules diffuse from blood to dialysate across the membrane. The two fluids counter flow to maintain a concentration gradient along the entire membrane and thus optimise removal. To compute drug clearance one must write the differential equations governing drug diffusion across the membrane between the two propagating fluids. The convective derivative ($D = \partial/\partial t + v\,\partial/\partial x$) of drug concentration C along the flow is proportional to the difference of drug concentration:

$$\left(\frac{\partial}{\partial t} + v_B\,\frac{\partial}{\partial x}\right) C_B = -\gamma\,(C_B - C_D)\,, \tag{2.50}$$

$$\left(\frac{\partial}{\partial t} - v_D\,\frac{\partial}{\partial x}\right) C_D = -\gamma\,(C_D - C_B)\,, \tag{2.51}$$

where C_B and C_D are drug concentrations in blood and dialysate, v_B and v_D blood and dialysate flow velocity, respectively (note the $-$ sign for the velocity of the dialysate which flows from right to left), and γ represents the diffusion coefficient between plasma and dialysate. I look for a stationary solution, i.e.

$$v_B\,\frac{\partial C_B(x)}{\partial x} = \gamma\,[C_D(x) - C_B(x)]\,, \tag{2.52}$$

$$v_D\,\frac{\partial C_D(x)}{\partial x} = \gamma\,[C_D(x) - C_B(x)]\,. \tag{2.53}$$

Subtracting the two equations, I find

$$v_B\,C_B(x) - v_D\,C_D(x) = A, \tag{2.54}$$

where A is a constant fixed by boundary conditions. At $x = L$, the length of the haemodialysis circuit, drug concentration in the dialysate is 0, and the blood concentration reaches its minimum final value C_{Bf}, before blood re-enters the patient circulation. Thus $A = v_B\, C_{Bf}$. Expressing $C_D(x)$ in terms of $C_B(x)$ as

$$C_D(x) = \frac{v_B}{v_D}\left[C_B(x) - C_{Bf}\right]. \tag{2.55}$$

and replacing in Eq. 2.52,

$$\frac{\partial C_B(x)}{\partial x} = -\frac{\gamma}{v_B}\left[\left(1 - \frac{v_B}{v_D}\right) C_B(x) + \frac{v_B}{v_D} C_{Bf}\right]. \tag{2.56}$$

The solution of this equation is

$$C_B(x) = B\, e^{-\kappa x} - \frac{v_B/v_D}{1 - v_B/v_D} C_{Bf}, \qquad \kappa = \frac{\gamma}{v_B}\left(1 - \frac{v_B}{v_D}\right). \tag{2.57}$$

The constant B is determined using the boundary condition at $x = 0$, where $C_B(0) = C_{Bi}$, the initial blood drug concentration:

$$B = C_{Bi} + \frac{v_B/v_D}{1 - v_B/v_D}\, C_{Bf}. \tag{2.58}$$

To find the final blood drug concentration, I compute Eq. (2.57) in $x = L$ and solve for C_{Bf}. I obtain

$$C_{Bf} = \frac{(1 - v_B/v_D)\, e^{-\kappa L}}{1 - (v_B/v_D) e^{-\kappa L}}\, C_{Bi}. \tag{2.59}$$

The effective drug clearance is

$$k_{\mathrm{HD}} = \frac{C_{Bi} - C_{Bf}}{C_{Bi}}\, F_B, \tag{2.60}$$

where F_B is the treated blood flow. Eventually, I obtain

$$k_{\mathrm{HD}} = \frac{1 - e^{-\kappa L}}{1 - (v_B/v_D) e^{-\kappa L}}\, F_B. \tag{2.61}$$

If dialysate and blood tubes have the same cross section, the ratio v_D/v_B equals the ratio between dialysate and blood flows F_D/F_B. In this case k_{HD} varies as a function of F_D/F_B as shown in Fig. 2.6. Removal efficiency rapidly goes to zero when the dialysate flow is smaller than blood flow, while it is maximum as soon as $F_D > F_B$. The maximum clearance depends on the detail of the dialysate membrane and blood flow and blood velocity as

$$k_{\mathrm{HD}}^{\max} = F_B\left(1 - e^{-\gamma L/v_B}\right). \tag{2.62}$$

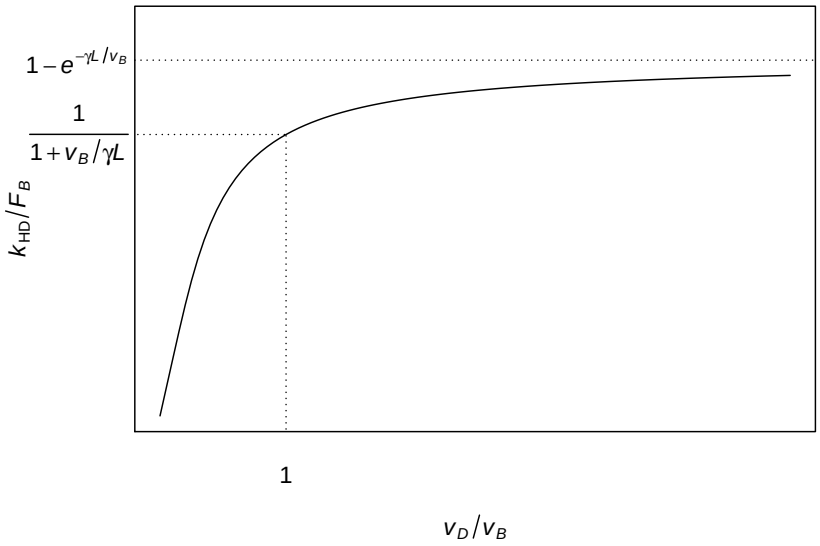

Figure 2.6: haemodialysis clearance as a function of the ratio between dialysate and blood velocity v_D/v_B.

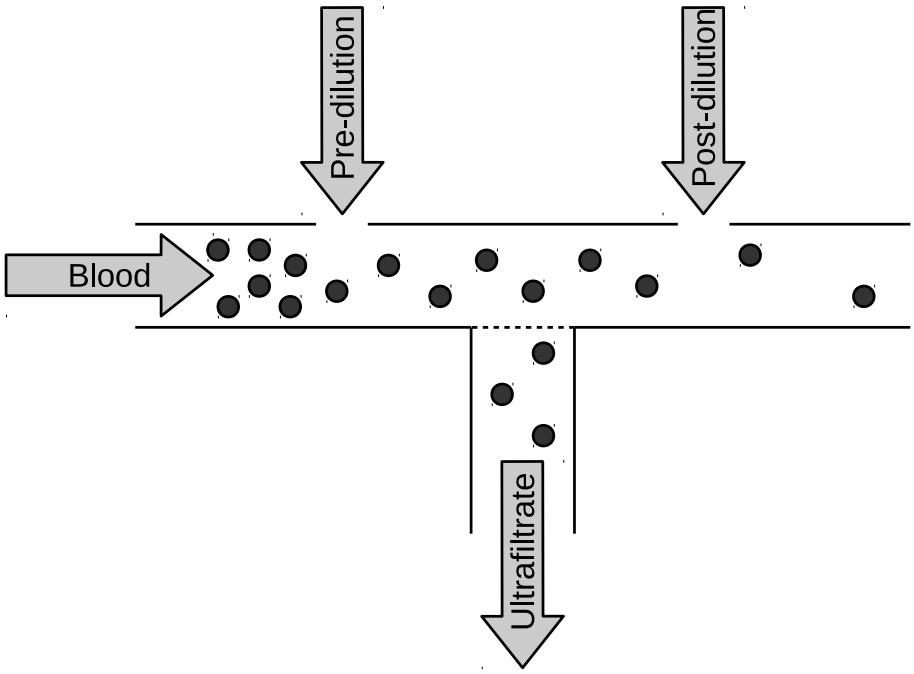

Figure 2.7: Schematic representation of haemofiltration. Molecules are dragged by convection from blood in the ultrafiltrate. Lost fluids are replaced by the replacement fluids in pre- and/or post-dilution.

This result shows that the maximum clearance is obtained for large blood flows with reduced blood velocity in the dialysis circuit. In this limit the maximum clearance is equal to the blood flow.

Haemofiltration. The main components of a haemofiltration circuit are schematically represented in Fig. 2.7. Molecules are dragged by convection from blood in the ultrafiltrate. A filter prevents large molecules ($> 30\,000 - 50\,000$ Da) from being eliminated. Since a large amount of plasma

water is eliminated with the ultrafiltrate, fluid must be re-infused to maintain the correct circulatory volume. Replacement fluid can be administered in pre- and/or post-dilution, *i.e.*, before and/or after the ultrafiltrate is extracted from blood. Having defined the sieving coefficient of the drug in the filter as S_c, and the flows of blood, ultrafiltrate, pre-dilution and post-dilution as F_B, F_{UF}, F_{pre}, and F_{post}, respectively, the drug clearance rate can be easily computed as follows.

If C_{Bi} is the initial drug blood concentration, the drug plasma concentration after pre-dilution is

$$C_{\mathrm{pre}} = \frac{F_B}{F_B\,(1-h) + F_{\mathrm{pre}}}\,C_{Bi}. \tag{2.63}$$

The concentration in the ultrafiltrate is simply

$$C_{\mathrm{UF}} = S_c\,C_{\mathrm{pre}}. \tag{2.64}$$

Thus, the total rate of drug removal is $S_c\,C_{\mathrm{pre}}\,F_{\mathrm{UF}}$ and the clearance due to haemofiltration is [134]

$$k_{\mathrm{HF}} = \frac{S_c\,C_{\mathrm{pre}}\,F_{\mathrm{UF}}}{C_{Bi}} = \frac{F_B}{F_B\,(1-h) + F_{\mathrm{pre}}}\,S_c\,F_{\mathrm{UF}}. \tag{2.65}$$

By means of haemofiltration the amount of fluids present in the body can be adjusted, either removed or added, if the flow of ultrafiltrate is greater or lower than the flow of replacement fluids $F_{\mathrm{pre}} + F_{\mathrm{post}}$. I define

$$\Delta = F_{Bf} - F_B = F_{\mathrm{pre}} + F_{\mathrm{post}} - F_{\mathrm{UF}} \tag{2.66}$$

as the difference between the blood flow returned to and extracted from the patient, and $f_{\mathrm{pre}} = F_{\mathrm{pre}}/(F_{\mathrm{post}} + F_{\mathrm{pre}})$ as the fraction of pre-dilution. With this notation, the total clearance can be expressed as

$$k_{\mathrm{HF}} = \frac{S_c\,C_{\mathrm{pre}}\,F_{\mathrm{UF}}}{C_{Bi}} = \frac{F_B}{F_B\,(1-h) + f_{\mathrm{pre}}\,(F_{\mathrm{UF}} + \Delta)}\,S_c\,F_{\mathrm{UF}}. \tag{2.67}$$

2.3 Secondary PK parameters and PK/PD indices

To design an appropriate dosage regimen it is not enough to know how fast and to what extent a drug is transported to the site of action and how rapidly it is eliminated from the body. It is necessary to understand what factors determine its therapeutic effects. Depending on the drug, its efficacy may depend on the concentration reached at the site of action or on how long the concentration is maintained. Although in this Thesis I do not investigate any pharmacodynamic properties of the considered drug, vancomycin, I shall study how therapeutic targets are reached

depending on dosage regimens and patient-specific pharmacokinetic features.

To measure the effect of a drug it is convenient to introduce a few secondary PK parameters and pharmacokinetic/pharmacodynamic (PK/PD) indices. First, I define $C_{\min}$ as the minimum concentration necessary for a drug to be effective. For antimicrobials, $C_{\min}$ is generally chosen as the minimum inhibitory concentration (MIC), that is the minimum drug concentration that prevents visible growth of a bacterium in vitro.

Maximum concentration $C_{\max}$. The efficacy of some drugs strongly depends on the concentration reached at the site of action. For this reason, such molecules are called concentration-dependent drugs. The simplest secondary PK parameter correlating with their efficacy is the maximum peak concentration $C_{\max}$ reached soon after drug administration and absorption. It is also useful to construct a dimensionless PK/PD index as the ratio $C_{\max}/C_{\min}$ between the maximum peak concentration and the minimum effective concentration.

Time above the minimum effective concentration $T_{>C_{\min}}$. Some drugs (time-dependent drugs) are effective only if their concentration remains above the therapeutic target concentration for a sufficiently long time. The PK/PD index that correlates the most with the efficacy of such drugs is the time $T_{>C_{\min}}$ for which drug concentration is greater than $C_{\min}$.

Area under the concentration-time curve (AUC). To quantify the potential activity of several drugs neither $C_{\max}$ and $T_{>C_{\min}}$ are good parameters. For many drugs it is important not only to reach a very large concentration for a very short period, but also to maintain it for a sufficiently long time. That is, several concentration-dependent drugs are effective only if their average concentration rather than the peak one is much larger than $C_{\min}$. To construct a PK/PD index that appropriately quantifies the effect of these drugs I need first to introduce a new secondary PK parameter, the area under the concentration-time curve (AUC, see Figure 2.8), defined as

$$A_C(t) = \int_0^t C(t')\,\mathrm{d}t'. \tag{2.68}$$

The mean concentration $\bar{C}$ in the time interval T is

$$\bar{C}_T = \frac{A_C(T)}{T}. \tag{2.69}$$

As a PK/PD index one usually adopts the ratio between the AUC $A_C(t = 24\,\mathrm{h})$ measured in the first 24 hours (indicated with $\mathrm{AUC}_{24\mathrm{h}}$) and the minimum concentration $C_{\min}$. This ratio $\mathrm{AUC}_{24\mathrm{h}}/C_{\min}$ expresses nothing more than the ratio between the concentration averaged over one

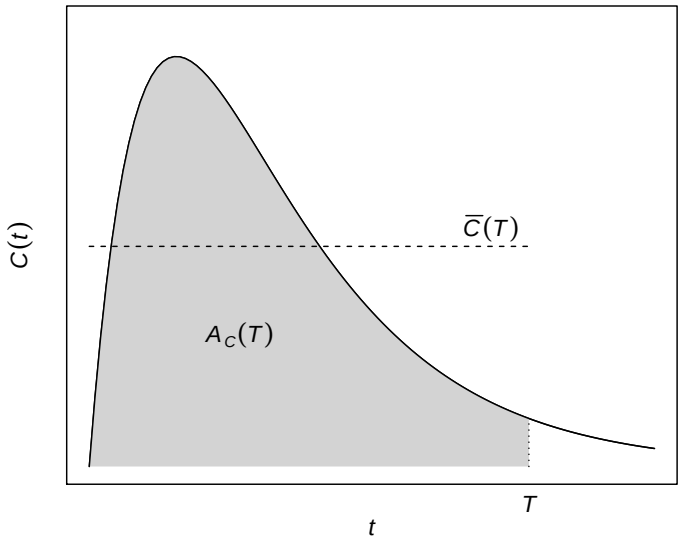

Figure 2.8: Graphical representation of the area under the concentration curve and the average concentration $\bar{C}$ (dashed line).

day and $C_{\min}$

$$\frac{\bar{C}_{24\mathrm{h}}}{C_{\min}} = \mathrm{AUC}_{24\mathrm{h}}/C_{\min} \times 24\,\mathrm{h}. \tag{2.70}$$

To empirically compute the area under the concentration-time curve it is necessary to measure the concentration of a drug with a sufficiently large time resolution and then to adopt a standard numerical approximation technique (e.g. rectangle, trapezoidal, Simpson's method) to evaluate the integral of Eq. (2.68).

The measurement of the AUC in an appropriate time interval can be used to compute the total drug clearance k_{drug} assuming that k_{drug} is constant during the time interval used to measure the AUC. If $I(t)$ is the drug administration rate, the total drug present in the body is the solution of the following differential equation

$$\frac{\mathrm{d}Q(t)}{\mathrm{d}t} = -k_{\mathrm{drug}}\, C(t) + I(t). \tag{2.71}$$

Integrating this equation from $t = 0$ to $t = T$ and assuming that k_{drug} is constant

$$k_{\mathrm{drug}} = \frac{D - (Q(T) - Q(0))}{A_C(T)}, \tag{2.72}$$

where D is the total dosage of administered drug

$$D = \int_0^T I(t)\,\mathrm{d}t. \tag{2.73}$$

Equation (2.72) simplifies to

$$k_{\text{drug}} = \frac{D}{A_C(T)} \tag{2.74}$$

when the total amount of drug present in the body at the beginning and the end of the time interval T are equal. To make sure that the two quantities are the same, one can measure the AUC starting before the first drug administration ($Q(0) = 0$) and waiting for a sufficiently long time after the end of the administration so that also $Q(T) = 0$.

2.4 Compartment models

Drug diffusion in the body can be quantitatively studied through kinetic models based on systems of differential equations, which describe the evolution of drug concentrations in blood, organs, and tissues. These equations should reproduce all the involved processes (absorption, distribution, metabolism, and excretion) through appropriate mathematical functions parametrised by kinetic parameters (absorption and diffusion rates, clearances, etc. . .). However, when a model must be fitted on data from a population of patients it is practically impossible to include all the physiological mechanisms presented in the previous chapter in a detailed form as done in physiologically based pharmacokinetic modelling [146]. Indeed only a few measured values of drug concentration are typically available for each patient.

It is therefore necessary to find approximate equations that model the relevant physiological processes in a coarse-grained form, adopting classical compartment models [69, 162]. The number of relevant compartments and the shape of the functions entering the equations must be adapted to reproduce the distinctive way each drug is absorbed, transported in body compartments, and eliminated, taking into account also the amount and the frequency of available data.

The simplest model of pharmacokinetics assumes that drugs distribute only in one compartment. This may be a good approximation not only when a drug effectively remains confined to a single compartment (e.g., blood) because other compartments have much smaller volumes than the main one, but also when drug concentration in all compartments is roughly the same and absorption and diffusion among different compartments are very rapid. Furthermore, if only a few data are available to develop the model, it may be practically impossible to appreciate the difference with more sophisticated multi-compartment models.

In this model, absorption time and specific mechanisms of diffusion across membranes are neglected and the full kinetic process is modelled as a flux of drug that enters and exits a volume V, where it is distributed with a homogeneous concentration C. The total amount Q of drug

present in the body is simply given by

$$Q = C\,V. \tag{2.75}$$

The amount of drug in this single compartment increases if the drug is administered to the patient and drug removal is generally proportionally to drug concentration. Accordingly, the differential equation governing the evolution of Q is

$$\frac{\mathrm{d}Q}{\mathrm{d}t} = -k\,C + I, \tag{2.76}$$

When drugs distribute in several tissues and organs and the diffusion times are not negligible with respect to the elimination time scale, its pharmacokinetic behaviour is not reliably approximated by a one-compartment model. In this case more complex mathematical models with two or more compartments must be adopted.

One can define C_1, C_2, V_1 and V_2 as the concentrations and distribution volumes in the two compartments. Accordingly, the total amounts of drug in the two compartments are $Q_1 = C_1\,V_1$ and $Q_2 = C_2\,V_2$. Assuming that the drug is infused in the first compartment at a rate I and is eliminated only from this compartment with an elimination rate κ_e, the system of differential equations reads

$$\frac{\mathrm{d}Q_1}{\mathrm{d}t} = -\kappa_e\,Q_1 - \kappa_{12}\,Q_1 + \kappa_{21}\,Q_2 + I, \tag{2.77}$$

$$\frac{\mathrm{d}Q_2}{\mathrm{d}t} = \kappa_{12}\,Q_1 - \kappa_{21}\,Q_2, \tag{2.78}$$

where κ_{12} and κ_{21} are the diffusion rates from the first to the second compartment and *vice versa*.

The choice of the most appropriate model to describe the kinetics of a certain drug is guided by physiological arguments, so that the mathematical structure of the model mimics the physiological mechanisms at the basis of drug kinetics. However, in the formalism of compartment pharmacokinetics the parameters entering the equations, such as κ and V in the one-compartment model or κ_{12}, κ_{21}, κ_e, V_1, and V_2 in the equations of the two-compartment system [Eqs. (4.14) and (4.15)] cannot be deduced on the basis of theoretical arguments. Thus, they must be determined by comparing the solutions of the differential equations against data measured in patients.

A mathematical model of pharmacokinetics becomes appealing from a clinical perspective when it is able to simulate the evolution of drug concentration for specific patient conditions and for a given dosage regimen. Such a model would indeed support the clinician to design the most appropriate pharmacological therapy by identifying the optimal loading dose and the optimal rate of continuous infusion. To simulate the evolution of drug concentration for a single patient, his/her kinetic parameters must first be estimated based on clinical conditions. Second, the differential

equations of the chosen compartment model can be integrated to obtain the predicted value of drug concentration.

Thus, the kinetic parameters must be expressed as a function of patient-specific variables, such as demographic factors, vital signs, and results of relevant laboratory tests. These functions, in turn, are parametrised by a set of free parameters. For instance, the clearance k_{drug} of a drug undergoing renal elimination depends on renal function, which can be parametrised by creatinine clearance k_{crea}, a commonly used estimation of glomerular filtration rate. As a first guess one may choose a linear link between k_{drug} and k_{crea}

$$k_{\text{drug}} = \theta_0 + \theta_c \, k_{\text{crea}}, \tag{2.79}$$

where θ_0 and θ_c are free parameters to be determined. This relation becomes more complicated when drug is eliminated through different mechanisms. If a patient undergoes renal replacement therapy, total drug clearance must take account of the dialysis dose d_{dial}:

$$k_{\text{drug}} = \theta_0 + \theta_c \, k_{\text{crea}} + \theta_d \, d_{\text{dial}}, \tag{2.80}$$

where I added an extra free parameter θ_d.

The mathematical and statistical techniques used to construct these population models are reviewed in Chap. 4.

2.5 Pharmacokinetics in critically ill patients

The pharmacokinetic properties presented in the previous section may be heavily modified by the extreme clinical conditions of critically ill patients [32, 143, 155, 173] and/or by the intensive treatments they received during their ICU stay [153]. These variations may eventually cause pharmacological therapies to fail [188] and, in the case of antimicrobials, yield the appearance of drug resistances. To construct a personalised pharmacokinetic model it is important to test as covariates an appropriate set of clinical variables that properly parametrise these variations. The most relevant causes of altered pharmacokinetics in critically ill patients are summarised in Table 2.9. In particular, the septic syndrome generates a cascade of alterations that significantly affect the pharmacokinetic behaviour of several drugs.

In this section I review how pharmacokinetics is modified by organ dysfunctions which may arise in critically ill patients [143]. Such modifications may be directly caused by organ failures or as a consequence of intensive treatments (e.g., fluid resuscitation or mechanical ventilation). These

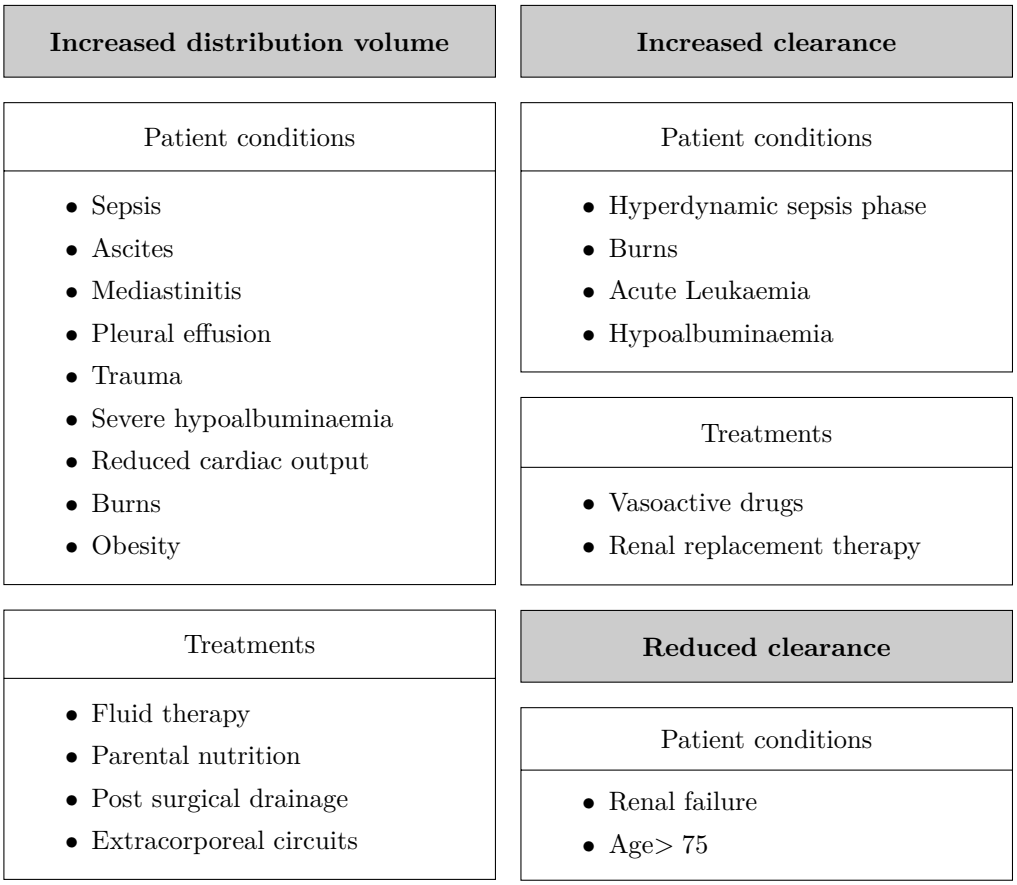

Figure 2.9: Impact of pathophysiology of critically ill patients on antibiotic kinetics and dynamics [189].

concepts will be applied to describe the changes in drug pharmacokinetics caused by sepsis [55].

2.5.1 Effect of organ dysfunctions on pharmacokinetics

Cardiovascular failure

Cardiovascular failure affects several pharmacokinetic processes as a consequence of reduced blood flow and perfusion.

- Drug clearance decreases because of reduced perfusion of liver and kidneys. This effect is amplified by homeostatic mechanisms attempting to maintain blood flow to heart, brain and muscles at the expense of renal and splanchnic flow.
- A second consequence of heart failure is fluid retention that, combined with the effect of fluids administered during fluid resuscitation, may increase the drug distribution volume.
- Anaerobic metabolism is enhanced as a consequence of reduced perfusion. This may yield metabolic acidosis which may alter the distribution of ionisable drugs.

Respiratory failure

Pharmacokinetics may be altered by respiratory failure though several mechanisms.

- Hypoxeamia may reduce the activity of hepatic enzymes, thus reducing hepatic clearance.
- The pH is affected by acidosis or alkalosis following respiratory failure. This may change how ionasible drugs are distributed or cleared.
- Mechanical ventilation may increase intrathoracic pressure, decreasing venous return and ventricular filling. This causes the reduction of cardiac output, generating the consequences above described (increase of intra and extra vascular water, reduction of liver blood flow, etc. . .)

Renal failure

Renal dysfunction, either associated with pre-renal or intrinsic origin, causes the reduction of drug excretion and, consequently, of drug clearance. However, renal impairment affects also other aspects of pharmacokinetics. Both chronic and acute renal failure causes fluid retention, with consequent changes in drug distribution volume. Furthermore, metabolic acidosis and respiratory acidosis are often associated with renal failure, resulting in pH alteration, and finally in modification of drug distribution or clearance.

Finally, renal replacement therapy remove drugs usually removed by renal excretion, thus increasing total drug clearance.

Hepatic dysfunction

As outlined in Sec. 2.2.2, hepatic clearance depends on several factors: blood flow, perfusion and activity of hepatic enzymes. Thus, pathological conditions may affect hepatic clearance by modifying these factors at different levels. Specifically, the clearance of drugs with high extraction ratio [see Eq. (2.35)] is mainly affected by variations of hepatic blood flow. Conversely, if the extraction ratio is low, drug clearance is more sensitive to variations of enzyme activity.

- Blood flow may increase in the early hyperdynamic stage of sepsis as a consequence of augmented cardiac output or decrease in the late hypodynamic stage of sepsis and in case of cardiovascular failure. The administration of vasoactive drugs has also an impact on hepatic blood flow. Vasopressors reduce this flow causing vasocostriction of the hepatic artery and portal vein. Conversely, vasodilators increase hepatic blood flow by reducing hepatic vascular resistance.

- The activity of hepatocellular enzymes is modified by several pathological states. Hypoxaemia may decrease hepatic clearance by reducing both enzyme production, their efficiency, and the oxygen available for drug oxidation. Also inflammation may inhibit hepatic drug metabolism by decreasing the activity of hepatic enzymes.

- Chronic liver diseases also affect hepatic drug clearance. Cirrhosis is associated with reduction of blood flow caused by the abnormal hepatic architecture, thus affecting clearance of drugs with high extraction ratio. Clearance of drugs with low-extraction ratio is instead reduced by hepatocellular injury as, for instance, in ischaemic or viral hepatitis.

Endothelial failure

Burns and systemic inflammatory response syndrome (SIRS) are among the most important causes of endothelial damage. As a consequence, the volume of interstitial fluid and total body water increase, thus increasing the drug distribution volume. This fluid shift may also cause hepatic and renal oedema, responsible for altered drug clearance. This phenomenon may be aggravated by fluid administration.

Finally, both burns and SIRS may modify serum protein levels, affecting drug protein binding and, consequently, distribution volume and clearance in a complex and hardly predictable way.

Endocrine disorders

Critically ill patients often show disorders in hormonal function as either cause of admission to ICU (e.g., hypoadrenalism or hypothyroidism) or stress response to the condition of critical illness. Stress response may influence drug pharmacokinetics by increasing the cardiac output or redistributing the cardiac output by reducing the splanchnic flow. It may also yields fluid retention and increase of circulating volumes. Complex changes in plasma proteins may also take place in stress conditions.

Central nervous system dysfunction

Although central nervous system failure does not directly alter drug pharmacokinetics, its consequences may alter several pharmacokinetic processes. For instance, hypo- and hyper-ventilation, which are quite common in central nervous system failure, result in pH disturbances. Head injured patients may show increased cardiac output, resulting in increased hepatic and renal blood flow and in augmented drug clearance.

2.5.2 Sepsis

Sepsis is a pathological condition arising when the inflammatory response to infection becomes systemic and causes injuries to tissues and organ dysfunctions. A cascade of effects are triggered by the onset of this condition often involving several systems and yielding multiple organ failure. These effects combine to produce complex modifications in drug distribution volume and clearance as describe above [55].

Distribution volume

In septic condition, drug distribution is altered by several mechanisms. First, the cardiac output is redistributed to heart and brain at the expense of less vital organs, as kidneys, spleen, and gut. Maldistribution of blood flow in the microcirculation results in compromised tissue perfusion, possibly changing the peripheral drug distribution volume.

Second, in a severe infection, endotoxins from bacteria may stimulate the production of endogenous mediators that may affect the vascular endothelium resulting in endothelial damage and increased capillary permeability. This yields a fluid shift to the interstitial space that increases the distribution volume, especially of hydrophilic drugs. Fluid resuscitation, a treatment recommended to control the haemodynamic status in septic patients [151], may contribute to increase distribution volumes. Similarly to the effect on the vascular endothelium, the inflammatory condition may alter the permeability of other tissue membranes. For instance, meningeal inflammation may increase the permeability of the blood-brain barrier, altering the diffusion rate of hydrophilic drugs in the cerebrospinal fluid.

Third, the distribution volume [see Eq. (2.24)] of molecules with significant protein binding is affected by variations of plasma protein concentration. During critical illness, reduced dietary protein intake, increased capillary permeability, haemodilution, and reduction of hepatic synthesis contribute to reduce the level of serum albumin. Hypoalbuminaemia increases the fraction on unbound drug and, consequently, the apparent distribution volume.

Finally, reduced organ perfusion causes anaerobic metabolism and acidosis, which may alter the pH and, consequently, the distribution of ionisable drugs, as described in the previous section.

Clearance

The complex conditions associated with the septic syndrome alter drug metabolism and excretion, the two mechanisms responsible for drug clearance.

During sepsis and septic shock renal clearance may be augmented by the enhancement of renal blood flow [see Eq. (2.43)], due to an increase in cardiac output associated with the first hyperdy-

namic stage of sepsis or to vasoactive drugs administered to compensate the shock condition [55]. At the same time, as illustrated in the above section, the administration of vasopressors may reduce the hepatic blood flow, reducing hepatic clearance.

On the other hand, worsening of the patient's condition could cause significant myocardial depression leading to decreased organ perfusion, failure of microvascular circulation [133], eventually progressing to multiple organ dysfunction syndrome. This may include renal and hepatic dysfunction which are associated with reduced drug clearance.

Drug clearance is also modified by therapies adopted to treat septic patients. Renal replacement therapy directly increases drug clearance, whereas mechanical ventilation indirectly reduces drug clearance as illustrated above.

Finally, hypoalbuminaemia may also affect drug clearance, since a decrease in the concentration of plasma proteins causes an increase in the clearance of renally excreted drugs, due to a larger drug unbound fraction.

Chapter 3

ANTIMICROBIALS IN CRITICALLY ILL PATIENTS

The design of effective antibiotic treatments for critically ill patients requires complex pharmacokinetic and pharmacodynamic issues to be addressed. Furthermore, antibiotic efficacy may be strongly modified by patient conditions, which may be extreme and rapidly changing, especially in critically ill patients. In this chapter, I briefly review the physico-chemical, pharmacokinetic, and pharmacodynamic properties of some of the most common antibiotic molecules used in ICU (see Table 3.1 for a schematic summary). In Sec. 3.2 I shall provide more details on vancomycin, focusing on those aspects that are more relevant for the construction of pharmacokinetic models. I shall also review a few population models of vancomycin pharmacokinetics in critically ill patients.

3.1 Basic concepts

3.1.1 Pharmacokinetics

The pharmacokinetic properties of antimicrobials are directly related to their chemical properties [189, 155, 189, 134, 48] (see Table 3.2). Hydrophilic drugs (e.g., β-lactams, aminoglycosides, glycopeptides, daptomycin) distribute only in plasma and in the extracellular fluids. Their distribution volume is small and their clearance is mainly renal. Renal replacement therapy may strongly contribute to drug elimination in patients receiving this kind of treatment. Conversely, lipophilic drugs (e.g., macrolides, colistin, linezolid, quinolones) may show a higher intracellular distribution, their distribution volume is larger, their kinetic properties are less affected by variation in renal clearance, and they are often eliminated by hepatic metabolism.

Drug size and protein binding are also important factors affecting apparent distribution vol-

Antibiotics	Physico-chemical Features			Antibiotic properties			PK/PD properties			
		binding	H/L	Germs	Mechanism	Effect	KC	V_d	clearance	RRT clearance
β-lactams (penicillins, cephalosporins, carbapenems, oxapenems)	β-lactam ring	poor	H	Gram +, most recent drug Gram −, no fungi	inhibit peptidoglycan synthesis	BC	TD	low	prevalently renal	high removal
Aminoglycosides (amikacin, gentamicin)	amino-modified glycoside	none	H	Gram −	inhibit protein synthesis interacting with ribosomes	BC	CD/CTD	low	almost completely renal	high removal
Macrolides (erythromycin)	lacton rings with more than 14 atoms		L	Gram +	inhibit protein synthesis interacting with ribosomes	BS	TD			
Glycopeptides (teicoplanin, vancomycin)	peptides containing glycans; high molecular weight	moderate	H	Gram +; cannot penetrate the outer barrier of Gram-	interfere with cell wall synthesis by forming a complex with the D-alanyl-Dalanine terminus of the intermediates	BC/BS	CTD	low	prevalently renal; influenced by pathophysiological conditions	to a very different extent according to RRT operating conditions
Cyclic peptides (polymyxin, colistin)	polypeptide chain with circular sequence of bonds		L	Gram − (specific to lipopolysaccharide molecule of many Gram − outer membrane)	membrane damage by means of hydrophobic tail	BC	CD		colistimethate: prevalently renal; when converted to colistin: mainly non-renal	
Cyclic peptides (daptomycin)	polypeptide chain with circular sequence of bonds		H	Gram +	cause membrane depolarisation, resulting in a loss of membrane potential and inhibition of macromolecular syntheses	BC	CD		prevalently renal	
Quinolones (levofloxacin, ciprofloxacin)	4-quinolone	moderate	L	Gram +, Gram −	inhibit bacteria enzymes: DNA gyrase and topoisomerase IV	BS/BC	CD/CTD	high	dependent on molecule characteristic	dependent on molecule characteristic
Oxazolidinones (linezolid)	oxazolidinone	poor	L	Gram +, including glycopeptide resistant germs	inhibit protein synthesis	BS/BC	TD/CTD	high	low renal	comparable with renal clearance

Table 3.1: Summary of main physico-chemical, pharmacokinetic and pharmacodynamic properties of the antibiotics most used for the treatment of infected critically ill patients [189, 155, 166, 134, 48, 74, 67]. Legend. H/L: H – hydrophilic, L – lipophilic. Germs: Gram +/− – Gram-positive/negative bacteria. Effect: BC – bactericidal, BS – bacteriostatic (BS). Kill characteristic (KC): TD – time dependent, CD – concentration dependent, CTD – concentration dependent with time dependence.

Hydrophilic	**Lipophilic**
β-lactams	Macrolides
Glycopeptides	Quinolones
Aminoglycosides	Linezolid
Daptomycin	Colistin
Limited volume of distribution	Large volume of distribution
Inability to passively diffuse through plasmatic membrane of eukaryotic cells	Freely diffuse through plasmatic membrane of eukaryotic cells
Inactive against intracellular pathogens	Active against intracellular pathogens
Eliminated renally as the unchanged drug	Eliminated often after hepatic metabolism

Table 3.2: Hydro and lipophilic antibiotics and their physico-chemical properties [134].

ume and clearance (both physiological and due to RRT). Indeed, only the unbound fraction can be eliminated by kidneys. Furthermore, large molecules (e.g., glycopeptides, colistin) are not well eliminated by renal replacement therapies, in particular by diffusive techniques such as haemodialysis [134]. Hence, drugs with large molecular size and moderate/high protein binding, as glycopeptides, have interesting and non-trivial pharmacokinetic properties which strongly depend on patient conditions.

3.1.2 Mechanisms of action

The choice of the most appropriate drug is guided by the characteristics of the microorganism and the mechanism of action required to kill it (bactericidal action) or inhibit its growth (bacteriostatic action). Indeed, each antibiotic acts in a distinctive way and it is effective on some germs only [74, 67].

Bacteria are commonly classified into two large groups on the basis of the Gram stain test. Gram-positive bacteria take up the stain used in the test, assuming a purple colour, because of a thick layer of peptidoglycan that forms the outer layer of their cell walls. The external layer of the cell wall of Gram-negative bacteria is made instead of a thin layer of peptidoglycan covered by an outer membrane of lipopolysaccharides and proteins. In this type of cell, the thin layer of peptidoglycan is dissolved in the Gram stain test. Thus, Gram-negative cells lose the initial colour. Because of the different structure of the cell wall, antibiotics penetrate differently in these two groups of germs, and different mechanisms of action must be exploited. For instance, glycopeptides are active only for Gram-positive bacteria because they cannot penetrate the outer barrier of Gram-negative bacteria. Conversely, polymyxins and colistin are active against Gram-negative bacteria thanks to their specificity to the lipopolysaccharide molecule that characterises the outer membrane of these bacteria.

Here I briefly illustrate the main types of mechanism of action of the molecules which are mostly used for the treatment of ICU patients (see Table 3.1).

Inhibitors of cell wall synthesis. The pathways underlying the synthesis of cell walls are very complex. So, antibiotics may act at several levels in order to interfere with this process. For instance, β-lactams intervene in the final phase of peptidoglycan synthesis by inhibiting different enzymes and ultimately inhibiting the formation of the three dimensional cell wall structure. They are active against both Gram-positive and Gram-negative bacteria. They cannot be effective against fungi, which do not have a peptidoglycan layer. Vancomycin and teicoplanin exploit a similar mechanism of action by inhibiting peptidoglycan synthesis. They are active only against Gram-positive bacteria.

Inhibitors of replication and transcription of nucleic acid. The process of synthesis of DNA and RNA consists of two phases: the synthesis of precursors (nucleotides and deoxynucleotides) from intermediate molecules of cell metabolism and the enzymatic polymerisation of nucleotides to form the DNA macromolecule. The correct sequence of bases is copied by the original DNA template. Antibiotics may inhibit the replication and transcription of DNA by interfering with different steps of these two complex phases. For instance quinolones, such as ciprofloxacin, inhibit DNA gyrase, a replication enzyme that compacts the DNA molecule by acting on its topology introducing supercoils.

Inhibitors of protein synthesis. Proteins are synthesised by polymerisation of amino acids according to an order determined by the sequence of nucleotide triplets in RNA. This is determined, in turn, by the sequence of deoxynucleotides in DNA. Antibiotics may inhibit the process of protein synthesis by interfering either with the first phase of activation and identification of the amino acids from the RNA or with the second phase of polymerisation of the amino acids that takes place in the ribosomes. For instance, erythromycin, a macrolide, inhibits ribosomal function by binding to a subunit of ribosomes. These antibiotics are generally bacteriostatic because they just interrupt the process of protein synthesis. Aminoglycosides such as gentamicin or amikacin, which also inhibit ribosomal functions, are an exception, being bactericidal. Interestingly, they do not show one-step resistance because they are able to bind to more than one ribosomal site. Linezolid also interferes with protein synthesis by inhibiting the very first step of the process, by preventing the formation of the initiation complex.

Inhibitors of cell membrane functions. Cell membranes separate the interior of the cell from the exterior and control the passage of molecules in both directions. They have a supermolecular

structure formed by a double lipid layer intercalated by proteins. Antibiotics may interfere with cell membrane functions either by disrupting the membrane structure or by affecting the transport of specific ions causing an abnormal accumulation or depletion of ions. For instance, polymyxins are made of a peptide ring with basic hydrophilic groups and a lipophilic chain. The hydrophilic groups bind with the phosphoric group of phospholipids while the lipophilic chain inserts itself between the lipidic chains of the membrane. This causes the membrane structure to disaggregate. They are more active on Gram-negative bacteria because they have a large affinity with the outer membrane. The action mechanism of daptomycin [182] is very different. It binds to cell membranes in a calcium-dependent manner and promotes the loss of intracellular K^+ ions, thus causing a collapse of the membrane potential. Consequently, it inhibits the cellular uptake of amino acids by active transport, which depends on membrane potential.

3.1.3 Kill characteristics

Since the desired effect of an antibiotic therapy is to kill the infective microorganisms or inhibit their growth, the PK/PD indices introduced in Sec. 2.3 have been related to the minimum inhibitory concentration (MIC). Thus, it is convenient to express these parameters using $C_{\min} = \text{MIC}$.

According to their kill characteristics antibiotics have been classified in three classes (see Table 3.3 [166, 155]):

Concentration-dependent: These molecules are effective if a peak concentration much larger than the MIC is attained. For those molecules the best PK/PD index correlating with efficacy is the ratio between the maximum concentration and the MIC ($C_{\max}/\text{MIC}$).

Time-dependent: These drugs are effective when a concentration larger than the MIC is maintained for a sufficiently long time. The best index to measure their efficacy is the time above the MIC, $T_{>\text{MIC}}$).

Concentration/time-dependent: The efficacy of these drugs is maximised when a high concentration is maintained for a sufficiently long time. The PK/PD index correlating best with their efficacy is the ratio between the area under the concentration-time curve and the MIC ($\text{AUC}_{0-24}/\text{MIC}$).

Concentration	**Time**	**Concentration/Time**
$C_{\max}$/MIC	$T_{>\mathrm{MIC}}$	AUC_{0-24}/MIC
Aminoglycosides	β-lactams	Aminoglycosides
Colistin	Erythromycin	Colistin
Daptomycin	Linezolid	Quinolones
Quinolones		Linezolid

Table 3.3: Killing dependence of antibiotics and relevant PK/PD indices [155].

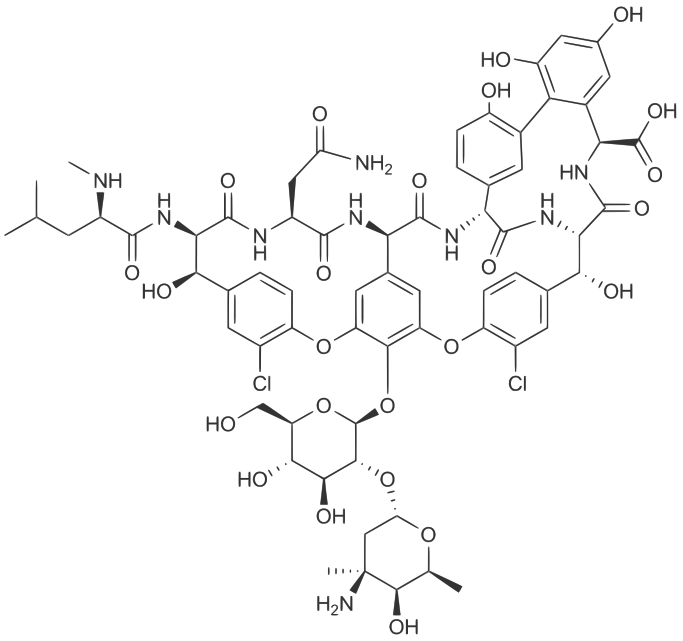

Figure 3.1: Chemical structure of vancomycin ($C_{66}H_{75}Cl2N_9O_{24}$) [206]. Molecular mass: 1449.3 g/mol.

3.2 Vancomycin

Vancomycin is a bactericidal drug which inhibits cell wall synthesis by interfering with peptidoglycan synthesis (see Table 3.1 and Fig 3.1). It is a hydrophilic glycopeptide with high molecular mass 1449.3 g/mol and moderate protein binding ($55\% - 60\%$) [179, 74, 134]. Because of these distinctive physico-chemical features vancomycin shows interesting and non-trivial pharmacokinetic and pharmacodynamic properties: It is active only against Gram-positive bacteria because it cannot cross the outer membrane of Gram-negative bacteria. Its distribution volume and clearance strongly depend on patient features (e.g., on serum albumin concentration). It is removed by RRT to a very different extent according to operating conditions [134]. The molecule is too large to be removed by haemodialysis with old cuprophane membranes (< 1000 Da) and is removed by haemofiltration with a sieving coefficient of about 0.8.

With reference to efficacy, vancomycin has shown concentration-time dependent killing prop-

erties (see Sec. 3.1, kill characteristics). The range between the minimum concentration at which this drug is effective and the concentration above which it shows nephrotoxic effects is quite narrow. The recommended range has been specified at 20–40 μg/ml for peak concentrations and 10–15 μg/ml for trough concentrations [164, 122]. Furthermore, several studies have shown that the AUC/MIC is the PK/PD index that best correlate with efficacy. In particular, it has been shown that AUC_{0-24}/MIC is a good predictor of clinical and bacteriological outcomes [165, 215, 164, 93], with higher clinical success rates in the subset of patients with $AUC_{0-24}/MIC > 350$ (400 for bacteria eradication) [125]. Using this value as the threshold to discriminate between effective and non-effective treatments, Monte Carlo simulations [154] have emphasised that the probability that an antibiotic treatment is effective is very low with standard dosage regimens [54, 150, 156, 27] (see Secs. 3.2.1, 3.2.3, 3.2.4, and 3.2.5).

For all the reasons mentioned above, it is very difficult to identify the appropriate dosage regimen for critically ill patients: PK/PD indices are very sensitive to patient conditions and to the received treatments and the range of concentrations at which vancomycin is effective without being toxic is extremely narrow. It is therefore important to develop reliable models of pharmacokinetics to optimise the dosage regimen [92]. Hence, a lot of effort has recently been devoted to the construction of pharmacokinetic models in critically ill patients [54, 117, 150, 156, 27]. For other analogue reasons, it is also strongly recommended to regularly monitor the plasma concentration of vancomycin during the treatment period [163, 122].

In the literature there are few population models of vancomycin pharmacokinetics in critically ill patients. Each reveals important features of vancomycin pharmacokinetics but all suffer from several drawbacks from clinical, physiological, epidemiological, or mathematical perspectives. I shall present five of the most relevant models highlighting their most interesting features and discussing their weaknesses. I selected only those works involving critically ill patients with a sample size of at least a few tens of patients, without aiming to provide a systematic review of vancomycin pharmacokinetic properties. Three of them are based on a single-compartment model, two on a two-compartment model. A critical analysis of these models represents the starting point for the construction of a more realistic model.

In Chap. 5 I shall construct a population model for vancomycin on a wide sample of ICU patients. I shall choose the model structure, the relevant covariates, and the functional forms expressing the dependence of pharmacokinetic parameters on patient conditions by following the properties presented and discussed here and in Chap. 2.

3.2.1 Pharmacokinetic/pharmacodynamic analysis of vancomycin in ICU patients

The study was conducted on 46 adult patients admitted to a single ICU of the teaching hospital of the University of Salamanca (2007 [54]). Patients with less than three measurements of vancomycin concentration, prior cardiac surgery, neoplastic disorders, or undergoing renal replacement therapy were excluded from the study. Serum vancomycin concentrations were measured using a fluorescence polarisation immunoassay (AxSYM), Abbott Laboratories, Abbott Park, IL, USA) with a quantification limit of 2.00 mg/l and inter-day variation coefficients smaller than 7%.

Pharmacokinetic analysis was performed assuming a one-compartment model. Population analysis was based on a two-stage approach. In the first stage, individual parameters were determined by non-linear regression using the software PKS (Abbottbase Pharmacokinetic System). In the secondtage stage, statistical analysis was applied to the parameters obtained in the first stage.

The distribution volume was normalised to body weight w

$$V = \theta_w \, w, \tag{3.1}$$

with $\theta_w = 0.72\,\mathrm{l/kg}$. No dependence on further variables was investigated.

Dependence of drug clearance k_{vanco} per body weight w was investigated as a function of covariates adopting multiple regression techniques. Interestingly drug clearance k_{vanco} was expressed as a function of age a, renal function (parametrised by creatinine clearance k_{crea}), patient severity (measured with Apache II Score s), and serum albumin concentration C_{alb}, which quantifies the level of protein binding:

$$\frac{k_{\mathrm{vanco}}}{w} = \theta_0 + \theta_a \, a - \theta_s \, s - \theta_{\mathrm{alb}} C_{\mathrm{alb}} + \theta_c \, \frac{k_{\mathrm{crea}}^L}{w}. \tag{3.2}$$

Two models were developed using either measured or computed creatinine clearance, through Levey's formula [111]. The performance of the two models is comparable, with an r^2 of 0.64 and 0.68, respectively. The fitted values of the free parameters are reported in Table 3.4. The variable included in the model accounted for more than 65% of the vancomycin clearance variability, of which 50% was by creatinine clearance.

Finally, a Monte Carlo simulation was performed to estimate the percentage of patients in whom the therapeutic target is achieved with standard vancomycin dosage for several pathogens (the MIC distribution for each pathogen was empirically based on reported data from the EUCAST database [2]). The considered goal for treatment optimisation was a ratio AUC/MIC for the first 24 h of treatment higher than 400 h.

covariate	parameter	units	measured k_{crea}	computed k_{crea}
–	θ_0	ml/(min kg)	0.660	0.872
age	θ_a	ml/(min kg yr)	0.016	0.015
Apache II Score	θ_s	ml/(min kg)	0.006	0.007
serum albumin concentration	θ_{alb}	ml dl/(min kg g)	0.380	0.234
creatinine clearance	θ_c	–	0.562	0.346

Table 3.4: Best-fit coefficients of model (3.2) using either measured (third column) or computed (fourth column) creatinine clearance.

This analysis emphasises the risk of vancomycin underdosing in critically ill patients. Indeed, according to a standard dosage of 2000 mg/day, it was found that the risk of not achieving the recommended $\text{AUC}_{24\text{h}}$/MIC is not negligible and varies from a minimum of less than 3% for *S. pneumoniae* to a maximum of 40% for coagulase-negative Staphylococci. The risk of not attaining the target with this dosage was 22% for *S. aureus*. This work shows that to overcome the risk of underdosing for glycopeptide-intermediate Staphylococcus aureus, doses as high as 5000 mg/day should be administered to have an 80% probability of achieving the therapeutic target.

Although the model of Eqs. 3.1 and 3.2 allows one to draw important conclusions at an epidemiological level it cannot provide reliable prediction at the patient level. Indeed, the development sample size was too small and contains only a few covariates. In particular, the distribution volume is not well characterised, being a function only of the total body weight.

3.2.2 Population pharmacokinetic parameters of vancomycin in critically ill patients

A pharmacokinetic model of vancomycin was developed on 234 serum vancomycin concentrations measured in 30 adult patients and validated on 40 plasma concentrations from 20 adult patients (2006 [117]). All included patients had fluctuations of plasma creatinine no higher than ± 0.5 mg/dl and none of them required renal replacement therapy. Non-steady state plasma concentrations were excluded.

All the analyses were performed using NONMEM software. Data were first fitted into one- and two-compartment models with no covariates. The result of this preliminary analysis suggested that the two-compartment model was more suitable to describe available data. The adopted two-compartment model is parametrised by drug clearance from first compartment k_{vanco}, distribution volume of the central (V_c) and peripheral (V_p) compartment, and intercompartmental clearance (k_{int}), describing drug exchanges between the two compartments. Adopting the notation of Sec. 4.2, $V_1 = V_c$, $V_2 = V_p$, and the three diffusion rates κ_e, κ_{12}, and κ_{21} defined in Sec. 4.2 are related to

these pharmacokinetic parameters as

$$\kappa_e = \frac{k_{\text{vanco}}}{V_c}, \qquad \kappa_{12} = \frac{k_{\text{int}}}{V_c}, \qquad \kappa_{21} = \frac{k_{\text{int}}}{V_p}, \tag{3.3}$$

therefore assuming that the membrane crossing is symmetric [see Eq. (4.17)] and the intercompartmental clearance is proportional to the diffusion coefficient d and the total membrane surface S, $k_{\text{int}} = d\,S$.

Inter-individual variability was described by a proportional error model for three pharmacokinetic parameters (k_{vanco}, V_c, and V_p):

$$k_{\text{vanco},i} = k_{\text{vanco}}\,(1+\eta_{k,i})\,, \qquad V_{c,i} = V_c\,(1+\eta_{V_c,i})\,, \qquad V_{p,i} = V_p\,\left(1+\eta_{V_p,i}\right). \tag{3.4}$$

No inter-individual variability was assumed for the intercompartmental clearance Q.

A proportional-additive error model was instead adopted to describe the residual (intraindividual) variability on concentration measurements

$$C_{ij} = C_i(t_{ij})\,(1+\varepsilon_{1,ij}) + \varepsilon_{2,ij}. \tag{3.5}$$

A linear relationship between vancomycin clearance and creatinine clearance was assumed

$$k_{\text{vanco}} = \theta_c\,k_{\text{crea}}^{\text{CG}} + \theta_w\,w, \tag{3.6}$$

where $\theta_w\,w$ is the non-renal component of the clearance (which is assumed to be proportional to the total body weight w) and $k_{\text{drug}}^{\text{CG}}$ is the creatinine clearance estimated by means of the Cockcroft–Gault formula [50]

$$k_{\text{vanco}}^{\text{CG}} = \frac{w_l/\text{kg}\,(140-a/\text{yr})}{72\,C_{\text{crea}}\,\text{dl/mg}}\,\text{ml/min} \times \begin{cases} 1 & \text{for men,} \\ 0.85 & \text{for women.} \end{cases} \tag{3.7}$$

where C_{crea} is the serum creatinine concentration, a is age, and w_l is lean body mass

$$w_l = w - w_{\text{fat}}, \tag{3.8}$$

obtained by subtracting fat mass w_{fat} from total body mass w. In patients with serum creatinine less than 0.5 mg/dl, a maximum value of $k_{\text{crea}}^{\text{CG}} = 120\,\text{ml/min}$ was adopted to avoid overestimated values.

The distribution volumes of the two compartments were found to be proportional to total body

PK parameter	covariate	parameter	units	value	95% CI
drug clearance	creatinine clearance	θ_c	–	0.57	0.17 – 0.93
	body weight	θ_w	ml/(min kg)	0.25	-0.02 – 0.65
central volume	–	θ_{V_c}	l/kg	0.41	0.36 – 0.47
peripheral volume	–	θ_{V_p}	l/kg	1.32	0.79 – 1.86
intercompartment diffusion	–	θ_i	ml/min	125	102 – 147

Table 3.5: Best-fit estimates of the parameters of the pharmacokinetic model of Eqs. (3.6), (3.9), and (3.10).

weight

$$V_c = \theta_{V_c}\, w, \qquad V_p = \theta_{V_p}\, w, \tag{3.9}$$

while no dependence on patient characteristics was assumed for the intercompartmental clearance

$$k_{\text{int}} = \theta_i. \tag{3.10}$$

The best-fit estimate of the free parameters θ is reported in Table 3.5. The model was validated on a validation sample.

With the final best-fit values, the vancomycin clearance of a typical ICU patient with $k_{\text{crea}} = 70\,\text{ml/min}$ and $w = 75\,\text{kg}$ is $k_{\text{vanco}} = 58\,\text{ml/min}$. The Authors stressed that this value, obtained for critically ill patients, is similar to those obtained in previous investigations, based on heterogeneous [212] or homogeneous populations of severely burned patients [161], oncology patients with hepatic dysfunction [37], and patients with infected prosthetic devices [92], but lower than the value reported for critically ill patients in Ref. [138]. Interestingly, with this analysis it was shown that vancomycin has a relatively important fraction of non-renal clearance, representing about 28% of total drug clearance.

In this work no Monte Carlo simulations were performed to estimate the probability of achieving the therapeutic target.

3.2.3 Vancomycin dosing assessment in intensive care unit patients based on a population pharmacokinetic/pharmacodynamic simulation

In this work a pharmacokinetic model was developed on a sample of 191 adult patients admitted to the medical ICU of the University Hospital of Salamanca (2010 [150]). As in Ref. [54], patients with neoplastic disorders, renal replacement therapy, or without measurements of vancomycin concentrations were excluded from the analysis. Pre-dose plasma vancomycin concentration was

measured by fluorescence polarisation immunoassay (AxSYM; Abbott Laboratories, Abbott Park, USA). The quantification limit was 2.00 mg/l and the intra- and inter-assay coefficients of variation were less than 7% over the calibration range (7 to 75 mg/l).

A population pharmacokinetic model was constructed from the 569 available vancomycin concentrations using the first-order conditional estimation method with interaction as implemented in NONMEM. Available information allowed to construct only a one-compartment model with first order elimination. Drug clearance and distribution volume were expressed as functions of clinical variables selected through a stepwise forward selection procedure based on the minimum value of the NONMEM objective function to compare nested models and using the Akaike information criterion to compare non-nested models.

After testing several error models, inter-individual variability was eventually modelled as an exponential random effect for both clearance and distribution volume

$$k_{\text{vanco},i} = k_{\text{vanco}}\, e^{\eta_{k,i}}, \qquad V_i = V\, e^{\eta_{V,i}}. \tag{3.11}$$

Residual variability was instead modelled with an additive error model

$$C_{ij} = C_i(t_{ij}) + \varepsilon_{ij}. \tag{3.12}$$

In the final covariate model, vancomycin clearance was estimated per body weight and depended on 24h-measured creatinine clearance k_{crea} per body weight w and age a as

$$\frac{k_{\text{vanco}}}{w} = \theta_{\text{c}} \frac{k_{\text{crea}}}{w} + \left(\frac{a}{\text{yr}}\right)^{-\theta_a} \frac{\text{ml}}{\text{min kg}}, \tag{3.13}$$

with $\theta_c = 0.67$ and $\theta_a = 0.24$. Thus, total drug clearance effectively depends on the interaction between age and body weight

$$k_{\text{vanco}} = \theta_{\text{c}}\, k_{\text{crea}} + w \left(\frac{a}{\text{yr}}\right)^{-\theta_a} \frac{\text{ml}}{\text{min kg}}, \tag{3.14}$$

where the heavier a patient, the higher his/her clearance.

Similarly, the distribution volume depends on serum creatinine concentration C_{crea} and body weight as

$$V = \theta_w\, w\, \times {\theta_{\text{crea}}}^{d_{\text{crea}}}, \tag{3.15}$$

where d_{crea} is a dichotomous variable which is 1 if the serum creatinine concentration C_{crea} is larger than 1 mg/dl and 0 otherwise. The best-fit values of the parameters θ are reported in Table 3.6. Interestingly, the introduction of serum creatinine as a dichotomous variable accounted for 60%

PK parameter	covariate	parameter	units	value	95% CI
drug clearance	creatinine clearance	θ_c	–	0.67	0.58 – 0.76
	age	θ_a	–	0.24	0.21 – 0.27
distribution volume	body weight	θ_w	l/kg	0.82	0.70 – 0.94
	creatinine clearance	θ_{crea}	–	2.49	2.00 – 2.98

Table 3.6: Best-fit estimates of the parameters of the pharmacokinetic model of Eqs. (3.14) and (3.15).

of interindividual variability. Apparently serum creatinine is a marker of critical illness which is typically associated with very large distribution volumes.

Finally, on the basis of a Monte Carlo simulation, the probability of attaining the target concentration for a specific drug dose and a specific population of microorganisms was calculated. As in Ref. [54], the considered goal for treatment optimisation was an AUC/MIC ratio for the first 24 h of treatment higher than 400 h. It was found that with a daily dose of 2 g, the therapeutic target was achieved in the treatment of vancomycin susceptible *S. aureus* in 95.5% of patients older than 65 years and with creatinine clearance lower than 60 ml/min, but only in 33.4% of cases younger than 65 and with creatinine clearance higher than 60 ml/min. The corresponding percentages for vancomycin-intermediate susceptibility strains falls to 23.9% and 0.2%, respectively. This result suggests that standard dosing often fails to achieve the therapeutic target in critically ill patients, especially in those with normal renal function.

3.2.4 Vancomycin dosing in critically ill patients: robust methods for improved continuous-infusion regimens

A one-compartment pharmacokinetic model was developed from 206 adult patients with a diagnosis of sepsis admitted to a single ICU at Erasme Hospital, Brussels, undergoing continuous infusion of vancomycin either in monotherapy or in combination with other antimicrobials. Patients with previous administration of vancomycin by intermittent infusion, or with continuous infusion lasting less than 48 hours, or undergoing renal replacement therapy were excluded (2011 [156]).

Blood samples were taken once a day and the serum concentration of vancomycin was immediately determined by fluorescence polarisation immunoassay. The assay limit was 0.6 mg/l, with intra- and inter-day coefficient of variation was 0.6%, and $r^2 = 0.999$.

Population one-, two-, and three-compartment kinetic models were tested using NONMEM with a first-order conditional estimation method with interaction. The best-fit model was one-compartment with zeroth order input and combined proportional and additive residual variability, i.e.

$$C_{ij} = C_i(t_{ij})\, e^{\varepsilon_{1,ij}} + \varepsilon_{2,ij}. \tag{3.16}$$

PK parameter	covariate	parameter	units	value	95% CI
drug clearance	creatinine clearance	θ_c	–	0.76	0.68 – 0.89
distribution volume	body weight	θ_w	l/kg	1.53	1.31 – 1.71

Table 3.7: Best-fit estimates of the parameters of the pharmacokinetic model of Eqs. (3.17) and (3.18) and 95% confidence intervals estimated by bootstrap technique.

and exponential inter-individual variability [see Eq. (3.11))]. Drug clearance was proportional to creatinine clearance normalised to body surface area S as

$$k_{\text{vanco}} = \theta_{\text{c}} \frac{k_{\text{crea}}}{S/1.73\,\text{m}^2}. \tag{3.17}$$

The distribution volume was expressed as

$$V = \theta_w\, w, \tag{3.18}$$

where w is the total body weight. The best-fit values of the parameters θ are reported in Table 3.7.

Simulations were performed to test the effect on vancomycin concentrations of different loading doses and continuous infusion rates for patients with different creatinine clearances. The effects of different weight-based dosing regimens for continuous infusions were also simulated. It was found that a loading dose of at least 35 mg/kg was necessary to rapidly achieve a vancomycin concentration of 20 mg/l, with an AUC in the first 24 h of 485 mg h/l, for a patient with a normalised creatinine clearance of 100 ml/min/1.73 m^2 and a continuous infusion rate of 35 mg/kg/day.

The Authors stressed the importance of choosing appropriate continuous infusion rates according to the patient's creatinine clearance. It was found that an infusion rate of 35 mg/kg/day was not enough to achieve the therapeutic target concentration in patients with creatinine clearance higher than 100 ml/min/1.73 m^2 while, it yielded toxic concentrations (above 30 mg/l) in patients with altered renal function ($k_{\text{crea}}/S < 50\,\text{ml/min/1.73}\,\text{m}^2$).

Although this model is quite simplistic, including only a few patient characteristics (creatinine clearance, body surface, and body weight), it reveals some important aspects of vancomycin kinetics and provides some estimates of optimal personalised dosing regimens.

3.2.5 A new regimen for continuous infusion of vancomycin during continuous renal replacement therapy

This study was conducted on 32 adult patients admitted to an ICU of the Erasme Hospital, Brussels (2013 [27]). Patients undergoing CRRT received a loading dose of 35 mg/kg given in

parameter	units	value	95% CI
θ_{CRRT}	kg	57	43 – 71
θ_i	ml/min	80	55 – 128
θ_{V_c}	l/kg	0.44	0.31 – 0.54
θ_{V_p}	l	60.5	35.4 – 98.3

Table 3.8: Best-fit estimates of the parameters of the pharmacokinetic model of Eqs. (3.19)–(3.22). Confidence intervals were computed by bootstrap technique.

4 h, followed by continuous infusion at a rate of 14 mg/kg/day. The loading dose was determined according to the results of Ref. [156] for patients without renal dysfunction. The continuous infusion rate was chosen assuming that CRRT provides a creatinine clearance equivalent to 20–50 ml/min.

Vancomycin concentration was measured at the end of the loading dose, 12 h and 24 h after the commencement of the treatment, and every subsequent day, using a particle-enhanced turbidimetric inhibition immunoassay (Dimension XPand, Siemens Healthcare Diagnostics, Newark, DJ, USA). The limit of quantification was 0.8 mg/l and the total imprecision was less than 5%.

A two-compartment pharmacokinetic model was fitted through a non-linear mixed-effect procedure using a first-order conditional estimation method with interaction. Between-subject variability was described with an exponential model [see Eq. (3.11)] and residual variability with a combined exponential-additive model [see Eq. (3.16)]. The final model, including all significant covariates, for the central and peripheral distribution volumes V_c and V_p, for drug clearance k_{vanco} and intercompartmental clearance k_{int} [see Eq. 3.3] reads

$$k_{\text{vanco}} = \theta_{\text{CRRT}}\, I_{\text{CRRT}}, \tag{3.19}$$

$$k_{\text{int}} = \theta_i, \tag{3.20}$$

$$V_c = \theta_{V_c}\, w, \tag{3.21}$$

$$V_p = \theta_{V_p}, \tag{3.22}$$

where w is the total body weight and I_{CRRT} the CRRT intensity, calculated as the sum of the dialysate rate and ultrafiltration rate. The values of the best fit parameters are reported in Table 3.8. For a typical CRRT intensity $I = 35$ ml/kg/h $= 0.58$ ml/kg/min, the resulting clearance of vancomycin is $k_{\text{vanco}} = 33$ ml/min (95% CI: 25 – 41 ml/min). Regarding the achievement of the therapeutic target, the Authors found that an $\text{AUC}_{24\text{h}} > 400$ was reached for 100% of pathogens with MIC < 1 mg/l, 72% with MIC $= 1.5$ mg/l, and 25% with MIC $= 2$ mg/l.

Although this study was conducted on a relatively low number of patients, it showed a significant correlation between CRRT intensity and total drug clearance in patients undergoing CRRT. It suggests that the vancomycin clearance provided by CRRT is comparable with the renal clearance

of a patient without renal failure.

Chapter 4

COMPARTMENT PHARMACOKINETICS

The construction of a pharmacokinetic model is a complex process which must take into account all the physiological aspects presented in the previous chapters. In this Chapter I shall present the mathematical and statistical techniques that will be adopted throughout this Thesis.

To clarify the important role played by the number of compartments and the complexity of the equations, in this Chapter I shall review two models, with one and two compartments, respectively (see, e.g, [69, 162]). I shall also briefly review the technique used to fit the model parameters on patient data (see Sec. 4.3). When the equations are linear with constant coefficients, their solutions can be analytically computed. A proper mathematical analysis of those solutions allows to understand the underlying approximations, the aspects of drug kinetics that can be modeled, and shows the limitations of this approach. Thus, such an analysis allows to acquire a deeper understanding of the mathematical properties of the system and is fundamental before proceeding with numerical integration and data fitting.

From the following discussion, it will be evident that the choice of the number of compartments and the form of the equations cannot be based only on physiological and biochemical arguments, but must take into account these mathematical aspects.

4.1 One-compartment model

As presented in Sec. 2.4, the simplest model of pharmacokinetics assumes that drugs distribute only in one compartment [69, 162]. Drug enters and exits a volume V, where it is distributed with

a homogeneous concentration C. The total amount Q of drug present in the body is

$$Q = C\,V \tag{4.1}$$

and, assuming that drug removal il proportional to drug concentration, the differential equation governing the evolution of Q is

$$\frac{\mathrm{d}Q}{\mathrm{d}t} = -k\,C + I, \tag{4.2}$$

where k is the drug clearance and I the external infusion rate. Eliminating C,

$$\frac{\mathrm{d}Q}{\mathrm{d}t} = -\kappa\,Q + I, \tag{4.3}$$

where the elimination rate $\kappa = k/V$ has dimension of the inverse of time.

Eq. (4.3) is a non-homogeneous linear first order equation. To solve it, I first look for a solution of the corresponding homogeneous equation

$$\frac{\mathrm{d}Q}{\mathrm{d}t} = -\kappa\,Q, \tag{4.4}$$

which describes the kinetics of the drug after a bolus and in the absence of continuous administration I. Assuming that the elimination rate k is constant, the solution for Q is

$$Q(t) = A\,e^{-\kappa t}, \tag{4.5}$$

where the integration constant A is fixed by initial condition. If a bolus of dose D is administered at time $t = 0$, the initial amount of drug $Q(0) = D$, yielding

$$Q(t) = D\,e^{-\kappa t}. \tag{4.6}$$

Drug concentration vanishes exponentially with half-life

$$t_{1/2} = \frac{\log(2)}{\kappa}, \tag{4.7}$$

as illustrated in the left panel of Fig. 4.1. The corresponding AUC [see Eq. (2.68)] is

$$A_C(t) = \int_0^t C(t')\,\mathrm{d}t' = \frac{D}{k}\left(1 - e^{-\kappa t}\right). \tag{4.8}$$

In the limit when $t \to \infty$, the area under the curve is $A_C = D/k$, as discussed in Sec. 2.3.

To compute the general solution of the non-homogeneous equation Eq. (4.3), it is enough to

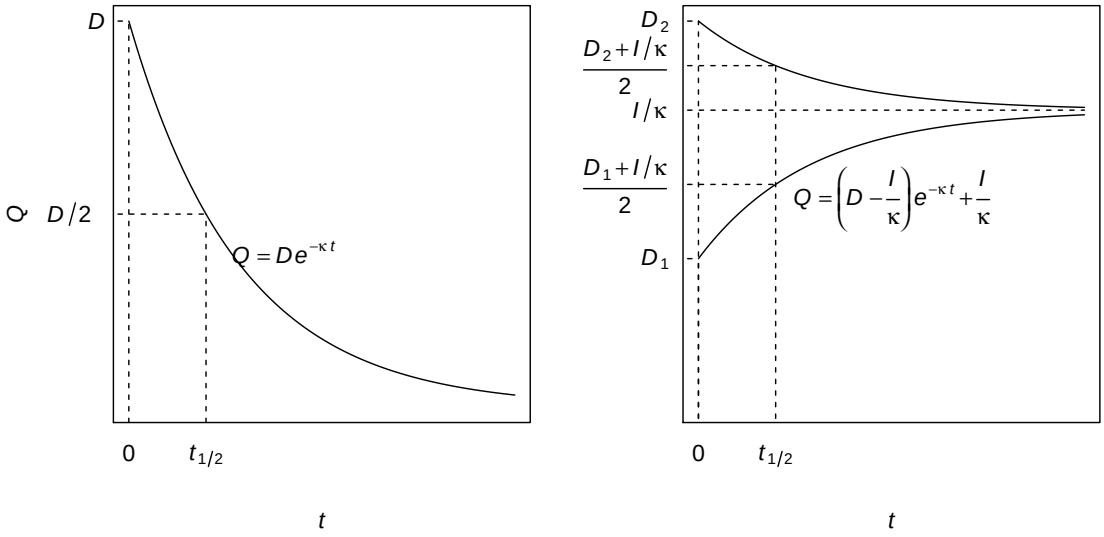

Figure 4.1: Time evolution of total drug amount in body Q after a bolus D without (left) and with (right) continuous infusion. $t_{1/2}$ is the drug half-life.

find a particular solution. Assuming a constant infusion rate I, the infusion is exactly balanced by elimination when the value of the drug amount has a constant value

$$\bar{Q} = \frac{I}{\kappa}, \tag{4.9}$$

and its derivative vanishes. The general solution of Eq. (4.3) is therefore

$$Q(t) = A\, e^{-\kappa t} + \frac{I}{\kappa}, \tag{4.10}$$

where A is again an integration constant fixed by the initial condition. If at time $t = 0$ a bolus D is administered to the patient, $Q(0) = D$, $A = (D - I/\kappa)$ and

$$Q(t) = \left(D - \frac{I}{\kappa}\right) e^{-\kappa t} + \frac{I}{\kappa}. \tag{4.11}$$

This solution is represented in the right panel of Fig. 4.1. For times t much larger than the drug half-life, the total drug amount Q converges to the stationary value $\bar{Q}$, whatever the loading dose D. In fact, if D is larger or smaller than $\bar{Q}$, Q decreases or increases, respectively, to reach $\bar{Q}$.

If an optimal concentration C_{opt} must be maintained to achieve some therapeutic goal, an optimal loading dose D_{opt}

$$D_{\text{opt}} = C_{\text{opt}} V \tag{4.12}$$

must be administered to reach the target concentration $C_{\rm opt}$. Hence, an optimal infusion

$$I_{\rm opt} = C_{\rm opt} V \kappa \tag{4.13}$$

will allow the steady state concentration $C_{\rm opt}$ to be maintain, corresponding to $\bar{Q} = C_{\rm opt} V$. The right panel of Fig. 4.1 shows that if the loading dose is non-optimal, say smaller (D_1) or larger (D_2) than $\bar{Q}$, the time scale to converge to the target concentration is the half-life time. This time cannot be controlled by adjusting I, because it depends only on the distribution volume and the drug clearance. In particular, being proportional $1/\kappa = V/k$, it may be very large for large volumes and/or reduced clearances. In these cases, the only way to promptly reach the therapeutic target is to perform an appropriate bolus $D_{\rm opt}$.

4.2 Two-compartment model

In this section I review the behaviour of the simple linear two-compartment model presented in Sec. 2.4 [69, 162]. This model is suitable to describe the kinetic properties of a drug administered by intravenous infusion that can diffuse into an extra-vascular compartment.

Defining the concentrations and distribution volumes in the two compartments C_1, C_2, V_1 and V_2 and the total amounts of drug in the two compartments $Q_1 = C_1 V_1$ and $Q_2 = C_2 V_2$, one obtains the following system of equations:

$$\frac{{\rm d}Q_1}{{\rm d}t} = -\kappa_e Q_1 - \kappa_{12} Q_1 + \kappa_{21} Q_2 + I, \tag{4.14}$$

$$\frac{{\rm d}Q_2}{{\rm d}t} = \kappa_{12} Q_1 - \kappa_{21} Q_2, \tag{4.15}$$

where κ_{12} and κ_{21} are the diffusion rates from the first to the second compartment and *vice versa*. Here we have assumed that the drug is infused in the first compartment at a rate I and eliminated only from this compartment with an elimination rate κ_e.

If the membrane separating the two compartments allows symmetric diffusion [see (2.1)], the quantity of drug per unit time crossing the membrane from compartment 1 to compartment 2 is

$$d\, S\, (C_1 - C_2)\,, \tag{4.16}$$

where d is the diffusion coefficient and S the total surface of the membrane. Comparing Eq. (4.16) with the diffusion terms in Eqs. (4.14) and (4.15), the diffusion rates are inversely proportional to

the two distribution volumes

$$\kappa_{12} = \frac{d\,S}{V_1}, \qquad \kappa_{21} = \frac{d\,S}{V_2}. \tag{4.17}$$

The system of Eqs. (4.14) and (4.15) is linear and non-homogeneous. Its general solution is the sum of the general solution of the homogeneous system (i.e., without continuous infusion) plus a particular solution of the non-homogeneous system.

4.2.1 Homogeneous solution

After a few calculations, the general solution of the homogeneous system is

$$Q_1(t) = A_1 \frac{\kappa_{21} - \lambda_1}{\kappa_{12}} e^{-\lambda_1 t} + A_2 \frac{\kappa_{21} - \lambda_2}{\kappa_{12}} e^{-\lambda_2 t}, \tag{4.18}$$

$$Q_2(t) = A_1\, e^{-\lambda_1 t} + A_2\, e^{-\lambda_2 t}. \tag{4.19}$$

where A_1 and A_2 are two integration constants and

$$\lambda_1 = \frac{A + \sqrt{A^2 - 4B}}{2}, \qquad \lambda_2 = \frac{A - \sqrt{A^2 - 4B}}{2} \tag{4.20}$$

are the two solutions of the second order equation

$$\lambda^2 - A\,\lambda + B = 0, \tag{4.21}$$

with

$$A = \kappa_e + \kappa_{12} + \kappa_{21}, \qquad B = \kappa_e\,\kappa_{21}. \tag{4.22}$$

Since all κ_i are positive, it is easy to show that $A^2 - 4B$ is positive, so that λ_1 and λ_2 are always real and positive. Thus, the homogeneous system always admits a decaying solution.

For later convenience, I shall also prove that

$$\lambda_2 < \kappa_{21} < \lambda_1. \tag{4.23}$$

This is equivalent to

$$\sqrt{A^2 - 4B} > 2\kappa_{21} - A, \qquad \sqrt{A^2 - 4B} > A - 2\kappa_{21}, \tag{4.24}$$

that is

$$\sqrt{A^2 - 4B} > |A - 2\kappa_{21}|\,. \tag{4.25}$$

Since $A^2 - 4B$ is always positive, it is enough to show that

$$A^2 - 4B > (A - 2\kappa_{21})^2 . \tag{4.26}$$

The above relation is proved by inserting the values of A and B from Eq. 4.22. Analogously, it may be proved that

$$\lambda_1 > \kappa_{12}. \tag{4.27}$$

The two integration constants A_1 and A_2 are easily determined by imposing the initial condition

$$Q_1(0) = D, \qquad Q_2(0) = 0, \tag{4.28}$$

which corresponds to a loading dose D administered to the first compartment. One obtains

$$A_2 = -A_1 = \frac{\kappa_{12}\, D}{\lambda_1 - \lambda_2}, \tag{4.29}$$

which yields

$$Q_1(t) = \frac{D}{\lambda_1 - \lambda_2} \left[(\kappa_{21} - \lambda_2)\, e^{-\lambda_2 t} + (\lambda_1 - \kappa_{21})\, e^{-\lambda_1 t} \right], \tag{4.30}$$

$$Q_2(t) = \frac{\kappa_{12}\, D}{\lambda_1 - \lambda_2} \left[e^{-\lambda_2 t} - e^{-\lambda_1 t} \right]. \tag{4.31}$$

Using Eq. (4.23), it is easy to prove that Q_1 and Q_2 are always positive. As illustrated in the left panel of Fig. 4.2, Q_1 is monotonic decreasing from D to 0, whereas Q_2 starts from 0 at $t = 0$, reaches a maximum

$$Q_{2\max} = \frac{\kappa_{12}\, D}{\lambda_1 - \lambda_2} \left(\frac{\lambda_2}{\lambda_1} \right)^{\lambda_2/(\lambda_1 - \lambda_2)} \left[1 - \frac{\lambda_2}{\lambda_1} \right] \tag{4.32}$$

at

$$t_{\max} = \frac{\log(\lambda_1/\lambda_2)}{\lambda_1 - \lambda_2} \tag{4.33}$$

and finally goes to 0.

In the left panel of Fig. 4.2, diffusion from the first to the second compartment is faster than elimination ($\kappa_{12} = 2\kappa_e$) and the diffusion rate from the second compartment back to the first one is $\kappa_{21} = \kappa_{12}/4$. In the case of symmetric membrane [see Eq. (4.17)], this corresponds to a distribution volume in the second compartment four times larger than the distribution volume in the first compartment. With this choice of the parameters, $\lambda_1 \approx 3.35\,\kappa_e$ and $\lambda_2 \approx 0.15\,\kappa_e$. The two exponentials of Eqs. (4.30) and (4.31) decay on very different time scales $\tau_1 = \lambda_1^{-1} \approx 0.30\,\kappa_e^{-1}$ and $\tau_2 = \lambda_2^{-1} \approx 6.7\,\kappa_e^{-1}$. Physically, the time scale τ_1 over which the drug leaves the first compartment and fills the second one is much shorter than the time scale τ_2 over which both compartments are

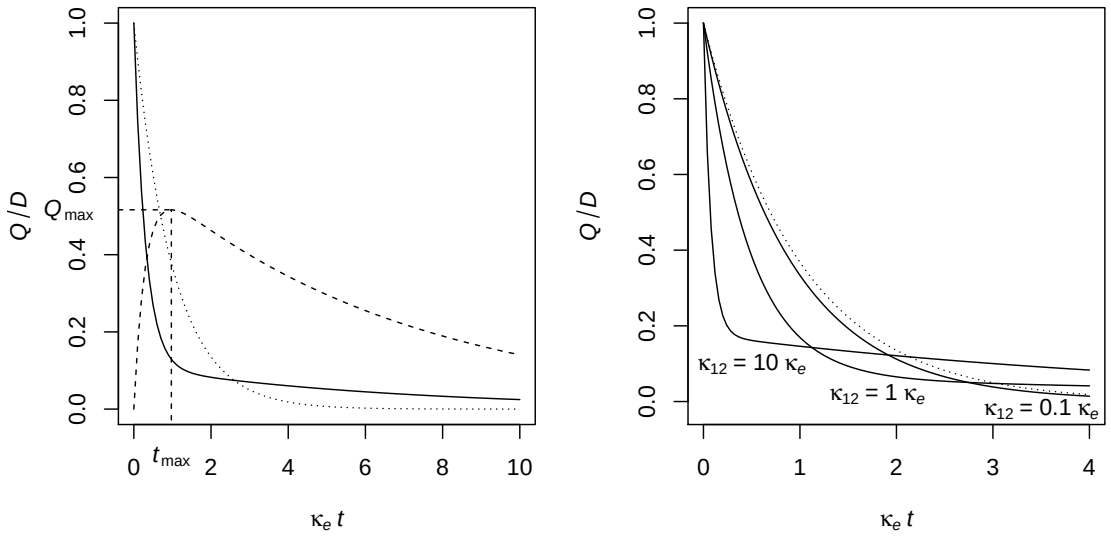

Figure 4.2: Left panel: Time evolution of drug amount in the two compartments Q_1 (solid line) and Q_2 (dashed line) after a bolus D, for $\kappa_{12} = 2\kappa_e$. Right panel: time evolution of Q_1 for three values of $\kappa_{12} = 10,\ 1,\ 0.1\kappa_e$ (solid lines). In both panels the dotted line represents the time evolution of Q in a one-compartment model with $\kappa = \kappa_e$. Q and t are measured in units of D and κ_e^{-1}, respectively, and $\kappa_{21} = \kappa_{12}/4$.

depleted and drug concentrations go to zero. In general when

$$\kappa_{21} \ll \kappa_e + \kappa_{21}, \quad \text{or} \quad \kappa_e \ll \kappa_{12} + \kappa_{21}, \tag{4.34}$$

the two solutions λ_1 and λ_2 can be approximated as

$$\lambda_1 \approx A = \kappa_e + \kappa_{12} + \kappa_{21}, \qquad \lambda_2 \approx \frac{B}{A} = \frac{\kappa_e \kappa_{21}}{\kappa_e + \kappa_{12} + \kappa_{21}}, \tag{4.35}$$

that is, the fastest decay rate λ_1 is given by the sum of the three rates κ_e, κ_{12}, and κ_{21}, while λ_2 is much smaller and is proportional to $\kappa_e\kappa_{21}$.

The dotted line in the left panel of Fig. 4.2 represents the solution $Q(t)$ of a one-compartment system with the same elimination rate $\kappa = \kappa_e$. Since in a clinical study drug concentrations are generally measured only in blood, only the predicted evolution of Q_1 (which represents drug concentration in the blood compartment) may be tested against measured concentrations, whilst Q_2 is not experimentally accessible. This implies that differences between one- and two-compartment models, if any, must be appreciated by comparing the two curves Q and Q_1. The plot shows that, just after bolus administration, drug blood concentration decreases much more rapidly in a two-compartment model than in a one-compartment one. In fact, in the two-compartment model drug diffuses from the first to the second compartment on a time scale τ_1 which is shorter than the elimination time scale $\tau = \kappa^{-1}$ in the corresponding one-compartment model. However, in the two-compartment model the body is completely depleted on a much longer time scale $\tau_2 \gg \tau$,

since drug stored in the second compartment is eliminated only after a slow diffusion back to the first compartment. Thus, at later times ($t \gtrsim 3\kappa_e^{-1}$), Q_1 becomes larger than Q and vanishes more slowly.

In the right panel of Fig. 4.2, the evolution of $Q_1(t)$ (solid lines) is compared against $Q(t)$ for three values of the diffusion coefficient $\kappa_{12} = 10,\, 1,\, 0.1\kappa_e$. The ratio κ_{21}/κ_{12} between the two diffusion rates is fixed at 1/4, and the elimination rate κ_e equals the elimination rate κ in the one-compartment model. When the membrane is highly permeable ($\kappa_{12} = 10\kappa_e$) the predictions of the two models are very different. In the opposite limit, when diffusion is negligible with respect to the elimination rate ($\kappa_{12}/\kappa_e \ll 1$), the blood compartment is insulated from the second one. In this case, the solution $Q_1(t)$ almost coincides with the one-compartment solution $Q(t)$.

The total drug clearance for this two-compartment model can be computed using Eq. (2.74). I first compute the AUC for C_1 (which represent the blood compartment)

$$A_C(t) = \frac{D}{V_1\,(\lambda_1 - \lambda_2)}\left[\frac{\kappa_{21} - \lambda_2}{\lambda_2}\left(1 - e^{-\lambda_2 t}\right) + \frac{\lambda_1 - \kappa_{21}}{\lambda_1}\left(1 - e^{-\lambda_1 t}\right)\right]. \tag{4.36}$$

In the limit when $t \to \infty$, A_C reduces to

$$A_C = \frac{D\,\kappa_{21}}{V_1\,\lambda_1\lambda_2}. \tag{4.37}$$

From Eqs. (4.21) and (4.22), $\lambda_1\lambda_2 = B = \kappa_e\kappa_{21}$. Finally, the total average drug clearance reads [Eq. (2.74)]

$$k_{\text{drug}} = \frac{D}{A_C} = \kappa_e\, V_1. \tag{4.38}$$

4.2.2 Non-homogeneous solutions

To compute the non-homogeneous solution of the system of Eqs. (4.14) and (4.15) (i.e., with a non-vanishing continuous infusion rate I) it is enough to compute the particular solution ($\bar{Q}_1$, $\bar{Q}_2$) corresponding to the stationary case $\dot{\bar{Q}}_1 = \dot{\bar{Q}}_2 = 0$:

$$\bar{Q}_1 = \frac{I}{\kappa_e}, \qquad \bar{Q}_2 = \frac{\kappa_{12}}{\kappa_e\,\kappa_{21}} I. \tag{4.39}$$

The general solution of the non-homogeneous is given by the sum of the stationary solutions with the general solution of the homogeneous system Eqs. (4.18) and (4.19). The two integration constants A_1 and A_2 are determined by imposing initial conditions as in Eq. (4.28), that is assuming

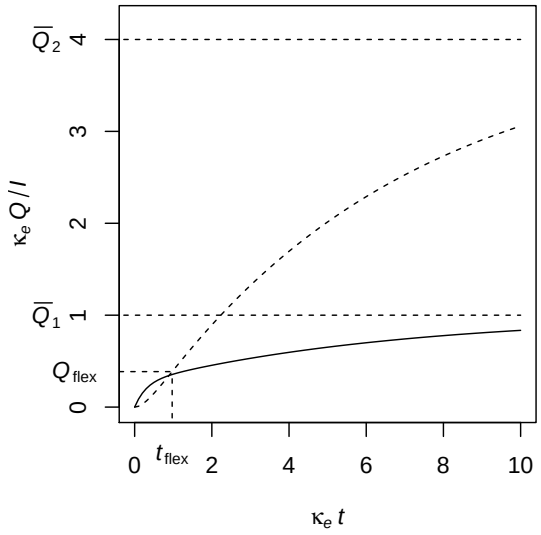

Figure 4.3: Time evolution of drug amount in the two compartments Q_1 (solid line) and Q_2 (dashed line) for a continuous infusion with constant rate I without loading dose, and for an optimal administration strategy with $D = C_{\text{opt}}\, V_2\, \kappa_{21}/\kappa_{12}$ and $I = C_{\text{opt}}\, V_2\, \kappa_e\, \kappa_{21}/\kappa_{12}$. Q and t are measured in units of I/κ_e and κ_e^{-1}, respectively, $\kappa_{12} = 2\kappa_e$, and $\kappa_{21} = \kappa_{12}/4$. $\bar{Q}_1 = I/\kappa_e$ and $\bar{Q}_2 = I\kappa_{12}/\kappa_e\kappa_{21}$ are the asymptotic stationary solutions.

that at time $t = 0$ a bolus D is administered in the first compartment. The solution reads

$$Q_1(t) = \frac{\kappa_{21} - \lambda_2}{\lambda_1 - \lambda_2}\left[D - \frac{\lambda_1}{\kappa_e\,\kappa_{21}} I\right] e^{-\lambda_2 t} + \frac{\lambda_1 - \kappa_{21}}{\lambda_1 - \lambda_2}\left[D - \frac{\lambda_2}{\kappa_e\kappa_{21}} I\right] e^{-\lambda_1 t} + \frac{I}{\kappa_e}, \tag{4.40}$$

$$Q_2(t) = \frac{\kappa_{12}}{\lambda_1 - \lambda_2}\left[D - \frac{\lambda_1}{\kappa_e\,\kappa_{21}} I\right] e^{-\lambda_2 t} - \frac{\kappa_{12}}{\lambda_1 - \lambda_2}\left[D - \frac{\lambda_2}{\kappa_e\kappa_{21}} I\right] e^{-\lambda_1 t} + \frac{\kappa_{12}}{\kappa_e\kappa_{21}} I. \tag{4.41}$$

Continuous infusion without loading dose. To study these solutions, it is convenient to start with the case of vanishing loading dose $D = 0$.

$$Q_1(t) = \frac{I}{\kappa_e}\left[1 - \frac{1}{(\lambda_1 - \lambda_2)\kappa_{21}}\left((\kappa_{21} - \lambda_2)\lambda_1\, e^{-\lambda_2 t} + (\lambda_1 - \kappa_{21})\lambda_2\, e^{-\lambda_1 t}\right)\right], \tag{4.42}$$

$$Q_2(t) = I\frac{\kappa_{12}}{\kappa_e\kappa_{21}}\left[1 - \frac{1}{\lambda_1 - \lambda_2}\left(\lambda_1 e^{-\lambda_2 t} - \lambda_2 e^{-\lambda_1 t}\right)\right], \tag{4.43}$$

The behaviour of Q_1 (solid line) and Q_2 (dashed line) is illustrated in Fig. 4.3, for $\kappa_{12} = 2\kappa_e$ and $\kappa_{21} = \kappa_{12}/4$.

$$\frac{\mathrm{d}Q_1}{\mathrm{d}t} = \frac{I}{\lambda_1 - \lambda_2}\left[(\kappa_{21} - \lambda_2)e^{-\lambda_2 t} + (\lambda_1 - \kappa_{21})e^{-\lambda_1 t}\right], \tag{4.44}$$

$$\frac{\mathrm{d}Q_2}{\mathrm{d}t} = \frac{\kappa_{12}\, I}{\lambda_1 - \lambda_2}\left[e^{-\lambda_2 t} - e^{-\lambda_1 t}\right] \tag{4.45}$$

are always non-negative. To derive these equations I used $\lambda_1\lambda_2 = \kappa_e\kappa_{21}$, from Eq. (4.21). The derivatives of Q_1 and Q_2 for a continuous infusion without loading dose coincide with Eqs. (4.30) and (4.31), after replacing D with I. In fact a continuous infusion with constant rate I can be

viewed as a series of infinitely small boluses. Thus, all the results found in the previous paragraph for Q_1 and Q_2 are valid in this case for $\dot{Q}_1$ and $\dot{Q}_2$. In particular, Q_2 is flat at time $t = 0$ since $\dot{Q}_2(0) = 0$, while, as expected $\dot{Q}_1(0) = I$. Furthermore $\dot{Q}_1$ and $\dot{Q}_2$ go to zero exponentially for $t \to \infty$, and Q_1 and Q_2 converges to the two stationary solutions $\hat{Q}_1$ and $\hat{Q}_2$ with a time scale $\tau_2 = \lambda_2^{-1}$. Furthermore, $\dot{\hat{Q}}_2$ has a maximum at

$$t_{\text{flex}} = \frac{\log(\lambda_1/\lambda_2)}{\lambda_1 - \lambda_2}, \tag{4.46}$$

where, consequently, Q_2 shows an inflection point

$$Q_{2\text{flex}} = \frac{\kappa_{12}\, I}{\kappa_e \kappa_{21}} \left[1 - \left(\frac{\lambda_2}{\lambda_1} \right)^{\lambda_2/(\lambda_1 - \lambda_2)} \left(1 + \frac{\lambda_2}{\lambda_1} \right) \right]. \tag{4.47}$$

Bolus plus a continuous infusion. Finally, the general solution, Eqs. (4.40) and (4.41), are the sum of the solutions corresponding to a bolus without continuous infusion [Eqs. (4.18) and (4.19)] and a continuous infusion without bolus [Eqs. (4.42) and (4.43)]. In the former case τ_2 is the time scale over which body is depleted, while in the second case, it represents the time required to fill it and maintain the stationary concentrations $\bar{C}_1 = \bar{Q}_1/V_1$ and $\bar{C}_2 = \bar{Q}_2/V_2$. If C_{opt} is the optimal concentration to treat an infection in the tissue compartment, the best therapeutic strategy consists of

(i) reaching the concentration C_{opt} as soon as possible,

(ii) never exceeding toxic concentrations,

(iii) maintaining C_{opt} with the continuous infusion.

The third objective is achieved by imposing that the stationary solution $\bar{Q}_2$ equals $V_2\, C_{\text{opt}}$:

$$I_{\text{opt}} = \frac{\kappa_e \kappa_{21}}{\kappa_{12}}\, V_2\, C_{\text{opt}}, \tag{4.48}$$

corresponding in the first compartment to

$$\bar{Q}_1 = \frac{\kappa_{21}}{\kappa_{12}}\, V_2\, C_{\text{opt}}, \qquad \bar{C}_1 = \frac{\kappa_{21} V_2}{\kappa_{12} V_1}\, C_{\text{opt}}, \tag{4.49}$$

which, in the case of a symmetric membrane [Eq. 4.17], obviously reduces to $\bar{C}_1 = \bar{C}_2 = C_{\text{opt}}$.

Conservative administration strategy. Regarding item (i), the time needed to fill the second compartment with a continuous infusion (roughly speaking $\tau_2 = \lambda^{-1}$) cannot be controlled since drug is administered only through the first compartment. The best one can do is to fill the first com-

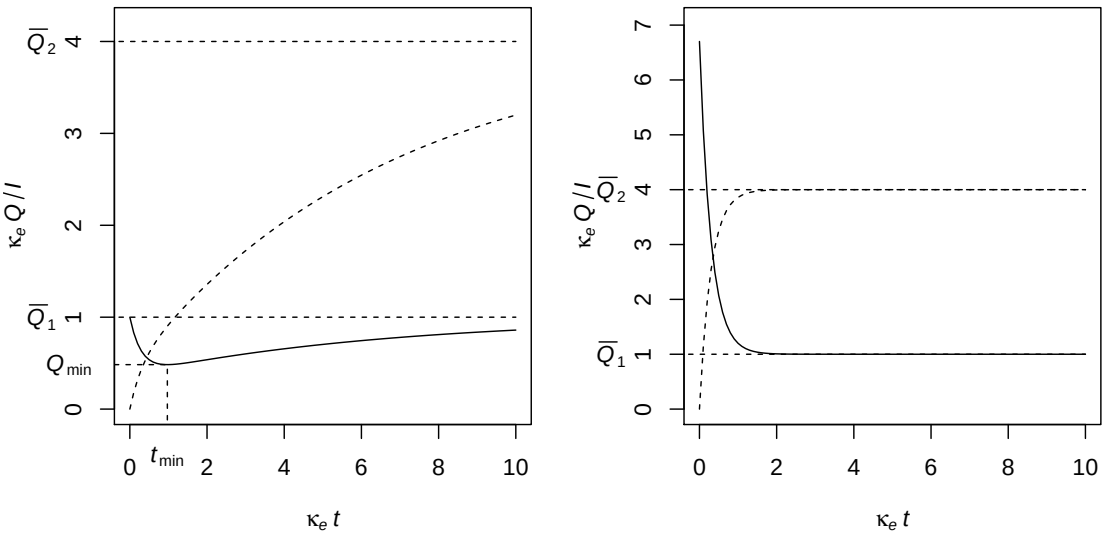

Figure 4.4: Time evolution of drug amount in the two compartments Q_1 (solid line) and Q_2 (dashed line) for an optimal administration strategy $I_{\rm opt} = V_2\, C_{\rm opt}\, \kappa_e\, \kappa_{21}/\kappa_{12}$ with $D = D_{\rm cons} = C_{\rm opt}\, V_2\, \kappa_{21}/\kappa_{12}$ (left panel) and $D = D_{\rm agg} = V_2\, C_{\rm opt}\, \lambda_1/\kappa_{12}$ (right panel). In both panels, Q and t are measured in units of I/κ_e and κ_e^{-1}, respectively, $\kappa_{12} = 2\kappa_e$, and $\kappa_{21} = \kappa_{12}/4$. $\bar{Q}_1 = I_{\rm opt}/\kappa_e$ and $\bar{Q}_2 = I_{\rm opt}\kappa_{12}/\kappa_e\kappa_{21}$ are the asymptotic stationary solutions corresponding to the optimal concentration $\bar{C}_2 = C_{\rm opt}$ in the second compartment.

partment up to the optimal concentration of Eq. (4.49), by administering a bolus

$$D_{\rm cons} = \bar{Q}_1 = \frac{\kappa_{21}}{\kappa_{12}}\, V_2\, C_{\rm opt}, \tag{4.50}$$

which reduces to

$$D_{\rm cons} = V_1 C_{\rm opt}, \tag{4.51}$$

in the case of a symmetric membrane. Inserting the values of $I_{\rm opt}$ and $D_{\rm cons}$ in Eqs. (4.40) and (4.41):

$$Q_1(t) = C_{\rm opt} V_2 \frac{\kappa_{21}}{\kappa_{12}} \left[1 - \frac{\kappa_{12}}{\lambda_1 - \lambda_2} \left(e^{-\lambda_2 t} - e^{-\lambda_1 t}\right)\right], \tag{4.52}$$

$$Q_2(t) = C_{\rm opt} V_2 \left[1 - \frac{1}{\lambda_1 - \lambda_2} \left((\lambda_1 - \kappa_{21})\, e^{-\lambda_2 t} + (\kappa_{21} - \lambda_1)\, e^{-\lambda_1 t}\right)\right] \tag{4.53}$$

where I used

$$(\lambda_1 - \kappa_{21})\,(\kappa_{21} - \lambda_2) = \kappa_{21}\kappa_{12}, \tag{4.54}$$

which is directly derived from Eq. (4.21). This solution is represented in the left panel of Fig. 4.4. The value of Q_1 in Eq. (4.52) is $C_{\rm opt} V_2 \kappa_{21}/\kappa_{12}$ for $t = 0$ and in the limit $t \to \infty$. It reaches a minimum

$$Q_{\rm min} = C_{\rm opt} V_2 \frac{\kappa_{21}}{\kappa_{12}} \left[1 - \frac{\kappa_{12}}{\lambda_1} \left(\frac{\lambda_2}{\lambda_1}\right)^{\lambda_2/(\lambda_1 - \lambda_2)}\right], \tag{4.55}$$

at

$$t_{\min} = \frac{\log(\lambda_1/\lambda_2)}{\lambda_1 - \lambda_2}. \tag{4.56}$$

The function $Q_1(t)$ is always positive, since its minimum $Q_{\min}$ is positive, because $\kappa_2 1/\lambda_1 < 1$ [see Eq. (4.27)], $\lambda_2/\lambda_1 < 1$, and the exponent $\lambda_2/(\lambda_1 - \lambda_2)$ is positive.

The quantity of drug in the second compartment $Q_2(t)$ [Eq. (4.53)] is 0 at $t = 0$ and monotonically increases, converging to the asymptotic stationary solution $\bar{Q}_2 = C_{\rm opt} V_2$. Indeed, it is easy to show that $\dot{Q}_2$ is always positive.

By choosing I and D I have used both two degrees of freedom to optimise items (i) and (iii). The maximum concentrations in the two compartments, that is item (ii), cannot be controlled independently. With this choice of I and D neither C_1 nor C_2 exceed the target concentration, so there is no risk of toxicity. However, for this administration strategy, the time needed to reach a concentration close to the optimal one $C_{\rm opt}$ in the second compartment is very large, in the order of $\tau_2 = \lambda^{-1}$. In fact, the second compartment is filled here by the slow convergence of the continuous infusion to the stationary solution $\bar{Q}_2$.

Aggressive administration strategy. A very different administration strategy consists of filling the second compartment through the fast depletion of the first compartment, which takes place on a time scale of order $\tau_1 = \lambda^{-1}$, just after the loading dose. This strategy requires a much larger loading dose to suppress the terms proportional to $\exp(-\lambda_2)t$ in Eqs. (4.40) and (4.41) that is

$$D_{\rm agg} = \frac{\lambda_1}{\kappa_e\, \kappa_{21}} I_{\rm opt} = \frac{\lambda_1}{\kappa_{12}}\, V_2\, C_{\rm opt}. \tag{4.57}$$

With this choice, the evolution of the drug amounts in the two compartments read

$$Q_1(t) = C_{\rm opt}\, V_2 \frac{\kappa_{21}}{\kappa_{12}} \left[\frac{\lambda_1 - \kappa_{21}}{\kappa_{21}} e^{-\lambda_1 t} + 1 \right], \tag{4.58}$$

$$Q_2(t) = C_{\rm opt}\, V_2 \left[1 - e^{-\lambda_1 t} \right]. \tag{4.59}$$

This solution is represented in the right panel of Fig. 4.4. The drug amount in the second compartment Q_2 (dashed line) rapidly reaches the stationary solution

$$\bar{Q}_2 = C_{\rm opt}\, V_2, \tag{4.60}$$

whereas Q_1 (solid line) is monotonically decreasing toward

$$\bar{Q}_1 = \frac{I_{\rm opt}}{\kappa_e} = C_{\rm opt}\, V_2 \frac{\kappa_{21}}{\kappa_{12}}, \tag{4.61}$$

and starts from the initial value

$$Q_1(0) = C_{\rm opt}\, V_2 \frac{\lambda_1}{\kappa_{12}}. \tag{4.62}$$

In the case of a symmetric membrane, this corresponds to an initial concentration

$$C_1(0) = \frac{\lambda_1}{\kappa_{21}} C_{\rm opt}. \tag{4.63}$$

that strongly exceeds the optimal concentration $C_{\rm opt}$.

Both Q_1 and Q_2 rapidly converge on a time scale $\tau_1 = \lambda_1^{-1}$ to their stationary asymptotic solutions $\bar{Q}_1$ and $\bar{Q}_2$, corresponding to the optimal concentration $C_{\rm opt}$ in the second compartment. However, the rapid convergence to the therapeutic target is achieved here through a large initial concentration in the blood compartment.

Generic administration strategies. Above I discussed two opposite strategies to reach an optimal therapeutic concentration in the tissue compartment. In the former case the second compartment is slowly filled through continuous infusion, while in the latter I exploited the rapid depletion of the first compartment toward the second. The advantage of the first approach is that the optimal concentration is never exceeded, whereas in the second case the loading dose is very large, possibly generating a risk of toxicity. Intermediate strategies can be adopted, balancing the advantages and disadvantages of the two approaches. In Fig. 4.5 I plot the evolution of $Q_1(t)$ (left panel) and $Q_2(t)$ (right panel) for different initial boluses but same infusion rate I. All the solutions converge to the same $\bar{Q}_1$ and $\bar{Q}_2$. Dashed and dotted lines represent the solutions for loading dose $D = D_{\rm cons} = \bar{Q}_1$ [Eq. (4.50)] and $D = D_{\rm agg}$ [Eq. (4.57)], respectively. The solid lines (from the lowermost to the uppermost) represent three solutions with three different boluses, one smaller than $D_{\rm cons}$ ($D = 0.5\bar{Q}_1$), one larger than $D_{\rm cons}$ ($D = 3\bar{Q}_1$) but smaller than $D_{\rm agg}$, the third larger than $D_{\rm agg}$ ($D = 8\bar{Q}_1$).

When $D < D_{\rm cons}$, Q_1 is always smaller than $\bar{Q}_1$ and converges to $\bar{Q}_1$ from below. The convergence of Q_2 to $\bar{Q}_2$ is very slow (on a time scale of order τ_2).

When $D_{\rm cons} < D < D_{\rm agg}$, Q_1 is initially larger than $\bar{Q}_1$, has a minimum smaller than $\bar{Q}_1$, and eventually converges to $\bar{Q}_1$ from below. The convergence of Q_2 to $\bar{Q}_2$ is more rapid. For $D = 3\bar{Q}_1$, the central line of the left panel of Fig. 4.5 reaches a value around $\bar{Q}_2/2$ very rapidly, on a time scale of order τ_1. Then, $\bar{Q}_2$ is approached on a time scale of order τ_2. With this strategy the concentration in the second compartment never exceeds $C_{\rm opt}$, but it can be adopted only if a concentration larger than $C_{\rm opt}$ can be tolerated in the first compartment for a time scale of order τ_1.

Finally, when $D > D_{\rm agg}$, Q_1 is always larger than $\bar{Q}_1$ and converges to $\bar{Q}_1$ from above. Q_2

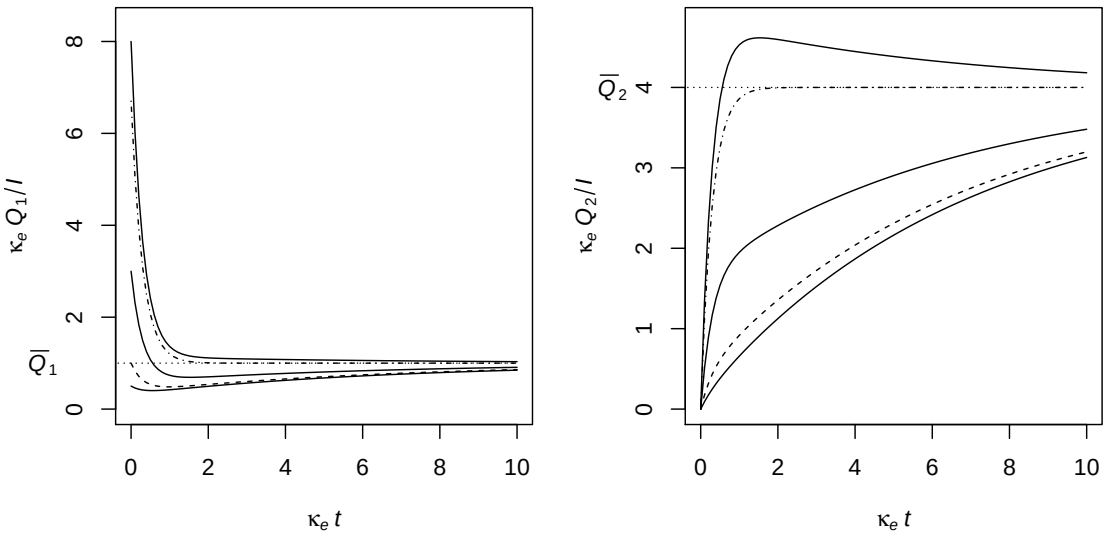

Figure 4.5: Time evolution of drug amount in the two compartments Q_1 (left panel) and Q_2 (right panel) for five administration strategies with the same infusion rate $I = I_{\rm opt} = V_2\, C_{\rm opt}\, \kappa_e\, \kappa_{21}/\kappa_{12}$ and different loading doses. Dashed and dotted lines represent the solutions for loading doses $D = D_{\rm cons} = C_{\rm opt}\, V_2\, \kappa_{21}/\kappa_{12}$ and $D = D_{\rm agg} = V_2\, C_{\rm opt}\, \lambda_1/\kappa_{12}$, respectively. In both panels, Q and t are measured in units of I/κ_e and κ_e^{-1}, respectively, $\kappa_{12} = 2\kappa_e$, and $\kappa_{21} = \kappa_{12}/4$. $\bar{Q}_1 = I_{\rm opt}/\kappa_e$ and $\bar{Q}_2 = I_{\rm opt}\kappa_{12}/\kappa_e\kappa_{21}$ are the asymptotic stationary solutions corresponding to the optimal concentration $\bar{C}_2 = C_{\rm opt}$ in the second compartment.

rapidly grows above $\bar{Q}_2$ (with τ_1), reaches a maximum and eventually converges to $\bar{Q}_2$ from above. Such a strategy should be adopted when it is very important to reach the target concentration $C_{\rm opt}$ in a very short time. However, it is possible to administer such a large bolus D only if very high concentrations are tolerated in the first compartment and a concentration slightly higher than $C_{\rm opt}$ is tolerated in the second compartment.

For all strategies the infusion rate is constant and must be tuned to obtain the optimal therapeutic concentration $C_{\rm opt}$ in the stationary late time regimen. The loading dose must be determined to reach the therapeutic concentration as soon as possible, without however exceeding toxic levels.

4.3 Population models of kinetics

In the previous sections I presented and discussed some features of two linear models of pharmacokinetics, with one and two compartments, respectively. The parameters entering the equations, such as κ and V in the one-compartment model of Eq. (4.3), or κ_{12}, κ_{21}, κ_e, V_1, and V_2 in the equations of the two-compartment system [Eqs. (4.14) and (4.15)] must be determined by comparing the solutions of the kinetic equations against data measured in patients. If several measurements of drug concentrations were available for a single patient, it would be possible to determine the relevant kinetic parameters of each patient, through ordinary non-linear fit procedures. This ap-

proach would provide a nice validation of the model for each patient but would be useless for clinical applications.

As discussed in Sec. 2.4, a mathematical model of pharmacokinetics is appealing from a clinical perspective when it is able to simulate the evolution of drug concentration for specific patient conditions and for a given dosage regimen, by expressing the kinetic parameters as a function of patient-specific variables. For instance, the clearance k_{drug} of a drug in a patient undergoing renal replacement therapy can be expressed as

$$k_{\text{drug}} = \theta_0 + \theta_c \, k_{\text{crea}} + \theta_d \, d_{\text{dial}}, \tag{4.64}$$

where k_{crea} is creatinine clearance, d_{dial} is the dialysis dose, and θ_0, θ_c, θ_d and are free parameters to be determined.

To formalise the problem in mathematical language, I must construct a so-called multilevel model with two levels. At patient level, kinetic parameters are computed as functions of patient variables plus some free parameters. At drug-concentration level, drug amounts are determined as solutions of a system of differential equations (compartment model) in terms of the kinetic parameters resulting from the former level.

To construct this model, measured drug concentrations and clinical variables must first be collected for several patients. Hence, a non-linear fitting procedure with mixed effect is the appropriate statistical tool to select significant patient variables and estimate optimal values of the free parameters. As illustrated in Sec. 4.3, this procedure allows the user to deal with statistical fluctuations at both patient and drug-concentration levels.

Imagine that two patients have the same value of creatinine clearance k_{crea} and do not receive renal replacement therapy. For both patients, Eq. (4.64) returns the same value of drug clearance k_{drug}. This value is called the population value of drug clearance. However, there may be unknown effects or unmeasured variables that may affect the clearance of each patient. Such effects may include, for instance, specific clinical conditions that are not represented in the development sample or the absence, in some patients, of frequently-enough measured values of important laboratory tests (e.g. creatinine clearance). In these cases, the individual drug clearance $k_{\text{drug},i}$ for the i-th patient may differ from the population value

$$k_{\text{drug},i} = k_{\text{drug}} + \eta_{k,i} \tag{4.65}$$

where $\eta_{\text{k},i}$ summarises all unknown and unmeasured effects. Similarly, all the relevant individual kinetic parameters can be expressed by a population parameter, obtained as a deterministic function of patient features plus some effect η_i. For instance the individual distribution volume can be

written as

$$V_i = V + \eta_{V,i} \tag{4.66}$$

For each patient the pharmacokinetic equations described in the previous sections must be solved using his/her individual values of pharmacokinetic parameters. The solution of these equations provides the predicted individual plasma drug concentrations $C_i(t)$ at any time for each patient. Let me define C_{ij} as the values of drug concentrations measured at times t_{ij}, with $j = 1, \dots, n_i$, for patient i. These values of C_{ij} will in general differ from the respective predicted values $C_i(t_{ij})$ for several reasons: measurement errors and uncertainties, approximations of the kinetic model, etc.... Thus, I write

$$C_{ij} = C_i(t_{ij}) + \varepsilon_{ij}. \tag{4.67}$$

The terms $\eta_{k,i}$, $\eta_{V,i}$, and ε_{ij} represent all the unknown and non-modelled effects at both patient (interindividual) and measurement (intraindividual) level, respectively. They can be statistically modelled assuming that they are a realisation of some stochastic variables with a certain probability distribution. As usual the simplest choice is to assume a normal distribution for both of them. If I define the vector of interindividual effects as $\eta_i = (\eta_{k,i}, \eta_{V,i}, \dots)$,

$$\eta_i \sim \mathcal{N}(0, \Omega), \qquad \varepsilon_{ij} \sim \mathcal{N}(0, \sigma^2), \tag{4.68}$$

where Ω is the covariance matrix of η_i and σ^2 is the variance of ε_{ij}. Under these assumptions it is possible to write a likelihood function

$$L(\theta, \Omega, \sigma; \{C_{ij}\}_{i=1,\dots,m; j=1,\dots n_i}), \tag{4.69}$$

for the vector θ of parameters describing the kinetic model (e.g., $\theta = (\theta_0, \theta_c, \theta_d, \dots)$, see Eq. (4.64)), Ω, and σ, and given the set of all the measured values of concentration C_{ij} for all m patients.

Maximum likelihood estimates of θ, Ω, and η can be obtained by approximation methods as detailed below. After parameter estimation it is also possible to obtain post-hoc estimates of the interindividual effects η_i by maximising their posterior probability given the maximum likelihood estimates $\hat{\theta}$, $\hat{\Omega}$, and $\hat{\eta}$.

To illustrate the procedure to fit a nonlinear model to a set of data which are clustered by patient, it is first convenient to describe how to fit data on a single subject. In Sec. 4.3.3 I shall extend this procedure to data measured on a population of subjects.

4.3.1 Single-subject model

Let me consider a model describing the evolution of a certain variable $y(t)$ (e.g., plasma drug concentration in a pharmacokinetic model, blood glucose concentration in a model of glucose metabolism, etc...) as a function of time t. In general, the function y depends also on a vector ψ of patient-dependent parameters:

$$y = y(t; \psi). \tag{4.70}$$

For instance, in the one-compartmental model, the solution of Eq. (4.11) can be expressed in terms of plasma drug concentration C as

$$C(t) = \left(\frac{D}{V} - \frac{I}{k}\right) e^{-\kappa t} + \frac{I}{k}. \tag{4.71}$$

In this case C represents the function y and the vector of free parameters is $\psi = (V, k)$, where V is the distribution volume and k is the drug clearance ($k = \kappa\, V$, with κ being the elimination rate).

If the variable y is measured n times on the same subject at different t_j, the measured values

$$y_j = y(t_j; \psi) + \varepsilon_j \tag{4.72}$$

will be affected by a residual error ε_j, which takes account of random statistical fluctuations around the theoretical value $y(t_j; \psi)$, associated with measurement errors and unpredictable effects which are not accounted for by the model.

If the residuals ε_j have probability density distribution $f(\varepsilon)$, the likelihood of observing the set of measured values y_j is

$$L(\psi, \sigma; \{y_j\}) = p(\{y_j\}|\psi, \sigma) = \prod_{j=1}^{n} p(y_j|\psi, \sigma) = \prod_{j=1}^{n} f\left(y_j - y(t_j; \psi)\right), \tag{4.73}$$

where $p(y_j|\psi, \sigma)$ is the probability of observing a single measured value y_j and $p(\{y_j\}|\psi)$ is the probability of observing the set of measured values $\{y_j\}$ for a given vector of parameters ψ and residual variance σ^2. If ε_j have a normal distribution with zero mean and variance σ^2

$$f(\varepsilon) = \frac{1}{\sigma\sqrt{2\pi}}\, e^{-\varepsilon^2/2\sigma^2}, \tag{4.74}$$

the logarithm $\mathcal{L}$ of the likelihood L is

$$\mathcal{L}(\psi, \sigma) = -n\, \log(\sigma\sqrt{2\pi}) - \frac{1}{2\sigma^2} \sum_{j=1}^{n} \left[y_j - y(t_j; \psi)\right]^2. \tag{4.75}$$

The parameters ψ and the residual variance σ^2 are eventually determined by a standard maximisation of the non-linear log-likelihood function $\mathcal{L}$. Defining the sum of squared residuals S as

$$S(\psi) = \sum_{j=1}^{n} \left[y_j - y(t_j; \psi) \right]^2 , \tag{4.76}$$

the maximum-likelihood values $\hat{\psi}$ and $\hat{\sigma}$ are obtained by imposing that the derivative of $\mathcal{L}$ with respect to σ and its gradient with respect to ψ vanish:

$$0 = \nabla_\psi \mathcal{L}|_{\psi=\hat{\psi}} = -\frac{1}{2\hat{\sigma}^2} \nabla_\psi S(\hat{\psi}), \tag{4.77}$$

$$0 = \left. \frac{\partial \mathcal{L}}{\partial \sigma} \right|_{\sigma=\hat{\sigma}, \psi=\hat{\psi}} = -\frac{n}{\hat{\sigma}} - \frac{1}{\hat{\sigma}^3} S(\hat{\psi}) \tag{4.78}$$

The first equation expresses the standard least-square condition, that is

$$\hat{\psi} = \arg\min S(\psi), \tag{4.79}$$

where $\arg\min f(x)$ indicates the value of the argument x that minimises the function f. The residual variance can be obtained from the second equation as

$$\hat{\sigma}^2 = \frac{S}{n}. \tag{4.80}$$

Different error models (i.e., models with different density distribution f) are treated in an analogous way. In the special case where the error is proportional to the value of y

$$y_j = y(t_j; \psi) + \varepsilon_j \, y(t_j; \psi), \tag{4.81}$$

with ε_j having a normal distribution, I may write

$$y_j \approx y(t_j; \psi) \exp(\varepsilon_j), \tag{4.82}$$

if the error term $\varepsilon_j \, y(t_j; \psi)$ is small with respect to the deterministic part $y(t_j; \psi)$, that is $\varepsilon_j \ll 1$. In this case, the analysis as for normal additional error terms can be applied on the log-transformed function $\log(y)$:

$$\log(y_j) \approx \log(y(t_j; \psi)) + \varepsilon_j. \tag{4.83}$$

4.3.2 Several subjects

Unique model

To fit the general model of Eq. (4.70) on data y_{ij} measured on m subjects i, one may first assume that the pharmacokinetic parameters ψ are the same for every subject, that is

$$y_{ij} = y(t_{ij};\psi) + \varepsilon_{ij}, \qquad i = 1,\dots,m, \quad j = 1,\dots,n_j. \tag{4.84}$$

In this way all the measurements y_{ij} are considered at the same level and $\hat{\psi}$ and $\hat{\sigma}$ are determined as discussed above for the case of a single patient

$$\hat{\psi} = \arg\min S(\psi), \qquad \hat{\sigma}^2 = \frac{S}{n}, \tag{4.85}$$

where S is the sum of all squared residuals, over all patients j and over all measurements i

$$S(\psi) = \sum_{i=1}^{m}\sum_{j=1}^{n_i} \left[y_{ij} - y(t_{ij};\psi)\right]^2. \tag{4.86}$$

Several models

The above approximation is certainly unrealistic because the parameters ψ are expected to be very different from one patient to another. For instance, in a pharmacokinetic model, drug clearance is expected to be much lower in a patient with renal failure than in a patient with normal renal function. To take this variability into account one may fit one model for each patient, as illustrated above, obtaining m vectors $\hat{\psi}_i$ and n residual variances σ_i. Such a procedure requires that the number of observations n_i for each patient is large enough to allow to construct a model out of the n_j couples (t_{ij}, y_{ij}). Furthermore, it does not allow the variability of the parameters ψ to be described as a function of patient characteristic.

4.3.3 Population model

In this Section, I present the procedure to construct a model, on data measured on several patients, which overcomes the drawbacks discussed in the above section. I require that the model

- be unique and estimated on available data from all patients,
- take account of inter-patient variability,
- describe inter-patient variability as a function of patient features.

To satisfy the last requirement, one must express the vector of parameters ψ as

$$\psi = \psi(x; \theta). \tag{4.87}$$

Thus, ψ are no longer free parameters. They are determined as a function of x, a vector of patient features (i.e., for a pharmacokinetic model, it may include creatinine clearance, body weight, plasma albumin concentration, etc...), and θ, a vector of free parameters.

The values of ψ computed with the above formula are called population parameters and usually denoted by ψ_{pop}. They represents the best estimate of the single-patient values ψ_j taking into account patient characteristics x. Thus, two patients with the same value of all the variables x have the same ψ_{pop}. However, in the same way as a single observation of a variable y_{ij} differs from its theoretical prediction $y(t_{ij})$ by the residual ε_{ij}, similarly the vector parameters ψ_i are expected to differ from their population values ψ_{pop} by residual terms η_i:

$$\psi_i = \psi(x_i; \theta) + \eta_i \tag{4.88}$$

Namely, η_i is a vector of random terms that describe residual inter-patient variability unexplained by the patient features x included in the model.

If the distribution of η_i is multinormal, with covariance matrix Ω, its probability density may be written as

$$g(\eta) = \frac{1}{\sqrt{(2\pi)^k \det \Omega}} e^{-\eta^T \Omega^{-1} \eta/2}, \tag{4.89}$$

where k is the length of the vector ψ. Then, the probability that a patient with feature x_i has a set of parameters ψ_i is

$$p(\psi_i(x_i)|\theta, \Omega) = g(\psi_i - \psi(x_i; \theta)). \tag{4.90}$$

From Eq. 4.73, the probability of observing the measured values $\{y_{ij}(t_{ij})\}_{j=1,\dots,n_i}$ at times $\{t_{ij}\}_{j=1,\dots,n_i}$ for subject i and for a given set ψ_i is

$$p(\{y_{ij}(t_{ij})\}_{j=1,\dots,n_i}|\psi_i, \sigma) = \prod_{j=1}^{n_i} f\left(y_{ij} - y(t_{ij}; \psi_i)\right). \tag{4.91}$$

Hence assuming a normal distribution for observations y_{ij} the probability of measuring $\{y_{ij}\}_{j=1,\dots,n_i}$

for a patient with feature x_i is

$$\begin{aligned} p(\{y_{ij}(t_{ij},x_i)\}_{j=1,\dots,n_i}|\theta,\sigma,\Omega) &= \int \mathrm{d}^k\psi_i\, p(\{y_{ij}(t_{ij})\}_{j=1,\dots,n_i}|\psi_i,\sigma)p(\psi_i|\theta,\Omega) \\ &= \int \mathrm{d}^k\eta \prod_{j=1}^{n_i} f\left[y_{ij}-y(t_{ij};\psi(x_i;\theta)+\eta)\right] g(\eta) \\ &= \frac{1}{\sigma^{n_i}\sqrt{(2\pi)^{k+n_i}\det\Omega}} \int \mathrm{d}^k\eta\, e^{-\left[S_i(\eta;\theta)/2\sigma^2+\eta^T\Omega^{-1}\eta/2\right]}, \end{aligned} \tag{4.92}$$

where

$$S_i(\eta;\theta) = \sum_{j=1}^{n_i}\left[y_{ij}-y(t_{ij};\psi(x_i;\theta)+\eta)\right]^2 \tag{4.93}$$

is the sum of squared residuals for subject i, computed at a given value of η.

Finally, the probability density of observing the whole set of measurements $\{y_{ij}\}$ at times $\{t_{ij}\}$ for all patients $i=1,\dots,m$ is

$$p(\{y_{ij}(t_{ij},x_i)\}|\theta_i\sigma,\Omega) = \prod_{i=1}^{m} p(\{y_{ij}(t_{ij},x_i)\}_{j=1,\dots,n_i}|\theta,\sigma,\Omega). \tag{4.94}$$

This probability gives the likelihood of the free parameters (θ,σ,Ω) for the given set of observations $\{y_{ij}\}$

$$L(\theta,\sigma,\Omega;\{y_{ij}\}) = p(\{y_{ij}(t_{ij},x_i)\}|\theta_i\sigma,\Omega), \tag{4.95}$$

which must be maximised to determine the best-fit values $\hat\theta$, $\hat\sigma$, and $\hat\Omega$ of all model parameters. The logarithm of the likelihood is

$$\mathcal{L}(\theta,\sigma,\Omega;\{y_{ij}\}) = \sum_{i=1}^{m}\mathcal{L}_i(\theta,\sigma,\Omega;\{y_{ij}\}_{j=1,\dots n_i}). \tag{4.96}$$

where $\mathcal{L}_i(\theta,\sigma,\Omega;\{y_{ij}\}_{j=1,\dots n_i})$ is the log-likelihood for a single subject i:

$$\begin{aligned} -2\mathcal{L}_i(\theta,\sigma,\Omega;\{y_{ij}\}_{j=1,\dots n_i}) &= (n_i+k)\log(2\pi)+2n_i\log\sigma+\log\det\Omega \\ &\quad -2\log\left[\int \mathrm{d}^k\eta\, e^{-\left[S_i(\eta;\theta)/\sigma^2+\eta^T\Omega^{-1}\eta\right]/2}\right] \end{aligned} \tag{4.97}$$

Post-hoc estimation of η

After the model parameters have been determined, the individual variability terms η_i can be estimated by maximising their Bayesian posterior density, where the parameters θ, σ, and Ω are fixed to their maximum-likelihood estimates $\hat\theta$, $\hat\sigma$, and $\hat\Omega$

$$p(\{y_{ij}(t_{ij})\}_{j=1,\dots,n_i}|\psi_i,\hat\sigma)p(\psi_i|\hat\theta,\hat\Omega). \tag{4.98}$$

Thus, η_i are determined by maximising

$$e^{-\left[S_i(\eta;\hat{\theta})/2\hat{\sigma}^2+\eta^T\hat{\Omega}^{-1}\eta/2\right]}, \tag{4.99}$$

that is solving the equation

$$\frac{\nabla_\eta S_i(\eta_i;\hat{\theta})}{2\hat{\sigma}^2}+\eta_i^T\hat{\Omega}^{-1}=0. \tag{4.100}$$

Laplace approximation of the likelihood

There exists several strategies to maximise the likelihood of Eq. (4.95). I evaluate the integral of Eq. (4.97) computed through the Laplace approximation.

I define $\Gamma_i(\eta;\theta)$ and $\Delta_i(\eta;\theta)$ the gradient and the Hessian of $S(\eta;\theta)$ with respect to the vector η. I expand the sum of squared residuals S_i up to the 1second order around a certain $\hat{\eta}_i$:

$$S_i(\eta;\theta)\approx\hat{S}_i+\hat{\Gamma}_i^T(\eta-\hat{\eta}_i)+\frac{1}{2}(\eta-\hat{\eta}_i)^T\hat{\Delta}_i(\eta-\hat{\eta}_i) \tag{4.101}$$

where

$$\hat{S}_i=S_i(\hat{\eta}_i;\theta),\qquad\hat{\Gamma}_i=\Gamma_i(\hat{\eta}_i;\theta),\qquad\hat{\Delta}_i=\Delta_i(\hat{\eta}_i;\theta). \tag{4.102}$$

To compute the integral in Eq. (4.97), it is convenient to define $\delta=\eta-\hat{\eta}_i$:

$$\frac{S_i}{\sigma^2}+\eta^T\Omega^{-1}\eta\approx\frac{\hat{S}_i}{\sigma^2}+\hat{\eta}_i^T\Omega^{-1}\hat{\eta}_i+\left(\frac{\hat{\Gamma}_i^T}{2\sigma^2}+\hat{\eta}_i^T\Omega^{-1}\right)\delta+\delta^T\left(\frac{\hat{\Gamma}_i}{2\sigma^2}+\Omega^{-1}\hat{\eta}_i\right)+\delta^T\left(\frac{\hat{\Delta}_i}{2\sigma^2}+\Omega^{-1}\right)\delta. \tag{4.103}$$

Defining

$$A=\left(\frac{\hat{\Delta}_i}{2\sigma^2}+\Omega^{-1}\right),\qquad B=\left(\frac{\hat{\Gamma}_i}{2\sigma^2}+\Omega^{-1}\hat{\eta}_i\right),\qquad C=\frac{\hat{S}_i}{\sigma^2}+\hat{\eta}_i^T\Omega^{-1}\hat{\eta}_i, \tag{4.104}$$

the above expression becomes

$$C+\delta^TA\delta+B^T\delta+\delta B^T=C-B^TA^{-1}B+\left(\delta+A^{-1}B\right)^TA\left(\delta+A^{-1}B\right) \tag{4.105}$$

Thus the last term in Eq. (4.97) simplifies as

$$\begin{aligned}-2\log\left[\int\mathrm{d}^k\eta\,e^{-\left[S_i(\eta;\theta)/\sigma^2+\eta^T\Omega^{-1}\eta\right]/2}\right]&\\ \approx C-B^TA^{-1}B-2\log\left[\int\mathrm{d}^k\delta\,e^{-\left(\delta+A^{-1}B\right)^TA\left(\delta+A^{-1}B\right)/2}\right]&\\ =C-B^TA^{-1}B+\log\det A-k\log(2\pi).&\end{aligned} \tag{4.106}$$

Eventually

$$-2\mathcal{L}_i(\theta,\sigma,\Omega;\{y_{ij}\}_{j=1,\dots n_i}) = \frac{\hat{S}_i}{\sigma^2} + \hat{\eta}_i^T\Omega^{-1}\hat{\eta}_i + n_i\log(2\pi\sigma^2) + \log\det\left(1+\frac{\Omega\hat{\Delta}_i}{2\sigma^2}\right) - \left[\frac{\hat{\Gamma}_i}{2\sigma^2}+\Omega^{-1}\hat{\eta}_i\right]^T\left[\frac{\hat{\Delta}_i}{2\sigma^2}+\Omega^{-1}\right]^{-1}\left[\frac{\hat{\Gamma}_i}{2\sigma^2}+\Omega^{-1}\hat{\eta}_i\right]. \quad (4.107)$$

All estimation methods for nonlinear mixed-effect models use a different variant of this approximation, by adopting different approximations for $\hat{\Gamma}_i$ and $\hat{\Delta}_i$ and a different choice for the vector $\hat{\eta}_i$. Here I present only the first order (FO) method and the first order conditional estimation (FOCE) method, as implemented in NONMEN [200], the program used to estimate the parameters of the pharmacokinetics model investigated in this Thesis. Both methods are based on the same approximation of $\hat{\Delta}_i$, but different choices of $\hat{\eta}_i$.

First order approximation of $\hat{\Delta}_i$

The Hessian matrix $\hat{\Delta}_i$ with its expectation value over the intraindividual model

$$\hat{\Delta}_i \approx \mathbb{E}(\hat{\Delta}_i) = \int \mathrm{d}^{n_i} y\, p(\{y_{ij}(t_{ij})\}_{j=1,\dots,n_i}|\psi_i,\sigma)\,\hat{\Delta}_i. \quad (4.108)$$

To compute this integral, I first prove a more general expression. Let p be the density probability of a stochastic variable x, and p depend on some parameter vector ν. Then

$$\int \mathrm{d}x\, p(x;\nu) = 1. \quad (4.109)$$

Let G and H be 1the gradient and the Hessian with respect to ν of the log-likelihood:

$$G = \nabla_\nu \log p = \frac{\nabla_\nu p}{p} \quad (4.110)$$

$$H = \nabla_\nu\nabla_\nu \log p = \frac{\nabla_\nu\nabla_\nu p}{p} - \frac{(\nabla_\nu p)(\nabla_\nu p)^T}{p^2} = \frac{\nabla_\nu\nabla_\nu p}{p} - GG^T. \quad (4.111)$$

Then, the expectation value over the realisation of x of the Hessian H is

$$\mathbb{E}(H) = \mathbb{E}\left(\frac{\nabla_\nu\nabla_\nu p}{p}\right) - \mathbb{E}\left(GG^T\right). \quad (4.112)$$

The first expectation value vanishes:

$$\mathbb{E}\left(\frac{\nabla_\nu\nabla_\nu p}{p}\right) = \int \mathrm{d}x\, p\,\frac{\nabla_\nu\nabla_\nu p}{p} = \nabla_\nu\nabla_\nu \int \mathrm{d}x\, p = 0. \quad (4.113)$$

I have therefore proved that

$$\mathbb{E}(H) = -\mathbb{E}\left(GG^T\right). \tag{4.114}$$

Using now the definition of $\hat{\Delta}_i$

$$\hat{\Delta}_i = \nabla_\eta \nabla_\eta S_i|_{\eta=\hat{\eta}}, \tag{4.115}$$

the expression for the probability p_i of measuring $\{y_{ij}\}$ for individual i of Eq. (4.91), and the definition of S_i of Eq. (4.93)

$$p_i = p(\{y_{ij}(t_{ij})\}_{j=1,\ldots,n_i}|\psi_i, \sigma) = \frac{1}{(2\pi\sigma^2)^{n_i/2}} e^{-S_i/2\sigma^2}, \tag{4.116}$$

it is easy to show that

$$\Gamma_i = \nabla_\eta S_i = -2\sigma^2 \nabla_\eta \log p_i, \tag{4.117}$$

$$\Delta_i = \nabla_\eta \nabla_\eta S_i = -2\sigma^2 \nabla_\eta \nabla_\eta \log p_i. \tag{4.118}$$

Thus, using Eq. (4.114)

$$\mathbb{E}(\hat{\Delta}_i) = \frac{1}{2\sigma^2}\mathbb{E}(\hat{\Gamma}_i \hat{\Gamma}_i^T). \tag{4.119}$$

To compute this expectation value I use the explicit form of S_i of Eq. (4.93) together with Eq. (4.116):

$$\Gamma_i = \nabla_\eta S_i(\eta;\theta) = 2\sum_{j=1}^{n_i} \left[y_{ij} - y(t_{ij};\psi(x_i;\theta)+\eta)\right] \nabla_\psi y(t_{ij};\psi(x_i;\theta)+\eta) \tag{4.120}$$

The observations $\{y_{ij}\}_{j=1,\ldots,n_i}$ of the i-th subject are statistically independent and each with expectation values $y(t_{ij};\psi(x_i;\theta)+\eta)$. As a consequence

$$\mathbb{E}(\hat{\Gamma}_i \hat{\Gamma}_i^T) = 4\sum_{j=1}^{n_i} \nabla_\psi y(t_{ij};\psi(x_i;\theta)+\eta) \nabla_\psi y(t_{ij};\psi(x_i;\theta)+\eta) \mathbb{E}\left[\left(y_{ij} - y(t_{ij};\psi(x_i;\theta)+\eta)\right)^2\right]\Bigg|_{\eta=\hat{\eta}}. \tag{4.121}$$

Since the variance of each observation is σ^2 I eventually find the expression for the first-order approximation of $\hat{\Delta}_i$

$$\hat{\Delta}_i \approx \mathbb{E}(\hat{\Delta}_i) = 2\sum_{j=1}^{n_i} \nabla_\psi y(t_{ij};\psi(x_i;\theta)+\eta) \nabla_\psi y(t_{ij};\psi(x_i;\theta)+\eta)\Big|_{\eta=\hat{\eta}}. \tag{4.122}$$

The first-order (FO) method

The simple first-order (FO) method consists of approximating $\hat{\Delta}_i$ as in Eq. (4.122) and expanding S_i around the population expectation value of the inter-individual effect η, i.e.

$$\hat{\eta}_i = \mathbb{E}(\eta_i) = 0. \tag{4.123}$$

With these assumptions Eq. (4.107) reads:

$$-2\mathcal{L}_i(\theta, \sigma, \Omega; \{y_{ij}\}_{j=1,\dots n_i}) = \frac{\hat{S}_i}{\sigma^2} + n_i \log(2\pi\sigma^2) + \log\det\left(1 + \frac{\Omega\hat{\Delta}_i}{2\sigma^2}\right) - \left[\frac{\hat{\Gamma}_i}{2\sigma^2}\right]^T \left[\frac{\hat{\Delta}_i}{2\sigma^2} + \Omega^{-1}\right]^{-1} \left[\frac{\hat{\Gamma}_i}{2\sigma^2}\right], \tag{4.124}$$

with

$$\hat{\Gamma}_i = \nabla_\eta S_i(\eta;\theta)|_{\eta=0} = 2\sum_{j=1}^{n_i} \left[y_{ij} - y(t_{ij}; \psi(x_i;\theta))\right] \nabla_\psi y(t_{ij}; \psi(x_i;\theta)) \tag{4.125}$$

and

$$\hat{\Delta}_i \approx 2\sum_{j=1}^{n_i} \nabla_\psi y(t_{ij}; \psi(x_i;\theta)) \nabla_\psi y(t_{ij}; \psi(x_i;\theta)). \tag{4.126}$$

The first-order conditional estimation (FOCE) method

The first-order conditional estimation (FOCE) method consists instead of expanding S_i for each subject i around the its post-hoc conditional estimate $\hat{\eta}_i$ obtained by maximising the posterior probability of η_i, that is by solving Eq. (4.100). This implies that the total log-likelihood of Eq. (4.96), obtained by summing over all patients the individual log-likelihood computed with the Laplace approximation of Eq. (4.107) must be maximised with $\hat{\eta}_i$ satisfying

$$\frac{\hat{\Gamma}_i}{2\hat{\sigma}^2} + \hat{\eta}_i^T \hat{\Omega}^{-1} = 0. \tag{4.127}$$

which yields

$$-2\mathcal{L}_i(\theta, \sigma, \Omega; \{y_{ij}\}_{j=1,\dots n_i}) = \frac{\hat{S}_i}{\sigma^2} + \hat{\eta}_i^T \Omega^{-1} \hat{\eta}_i + n_i \log(2\pi\sigma^2) + \log\det\left(1 + \frac{\Omega\hat{\Delta}_i}{2\sigma^2}\right). \tag{4.128}$$

In practice, the parameter estimates are determined by iteratively executing the following steps until convergence:

1. determine $\hat{\theta}$, $\hat{\sigma}$, and $\hat{\Omega}$, by maximising the total log-likelihood;
2. compute the post-hoc value of $\hat{\eta}_i$, for $i = \dots, m$ using Eq. (4.127);

3. evaluate again the log-likelihood using the new values of $\hat{\eta}_i$ in Eq. (4.128).

To efficiently estimate the model parameters, it is convenient to adopt first the FO method to get an estimate of the post-hoc values $\hat{\eta}_i$. Second, these values can be used as initial conditions for $\hat{\eta}_i$ to refine the estimate of the parameters through the FOCE method.

Chapter 5

PHARMACOKINETIC MODELS OF VANCOMYCIN

5.1 Methods

5.1.1 Development sample

The models presented in this Chapter were developed using retrospective data collected from the electronic health record *MargheritaTre* (Chap. 1) in the general ICU of San Giovanni Bosco Hospital, Turin from 2008 to 2017. During this period *MargheritaTre* recorded 4689 admissions to the ICU, of whom 871 patients received intravenous vancomycin. Plasma drug concentration was measured in 157 patients of whom 141 patients had at least one measurement of creatinine clearance. Vancomycin concentration was measured using the analyser system Vista 1500® by Siemens.

Among all the ICUs using *MargheritaTre*, the integration with the laboratory information system (LIS) has been active since 2008 only in Turin ICU. For technical issues, integrations with the LIS have been recently installed in the other ICUs and only a few patients with vancomycin concentrations have been recorded in the databases of 5 ICUs. Furthermore, the number of patients with measured vancomycin concentrations and the number of measurements per patients is highly variable (see Table 5.2). Data quality was also suboptimal because of technical problems of the LIS in the centre with the highest number of patients (centre 2). For several patients the withdrawal time of blood samples for laboratory tests was missing and only the date was available.

A study conducted on data from all the ICU would have introduced spurious variability without being truly multicentric, but representative almost exclusively of Turin situation. I have therefore decided to develop the models presented in this Chapter using data only from Turin centre. Data from the other ICUs were used for external validation.

	N	%
Sex (male)	85	60.3
Mechanical ventilation	120	85.1
Vasoactive drugs	95	67.4
Continuous renal replacement therapy	9	6.4

	Mean	SD	Q1	Median	Q3	Missing
Age (yr)	61.5	14.7	53	64	73	0
Height (cm)	167	8.6	161	167.5	174	11
Weight (kg)	80.5	20.0	67	76.5	92	0
Mean arterial pressure (mmHg)	84.5	14.8	74	83	92	0
Systolic arterial pressure (mmHg)	130	22	114	130	145	0
Diastolic arterial pressure (mmHg)	61	12	52	60	69	0
Heart rate (min^{-1})	85	17	72	85	96	0
Urine output (ml/d)	1284	1579	125	300	2400	0
Tympanic temperature (°C)	37.2	0.7	36.7	37.2	37.7	6
Arterial lactate (mmol/l)	1.2	0.7	0.8	1	1.4	0
Arterial pH	7.46	0.06	7.43	7.46	7.5	0
Arterial blood glucose (mg/dl)	147	36	122	139	169	0
Arterial oxygen pressure (mmHg)	115	36	89	110	134	0
White blood cells ($10^3 \times \mu\text{l}^{-1}$)	13.8	7.1	9.0	12.2	16.7	0
Haematocrit (%)	30.0	4.1	27.4	29.4	32	0
Platelets ($10^3 \times \mu\text{l}^{-1}$)	257	172	140	222	345	0
Plasma albumin (g/l)	25.6	5.0	22.5	26	29	2
Plasma creatinine (mg/dl)	1.1	0.8	0.6	0.8	1.3	0
Creatinine clearance (ml/min)	89.6	74.5	32	71	143	0
Alanine transaminase – ALT (IU/l)	71	194	19	29	52	0
Aspartate transaminase – AST (IU/l)	84	261	21	33	48	0
Direct bilirubin (mg/dl)	0.79	1.57	0.18	0.28	0.54	0
Indirect bilirubin (mg/dl)	0.21	0.38	0.08	0.13	0.19	0
Total bilirubin (mg/dl)	1.0	1.8	0.29	0.45	0.68	0

	Patients	Mean	SD	Q1	Median	Q3
Dopamine (μg/min/kg)	33	8.3	4.2	5.1	7.3	10.3
Dobutamine (μg/min/kg)	9	4.1	1.5	3.0	3.8	5.3
Epinephrine (μg/min/kg)	91	0.10	0.05	0.064	0.085	0.11
Norepinephrine (μg/min/kg)	89	0.10	0.05	0.065	0.089	0.11
VIS	95	21	12	12	18	24

Table 5.1: Patient characteristics and treatments. Upper table: dichotomous variables. Central table: patient characteristics – continuous variables. Lower table: dosage of vasoactive drugs and vasoactive inotropic score (VIS) – continuous variables.

5.1.2 Covariates

A descriptive analysis of patient characteristics and treatments received is provided in Table 5.1 for categorical and continuous variables, respectively. The mean age was 61.5 yr, 85 patients were males (60.3%), 120 received mechanical ventilation (85.1%), 95 (67.4%) vasoactive drugs, and 9 continuous renal replacement therapy (6.4%).

The model was developed on 300 serum vancomycin concentrations (2.1 measurements per

centre ID	patients	observations	observations/patient	model	manufacturer
1	1	5	5	Taurus	Werfen
2	41	223	5.4	Vista 1500	Siemens
3	12	31	2.6	Dimention	Siemens
4	8	13	1.6	Vista 1500	Siemens
5	1	3	3	Taurus	Werfen
total	63	275	4.4		

Table 5.2: Number of patients per centre, measured vancomycin concentrations, and measurement system in the validation set.

patient on average) testing as covariates all the variables presented in Table 5.1. Validation was performed on 275 serum vancomycin concentrations from 63 patients from 5 ICUs.

Given the retrospective and observational nature of the study, neither the sampling-time schedule nor the drug-dose protocol could be designed to optimise the estimation of pharmacokinetic parameters according to ED optimality concepts [183]. Variables tested as possible model covariates where chosen to account for sources of variation in the pharmacokinetic parameters, associated either with patient conditions (altered renal, hepatic, cardiovascular function) or with treatments received during the ICU stay, as reviewed in Sec. 2.5 (see also Fig. 2.9). Those variables were selected by a panel of experts, including intensivists and pharmacologists.

As demonstrated in previous investigations (see Sec. 3.2), the most important predictive factor of vancomycin clearance is the GFR, since renal excretion is the main mechanism responsible for the elimination of this drug. A good estimate of GFR is given by creatinine clearance [203, 187] measured on the basis of 8, 12, or 24-hour urine collection. Serum creatinine and estimated creatinine clearance obtained by Cockcroft–Gault or Modified-Diet-in-Renal-Disease formulas [50, 111] fail instead to provide reliable estimates of renal function [87], especially in critically ill patients [55, 155, 168, 173]. Accordingly, the models presented in this Chapter have been constructed using only measured values of creatinine clearance obtained by directly measuring serum creatinine concentration, urine creatinine concentration, and urine flow.

For each treatment I recorded the initial and final dates and times. Ventilation and continuous renal replacement therapy were tested in the model as dichotomous variables with value 1 in the period when the patient received the treatment, 0 otherwise. I did not introduce in the model any further details on those treatments (e.g., ventilator parameters or setting of CRRT) since available data were not reliable. Conversely, more precise information was available on the administration of vasoactive drugs. I tested both the dosage of each molecule and the vasoactive inotropic score, an aggregated variable introduced to quantify the impact of the pharmacological cardiovascular

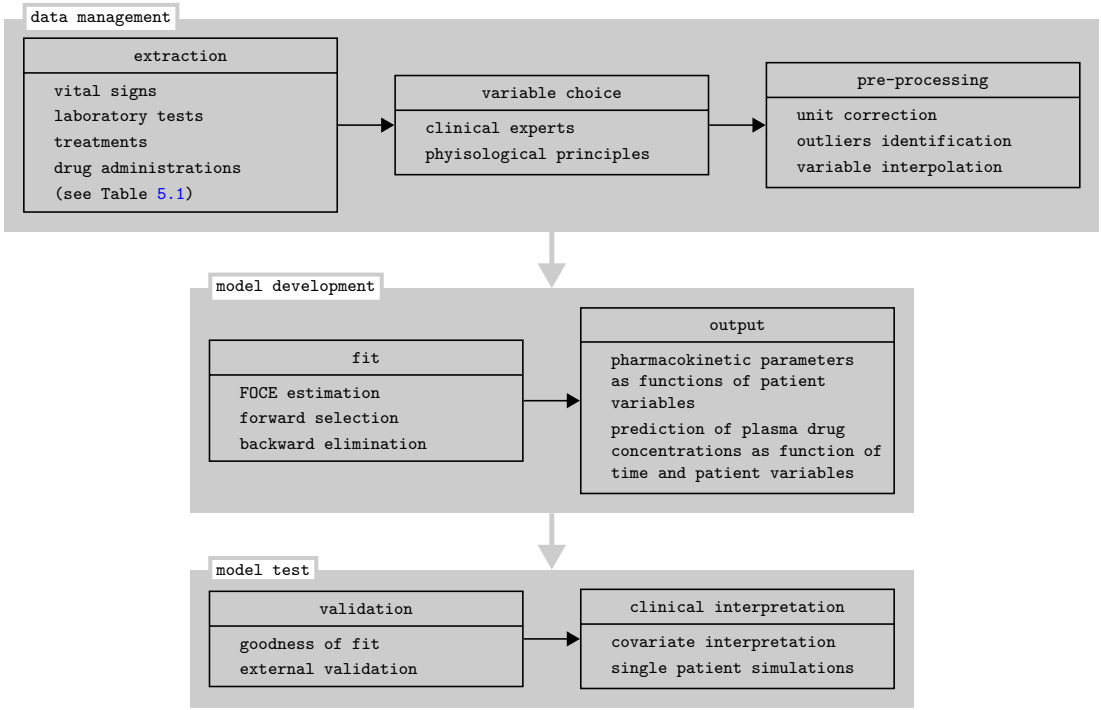

Figure 5.1: Workflow of model construction.

support [205]. The score weights the dosage of each molecule according to the formula

$$\begin{aligned}\text{VIS} = \frac{\text{dopamine}}{\mu\text{g/kg/min}} + \frac{\text{dobutamine}}{\mu\text{g/kg/min}} + 10 \times \frac{\text{milrinone}}{\mu\text{g/kg/min}} + 100 \times \frac{\text{epinephrine}}{\mu\text{g/kg/min}} \\ + 100 \times \frac{\text{norepinephrine}}{\mu\text{g/kg/min}} + 10\,000 \times \frac{\text{vasopressin}}{\text{U/kg/min}}. \quad (5.1)\end{aligned}$$

5.1.3 Data management

Data were loaded into R data frames from *MargheritaTre* servers using the data load tools presented in Sec. 1.3 and eligible patients selected as described in the previous section. I plotted the distribution of every variable (laboratory tests, vital signs, drug administrations) to identify outliers and possible errors in the unit of measurement. Errors were corrected and clinically non-plausible outliers were eliminated (see Fig. 5.1 for a workflow diagram of the process of model construction).

I then wrote a NONMEM data input file (`.dta`), using, for each patient, only data (laboratory test and vital signs and treatments) relative to the period elapsing between the first vancomycin administration (t_{first}) and the last measurement of plasma vancomycin concentration (t_{last}). NONMEM input files are space separated text files with the following required columns [5]:

ID: Numeric ID for patients.

DAT1, TIME: Event date and time.

EVID: Event type.

0. Observation — measured value of plasma drug concentrations in the central compartment. When EVID = 0, DV must not be null.

1. Drug administration. When EVID = 1, the fields AMT and RATE must not be null and DAT1 and TIME contains the initial date and time of drug administration.

2. Other event — change of value of other variables.

DV: Measured value of drug concentration.

AMT, RATE: Amount and rate of drug administration.

In addition, further variables may be added to the `.dat` file with any column name. The rows must be written in ascending order of date and time (DAT1 and TIME) and the values of covariates in each row are valid from the date-time of the previous row to the date-time of the current row. Said v_i the value of the covariate v in the i-th row,

$$v(t) = v_i, \qquad \text{for} \quad t_{i-i} < t \leq t_i. \tag{5.2}$$

The NONMEM routines (ADVAN1 and ADVAN3) used to develop the model integrate the linear differential equations Eqs. (4.3), (4.14), and (4.15) piecewise in every time interval $[t_{i-i}, t_i]$. The coefficients of the equations are kept constant for the whole interval and computed using the expressions of the structural model (see Sec. 4.3) as functions of covariate values from the i-th record.

The rules to create the rows of the `.dta` input file must be fixed according to these behaviours of NONMEM. In particular, it is important to adopt the most suitable approximation for the choice of the initial and final validity times for each type of variable.

Treatment variables. For variables describing treatment settings, such as the dosage of a drug, the initial and final validity times coincide with the start and the end of the treatment. In Table 5.3 I illustrate how to complete the NONMEM input file with the dosage of a drug administered from time 2 to time 3 with dosage 10, from time 4 to time 5 with dosage 20, and from time 5 to time 7 dosage 15. Five NONMEM events are needed to represent this sequence of administrations

1st row: Start of the first administration at time 2. The variable DOS has value 0 because the drug is not administered at times earlier than 2.

2nd row: End of the first administration at time 3. DOS = 10 indicates that the dosage is 10 starting from the time of the previous record.

TIME	DOS
2	0
3	10
4	0
5	20
7	15

Table 5.3: Columns of NONMEM input file relative to drug dosage for a drug administered from time 2 to time 3 with dosage 10, from time 4 to time 5 with dosage 20, and from time 5 to time 7 dosage 15.

3$^{\mathbf{rd}}$ row: Start of the second administration ad time 4. DOS = 0 indicates that no drug is administered from $t = 3$ to $t = 4$.

4$^{\mathbf{th}}$ row: Change of dosage at time 5, from 20 to 15. DOS = 20 indicates that the drug dosage is 20 from $t = 4$ to $t = 5$.

5$^{\mathbf{th}}$ row: End of drug administration at time 7. DOS = 15 indicates the dosage of the last period of administration, $t = 5$ to $t = 7$.

Vital signs and laboratory tests. If two values of the same variable are measured at two different times t_a and t_b, the variable changed its value at a certain time in between t_a and t_b. In the absence of further information (e.g., details on measurement technique or treatments that may affect the value of the variable), it is reasonable to assume that the change happened at $\bar{t} = (t_a + t_b)/2$. Thus, if numerical values v_a, v_b, v_c are measured at times t_a, t_b, t_c, I assume that v_a, v_b, v_c are valid for any $t < t_1$, $t_1 < t < t_2$, and $t > t_2$, respectively, with $t_1 = (t_a + t_b)/2$, $t_2 = (t_b + t_c)/2$ (see Fig. 5.2). Accordingly, the events in the NONMEM input file are coded as illustrated in Fig. 5.2, right panel. In the first row I write the value v_a with the time t_1 ($v = v_a$ before t_1), v_b with time t_2 ($v = v_b$ from t_1 to t_2), and v_c with t_{last} ($v = v_c$ for any after t_2, up to the time of the last record $t_3 = t_{\text{last}}$, corresponding to the last measurement of plasma drug concentration).

Creatinine clearance. The above construction of the validity time intervals cannot be applied to creatinine clearance. This test is performed by measuring the total amount of drug eliminated in urine in 24 hours, according to Eq. (2.43). For instance, let assume the measured value of creatinine clearance be 90 ml/min at 7:00 a.m. on day 3, and 110 ml/min at 7:00 a.m on day 5. It is reasonable to assume that creatinine clearance is 90 ml/min during the 24 h preceding the first observation (from 7:00 a.m. of day 2 to 7:00 a.m. of day 3) and 110 ml/min during the 24 h preceding the second observation (from 7:00 a.m. of day 4 to 7:00 a.m. of day 5). In the time interval from 7:00 a.m. of day 3 to 7 a.m. of day 4, no measured value is present. With no further available information, I halve this period and assume that creatinine clearance is 90 ml/min until 7:00 p.m. of day 3, and 110 ml/min afterwards. If I had instead applied the naive construction

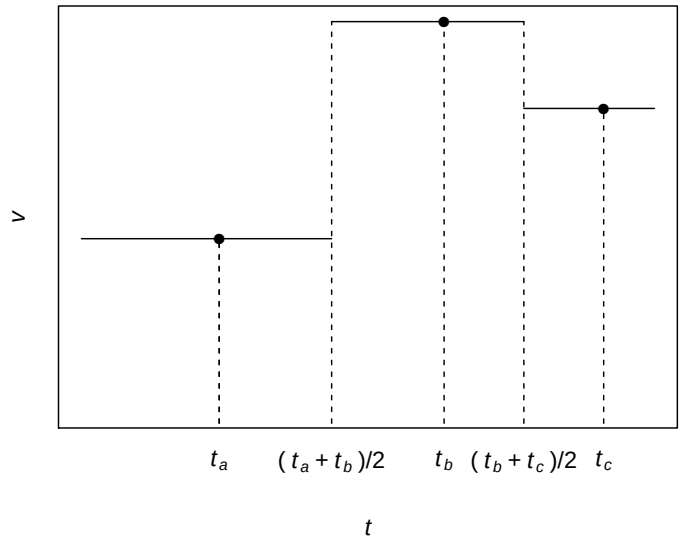

TIME	VAR
$t_1 = (t_a + t_b)/2$	v_a
$t_2 = (t_a + t_b)/2$	v_b
$t_3 = t_{\text{last}}$	v_c

Figure 5.2: Left panel: Construction of validity time intervals for the values of a generic patient variable measured at times t_a, t_b, and t_c. Right panel: Corresponding columns of NONMEM input file. t_{last} is the time of the last record, corresponding to the last measurement of plasma drug concentration.

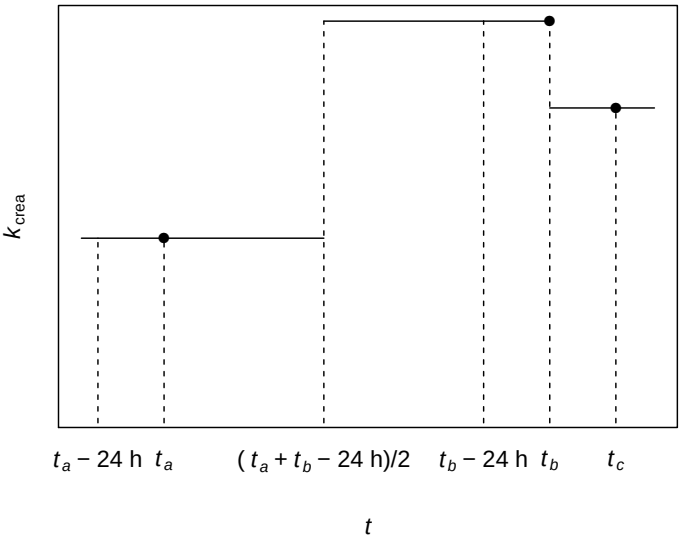

TIME	CLCR
$t_1 = (t_a + t_b - 24\,\text{h})/2$	$k_{\text{crea},a}$
$t_2 = t_b$	$k_{\text{crea},b}$
$t_3 = t_{\text{last}}$	$k_{\text{crea},c}$

Figure 5.3: Left panel: Construction of validity time intervals for the values of creatinine clearance measured at times t_a, t_b, and t_c. Right panel: Corresponding columns of NONMEM input file. t_{last} is the time of the last record, corresponding to the last measurement of plasma drug concentration.

introduced in the previous paragraph, I would have used the first measured value of 90 ml/min up to 7:00 a.m. of day 4.

This construction is graphically represented in the left panel Fig. 5.3, for three measured concentrations of creatinine clearance $k_{\text{crea},a}$, $k_{\text{crea},b}$, and $k_{\text{crea},c}$ at times t_a, t_b, and t_c, respectively, with $t_b - t_a > 24\,\text{h}$ and $t_c - t_b = 24\,\text{h}$. The table in the right panel reports the two corresponding columns in the NONMEM data input file. The times where the value of creatinine clearance is assumed to vary are $t_1 = (t_b - t_a - 24\,\text{h})/2$ and t_b.

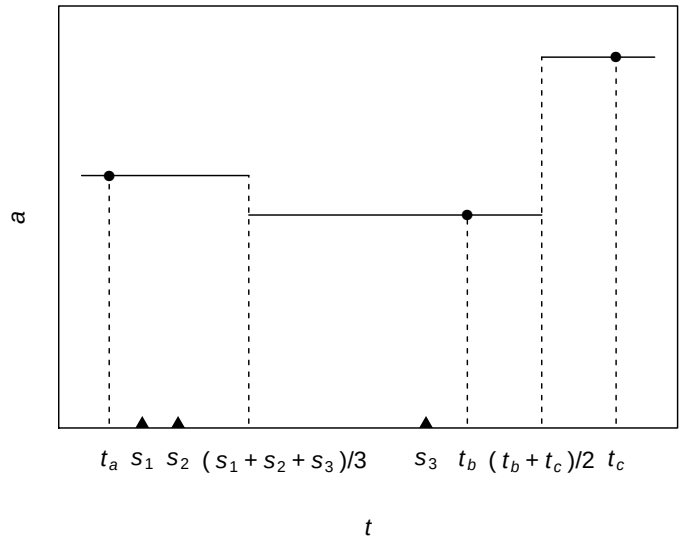

TIME	ALB
$t_1 = (s_1 + s_2 + s_3)/3$	a_a
$t_2 = (t_b + t_c)$	a_b
$t_3 = t_{\text{last}}$	a_c

Figure 5.4: Left panel: Construction of validity time intervals for the values of plasma albumin concentration measured at times t_a, t_b, and t_c. Albumin is administered at times s_1, s_2, and s_3 (triangles). Right panel: Corresponding columns of NONMEM input file. t_{last} is the time of the last record, corresponding to the last measurement of plasma drug concentration.

Plasma albumin concentration. The simple construction illustrated in Fig. 5.2 may be improved if additional information is known about factors that can affect the value of the considered variable. Plasma albumin concentration, for instance, is artificially modified by intravenous administration of albumin. I construct the times at which this variable changes between two measurements as the mean of the times at which albumin is administered. If there is no administration, I follow the general procedure of 5.2. This construction is represented in Fig. 5.4 for three measurements of albumin a_a, a_b, and a_c measured at times t_a, t_b, and t_c. Albumin is administered at times s_1, s_2, and s_3, all within t_a and t_b. Plasma albumin concentration is assumed to change from a_a to a_b at time $t_1 = (s_1 + s_2 + s_3)/3$ and from a_b to a_v at time $t_2 = (t_b + t_c)/2$.

5.1.4 Model construction and variable selection

Model covariates were automatically selected among the set of clinically relevant variables presented in Table 5.1 in a forward stepwise procedure, followed by a backward elimination. Variables were included in the model if the difference in the objective function value (OFV, namely the log-likelihood statistic) was statistically significant (using log-likelihood ratio test) with $p < 0.05$. At each step, I tested different mathematical relationships between the pharmacokinetic parameters and the covariate: linear, power-law, logarithmic, and in interaction with the other covariates already selected.

Goodness-of-fit of final models was assessed by graphically comparing observations and predictions, plotting conditional weighted residuals (CWRES [86]) versus time and observed con-

centrations, and computing the shrinkage. The distribution of estimated model parameters was constructed by bootstrap technique with 1000 resamplings with replacement. Monte Carlo simulations (1000 runs) were performed to draw confidence bands of model predictions. Using the results of those simulations, variance-prediction-corrected visual predictive checks (vpcVPC [26]) and mirror plots were constructed. I also computed extended normalised predicted distribution errors (NPDE [35, 51]), namely, empirical Bayes estimate (EBE) NPDE and CWRES NPDE to investigate separately possible issues associated with between-subject variability and residual errors [106]. I plotted their distribution and compared their quantiles against the quantiles of the normal distribution in QQ plots. Formal non-parametric tests of normality were performed. I performed the Wilcoxon rank-test with null hypothesis of symmetric distribution around zero, the Kolmogorov–Smirnov test with null hypothesis of gaussian distribution with mean equal to the sample mean and variance one, and, finally, the Shapiro–Wilk test for normality. Those analyses were performed both in internal and external validation on the development sample (Turin ICU) and on the validation sample (other ICUs), see Sec. 5.1.1.

All the following models were constructed using NONMEM v.7.4.1, with the FOCE method with interaction. In the NONMEM model file `.mod` I included $TABLE records to export output data to Xpose4 [9], the R package used to perform some post-processing analyses of the results of NONMEM runs. I implemented a semi-automatic forward selection procedure of patient variables through an R script that creates a model file for each tested variable, runs it using Perl-speaks-NONMEM (PsN) v.4.8.1 [6], appends the output parameters to a `.csv` file, and logs the path containing the results of the run, some notes, and the OFV to a file. The R script is parallelised on 4 cores to speed up calculations. Thanks to this script it is possible, at each step of the forward procedure, to compare the value of the OFV among all variables, perform the likelihood ratio test, and eventually select the most significant variable that improve the goodness of fit. For each run I also computed the covariance matrix of the estimated parameters through the NONMEM $COVARIANCE record. The successful execution of the covariance step ensures that convergence is properly reached and the estimated parameters are reliable. Bootstrap analyses and simulations were performed using PsN. Plots were realised through Xpose4 library of R.

Testing all variables of Table 5.1 by replacing them one by one in the formula of a single pharmacokinetic parameter (e.g., clearance or distribution volume) takes about 1.5 h. For a one-compartment model (two pharmacokinetic parameters) it takes about 3 h on a machine with 4 Intel-i7 – 2 GHz cores with 8 GB memory to perform a single step of the forward procedure and identify the most significant new variable. For a two-compartment model, there are twice as many combinations to screen as in the one-compartment model. In this case it takes about 6 hours to perform a single step of the forward procedure.

5.2 One-compartment model

5.2.1 Model development

One-compartment models were constructed using the NONMEM ADVAN1 routine. A minimal one-compartment model [see Eq. 4.3] without patient covariates was first constructed as

$$k_{\text{vanco},i} = \theta_k \, e^{\eta_{k,i}}, \tag{5.3}$$

$$V_i = \theta_V \, e^{\eta_{V,i}}, \tag{5.4}$$

$$C_{ij} = C(t_{ij})(1 + \varepsilon_{ij}). \tag{5.5}$$

Inter-individual variability was modelled as an exponential random effect to ensure that both k and V are positive. Residual variability was modelled with a proportional error. The minimal model provides very poor estimates in terms of population predictions (Fig. 5.5, left panel). The population predictions are computed using for all patients the same average values of the pharmacokinetic parameters, $k_{\text{drug}} = \theta_k$, $V = \theta_V$. That is, no patient-specific variables are taken into account at this stage. However, the individual predictions, computed using Eqs. (5.3) and (5.4) and the post-hoc estimates of $\eta_{k,i}$ and $\eta_{V,i}$ (see Appendix 4.3.3), already provide quite precise estimates of the observed concentrations (Fig. 5.5, right panel). These results suggest that the one-compartment model may represent a fair approximation of the kinetics of vancomycin, but the pharmacokinetic parameters must be personalised according to the patient's conditions. Relevant patient covariates to explain observations were identified by visual inspection of residuals-vs-covariate using the R package Xpose4. Plots of pharmacokinetic parameters versus covariates were used to guess the relationship between each covariate and V and k. The mathematical forms of the relations between covariates and pharmacokinetic parameters were chosen according to the underlying physiological mechanisms discussed in Chap. 2 and to the result of this visual inspection.

Significant terms and the corresponding free parameters were selected using the likelihood ratio test in a forward selection procedure, whose steps are reported in Table 5.4. All variables were normalised using their median value. In a first phase I tested linear effects [steps (1)–(4)] and introduced multiplicative terms with the main effects [steps (5)–(7)]. Moreover, from step (3) to step (4) the intercept of k_{vanco} was removed because it was not significantly different from 0, after the introduction of the term proportional to the total body weight w.

In a second phase, the model was refined by testing non-linear effects to make the dependence on covariates sharper (for exponents larger than 1) or flatter (Table 5.5). Nonlinearities were introduced through power-law terms and the corresponding exponents were estimated as free

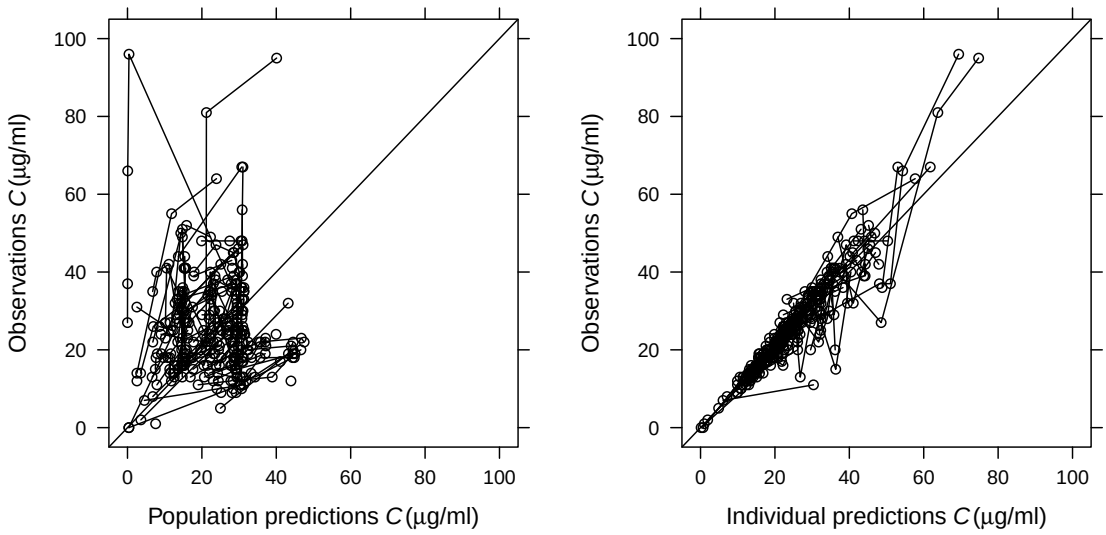

Figure 5.5: Measured plasma vancomycin concentrations versus population (left panel) and individual prediction (right panel). Population predictions are computed evolving Eq. 4.3 using for all patients the average value of drug clearance $k_{\text{drug}} = \theta_k$ and distribution volume $V = \theta_V$. Individual predictions are computed taking into account the post-hoc estimates of $\eta_{k,i}$ and $\eta_{V,i}$.

parameters. Statistical significance of these terms was assessed by the likelihood ratio test. For variables like age, creatinine, and VIS, appearing in the model in the form $(1 + \theta_x\, x/\bar{x})$ (where I indicate with $\bar{x}$ the median value of the variable x), I tested both forms

$$\left[1 + \theta_x \left(\frac{x}{\bar{x}}\right)^{\alpha_x}\right], \qquad \theta_x \in \mathbb{R}, \qquad \alpha_x > 0, \tag{5.6}$$

and

$$\left(\frac{x}{\bar{x}}\right)^{\beta_x}, \qquad \beta_x \in \mathbb{R}. \tag{5.7}$$

The OFV decreased significantly by introducing a power-law dependence for the creatinine clearance k_{crea} with an exponent $\beta_{\text{cr}} \approx 0.61$. The relationship between creatinine clearance and vancomycin clearance is therefore sublinear, implying that vancomycin clearance is not affected by the very large values that creatinine clearance may assume (Q3 = 143 ml/min (see Table 5.1). The OFV of the model decreased significantly by expressing the dependence of the distribution volume on creatinine plasma concentration as a decreasing exponential low. Conversely, it did not decrease significantly by replacing the other variables with either Eqs. (5.6) or (5.7). However, since the OFV did not increase by introducing a power-law for the covariate age, I decided to implement this step also. Indeed power-law terms, being always positive, make the model more robust than linear terms, which, conversely, can generate negative pharmacokinetic parameters if the values of the associated covariate are very large.

As the last step in the construction of the structural model, I performed a final screening of the

	Model structure	n	OFV
(0)	$k_{\text{vanco}} = \theta_k$ $V = \theta_V$	2	1693.9
(1)	$k_{\text{vanco}} = \theta_k \left[1 + \theta_{\text{cr}} \left(\frac{k_{\text{crea}}}{71\,\text{ml/min}}\right)\right]$ $V = \theta_V$	3	1547.6
(2)	$k_{\text{vanco}} = \theta_k \left[1 + \theta_{\text{cr}} \left(\frac{k_{\text{crea}}}{71\,\text{ml/min}}\right) + \theta_{\text{CRRT}}\delta_{\text{CRRT}}\right]$ $V = \theta_V$	4	1506.4
(3)	$k_{\text{vanco}} = \theta_k \left[1 + \theta_{\text{cr}} \left(\frac{k_{\text{crea}}}{71\,\text{ml/min}}\right) + \theta_{\text{CRRT}}\delta_{\text{CRRT}}\right]$ $V = \theta_V \left[1 + \theta_{\text{crea}} \frac{C_{\text{crea}}}{0.8\,\text{mg/dl}}\right]$	5	1492.1
(4)	$k_{\text{vanco}} = \theta_{\text{cr}} \left(\frac{k_{\text{crea}}}{71\,\text{ml/min}}\right) + \theta_w \left(\frac{w}{76.5\,\text{kg}}\right) + \theta_{\text{CRRT}}\delta_{\text{CRRT}}$ $V = \theta_V \left[1 + \theta_{\text{crea}} \frac{C_{\text{crea}}}{0.8\,\text{mg/dl}}\right]$	5	1480.6
(5)	$k_{\text{vanco}} = \theta_{\text{cr}} \left(\frac{k_{\text{crea}}}{71\,\text{ml/min}}\right) \left[1 + \theta_a \left(\frac{a}{64\,\text{yr}}\right)\right] + \theta_w \left(\frac{w}{76.5\,\text{kg}}\right) + \theta_{\text{CRRT}}\delta_{\text{CRRT}}$ $V = \theta_V \left[1 + \theta_{\text{crea}} \frac{C_{\text{crea}}}{0.8\,\text{mg/dl}}\right]$	6	1469.8
(6)	$k_{\text{vanco}} = \theta_{\text{cr}} \left(\frac{k_{\text{crea}}}{71\,\text{ml/min}}\right) \left[1 + \theta_a \left(\frac{a}{64\,\text{yr}}\right)\right] \left[1 + \theta_{k,\text{crea}} \frac{C_{\text{crea}}}{0.8\,\text{mg/dl}}\right] + \theta_w \left(\frac{w}{76.5\,\text{kg}}\right) + \theta_{\text{CRRT}}\delta_{\text{CRRT}}$ $V = \theta_V \left[1 + \theta_{V,\text{crea}} \frac{C_{\text{crea}}}{0.8\,\text{mg/dl}}\right]$	7	1462.7
(7)	$k_{\text{vanco}} = \theta_{\text{cr}} \left(\frac{k_{\text{crea}}}{71\,\text{ml/min}}\right) \left[1 + \theta_a \left(\frac{a}{64\,\text{yr}}\right)\right] \left[1 + \theta_{k,\text{crea}} \frac{C_{\text{crea}}}{0.8\,\text{mg/dl}}\right] \times \left[1 + \theta_{\text{VIS}} \frac{\text{VIS}}{18}\right] + \theta_w \left(\frac{w}{76.5\,\text{kg}}\right) + \theta_{\text{CRRT}}\delta_{\text{CRRT}}$ $V = \theta_V \left[1 + \theta_{V,\text{crea}} \frac{C_{\text{crea}}}{0.8\,\text{mg/dl}}\right]$	8	1457.7

Table 5.4: First phases of the development of the structural model with the corresponding number of free parameters n and the value of the objective function value, OFV $= -2\mathcal{L}$. Parameters were introduced in the model if the corresponding likelihood ratio test was significant. From step (3) to step (4) the intercept of k_{vanco} was removed because it vanished after the introduction of the total body weight w.

variables not included in the model by testing them in power-law form multiplying (one by one) the four additive terms presented in the model: the three terms in k_{vanco} proportional to k_{crea}, w and δ_{CRRT}, respectively, and the unique term forming the expression of V). I finally obtain the

	Model structure	n	OFV
(8)	$k_{\text{vanco}} = \theta_{\text{cr}} \left(\frac{k_{\text{crea}}}{71\,\text{ml/min}}\right)^{\beta_{\text{cr}}} \left[1 + \theta_a \left(\frac{a}{64\,\text{yr}}\right)\right] \left[1 + \theta_{k,\text{crea}} \frac{C_{\text{crea}}}{0.8\,\text{mg/dl}}\right] \times \left[1 + \theta_{\text{VIS}} \frac{\text{VIS}}{16.4}\right] + \theta_w \left(\frac{w}{76.5\,\text{kg}}\right) + \theta_{\text{CRRT}} \delta_{\text{CRRT}}$ $V = \theta_V \left[1 + \theta_{V,\text{crea}} \frac{C_{\text{crea}}}{0.8\,\text{mg/dl}}\right]$	9	1448.0
(9)	$k_{\text{vanco}} = \theta_{\text{cr}} \left(\frac{k_{\text{crea}}}{71\,\text{ml/min}}\right)^{\beta_{\text{cr}}} \left[1 + \theta_a \left(\frac{a}{64\,\text{yr}}\right)\right] \left[1 + \theta_{k,\text{crea}} \frac{C_{\text{crea}}}{0.8\,\text{mg/dl}}\right] \times \left[1 + \theta_{\text{VIS}} \frac{\text{VIS}}{16.4}\right] + \theta_w \left(\frac{w}{76.5\,\text{kg}}\right) + \theta_{\text{CRRT}} \delta_{\text{CRRT}}$ $V = \theta_V \left(\frac{C_{\text{crea}}}{0.8\,\text{mg/dl}}\right)^{\beta_{\text{crea}}}$	9	1443.3
(10)	$k_{\text{vanco}} = \theta_{\text{cr}} \left(\frac{k_{\text{crea}}}{71\,\text{ml/min}}\right)^{\beta_{\text{cr}}} \left(\frac{a}{64\,\text{yr}}\right)^{\beta_a} \left[1 + \theta_{k,\text{crea}} \frac{C_{\text{crea}}}{0.8\,\text{mg/dl}}\right] \times \left[1 + \theta_{\text{VIS}} \frac{\text{VIS}}{16.4}\right] + \theta_w \left(\frac{w}{76.5\,\text{kg}}\right) + \theta_{\text{CRRT}} \delta_{\text{CRRT}}$ $V = \theta_V \left(\frac{C_{\text{crea}}}{0.8\,\text{mg/dl}}\right)^{\beta_{\text{crea}}}$	9	1443.1

Table 5.5: Model refinement with testing of various functional forms relating the covariate with the pharmacokinetic parameters. n is the number of free parameters and OFV is the objective function value, OFV $= -2\mathcal{L}$.

following structural model:

$$k_{\text{vanco}} = \theta_{\text{cr}} \left(\frac{k_{\text{crea}}}{71\,\text{ml/min}}\right)^{\beta_{\text{cr}}} \left(\frac{a}{64\,\text{yr}}\right)^{\beta_a} \left[1 + \theta_{k,\text{crea}} \frac{C_{\text{crea}}}{0.8\,\text{mg/dl}}\right] \left[1 + \theta_{\text{VIS}} \frac{\text{VIS}}{16.4}\right] + \theta_w \left(\frac{w}{76.5\,\text{kg}}\right) + \theta_{\text{CRRT}} \delta_{\text{CRRT}}, \tag{5.8}$$

$$V = \theta_V \left(\frac{C_{\text{crea}}}{0.8\,\text{mg/dl}}\right)^{\beta_{\text{crea}}}, \tag{5.9}$$

where k_{crea} and C_{crea} are creatinine clearance and plasma concentration, respectively, a is age, w total body weight, and δ_{CRRT} is a dichotomous variable that assumes value 1 when the patient undergoes renal replacement therapy. In Table 5.6 I report the matrix of correlations among variables included in the final model. As discussed in Ref. [30] variables with correlation greater than 0.5 should normally not be included in the model. However, although collinearity makes more difficult the clinical interpretation of the structure of the model (see Sec. 5.2.4), affects the coefficients and p-values of the parameters, it does not influence the predictions and the goodness-of-fit [109].

Finally, I reconsidered the statistical structure of the model, testing exponential and proportional residual errors. The best results in terms of precision of the estimates of the fixed effects and of the description of interindividual and residual variability were obtained with only additive

	k_{crea}	a	C_{crea}	VIS	w
k_{crea}	1.00	-0.36	-0.50	-0.21	-0.07
a	-0.36	1.00	0.08	-0.08	-0.06
C_{crea}	-0.50	0.08	1.00	0.23	0.19
VIS	-0.21	-0.08	0.23	1.00	-0.08
w	-0.07	-0.06	0.19	-0.08	1.00

Table 5.6: Correlation matrix of the continuous variables included in the final one-compartment model of Eqs. (5.8) and (5.9).

parameter	units	value	SD	95% CI
θ_{cr}	ml/min	37.3	2.4	36.6 – 42.1
$\theta_{k,\text{crea}}$	–	-0.17	0.02	−0.20 – −0.12
θ_w	ml/min	12.4	1.6	10.3 – 15.1
θ_{CRRT}	ml/min	17.3	2.9	10.7 – 24.6
θ_{VIS}	–	0.080	0.046	0.015 – 0.18
β_{cr}	–	0.72	0.08	0.58 – 0.94
β_a	–	-0.55	0.11	−0.33 – −0.79
θ_V	l	77.7	6.6	64 – 90
β_{crea}	–	-0.35	0.06	−0.46 – −0.19
$\Omega_{\eta_k\eta_k}$	–	0.064	0.014	0.037 – 0.091
$\Omega_{\eta_V\eta_V}$	–	0.21	0.06	0.07 – 0.32
σ^2	$(\mu\text{g/ml})^2$	10.0	1.7	6.5 – 13.5

Table 5.7: Best-fit estimates and estimated standard deviations of the parameters of the pharmacokinetic model of Eqs. (5.8)–(5.12). Confidence intervals were computed by bootstrap technique.

random residual effects as

$$k_{\text{vanco},i} = k_{\text{vanco}}\, e^{\eta_{k,i}}, \tag{5.10}$$

$$V_i = V\, e^{\eta_{V,i}}, \tag{5.11}$$

$$C_{ij} = C_i(t_{ij}) + \varepsilon_{ij}. \tag{5.12}$$

The best-fit values of the model parameters and of the random-effect variances are reported in Table 5.7, together with their maximum-likelihood standard deviation. The last column reports the 95% confidence interval of the empirical parameter distribution obtained by constructing 1000 pharmacokinetic models starting from samples bootstrapped with repetition from the original population. In Fig. 5.6 I compare the marginal probability density of each parameter, obtained by bootstrap technique (histogram), with the corresponding normal distribution (solid line) built using the maximum-likelihood estimates of mean and variance. The normal approximations of the parameter distributions are generally good, except for a few parameters, especially the exponents β and the variances of the random effects Ω and σ^2, which show a small bias between the two distributions. In Sec. 5.4 I shall compare confidence and prediction intervals at single-patient level, obtained with either normal or empirical distribution.

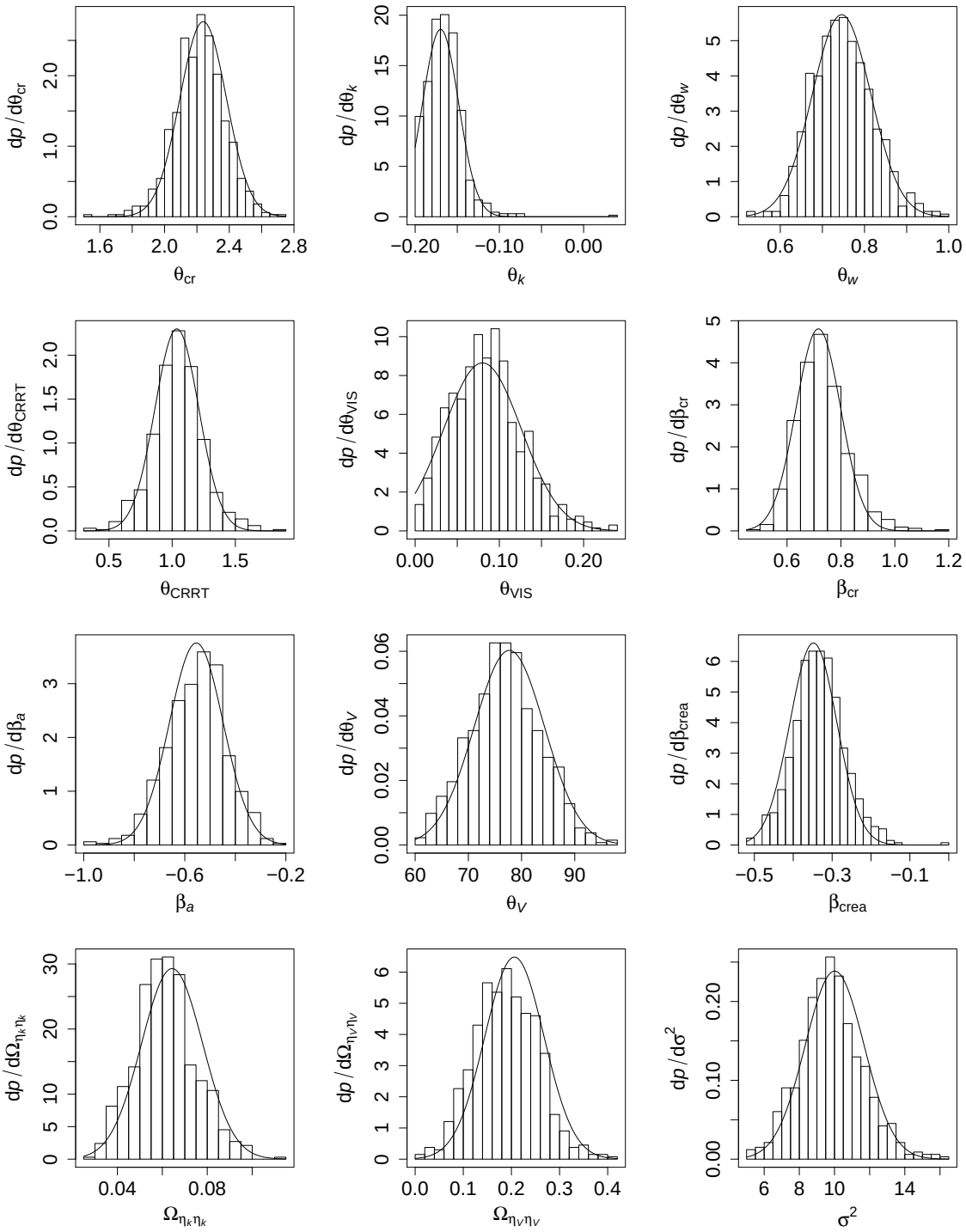

Figure 5.6: Normal distribution with maximum-likelihood estimates of mean and variance of the parameters (solid lines) and bootstrap distribution (histogram) for each parameter of the one-compartment model (see Table 5.12).

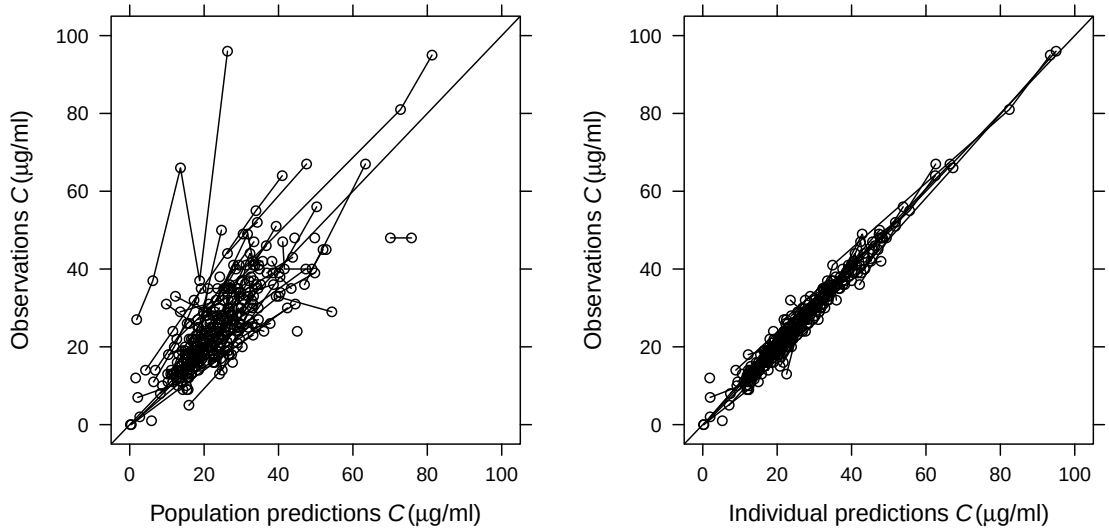

Figure 5.7: Measured plasma vancomycin concentrations versus population (left panel) and individual prediction (right panel) for the final one-compartment model of Eqs. (5.8) and (5.9) with random interindividual and residual variabilities expressed by Eq. (5.10), (5.11), and (5.12).

5.2.2 Goodness of fit

In Fig. 5.7, measured drug concentrations are plotted versus population and individual predictions for this final one-compartment model. The concordance between measured concentrations and population predictions has been considerably improved with respect to the minimal model (see Fig. 5.5) thanks to the introduction of patient covariates in Eqs. (5.8) and (5.9). The residual variability not explained by patient covariates and interindividual variability has been also significantly reduced, as shown in the right panel of Fig. 5.7. The standard deviation of the difference between observations and population predictions is 9.1 μg/ml, whereas it is 2.2 μg/ml between observations and individual predictions. Observations fall in 94.6% of cases in the 95%-confidence interval of predictions, estimated with bootstrap techniques. This suggests that the structural model and the covariance structure are properly modelled. However the distance between observations and population predictions is too wide to implement the population-model in a bedside simulator of pharmacokinetics without measuring any concentration on the patient. Nevertheless, since individual predictions are reliably close to observations, it would be possible to use individual *post-hoc* estimated pharmacokinetic parameters to predict the evolution of drug concentration. One or two values of plasma concentration of the patient, measured at the beginning of the antibiotic therapy, should be input in the simulator to adapt the population values of k and V.

Shrinkage of individual weighted residual is 63%, of η_k is 16%, and of η_V is 41%. Although it is difficult to interpret the sources of shrinkage since its value is affected by several factors [211], it is reasonable to conclude that the large shrinkage is caused in this case by the low number of

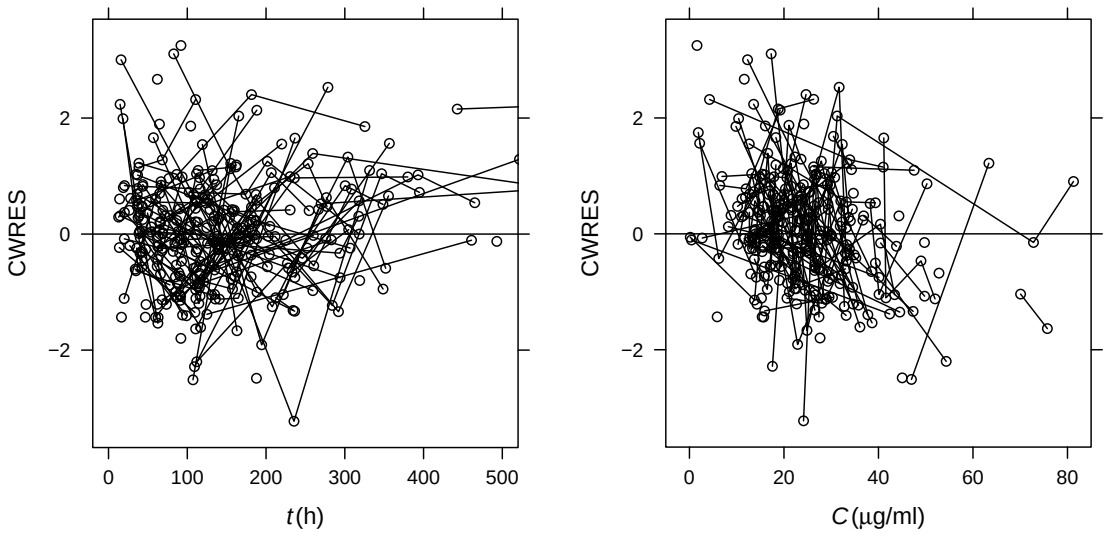

Figure 5.8: Conditional weighted residuals (CWRES) versus time (left panel) and predicted plasma concentrations (right panel) for the final one-compartment model of Eqs. (5.8) and (5.9).

measured samples per patient (see Sec. 5.1.1).

Conditional weighted residuals are plotted in Fig. 5.8 versus time (left panel) and predicted plasma concentration (right panel). No substantial model misspecification appears from those plots.

To compare predictions on patients with different dosage regimen, sampling time, and possibly different variability, visual predictive checks were corrected for prediction and variance and plotted in Fig. 5.9. To construct vpcVPC, 1000 simulations were performed starting from 1000 bootstrap sets of estimated parameters, as described above. No significant difference between model predictions and simulations appears from this plot. However, simulated confidence intervals are quite wide.

Extended NPDE of η_k and η_V EBE and CWRES were constructed using PsN and NONMEM. In Fig. 5.10 I report their distributions (left panels) and compare their empirical quantiles versus the theoretical quantiles of the normal distribution. The p-values of Wilcoxon (W), Kolmogorov–Smirnov (KS), and Shapiro–Wilk (SW) tests are reported in Table 5.8. The agreement between simulated and theoretical distributions is good and the confidence envelope of the observed quantiles always contains the bisector. Means and variances of the empirical NPDE are not significantly different from 0 and 1, except for the W test for CWRES is mildly significant. The Shapiro–Wilk test for normality is not significant for the CWRES and mildly significant for the two EBE distributions.

Three simulations were used to construct mirror plots (Fig. 5.11) of observations versus population predictions (upper panels) and observations versus individual predictions (lower panels).

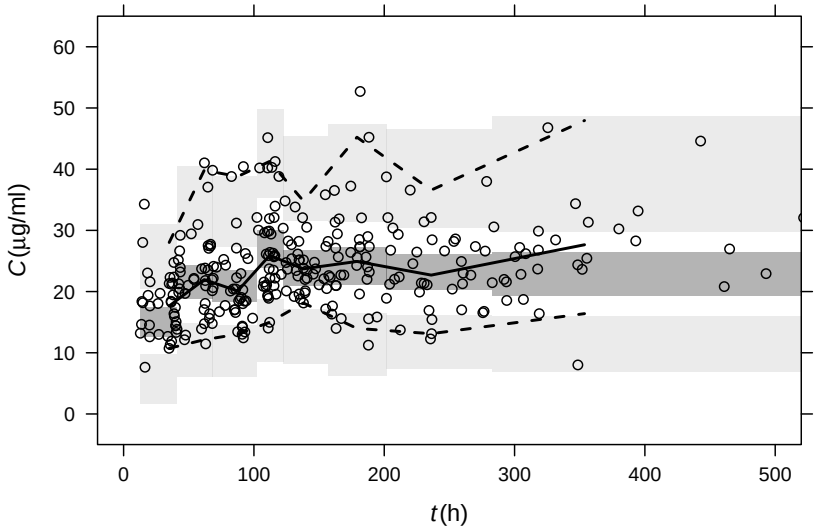

Figure 5.9: Variance and prediction corrected visual predictive checks (vpcVPC) versus time for the final one-compartment model of Eqs. (5.8) and (5.9). The solid line represents the median of the observed variance-prediction corrected plasma concentration and the dark grey area represents a simulation-based 95% confidence interval of the median. The dashed lines represent the 5% and 95% percentiles of the observed variance-prediction corrected plasma concentration and the light grey areas represent the corresponding simulation-based 95% confidence intervals.

NPDE	mean	p (W)	variance	p (KS)	skewness	kurtosis	p (SW)
η_k	-0.084	0.62	0.98	0.58	-0.55	0.30	0.007
η_V	-0.044	0.55	1.07	0.59	-0.13	0.82	0.012
CWRES	0.147	0.02	0.96	0.91	0.17	0.38	0.13

Table 5.8: Mean, variance, skewness, and kurtosis of EBE and CWRES NPDEs and p-values of Wilcoxon (W) test for zero-mean, Kolmogorov–Smirnov (KS) test for gaussian distribution with mean equal to the sample mean and unit-variance, and Shapiro–Wilk (SW) test for normality.

Comparison with Fig. 5.7 shows that there is no apparent issue with the variance-covariance structure.

These analyses show that the model correctly describes data. It is correctly specified, both in term of population model structure and error structure, and properly predicts the observed concentrations on the development sample. However, the width of the confidence intervals of the predictions is still too large to make this model usable in every-day clinical practice. Possible clinical utilisations of this model will be widely discussed with two examples in Sec. 5.4. The high value of the shrinkage suggests that a study with a higher number of observations per patient should be conducted to construct a model offering more reliable and precise predictions.

5.2.3 External validation

The model was validated on data from 63 patients from 5 ICUs (see Table 5.2). Measured plasma vancomycin concentrations versus population and individual predictions, CWRES versus

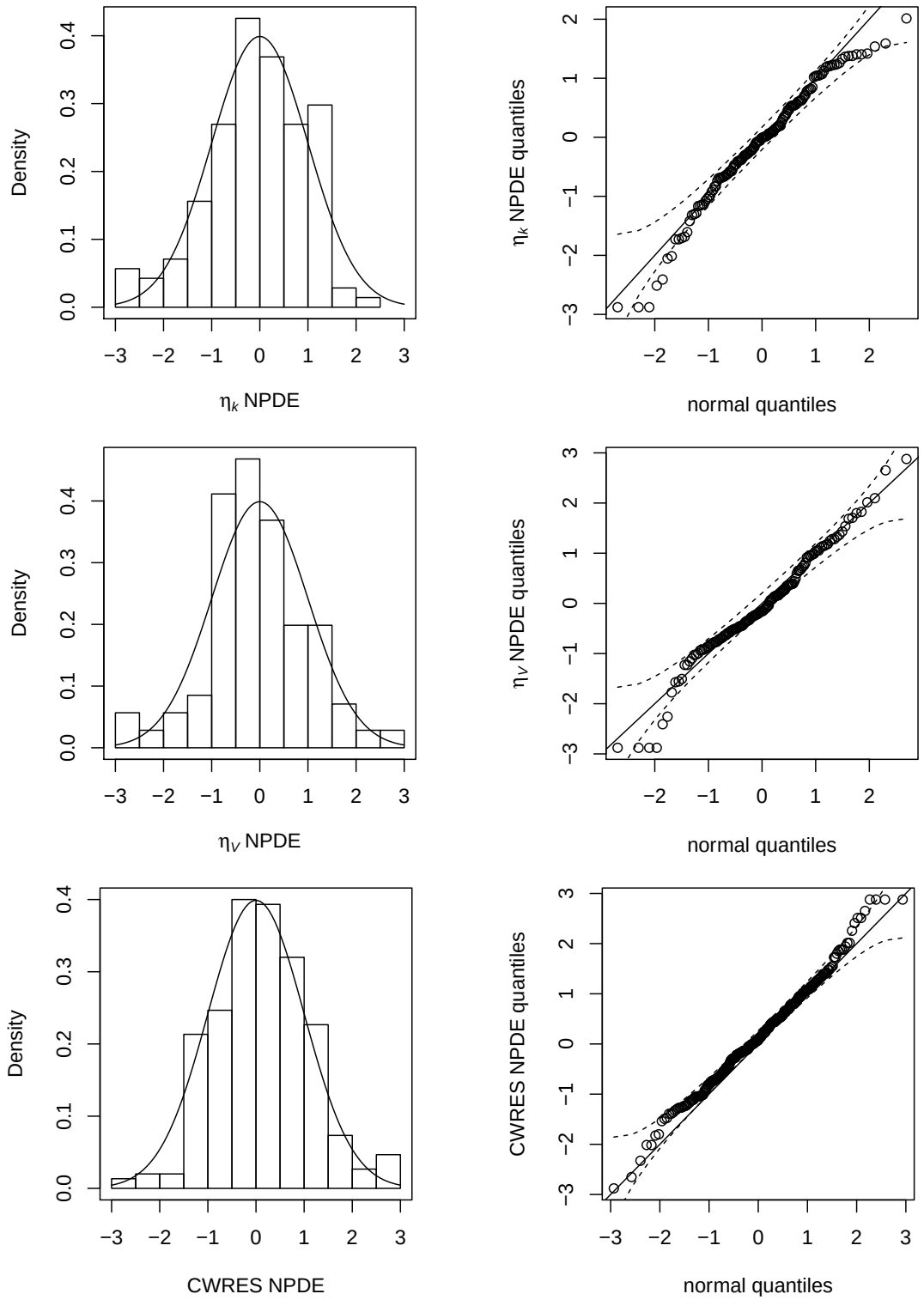

Figure 5.10: Extended normalised predicted distribution error (NPDE) for the final one-compartment model of Eqs. (5.8) and (5.9): η_k (upper panels) and η_V (central panels) EBE NPDE, and CWRES NPDE (lower panels). Left panels: probability density of the simulated empirical distributions (histogram) and of the normal distribution (solid line). Right panels: QQ plots comparing the quantiles of the simulated NPDE versus the theoretical normal quantiles (right panels). Dashed lines represent the 95% confidence interval. The solid line is the bisector. Results of formal tests are reported in Table 5.8.

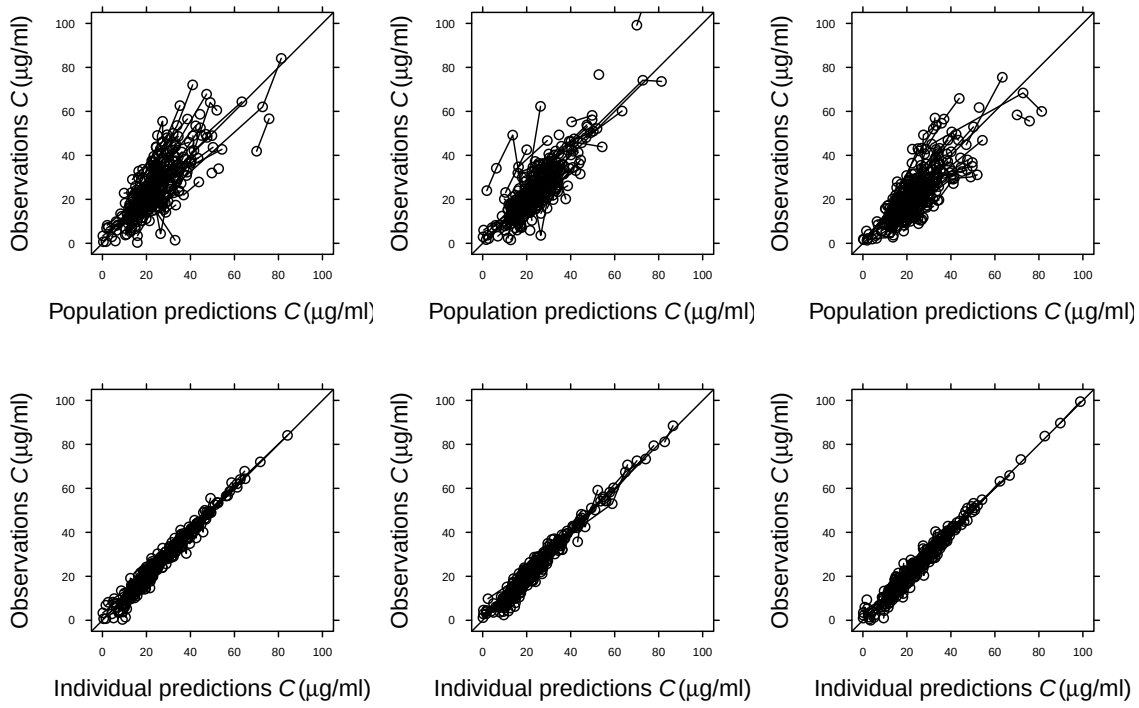

Figure 5.11: Mirror plots of observations versus population predictions (upper panels) and individual predictions (lower panels) for three simulated datasets using the final one-compartment model of Eqs. (5.8) and (5.9).

NPDE	mean	p (W)	variance	p (KS)	skewness	kurtosis	p (SW)
η_k	0.066	1.0	1.5	0.61	0.37	0.19	0.23
η_V	-0.31	0.02	1.3	0.05	-0.22	1.8	< 0.001
CWRES	0.16	0.003	0.81	0.02	0.21	1.3	< 0.001

Table 5.9: Mean, variance, skewness, and kurtosis of EBE and CWRES NPDEs and p-values of Wilcoxon (W) test for zero-mean, Kolmogorov–Smirnov (KS) test for gaussian distribution with mean equal to the sample mean and unit-variance, and Shapiro–Wilk (SW) test for normality on the validation set.

time, and CWRES versus predicted concentrations are plotted in Fig. 5.12. In Fig. 5.13 I report variance and prediction corrected VPC. NPDE for EBE and CWRES are reported in Fig. 5.14 along with the results of formal statistical tests for normality in Table 5.9.

As expected, discrepancy between observations and predictions (upper panels of Fig. 5.12) is slightly larger for individual predictions than in the development dataset (Fig. 5.7), whereas it is similar for population predictions. The standard deviation of the difference between population predictions and observations is indeed 8.5 μg/ml, comparable with the discrepancy observed in the development sample. The number of observations included in the 95%-confidence interval of population predictions is 93.1%, compatible with a fraction of type I error of 5%.

CWRES are distributed homogeneously with time but a small bias in CWRES appears in the right lower panel of Fig. 5.12, suggesting that the model underestimates plasma concentrations

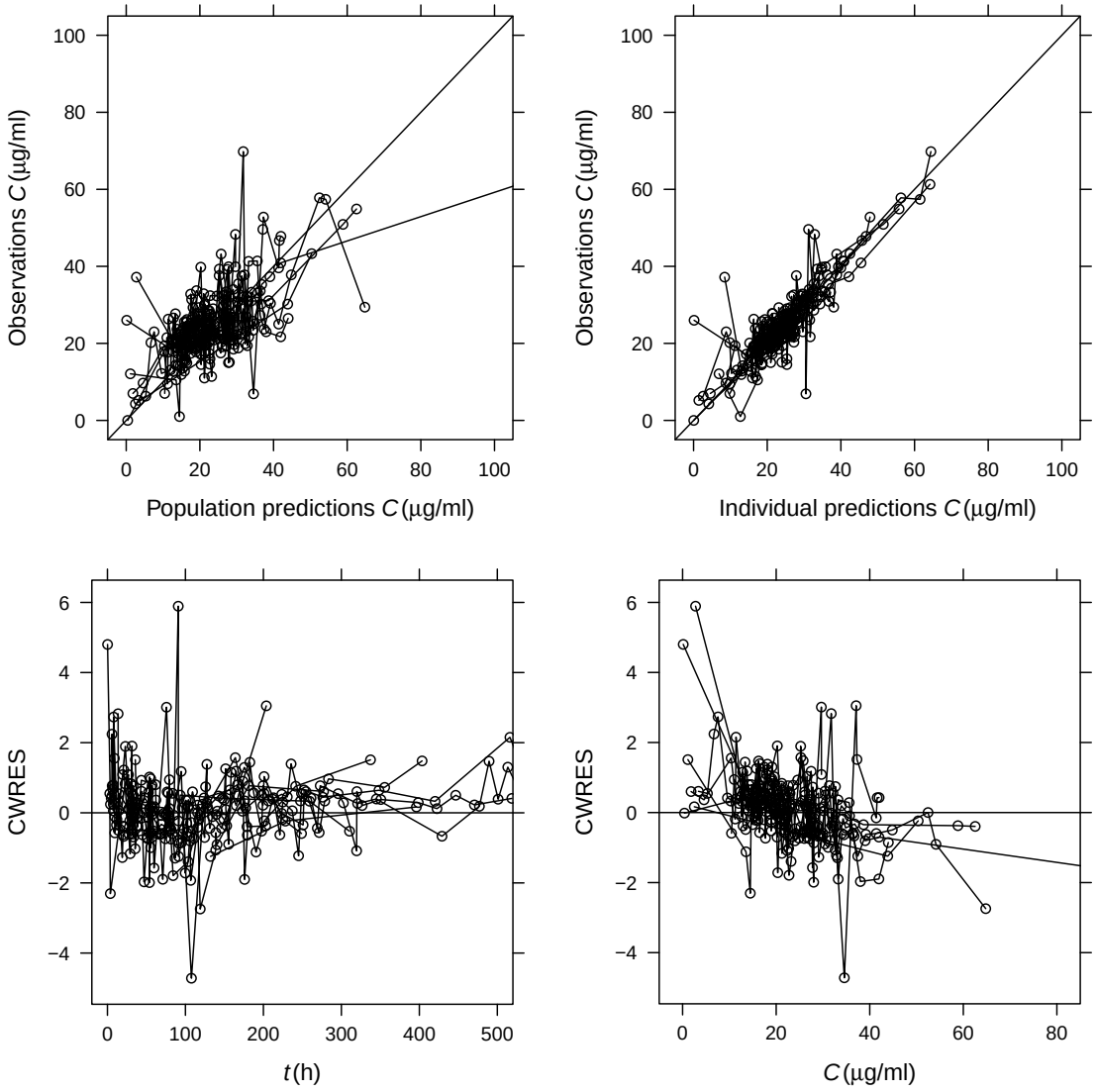

Figure 5.12: Measured plasma vancomycin concentrations versus population predictions (left upper panel), individual predictions (right upper panel), CWRES versus time (left lower panel) and predicted plasma concentrations (right lower panel) for the final one-compartment model of Eqs. (5.8) and (5.9) on the validation set.

at very low concentrations, and overestimates it at high concentrations. Variance and prediction VPC confirms that the agreement between predictions and observations is fair. However, confidence intervals are wide and the agreement worsens at very large times ($t > 300\,\text{h}$) after the first drug administration.

Although the overall agreement between predictions and observations is good, some discrepancy appears when looking at the distribution of the random parameters (see Fig. 5.14). Inter-subject variability of drug clearance is properly modelled, as proved by the normal distribution of NPDE of η_k. The other NPDEs, in particular for the EBE of V, deviate from the normal distribution. This issue may be associated with the poor capacity of the model of describing inter-subject variability

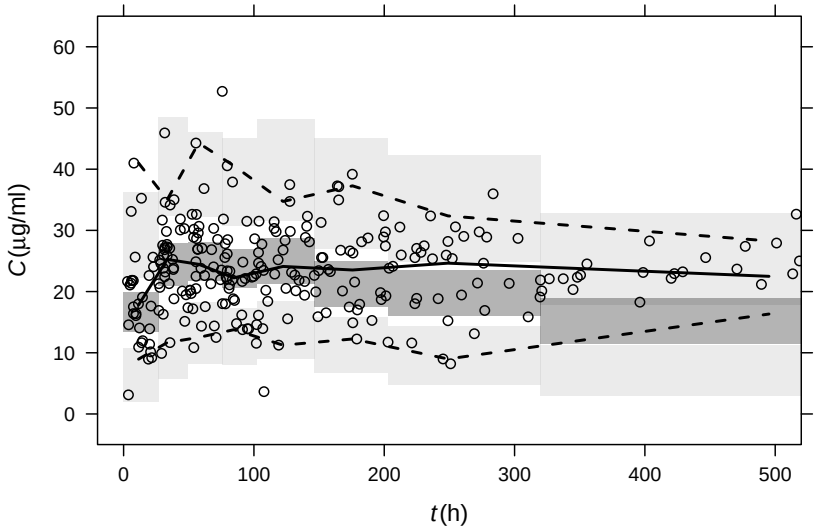

Figure 5.13: Variance and prediction corrected visual predictive checks (vpcVPC) versus time for the final one-compartment model of Eqs. (5.8) and (5.9) on the validation set. See caption of Fig. 5.9.

of the distribution volume V (only one covariate was included in Eq. 5.9). This generates a larger residual variability that does not follow a simple lognormal distribution as assumed in Eq. (5.11).

5.2.4 Clinical interpretation

In this model one can envisage several aspects of the pharmacokinetics of vancomycin presented in Chaps. 2 and 3. Since vancomycin is mostly eliminated by the kidneys, drug clearance strongly depends on renal function, which is parametrised in the model by creatinine clearance. Patients with severe renal failure have low renal clearance but they undergo renal replacement therapy. In these patients drug clearance is mainly due to CRRT.

The renal capacity of eliminating vancomycin appears to be modulated also by age, creatinine plasma concentration, body weight, and VIS. In particular age, creatinine concentration, and weight are known to be correlated with renal function, appearing in the Cockroft–Gault formula for the estimation of the creatinine clerance [50] (see also the correlation matrix in Table 5.6).

The appearance of these factors is however surprising, given that the measured clearance is already included in the model. Although renal clearance is lower in elderly patients and is increased by the administration of vasoactive drugs, one may conjecture that these factors influence both creatinine and vancomycin clearance. Similarly, creatinine and drug concentrations should be affected by the rate of renal removal in exactly the same way. Thus, once creatinine clearance is included in the model, those three variables should not add any further information.

However, creatinine clearance is measured quite rarely, every few days. Conversely, creatinine plasma concentration is measured daily and the times of vasoactive administrations are precisely

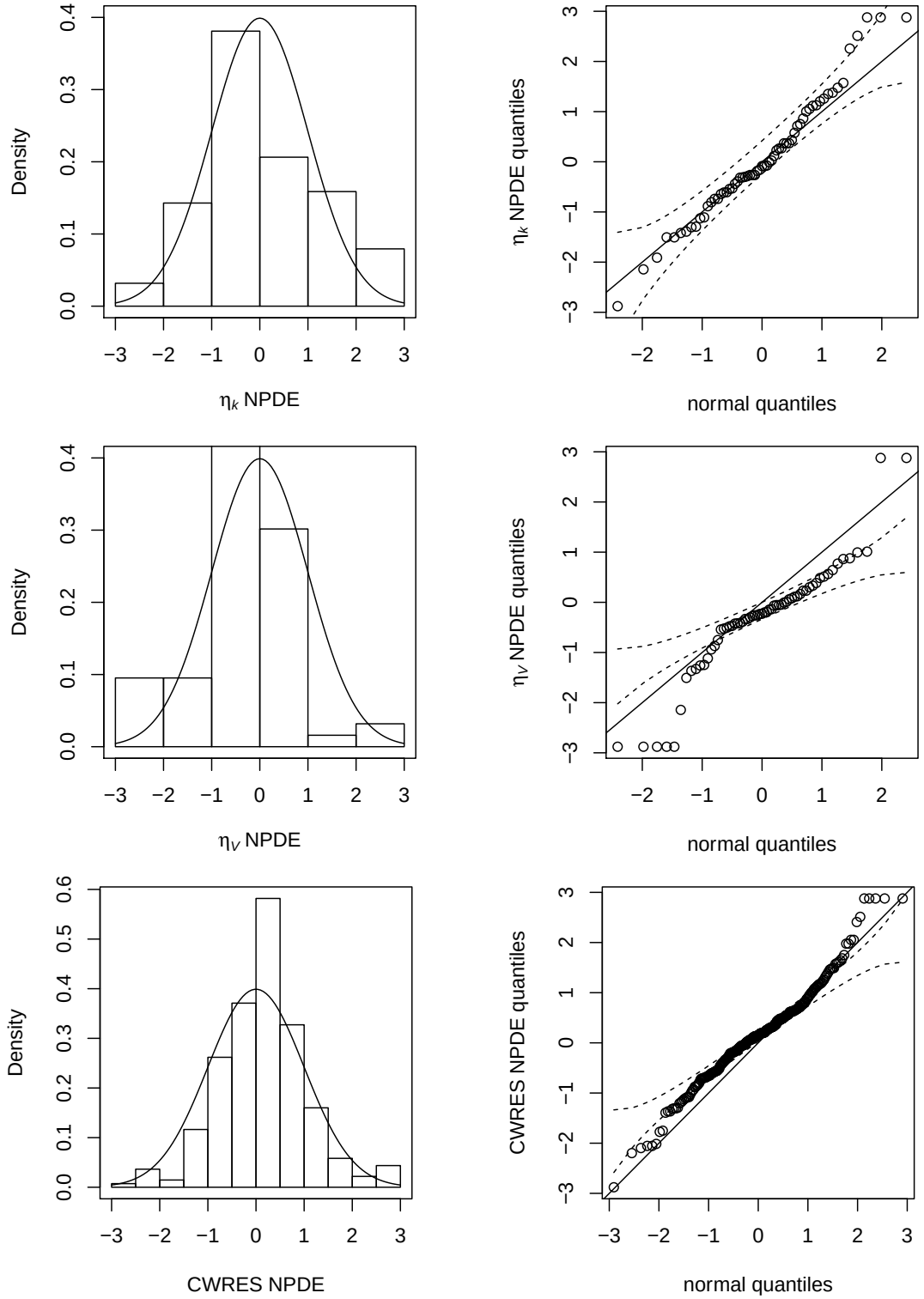

Figure 5.14: Extended normalised predicted distribution error (NPDE) for the final one-compartment model of Eqs. (5.8) and (5.9) on the validation set: η_k (upper panels) and η_V (central panels) EBE NPDE, and CWRES NPDE (lower panels). See caption of Fig. 5.10. Results of formal tests are reported in Table 5.9.

known from *MargheritaTre*. Thus, these two variables are not redundant and do not generate any problem of collinearity in the estimate of the pharmacokinetic parameters. In fact, they contribute to provide information on renal clearance with higher time resolution with respect to the measurements of creatinine clearance. The opposite argument may hold for age. Creatinine clearance may be subject to important variations depending on the patient's condition and measurement errors. The presence of the variable age may contribute to make the estimate of drug clearance more stable and less affected by such fluctuations.

In this model the distribution volume is not as well characterised as clearance, since only creatinine concentration appeared in Eq. (5.9) to explain part of volume variability. One may argue that creatinine concentration is a weak marker of volaemic status and of vessel leakage or of augmented creatinine secretion. Also the interpretation of the term proportional to body weight w in k_{vanco} is not straightforward. It may represent non-renal elimination of vancomycin or residual renal drug elimination still present when creatinine clearance vanishes.

However, these unexpected features may signal either the lack of sufficient data to accurately estimate both k_{vanco} and V or the presence of a problem in the fundamental mathematical structure of the adopted model.

On the one hand, k_{vanco} and V are not properly decoupled: k_{vanco} contains a covariate (the body weight) that would rather be expected to explain volume variability and *vice versa*. Unfortunately, in a simple one-compartment model only the elimination constant $\kappa = k_{\text{drug}}/V$ can be easily estimated by observing time variations in drug concentration (see Sec. 4.1). To properly estimate V and disentangle it from k_{vanco}, it would be necessary to measure C_{vanco} soon after the initial loading dose before the effects of elimination become appreciable.

On the other hand, the term proportional to w in the clearance equation may represent drug accumulation in a second compartment that cannot be modelled by this simple one-compartment model. In the following section I shall address this issue by constructing a two-compartment model.

5.3 Two-compartment model

5.3.1 Model development

Two-compartment models were constructed using NONMEM v.7.4.1, with the FOCE method with interaction, using the ADVAN3 routine. Following the same procedure adopted in building

the one-compartment model I start from a minimal model of the form

$$k_{\text{vanco},i} = \theta_k \, e^{\eta_{k,i}}, \tag{5.13}$$

$$k_{\text{int},i} = \theta_{k_{\text{int}}} \, e^{\eta_{k_{\text{int}},i}}, \tag{5.14}$$

$$V_c = \theta_{V_c} \, e^{\eta_{V_c,i}}, \tag{5.15}$$

$$V_p = \theta_{V_p} \, e^{\eta_{V_p,i}}, \tag{5.16}$$

$$C_{ij} = C(t_{ij})(1 + \varepsilon_{ij}). \tag{5.17}$$

The model parameters of Eqs. 4.14 and 4.15 have been re-parametrised as

$$Q_1 = Q_c, \qquad Q_2 = Q_p, \qquad \kappa_e = \frac{k_{\text{drug}}}{V_c}, \qquad \kappa_{12} = \frac{k_{\text{int}}}{V_c}, \qquad \kappa_{21} = \frac{k_{\text{int}}}{V_p}, \tag{5.18}$$

within the approximation of symmetric membrane [Eq. (4.17)].

Unfortunately, I could not introduce interindividual-variability terms for every pharmacokinetic parameter because data did not support the estimation of all these effects. Indeed, only a few measured values of drug concentration per patient were available. Roughly speaking, in this kind of model it is possible to estimate a number of interindividual-variability terms smaller than the number of observations per subject. Since intra-vascular volume is not expected to vary significantly among patients and inter-compartment clearance should depend only on membrane permeability to vancomycin, I set to zero the interindividual effects associated with the central volume and with k_{int} ($\eta_{V_c} = \eta_{k_{\text{int}}} = 0$). Populations and individual predictions are compared with measured concentrations for the two-compartment minimal model in Fig. 5.15.

Analogous to what I observed for the one-compartment model (Fig. 5.5), the agreement between population predictions and observations was very poor, whereas the individual predictions already provide quite precise estimates of the observed concentrations. The two-compartment model represent a good mathematical model to describe the kinetics of vancomycin, but the four pharmacokinetic parameters need to be estimated as functions of the patients' covariates.

The structural model was constructed by forward selection of covariates as illustrated in Sec. 5.2.1 using the Likelihood ratio test. However, I adopted a slightly different strategy due to the complexity of the two-compartment model in terms of possible combinations between pharmacokinetic parameters and patient variables. Differently from what was done for the one-compartment model, where I tested the best functional forms (additive, proportional, power-laws) for the included variables only at the end of the selection process (see Tables 5.4 and 5.5), here I tested different functional forms for each variable step by step during the forward procedure. All the steps of the construction of the structural model are reported in Table 5.10. In the end I tested

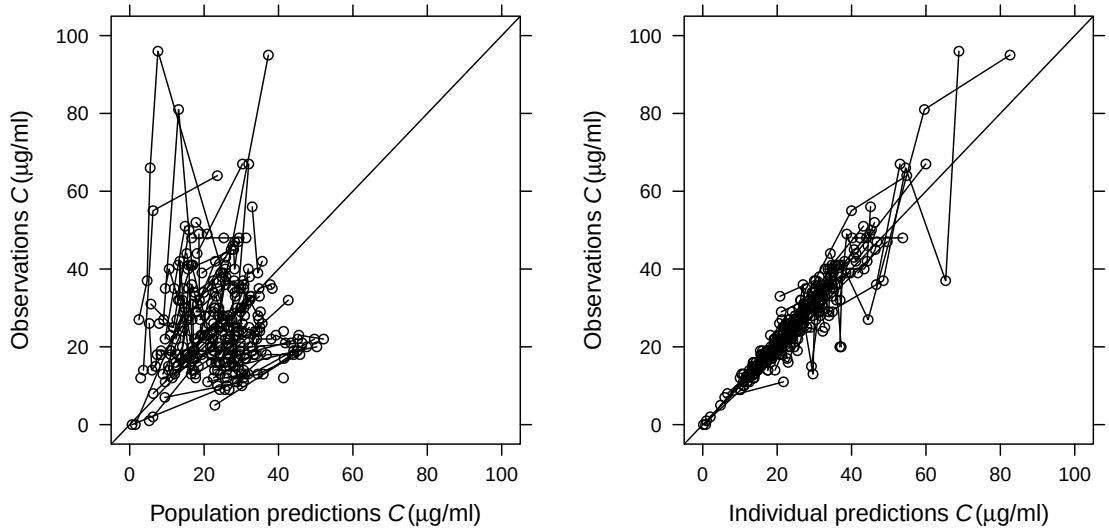

Figure 5.15: Measured plasma vancomycin concentrations versus population (left panel) and individual prediction (right panel). Population predictions are computed evolving Eqs. 4.14 and 4.15 using for all patients the average value of pharmacokinetic parameters $k_{\text{drug}}] = \theta_k$, $k_{\text{int}} = \theta_{k_{\text{int}}}$, $V_c = \theta_{V_c}$, and $V_p = \theta_{V_p}$. Individual predictions are computed taking into account the post-hoc estimates of $\eta_{k,i}$ and $\eta_{V_p,i}$ ($\eta_{k_{\text{int}},i} = \eta_{V_c,i} = 0$, see text).

	Model structure	n	OFV
(0)	$k_{\text{vanco}} = \theta_k \qquad k_{\text{int}} = \theta_{k_{\text{int}}}$ $V_c = \theta_{V_c} \qquad V_p = \theta_{V_p}$	4	1674.2
(1)	$k_{\text{vanco}} = \theta_k \left[1 + \theta_{\text{cr}} \left(\frac{k_{\text{crea}}}{71\,\text{ml/min}}\right)\right]$ $k_{\text{int}} = \theta_{k_{\text{int}}} \qquad V_c = \theta_{V_c} \qquad V_p = \theta_{V_p}$	5	1517.2
(2)	$k_{\text{vanco}} = \theta_k \left[1 + \theta_{\text{cr}} \left(\frac{k_{\text{crea}}}{71\,\text{ml/min}}\right) + \theta_{\text{CRRT}}\delta_{\text{CRRT}}\right]$ $k_{\text{int}} = \theta_{k_{\text{int}}} \qquad V_c = \theta_{V_c} \qquad V_p = \theta_{V_p}$	6	1470.8
(3)	$k_{\text{vanco}} = \theta_k \left[1 + \theta_{\text{cr}} \left(\frac{k_{\text{crea}}}{71\,\text{ml/min}}\right) + \theta_{\text{CRRT}}\delta_{\text{CRRT}}\right]$ $k_{\text{int}} = \theta_{k_{\text{int}}} \qquad V_c = \theta_{V_c}$ $V_p = \theta_{V_p} \left(\frac{C_{\text{crea}}}{0.8\,\text{mg/dl}}\right)^{\beta_{\text{crea}}}$	7	1440.3
(4)	$k_{\text{vanco}} = \theta_k \left[1 + \theta_{\text{cr}} \left(\frac{k_{\text{crea}}}{71\,\text{ml/min}}\right) + \theta_{\text{CRRT}}\delta_{\text{CRRT}}\right]$ $k_{\text{int}} = \theta_{k_{\text{int}}} \qquad V_c = \theta_{V_c}$ $V_p = \theta_{V_p} \left(\frac{C_{\text{crea}}}{0.8\,\text{mg/dl}}\right)^{\beta_{\text{crea}}} \left(\frac{w}{76.5\,\text{kg}}\right)$	7	1426.9

(5)	$k_{\text{vanco}} = \theta_k \left[1 + \theta_{\text{cr}} \left(\frac{k_{\text{crea}}}{71\,\text{ml/min}}\right) + \theta_{\text{CRRT}}\delta_{\text{CRRT}}\right]$ $k_{\text{int}} = \theta_{k_{\text{int}}} \log\left(\frac{C_{\text{ALT}}}{\text{IU/l}}\right)$ $V_c = \theta_{V_c}$ $V_p = \theta_{V_p} \left(\frac{C_{\text{crea}}}{0.8\,\text{mg/dl}}\right)^{\beta_{\text{crea}}} \left(\frac{w}{76.5\,\text{kg}}\right)$	7	1417.4
(6)	$k_{\text{vanco}} = \theta_k \left[1 + \theta_{\text{cr}} \left(\frac{k_{\text{crea}}}{71\,\text{ml/min}}\right) + \theta_{\text{CRRT}}\delta_{\text{CRRT}}\right]$ $k_{\text{int}} = \theta_{k_{\text{int}}} \log\left(\frac{C_{\text{ALT}}}{\text{IU/l}}\right)$ $V_c = \theta_{V_c} \left(\frac{29.4}{h}\right)$ $V_p = \theta_{V_p} \left(\frac{C_{\text{crea}}}{0.8\,\text{mg/dl}}\right)^{\beta_{\text{crea}}} \left(\frac{w}{76.5\,\text{kg}}\right)$	7	1412.0
(7)	$k_{\text{vanco}} = \theta_k \left[1 + \theta_{\text{cr}} \left(\frac{k_{\text{crea}}}{71\,\text{ml/min}}\right) + \theta_{\text{SEX}}\delta_{\text{SEX}} + \theta_{\text{CRRT}}\delta_{\text{CRRT}}\right]$ $k_{\text{int}} = \theta_{k_{\text{int}}} \log\left(\frac{C_{\text{ALT}}}{\text{IU/l}}\right)$ $V_c = \theta_{V_c} \left(\frac{29.4}{h}\right)$ $V_p = \theta_{V_p} \left(\frac{C_{\text{crea}}}{0.8\,\text{mg/dl}}\right)^{\beta_{\text{crea}}} \left(\frac{w}{76.5\,\text{kg}}\right)$	8	1405.4
(8)	$k_{\text{vanco}} = \theta_{\text{cr}} \left(\frac{k_{\text{crea}}}{71\,\text{ml/min}}\right) + \theta_{\text{SEX}}\delta_{\text{SEX}} + \theta_w \left(\frac{w}{76.5\,\text{kg}}\right) + \theta_{\text{CRRT}}\delta_{\text{CRRT}}$ $k_{\text{int}} = \theta_{k_{\text{int}}} \log\left(\frac{C_{\text{ALT}}}{\text{IU/l}}\right)$ $V_c = \theta_{V_c} \left(\frac{29.4}{h}\right)$ $V_p = \theta_{V_p} \left(\frac{C_{\text{crea}}}{0.8\,\text{mg/dl}}\right)^{\beta_{\text{crea}}} \left(\frac{w}{76.5\,\text{kg}}\right)$	8	1401.8
(9)	$k_{\text{vanco}} = \theta_{\text{cr}} \left(\frac{k_{\text{crea}}}{71\,\text{ml/min}}\right) \left(\frac{a}{64\,\text{yr}}\right)^{\beta_a} + \theta_{\text{SEX}}\delta_{\text{SEX}} + \theta_w \left(\frac{w}{76.5\,\text{kg}}\right) + \theta_{\text{CRRT}}\delta_{\text{CRRT}}$ $k_{\text{int}} = \theta_{k_{\text{int}}} \log\left(\frac{C_{\text{ALT}}}{\text{IU/l}}\right)$ $V_c = \theta_{V_c} \left(\frac{29.4}{h}\right)$ $V_p = \theta_{V_p} \left(\frac{C_{\text{crea}}}{0.8\,\text{mg/dl}}\right)^{\beta_{\text{crea}}} \left(\frac{w}{76.5\,\text{kg}}\right)$	9	1384.5
(10)	$k_{\text{vanco}} = \theta_{\text{cr}} \left(\frac{k_{\text{crea}}}{71\,\text{ml/min}}\right) \left(\frac{a}{64\,\text{yr}}\right)^{\beta_a} \left(\frac{h}{29.4}\right) + \theta_{\text{SEX}}\delta_{\text{SEX}} + \theta_w \left(\frac{w}{76.5\,\text{kg}}\right) + \theta_{\text{CRRT}}\delta_{\text{CRRT}}$ $k_{\text{int}} = \theta_{k_{\text{int}}} \log\left(\frac{C_{\text{ALT}}}{\text{IU/l}}\right)$ $V_c = \theta_{V_c} \left(\frac{29.4}{h}\right)$ $V_p = \theta_{V_p} \left(\frac{C_{\text{crea}}}{0.8\,\text{mg/dl}}\right)^{\beta_{\text{crea}}} \left(\frac{w}{76.5\,\text{kg}}\right)$	9	1380.8

	k_{crea}	a	C_{crea}	h	w	$\log(C_{\text{ALT}})$
k_{crea}	1.00	-0.36	-0.50	-0.08	-0.07	0.16
a	-0.36	1.00	0.08	0.12	-0.06	-0.32
C_{crea}	-0.50	0.08	1.00	0.11	0.19	0.05
h	-0.08	0.12	0.11	1.00	0.28	-0.04
w	-0.07	-0.06	0.19	0.28	1.00	0.04
$\log(C_{\text{ALT}})$	0.16	-0.32	0.05	-0.04	0.04	1.00

Table 5.11: Correlation matrix of the continuous variables included in the final two-compartment model of Eqs. (5.19)– (5.22).

$k_{\text{vanco}} = \theta_{\text{cr}} \left(\frac{k_{\text{crea}}}{71\,\text{ml/min}}\right) \left(\frac{a}{64\,\text{yr}}\right)^{\beta_a} \left(\frac{h}{29.4}\right) + \theta_{\text{SEX}}\delta_{\text{SEX}} + \theta_w \left(\frac{w}{76.5\,\text{kg}}\right) + \theta_{\text{CRRT}}\delta_{\text{CRRT}}$		
$k_{\text{int}} = \theta_{k_{\text{int}}} \log\left(\frac{C_{\text{ALT}}}{\text{IU/l}}\right) (1 + \theta_{k_{\text{int}},\text{SEX}}\delta_{\text{SEX}})$	10	1374.9
$V_c = \theta_{V_c} \left(\frac{29.4}{h}\right)$		
$V_p = \theta_{V_p} \left(\frac{C_{\text{crea}}}{0.8\,\text{mg/dl}}\right)^{\beta_{\text{crea}}} \left(\frac{w}{76.5\,\text{kg}}\right)$		

Table 5.10: Development of the structural part of a two-compartment model with the corresponding number of free parameters n and the value of the objective function value, OFV $= -2\mathcal{L}$. Parameters were introduced in the model if the corresponding likelihood ratio test was significant. C_i is the concentration of the molecule i, h the haematocrit. $\delta_{\text{SEX}} = 1$ for male patients and -1 for females. $\delta_{\text{CRRT}} = 1$ if the patient undergoes continuous renal replacement therapy, 0 otherwise.

the significance of all the parameters entered in the model and non-significant parameters were removed. I eventually obtained

$$k_{\text{vanco}} = \theta_{\text{cr}} \left(\frac{k_{\text{crea}}}{71\,\text{ml/min}}\right) \left(\frac{a}{64\,\text{yr}}\right)^{\beta_a} \left(\frac{h}{29.4}\right) + \theta_{\text{SEX}}\delta_{\text{SEX}} + \theta_w \left(\frac{w}{76.5\,\text{kg}}\right) + \theta_{\text{CRRT}}\delta_{\text{CRRT}}, \tag{5.19}$$

$$k_{\text{int}} = \theta_{k_{\text{int}}} \log\left(\frac{C_{\text{ALT}}}{\text{IU/l}}\right) (1 + \theta_{k_{\text{int}},\text{SEX}}\delta_{\text{SEX}}), \tag{5.20}$$

$$V_c = \theta_{V_c} \left(\frac{29.4}{h}\right), \tag{5.21}$$

$$V_p = \theta_{V_p} \left(\frac{C_{\text{crea}}}{0.8\,\text{mg/dl}}\right)^{\beta_{\text{crea}}} \left(\frac{w}{76.5\,\text{kg}}\right), \tag{5.22}$$

where h is the haematocrit, C_{ALT} is the concentration of alanine transaminase, and $\delta_{\text{SEX}} = 1$ for male patients and -1 for females. In Table 5.11 I report the matrix of correlations among variables included in the final model. No covariate with more than 0.5 correlation were selected [30].

Finally, I explored different error models by testing inter-individual random effects on every

parameter	units	value	SD	95% CI
θ_{cr}	ml/min	19.2	2.0	15.3 – 24.1
θ_w	ml/min	12.3	1.0	10.1 – 14.6
θ_{SEX}	ml/min	3.1	0.7	0.09 – 0.27
θ_{CRRT}	ml/min	16.4	3.0	9.1 – 22.5
β_a	–	−0.74	0.15	−1.10 – −0.48
$\theta_{k_{\text{int}}}$	ml/min	10.8	1.5	8.2 – 16.8
$\theta_{k_{\text{int}},\text{SEX}}$	–	−0.28	0.11	−0.50 – 0.08
θ_{V_c}	l	33.7	4.1	21.2 – 42.0
θ_{V_p}	l	140	27	77 – 212
β_{crea}	–	−1.17	0.16	−1.56 – −0.71
$\Omega_{\eta_k\eta_k}$	–	0.038	0.011	0.012 – 0.071
$\Omega_{\eta_{V_p}\eta_{V_p}}$	–	0.67	0.23	0.29 – 1.42
σ_1^2	–	0.008	0.003	0.001 – 0.017
σ_2^2	$(\mu\text{g/ml})^2$	6.4	2.9	0.06 – 11.9

Table 5.12: Best-fit estimates and estimated standard deviations of the parameters of the pharmacokinetic model of Eqs. (5.19)–(5.27). Confidence intervals were computed by bootstrap technique.

pharmacokinetic parameter and various forms (additive, proportional, exponential, and their combinations) for the residual error term. The final model had exponential interindividual variability on clearance and peripheral volume and combined exponential and additive residual variability:

$$k_{\text{vanco},i} = \theta_k \, e^{\eta_{k,i}}, \tag{5.23}$$

$$k_{\text{int},i} = \theta_{k_{\text{int}}}, \tag{5.24}$$

$$V_c = \theta_{V_c}, \tag{5.25}$$

$$V_p = \theta_{V_p} \, e^{\eta_{V_p,i}}, \tag{5.26}$$

$$C_{ij} = C_i(t_{ij}) \, e^{\varepsilon_{1,ij}} + \varepsilon_{2,ij}. \tag{5.27}$$

The best-fit parameters of the structural model and the covariance of random effects are reported in Table 5.12, together with their maximum-likelihood standard deviation. The last column reports the 95% confidence interval of the empirical parameter distribution obtained by constructing 1000 pharmacokinetic models starting from samples bootstrapped with repetition from the original population. In Fig. 5.16 I compare the marginal probability density of each parameter, obtained by a bootstrap technique (histogram), with the corresponding normal distribution (solid line) built with the maximum-likelihood estimates of mean and variance. The agreement between the two distributions is very good except for the variances σ_1^2 and σ_2^2 of the two components (exponential and additive) of the residual variability, whose empirical distributions show strong non-gaussianities. The effect of this non-gaussian distribution on single-patient prediction is investigated in Sec. 5.4.

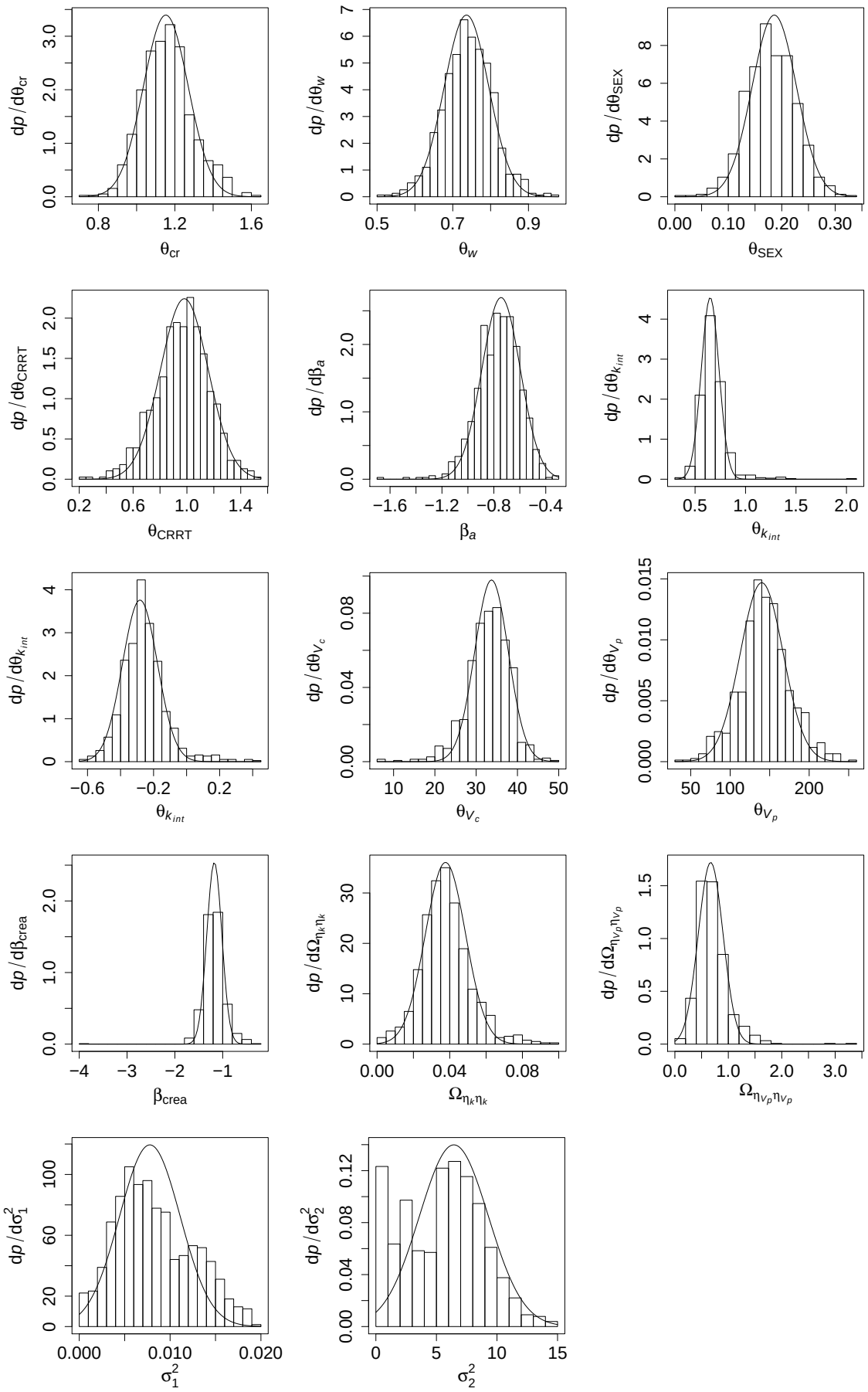

Figure 5.16: Normal distribution with maximum-likelihood estimates of mean and variance of the parameters (solid lines) and bootstrap distribution (histogram) for each parameter of the two-compartment model (see Table 5.12).

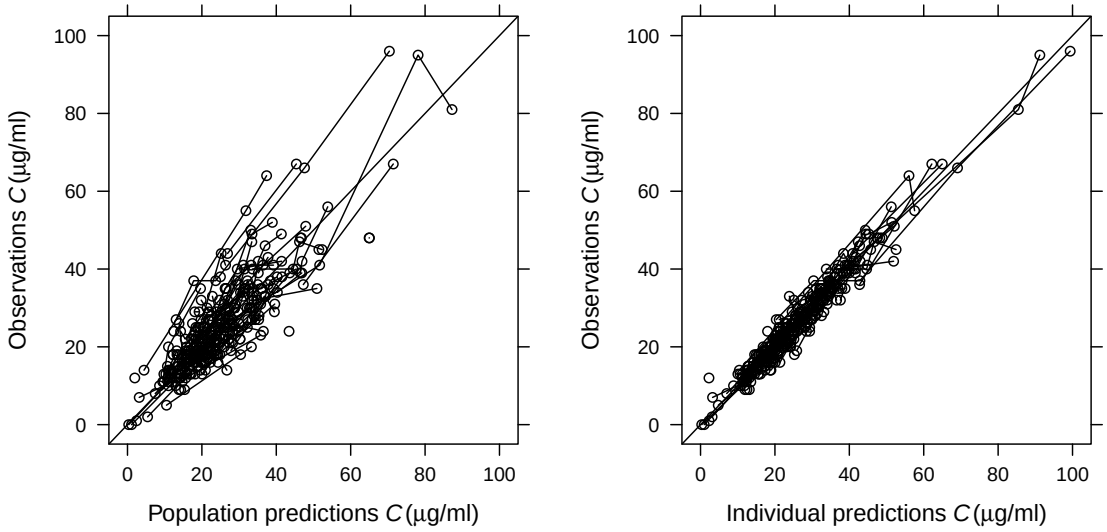

Figure 5.17: Measured plasma vancomycin concentrations versus population (left panel) and individual predictions (right panel) for the final two-compartment model of Eqs. (5.19)–(5.22) with random interindividual and residual variabilities expressed by Eqs. (5.23)–(5.27).

5.3.2 Goodness of fit

In Fig. 5.17, measured drug concentrations are plotted versus population and individual predictions for this final two-compartment model. The concordance between measured concentrations and population predictions has been improved with respect to the minimal model (see Fig. 5.15) thanks to the introduction of patient covariates. Furthermore, the two-compartment model also provides reliable predictions in those few cases in which the one-compartment model failed to reproduce the observed concentrations (left panel of Fig. 5.7). The variability unexplained by patient covariates has also been significantly reduced, as shown in the left panel of Fig. 5.17. However, the unexplained residual variability is slightly higher than in the one-compartment model (Fig. 5.7, right panel). Accordingly, the standard deviation of the difference between observations and population predictions is reduced to 6.9 μg/ml, whereas the standard deviation of the difference with individual predictions (2.8 μg/ml) is slightly larger than in the one-compartment model.

Shrinkage of individual weighted residual is 71%, of η_k is 36%, and of η_{V_p} is 38%. The shrinkage is higher than in the one-compartment model. Again, those high values are probably associated with the low number of measured samples per patient [211] (see Sec. 5.1.1).

Conditional weighted residuals are plotted in Fig. 5.18 versus time (left panel) and predicted plasma concentration (right panel). No model misspecification appears from these plots.

To compare predictions on patients with different dosage regimen, sampling time, and possibly different variability, visual predictive checks were corrected for prediction and variance and plotted in Fig. 5.19. To construct vpcVPC, 1000 simulations were performed starting from 1000 bootstrap

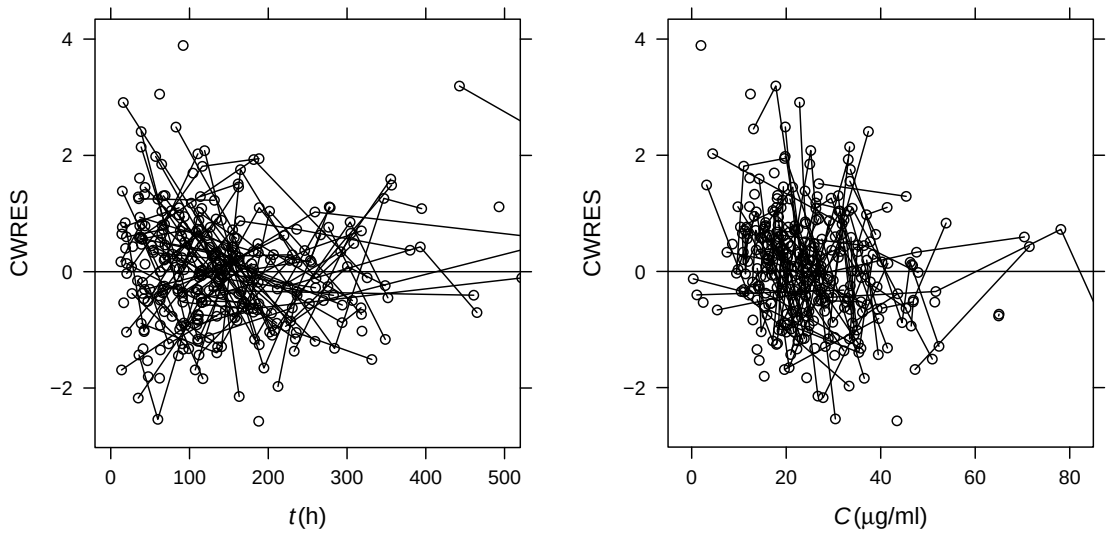

Figure 5.18: Conditional weighted residuals (CWRES) versus time (left panel) and predicted plasma concentrations (right panel) for the final two-compartment model of Eqs. (5.19)–(5.22).

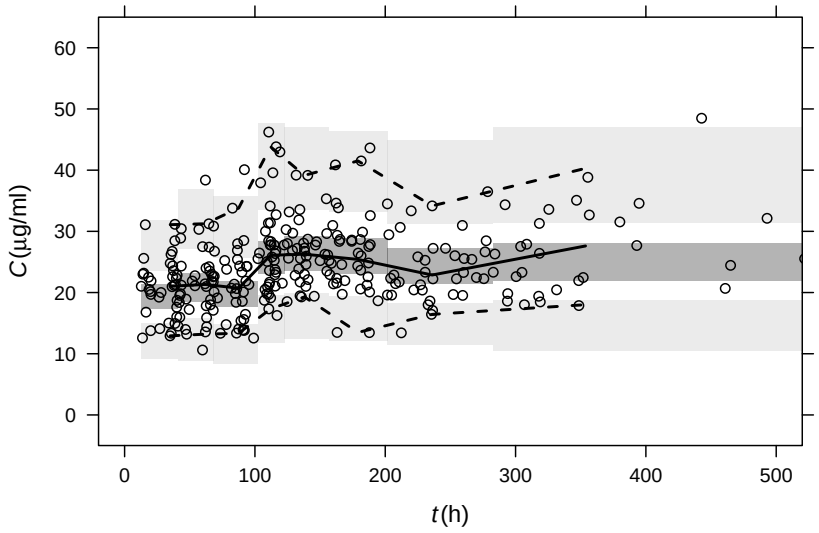

Figure 5.19: Variance and prediction corrected visual predictive checks (vpcVPC) versus time for the final two-compartment model of Eqs. (5.19)–(5.22). The solid line represents the median of the observed variance-prediction corrected plasma concentration and the dark grey area represents a simulation-based 95% confidence interval of the median. The dashed lines represent the 5% and 95% percentiles of the observed variance-prediction corrected plasma concentration and the light grey areas represent the corresponding simulation-based 95% confidence intervals.

sets of estimated parameters, as described above. No significant difference between model predictions and simulations appears from this plot. However, simulated confidence intervals are quite wide.

Extended NPDE of η_k and η_V EBE and CWRES were constructed using PsN and NONMEM. In Fig. 5.20 I report their distributions (left panels) and compare their empirical quantiles versus the theoretical quantiles of the normal distribution. The p-values of Wilcoxon (W), Kolmogorov–

NPDE	mean	p (W)	variance	p (KS)	skewness	kurtosis	p (SW)
η_k	-0.032	0.89	1.05	0.74	-0.43	0.32	0.081
η_{V_p}	-0.029	0.71	1.14	0.78	0.053	0.39	0.41
CWRES	0.092	0.19	0.99	0.87	0.22	0.21	0.15

Table 5.13: Mean, variance, skewness, and kurtosis of EBE and CWRES NPDEs and p-values of Wilcoxon (W) test for zero-mean, Kolmogorov–Smirnov (KS) test for gaussian distribution with mean equal to the sample mean and unit-variance, and Shapiro–Wilk (SW) test for normality for the two-compartment model.

Smirnov (KS), and Shapiro–Wilk (SW) tests are reported in Table 5.13. The agreement between simulated and theoretical distributions is very good and the confidence envelope of the observed quantiles always contains the bisector. Means and variances of the empirical EBE NPDE are not significantly different from 0 and 1. The Shapiro–Wilk test for normality is always non-significant.

Three simulations were used to construct mirror plots (Fig. 5.21) of observations versus population predictions (upper panels) and observations versus individual predictions (lower panels). Comparison with Fig. 5.17 shows that there is no apparent issue with the variance-covariance structure.

Similarly to what observed for the one-compartment model (see Sec. 5.2), these analyses show that the model fairly describe data. It is correctly specified, both in term of population model structure and error structure. The population predictions are closer to the observations than in the one-compartment model but the width of the confidence intervals of the predictions is slightly larger. There is no striking advantage with respect to the simpler model constructed in Sec. 5.2. Higher number of observations per patient would be required to appreciate the difference between the two models.

5.3.3 External validation

This model was validated on the same validation set used to validate the one-compartment model (see Table 5.2). Measured plasma vancomycin concentrations versus population and individual predictions, CWRES versus time, and CWRES versus predicted concentrations are plotted in Fig. 5.22. In Fig. 5.23 I report variance and prediction corrected VPC. NPDE for EBE and CWRES are reported in Fig. 5.24 along with the results of formal statistical tests for normality in Table 5.14.

Similarly to what observed for the one-compartment model, discrepancy between observations and predictions (upper panels of Fig. 5.22) is slightly larger for individual predictions than in the development dataset (Fig. 5.17), whereas it is similar for population predictions. The standard deviation of the difference between population predictions and observations is indeed 9.4 μg/ml,

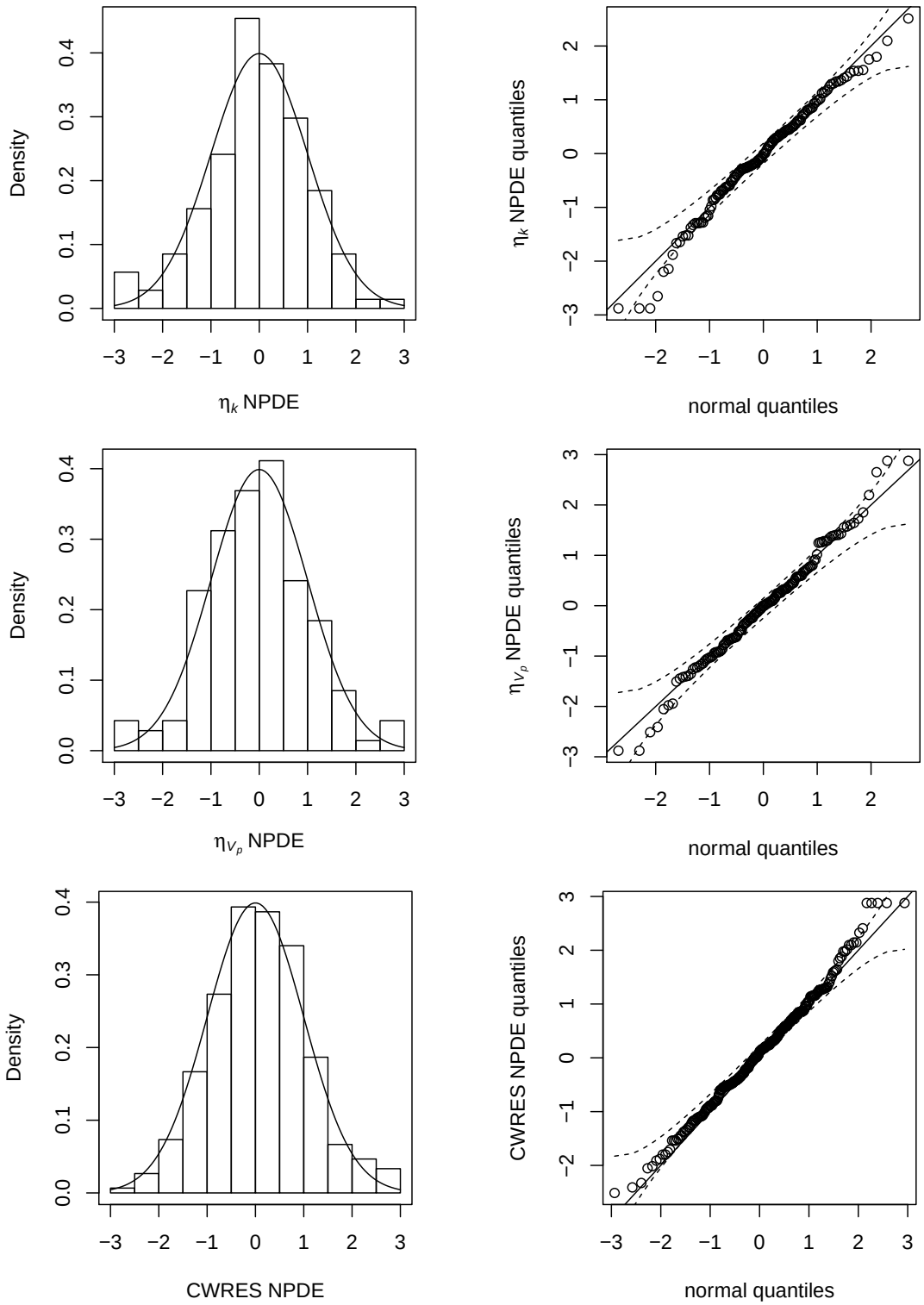

Figure 5.20: Extended normalised predicted distribution error (NPDE) for the final two-compartment model of Eqs. (5.19)–(5.22): η_k (upper panels) and η_{V_p} (central panels) EBE NPDE, and CWRES NPDE (lower panels). Left panels: probability density of the simulated empirical distributions (histogram) and of the normal distribution (solid line). Right panels: QQ plots comparing the quantiles of the simulated NPDE versus the theoretical normal quantiles (right panels). Dashed lines represent the 95% confidence interval. The solid line is the bisector. Results of formal tests are reported in Table 5.13.

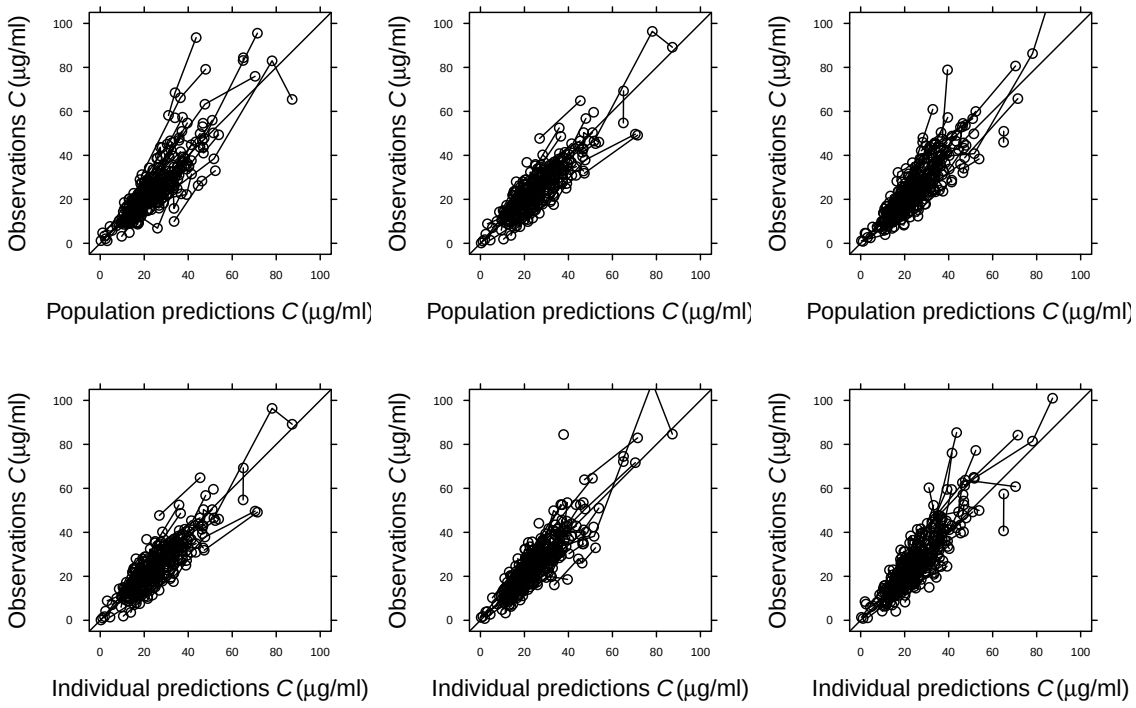

Figure 5.21: Mirror plots of observations versus population predictions (upper panels) and individual predictions (lower panels) for three simulated datasets using the final two-compartment model of Eqs. (5.19)–(5.22).

NPDE	mean	p (W)	variance	p (KS)	skewness	kurtosis	p (SW)
η_k	-0.13	0.20	2.6	0.008	0.36	-0.66	< 0.001
η_{V_p}	-0.20	0.15	3.5	< 0.001	0.16	-0.97	< 0.001
CWRES	0.13	0.001	0.91	0.004	0.22	1.2	< 0.001

Table 5.14: Mean, variance, skewness, and kurtosis of EBE and CWRES NPDEs and p-values of Wilcoxon (W) test for zero-mean, Kolmogorov–Smirnov (KS) test for gaussian distribution with mean equal to the sample mean and unit-variance, and Shapiro–Wilk (SW) test for normality on the validation set for the two compartment model.

comparable with the discrepancy observed in the one-compartment model. The number of observations included in the 95%-confidence interval of population predictions is 90.8%, lower than expected.

CWRES are distributed quite homogeneously with time but a small bias in CWRES appears at large times $t \gtrsim 250\,\mathrm{h}$ and in the right lower panel of Fig. 5.12, suggesting that the model underestimates plasma concentrations at very low concentrations, and overestimates it at high concentrations. Variance and prediction VPC shows that the agreement between the distribution of predictions and observations is not optimal, especially at low concentrations. Furthermore, confidence intervals are wide and the agreement worsens at very large times ($t > 300\,\mathrm{h}$). Significant discrepancies appear in the distribution of the random parameters (see Fig. 5.14). Deviations from normal distribution are stronger than in the one-compartment model.

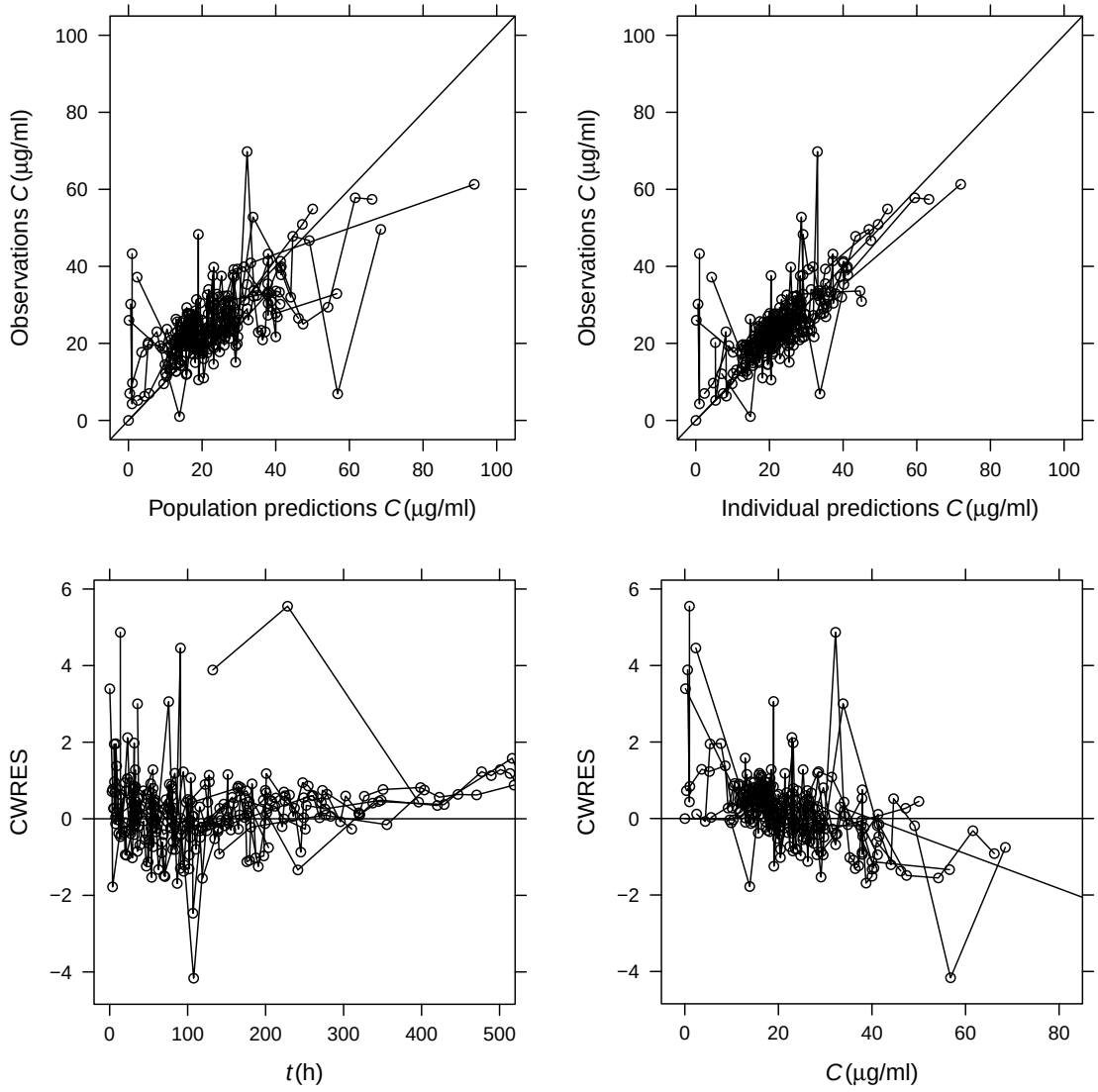

Figure 5.22: Measured plasma vancomycin concentrations versus population predictions (left upper panel), individual predictions (right upper panel), CWRES versus time (left lower panel) and predicted plasma concentrations (right lower panel) for the final two-compartment model of Eqs. (5.19)–(5.22) on the validation set.

Even if the goodness of fit of the two-compartment model on the development sample is good, the results of the external validation are worse for the two-compartment model than for the one-compartment one, suggesting that this model is probably overparametrised.

5.3.4 Clinical interpretation

Covariates entered this two-compartment model in a very similar way to what was obtained for the one-compartment model (see Table 5.4), confirming the robustness of the adopted approach and the reliability of the one-compartment approximation. The most important factors affecting drug clearance [Eq. (5.19)] are again creatinine clearance, total body weight, and renal replacement

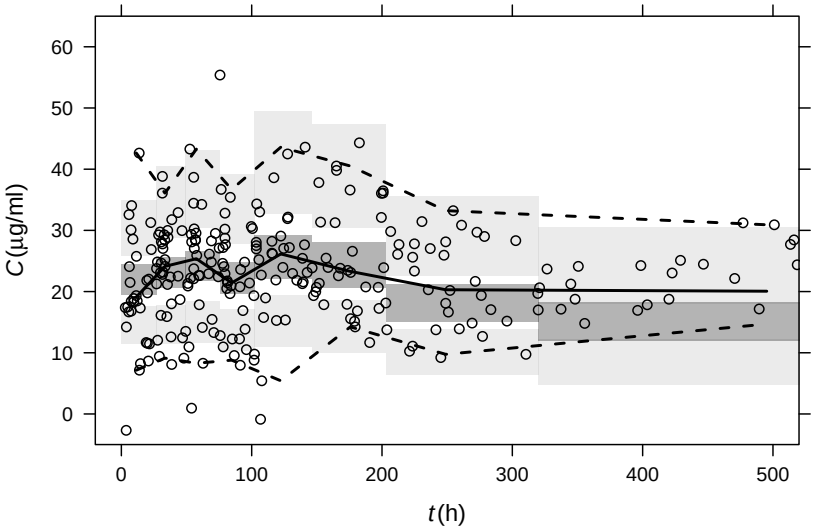

Figure 5.23: Variance and prediction corrected visual predictive checks (vpcVPC) versus time for the final two-compartment model of Eqs. (5.19)–(5.22) on the validation set. See caption of Fig. 5.19.

therapy. A new additive term depending on sex entered the expression for k_{vanco}. As expected, clearance is higher for males than females. The term proportional to creatinine clearance is modulated by age and haematocrit. Although these variables are expected to be correlated to creatinine clearance [50] (see Table 5.11), they are not redundant and provide extra-information to the model since they are measured with different frequency (see Sec. 5.2.4).

The inter-compartment clearance k_{int} [Eq. (5.20)], which parametrises the diffusion rate between the central and peripheral compartments [see Eq. (5.18)], depends on sex and on the logarithm of alanine transaminase. The increase of both ALT levels, a marker of liver injury, and drug diffusion rate may have a common origin that explains the correlation between these two variables. For instance, the onset of right-sided heart failure may cause congestion of organs upstream of the right ventricle [71]. This causes both congestive hepatopathy [84] and peripheral oedema, which may be associated with increased inter-compartment clearance.

The central volume V_c [Eq. (5.21)] is inversely proportional to the haematocrit. Assuming that vancomycin can easily diffuse from blood to the extracellular fluid, the central volume represents the total volume of fluid into which vancomycin can diffuse. Thus, haematocrit provides a reasonable estimate of the fluid status: the lower the haematocrit, the higher the amount of fluids.

The peripheral volume V_p [Eq. (5.21)], representing the volume of tissue where vancomycin accumulates, is proportional to total body weight. It also decreases when plasma creatinine concentration increases. A possible explanation of the correlation between V_c and C_{crea} was formulated on page 131. The peripheral volume for a patient with median creatinine concentration (0.8 mg/dl) and median total body weight (76.5 kg) is $V_p = \theta_{V_c} = (140 \pm 27)$ l, about twice as large as the

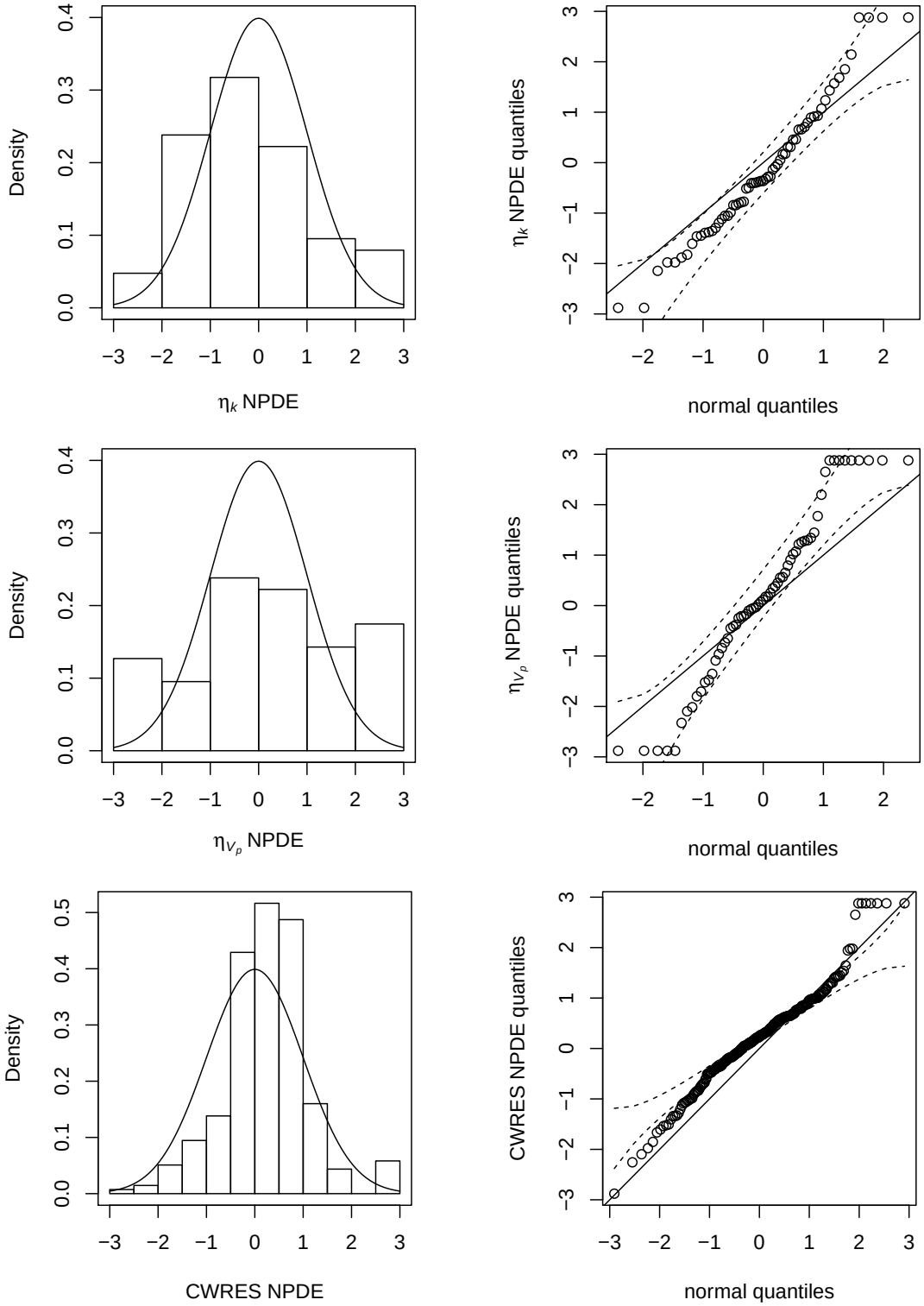

Figure 5.24: Extended normalised predicted distribution error (NPDE) for the final two-compartment model of Eqs. (5.19)–(5.22): η_k (upper panels) and η_{V_p} (central panels) EBE NPDE, and CWRES NPDE (lower panels) on the validation set. See caption of Fig. 5.20. Results of formal tests are reported in Table 5.13.

total body volume. This suggests that vancomycin concentration in tissues is about twice as high as vancomycin concentration in the central compartment [see Eqs. (2.13) and (2.15)].

I concluded Sec. 5.2 observing that the pharmacokinetic parameters in the one-compartment model were not completely decoupled, probably due to the approximated nature of the model. Conversely, the two-compartment model reproduces the physiological processes governing the evolution of vancomycin concentration in a more realistic way. However, only variations of drug clearance are well explained by patient variables. The model structure of the other pharmacokinetic parameters is richer than in the one-compartment model but still poorer than the equation for drug clearance. Indeed, the estimates of the parameters of Eq. (5.19) are much more precise than those of V_c and V_p and the variance of the inter-individual random effect $\Omega_{\eta_k\eta_k}$ (see Table 5.12) is much smaller than $\Omega_{\eta_{V_p}\eta_{V_p}}$. Even with a two-compartment model, available data do not allow to explain the variations of the distribution volumes as functions of patient covariates. As underlined in Sec. 5.2, in order to obtain more precise estimates of V_c and V_p, it would be necessary to measure C_{vanco} soon after the initial loading dose. To collect the data needed to build more accurate pharmacokinetic models we have started the AbioKin project (see Sec. 5.6).

5.4 Single-patient predictions

Pharmacokinetic models can be used to predict the evolution of drug concentration in patients for a few hours after drug administration and to adjust the dosage regimen accordingly. In this Section I graphically study the performance of the one- and two-compartment models in predicting the plasma vancomycin concentration in the same patients used to develop the model. All the analyses were performed in R v.3.3.3.

5.4.1 Simulated concentrations and graphical representation

In Fig. 5.25 I plot the observed and predicted plasma vancomycin concentrations of one- (left panels) and two-compartment models (right panels) for a 79-year-old female patient. Dots indicate measured concentrations. Solid lines are population expected mean concentrations. They were obtained by integration of the dynamic equation using the typical values of the pharmacokinetic parameters from Eqs. (5.8) and (5.9) for the one-compartment model and Eqs. (5.19)–(5.22) for the two-compartment model.

The dark grey band is the 95% confidence band of this curve. In the top panels, it was constructed by simulating 1000 evolutions of drug concentration by randomly sampling the parameters by a multivariate normal distribution with mean $\hat{\theta}$ and covariance $\text{cov}(\hat{\theta})$, where $\hat{\theta}$ is the vector

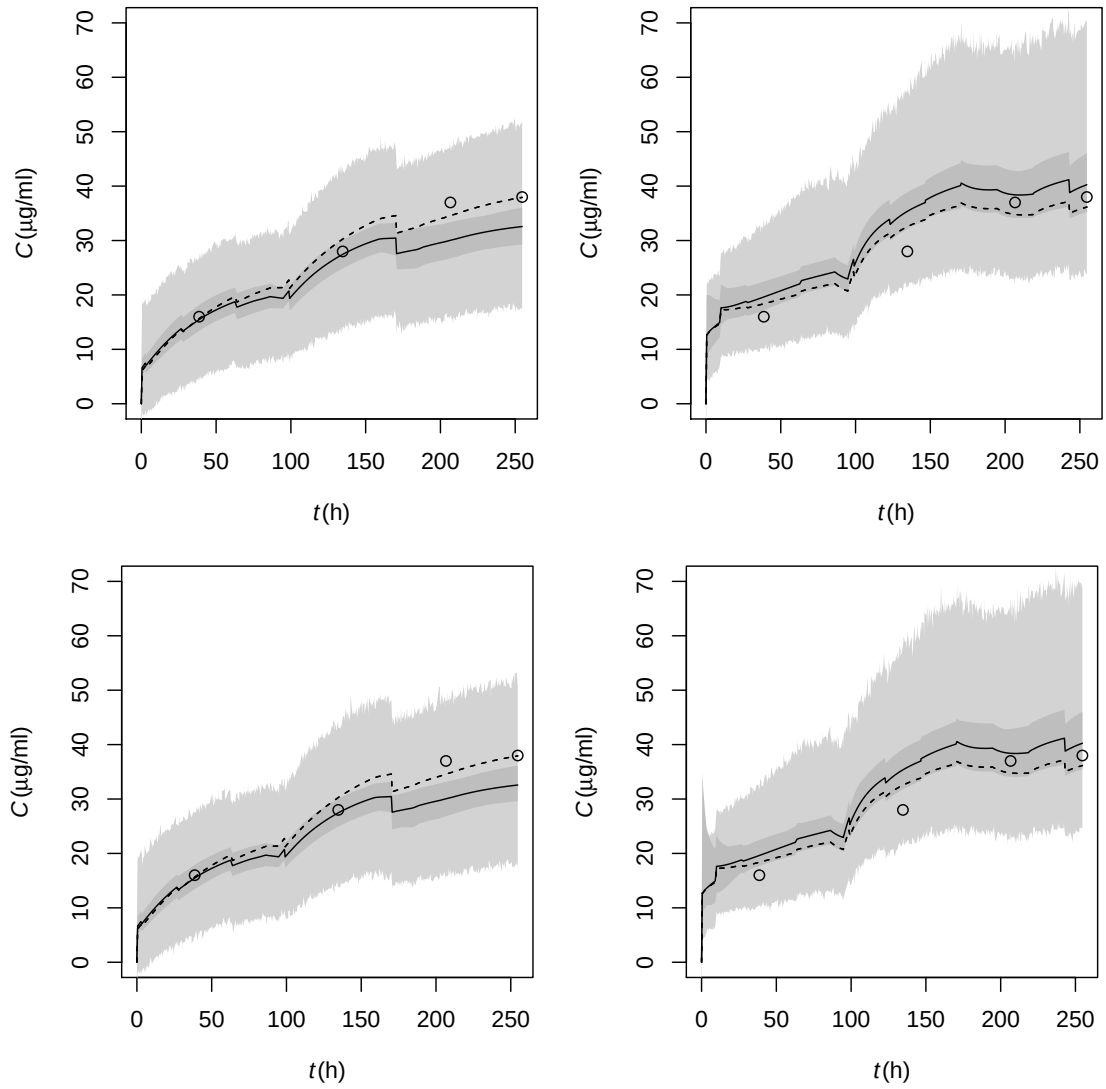

Figure 5.25: Population (solid line) and individual (dashed line) mean predicted concentrations and measured concentrations for a 79-year-old female patient admitted to ICU with a pneumonia and septic-shock, from the first administration of vancomycin ($t = 0$, loading dose) to the last measurement of plasma drug concentration. Dark grey band: 95% confidence interval of the population mean concentration. Light grey: 95% prediction interval for observed concentrations. Left panels: one-compartment model. Right panels: two-compartment model. Upper panels: confidence and prediction intervals are computed with the multivariate normal distribution of the parameters, using the maximum-likelihood estimates of the expected values $(\hat{\theta}, \hat{\Omega}, \hat{\sigma}^2)$ and of their covariance matrix. Lower panels: confidence and prediction intervals are computed with the empirical bootstrap distribution of $(\hat{\theta}, \hat{\Omega}, \hat{\sigma}^2)$.

of the best-fit estimates of the model parameters (see Tables 5.7 and 5.12) and $\text{cov}(\hat{\theta})$ is the maximum-likelihood estimate of the covariance matrix. In the bottom panels, 1000 pharmacokinetic population models were first constructed starting from samples bootstrapped with repetition from the original population. The dark grey band has been drawn by simulating 1000 evolutions of drug concentration, each one constructed from the set of values of θ obtained by a single bootstrapped model. For both models, the width of the confidence-band is quite narrow, confirming that the structural models provide precise estimates of the expected concentrations The evolution

predicted by the two-compartment model is more sensitive to small variations of pharmacokinetic parameters. The shapes and widths of the confidence bands computed with the multivariate normal distributions of the parameters or using their exact bootstrap distributions are similar. This result confirms what was observed in Figs. 5.6 and 5.16 where I compared the marginal empirical and normal distributions of the parameters θ.

The dashed line represents the individual predictions computed evolving the dynamical equations by adjusting the population estimates of the pharmacokinetic parameters with the *post-hoc* estimates of the interindividual random parameters $\eta_{k,i}$ and $\eta_{V,i}$ for the one-compartment model [Eqs. (5.10) and (5.11)] and of $\eta_{k,i}$ and $\eta_{V_p,i}$ [Eqs. (5.23)–(5.26)]. The agreement of the values of observed concentrations with the individual predictions represented by the dashed curve is, of course, stricter than the agreement with population predictions (see also Figs 5.7 and 5.17). Unfortunately, the *post-hoc* values of η_i are available only after concentrations are measured. Thus, the dashed curve cannot be used to formulate predictions of plasma drug concentration for a new patient at the time of drug prescription.

Hence, real-time simulations to support clinicians in designing antibiotic treatments must be built starting from the typical population estimates (solid curve) and constructing appropriate prediction intervals around them. For each realisation of $(\hat{\theta}, \hat{\Omega}, \hat{\sigma})$, from either the multivariate normal or the bootstrap distribution, one must perform the following steps:

1. Compute the values of the population pharmacokinetic parameters from Eqs. (5.8) and (5.9) or Eqs. (5.19)–(5.22), for the one- or two-compartment model, respectively.

2. Sample $\eta_{k,i}$ and $\eta_{V,i}$ (or $\eta_{k,i}$ and $\eta_{V_p,i}$, respectively) from a multivariate normal distribution with zero mean and variance $\hat{\Omega}$ and compute the simulated values of the pharmacokinetic parameters for that realisation of $(\hat{\theta}, \hat{\Omega}, \hat{\sigma})$, using Eqs. (5.10) and (5.11) [Eqs. (5.23)–(5.26), respectively].

3. Evolve the dynamic equations to obtain a simulated curve of drug concentrations with values of the pharmacokinetic parameters determined at step 2.

4. For each time, sample a value of ε_1 and ε_2 from two normal distributions with zero mean and variance $\hat{\sigma}^2_{1,2}$ and insert them in Eq. (5.12) [Eq. (5.12), respectively] to obtain a time series of simulated observed drug concentrations.

Repeating these steps n times (I used $n = 1000$), I obtained for each time t a set of n values of simulated concentrations $\{C_i(t)\}_{i=1,\dots n}$. A prediction interval at 95% confidence level is obtained for $C(t)$ taking, for each t, the 2.5% and 97.5% quantiles of $\{C_i(t)\}_{i=1,\dots n}$. The light grey bands of Fig. 5.25 were eventually built by plotting this confidence interval for every t.

Both covariance-matrix and bootstrap prediction bands are qualitatively similar (compare top and bottom panels). However, the bootstrap prediction band is larger, in particular for the two-compartment model. This is in perfect agreement with the results shown in Fig. 5.16 for the marginal distribution of the random-effect variances σ_1^2 and σ_2^2. The bootstrap distributions of these parameters are indeed strongly non-gaussian and much broader than the corresponding normal distributions. Non-gaussian deviations are much milder for the residual variance σ^2 of the one-compartment model (see Fig. 5.6). I also computed with numerical simulations the number of type-I errors for both constructions. I found that covariance-matrix confidence bands give a higher number of type-I errors with respect to bootstrap-based bands which are more reliable.

Prediction bands of the two-compartment model are larger than bands of the one-compartment model (right versus left panels). Although the two-compartment model seems to more faithfully reproduce drug kinetics at the level of population estimates (solid line) and has a clearer physiological interpretation, it suffers from overfitting more than the one-compartment model, which offers instead more precise predictions in terms of residual variability.

The very same procedure used to construct the prediction interval of $C(t)$ can be adopted to compute the probability of reaching the therapeutic target (in terms of either drug concentration, or more sophisticated PK parameters as $\mathrm{AUC}_{0-24\,\mathrm{h}}$) for given patient conditions and dosage regimen.

5.4.2 Clinical relevance

Individual plots of the evolution of vancomycin concentrations are useful not only to simulate drug kinetics to adjust dosage regimens, but also as tools to critically review adopted administration strategies in clinical case reports. They allow clinicians to review clinical practice, identify commonly adopted strategies, and improve internal protocols. Indeed, the curve of individual predictions (dashed line in Fig. 5.25) is the best approximation of the evolution of plasma drug concentration. It offers a sort of continuous interpolation of the measured concentrations based on the population pharmacokinetic model and adjusted to a single patient, thanks to the *post-hoc* estimates of the interindividual variability.

The curves of Fig. 5.25 refer to a 79-year-old female patient admitted to ICU with pneumonia and septic-shock. Microbiological analysis at ICU admission revealed an infection caused by *Streptococcus pneumoniae*, initially treated with ceftriaxone and levofloxacin for 15 days. After isolation of a methicillin-resistant *Staphylococcus aureus*, the antibiotic therapy was suspended and treatment with vancomycin (loading dose followed by continuous infusion) was started on the 17^{th} day after ICU admission ($t = 0$) and eventually suspended on the 28^{th} day. During the administration of vancomycin, plasma drug concentration was measured four times, the last one on the 28^{th} day ($t = 254\,\mathrm{h}$).

Both the one- and two-compartment models agree on the fact that the loading dose (500 mg) was not sufficient to reach the target therapeutic concentration of about 20–30 μg/ml (see Chap. 5), even though the values of vancomycin concentrations estimated by the two models after the bolus were quite different, about 8 μg/ml and 15 μg/ml, respectively. The loading dose is followed by a continuous infusion with a rate of 42 mg/h. The first measured value of drug concentration [$C(t = 39\,\text{h}) = 16\,\mu\text{g/ml}$] was likely judged too low and the rate of continuous infusion was increased to 80 mg/h at $t = 95$ h. This apparently yielded a quite satisfactory value of drug concentration at the second measurement [$C(t = 135\,\text{h}) = 28\,\mu\text{g/ml}$]. However, C kept growing in the following hours up to values of 37 μg/ml and 38 μg/ml, measured at $t = 206$ h and $t = 254$ h, respectively.

Fig. 5.25 helps to interpret what happened. The initial infusion rate (42 mg/h) was probably appropriate for this patient since her renal clearance was quite low ($k_{\text{crea}} = 43$ ml/min). However, the time scale τ to converge to the stationary solution is inversely proportional to drug clearance ($\tau = 1/\kappa_e = V/k_{\text{drug}}$ in the one-compartment approximation). Thus, in this patient τ is more than twice as large as the respective value for a patient with normal renal function. Hence, when drug concentration was measured at $t = 38$ h, the stationary state had not yet been attained. Indeed, drug concentration continued to increase, reaching an almost stationary value of about 20 μg/ml, even before the change in the infusion rate at $t = 95$ h. The new rate (80 mg/h) was twice as high as the old one. Accordingly, the corresponding stationary concentration, about 40 μg/ml, was twice as high as the previous stationary concentration (20 μg/ml).

The analysis of this case shows that the initial infusion rate was correctly adjusted (1 g/day), according to the reduced renal function. However, it was probably not realised that the time to reach the stationary state is roughly inversely proportional to renal clearance. In patients with renal failure it is fundamental to administer the appropriate loading dose, otherwise it could take days to reach the stationary concentration by means of continuous infusion only. When it was noticed that drug concentration was too low, the clinicians should have administered a second small loading dose, maintained the same continuous infusion rate, rather than increasing the infusion rate to 2 mg/d.

In Fig. 5.26 I present a further example. As in Fig. 5.25, prediction curves were constructed with the one- and two- compartment model in the left and right panel, respectively. Confidence and prediction bands were constructed using the bootstrap-based distribution of estimated parameters ($\hat{\theta}$, $\hat{\Omega}$, $\hat{\sigma}^2$), as illustrated in Sec. 5.4.1.

The plots report the evolution of plasma vancomycin concentration in a 48-year-old female patient receiving haemofiltration. The patient was admitted to the ICU in a shock condition following a pneumonia. Both H1N1 influenza and methicillin-resistant *Staphylococcus aureus* tests

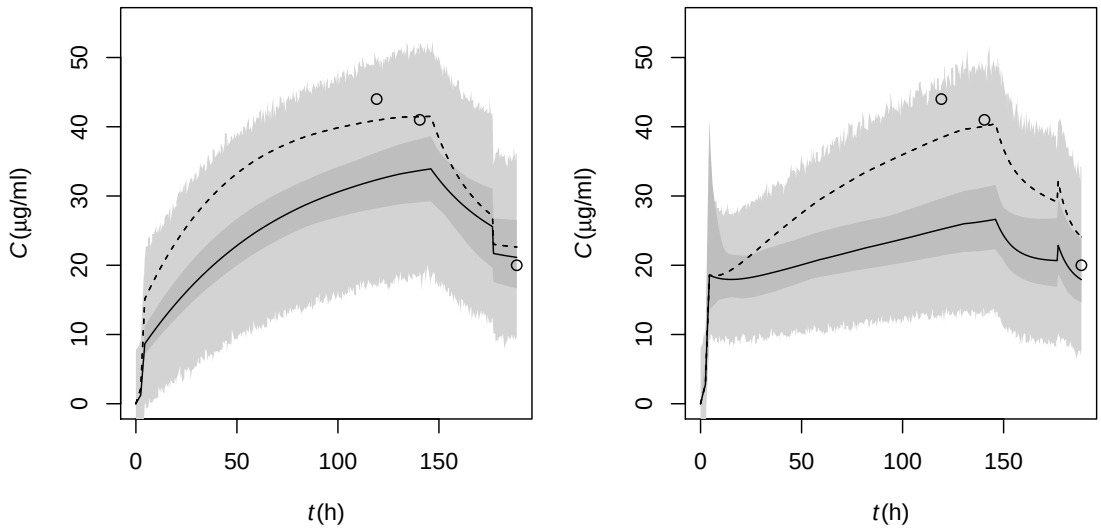

Figure 5.26: Population (solid line) and individual (dashed line) mean predicted concentrations, obtained with the one- (left panel) and two-compartment model (right panel), and measured concentrations for a 48-year-old female patient with pneumonia receiving continuous renal replacement therapy starting at $t = 146\,\text{h}$ after the first administration of vancomycin ($t = 0$, loading dose) and continuing after the last measurement of plasma drug concentration. Dark grey band: 95% confidence interval of the population mean concentration. Light grey: 95% prediction interval for observed concentrations. Confidence and prediction bands were computed using the empirical bootstrap distribution of the model parameters $(\hat{\theta}, \hat{\Omega}, \hat{\sigma}^2)$.

were positive. Antibiotic therapy with levofloxacin, linezolid and piperacillin/tazobactam was started on admission. Levofloxacin and piperacillin/tazobactam were suspended on the 10^{th} day after admission. On the 15^{th} day linezolid was suspended due to thrombocytopenia and vancomycin administration started ($t = 0$). Eventually, vancomycin was suspended on the 30^{th} day ($t = 366\,\text{h}$). Plasma vancomycin concentration was measured three times at $t = 119\,\text{h}$, 141 h, and 189 h. The patient started to receive haemofiltration at $t = 146\,\text{h}$.

With respect to the previous patient, in this case the optimal therapeutic concentration was almost attained after the loading dose (500 mg). The value reported by the dashed line just after the administration of the first bolus is indeed about $16\,\mu\text{g/ml}$ in the one-compartment model and $19\,\mu\text{g/ml}$ in the two-compartment one. After the initial bolus, a continuous infusion was started at a rate of 42 mg/h (1 g/d). The patient was however in renal failure and vancomycin concentration increased (dashed line) to about $40\,\mu\text{g/ml}$. When vancomycin concentration was measured both at $t = 119\,\text{h}$ and 141 h, $C = 44\,\mu\text{g/ml}$ and $41\,\mu\text{g/ml}$. After a few hours haemodialysis started, total clearance was increased to normal values, and, consequently, the drug concentration dropped down to about $20\,\mu\text{g/ml}$ (value measured at $t = 189\,\text{h}$).

Although already very low (1 g/d), the rate of continuous infusion was about twice as high as needed, since renal function was extremely compromised. Because of the reduced renal function, the time to reach the stationary state was also extremely long (about four days). Unfortunately, no

measured values of creatinine clearance were available when vancomycin was prescribed. On the one hand, the lack of this information did not allow the appropriate dosage regimen to be chosen. On the other hand it does not permit reliable predictions to be made using the typical population value of drug clearance in either the one- or two-compartment model. This explains the large discrepancy between population (solid line) and individual (dashed line) predictions in Fig. 5.26, where I had to use a single value of creatinine clearance measured a long time after vancomycin administration. Without up-to-date values of laboratory tests and other patient variables, the population model fails to provide reliable estimates of drug concentration. Nevertheless, the agreement between observations and individual prediction is very good, since the latter are adjusted using the *post-hoc* estimates of inter-individual variability.

Finally, in both cases I note that the value of plasma concentration of vancomycin after the loading dose estimated by the two-compartment model is higher and definitely more realistic than in the one-compartment model. In the two-compartment model the distribution volume is divided into a relatively small central volume V_c, which is rapidly filled by intravascular administrations, and a large volume V_p accounting for slower tissue accumulation. Conversely, in a one-compartment model, the unique volume V must describe both effects, so that $V_c < V < (V_p + V_c)$. This result shows again both the importance and the difficulty of building a pharmacokinetic model that properly estimates distribution volume. This is possible only if plasma drug concentration is measured soon after the loading dose, as already discussed at the end of both Secs. 5.2 and 5.3.

5.5 Discussion

The results presented in this Chapter have shown on the one hand that the choice of the dosage regimen for antibiotics is complex, and on the other hand that *MargheritaTre* offers an invaluable mine of data to investigate drug pharmacokinetics. The clinical parameters recorded in electronic health records allow one to construct complex compartment models. However the analyses of this Chapter have also shown that the schedule of measurements of plasma drug concentrations present in *MargheritaTre* was not optimal to develop models with good predictive performance. The one- and two-compartment models have similar goodness of fit and predictive performance on external validation sets. However, residual variability was modelled worse in the two-compartment model, as shown in external validation. In particular, inter-subject variability of the distribution volume was poorly modelled since vancomycin concentration was seldom measured after the initial bolus. Furthermore, the confidence interval of the population predicted values of vancomycin concentration are still too wide for a practical application at patient bedside.

Both models have a sensible clinical interpretation. Vancomycin clearance strongly depends on renal functions, which is parametrised by creatinine clearance and on renal replacement therapy. Unfortunately data on flows of haemofiltration were not available. Only the average clearance associated with haemofiltration was derived and it was not possible to estimate it as a function of the characteristic of the treatment, as recently done in Ref. [61] in a prospective observational study conducted on nine septic-shock patients.

The approach adopted in this Thesis was more empirical with respect to recent physiologically based pharmacokinetic modelling [146]. As discussed in Sec. 2.4 one must find a proper balance between the capacity of the model of describing the details of physiological processes and the ability of fitting available data. The frequency of data collected for standard clinical practice is not high enough to appreciate the difference between a complex model with several compartments and a simpler one- or two- compartment model. The strengths of this work are instead the numerous sample size, the availability of several clinical parameters, and the measurement of drug concentrations measured for several days. This allows one to better model the inter-subject variability end the evolution of clinical conditions. Analyses focused on very specific populations, with high-frequency sampling, on the one hand provide very precise results, on the other hand can be hardly generalised to a population of critically ill patients, where variability is typically large.

The most important limitations of this analysis are the low number of plasma vancomycin concentrations per patients and the lack of observations soon after the administration of the initial bolus. This resulted in wide prediction intervals and poor modelling of drug distribution volume as function of patient conditions. Furthermore no data on haemofiltration flows were available.

5.6 Future perspectives

To overcome the issues discussed in Sec. 5.5, we decided to start AbioKin [1], a multicentric prospective study to investigate the kinetics of four among the most administered molecules in ICUs (linezolid, meropenem, piperacillin/tazobactam, and vancomycin). The study involves 10 Italian general ICUs and about 1600 patients, 400 per molecule. We consider eligible adult patients admitted to ICU with an expected length of stay longer than two days and receiving intra-vascular administrations of at least one of the considered molecules. For patients that started the antibiotic therapy before admission, we ask clinicians to record in *MargheritaTre* information about administration times and amounts of all the doses received. To avoid unreliable data we excluded patients that started the antibiotic treatment more then 24 h before admission in the ICU.

Up to five (nine for patients undergoing renal replacement therapy) 6 ml blood samples are

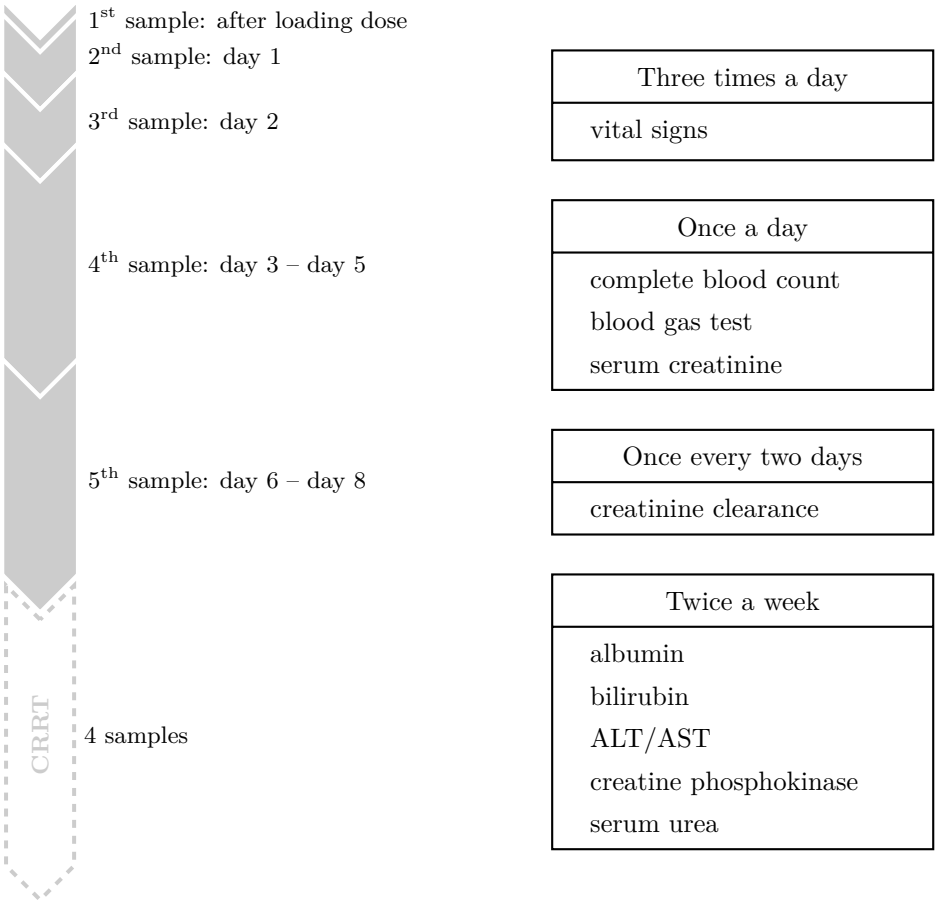

Figure 5.27: Schedule of blood sample withdrawals and laboratory tests for the AbioKin study [1].

withdrawn from enrolled patients during the period of the antibiotic treatment. Blood samples are spin dried for 10 min at 4000 rpm within one hour. Plasma is then separated in two collection tubes and stored at -80 °C in the hospital laboratory. Collection tubes are then centralised in the bio-bank of the Mario Negri Institute for Pharmacological Research. For each sample, one of the two tubes will be sent to the Laboratory of Pharmacology of the University of Pisa to measure antibiotic concentration. The other will be stored in the bio-bank for 20 years for future projects. The schedule of blood withdrawals has been designed to ensure that all the pharmacokinetic parameters can be estimated (see Fig. 5.27, left panel). Since the study is observational administered drug doses are chosen according to standard clinical practice by clinicians. No ED criteria [183] were adopted to design the sampling schedule for both theoretical and logistic reasons. The structure of the pharmacokinetic model, the covariate structure, and the error measurement structures are not known [85]. Furthermore, for logistic reasons we had to adopt the same sampling schedule for all the investigated molecules to interfere as least as possible with the standard daily schedule of blood withdrawals in the participating ICUs.

To improve identification of the distribution volume the first blood sample must be collected between 20 min and one hour after the end of the loading dose. To be able to estimate parame-

ters affecting both short and long time-scale kinetics, the other four samples must be withdrawn as follows: one on day one, one on day two, two between day three and day eight. Four extra samples may be collected in the following days if the patient starts to receive a continuous renal replacement therapy in order to increase the power of the model. To correlate the pharmacokinetic parameters with CRRT, operating characteristics of haemofiltration and haemodialysis are recorded in *MargheritaTre*.

To ensure that all necessary data will be available for the development of the model, we ask to perform complete blood count test every day, to measure serum creatinine concentration every day, creatinine clearance by 24 h urine collection at least once every two days, serum concentrations of albumin, bilirubin, ALT and AST transaminase, creatine phosphokinase, and urea at least twice a week (see Fig. 5.27, right panel). Blood gas test must be performed at least once a day and vital signs must be recorded at least three times a day.

The long-term goal of these investigations is the realisation of a simulator of pharmacokinetics to be integrated in the electronic health record *MargheritaTre*. Starting from the patient's data present in the electronic record, the simulator will allow clinicians to simulate the evolution of plasma concentrations of the molecules studied in the AbioKin study with the correct confidence bands constructed as described in Sec. 5.4.

Thanks to this tool, clinicians will be able to compute the probability of reaching the therapeutic target. By adjusting the antibiotic doses according to the patient's condition one will be able to identify an optimal therapeutic strategy that maximises the probability of attaining the therapeutic concentration and minimises the probability of overcoming the toxicity threshold.

Part II

GLUCOSE DYNAMICS

Chapter 6

PHYSIOLOGY OF GLUCOSE DYNAMICS AND MATHEMATICAL MODELS

With a concentration of about 100 mg of glucose per decilitre of blood and a blood volume of 5 l, the total amount of glucose in our blood is approximately 5 g, equivalent to a teaspoon of sugar. Considering that 1 g of glucose provides about 4 kcal, the total amount of glucose present in the bloodstream can provide only 20 kcal, which is a tiny fraction of the daily energetic requirement of about 2000 kcal. Hence, without continuous replacement, blood glucose would be completely depleted in a few minutes because of uptake by muscles and the central nervous system. The rate of glucose uptake may also vary significantly depending, for instance, on physical activity. Accordingly, the flux of glucose released into blood must be rapidly adjusted in relation to energy requirements. Similarly, after meals, glucose must be rapidly removed from blood and stored to prevent glucose concentration from increasing beyond dangerous levels.

In this Chapter, I shall briefly illustrate how each organ intervenes in maintaining glucose homoeostasis (Sec. 6.1) and review some of the existing mathematical models of coupled glucose-insulin dynamics, discussing the underlying approximations and their regimes of applicability (Secs. 6.2, 6.3, and 6.4).

In Chap. 7 I shall introduce my model, based on a system of three delay differential equations, that describes the couple dynamics of glucose, insulin, and glucagon, and test its performance with analytical and numerical analysis.

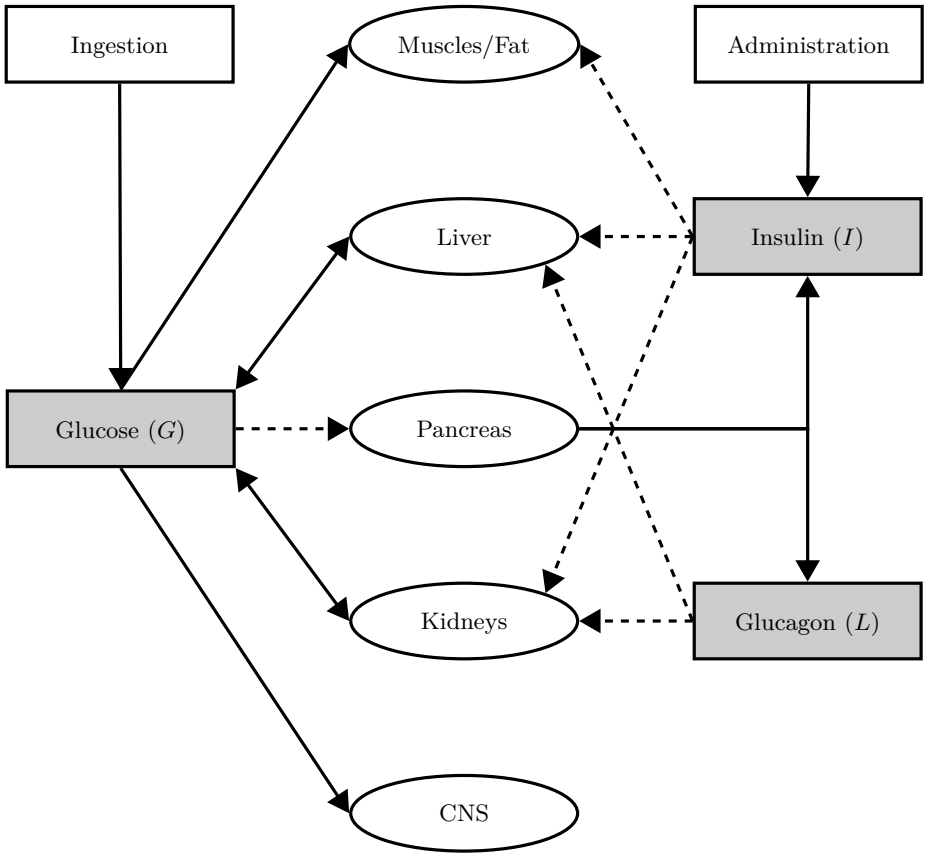

Figure 6.1: Schematic representation of physiological interactions at the basis of glucose control. Molecules (glucose, glucagon, and insulin), organs, external sources (food ingestion and insulin infusion) are represented by grey boxes, ellipses, and white boxes, respectively. Fluxes of molecules are denoted by solid arrow. Dashed arrows indicate the capability of a molecule to stimulate the reaction of an organ.

6.1 Physiology of glucose homoeostasis

The maintenance of a constant blood glucose level rests on a very fragile equilibrium, which is ensured by the cooperation of several organs. An illustrative description of the main mechanisms underlying the control of blood glucose concentration is provided in Fig. 6.1. The two key organs involved in this process are the pancreas and the liver. The former continuously monitors the blood glucose level and releases two hormones, insulin and glucagon when glucose concentration increases or decreases, respectively, beyond normal levels. The latter removes glucose from blood and stores it as glycogen when stimulated by a high concentration of blood insulin. Conversely, liver transforms glycogen into glucose and releases it in blood when stimulated by a high level of glucagon. Insulin has also the effect of stimulating glucose uptake by muscles and adipose tissue, whereas the central nervous systems consumes glucose at a constant rate, independently of insulin concentration.

Although this picture is extremely simplified (e.g., I neglected the contribution of several other

hormones), it provides a good approximation of the physiological mechanisms at the basis of glucose regulation, describing the response to both high and low levels of blood glucose.

6.1.1 Pancreas

Pancreas is a primary endocrine organ. It works as an exocrine gland, secreting enzymes and fluid into the gastrointestinal tract, and an endocrine gland, secreting hormones involved in blood glucose control and metabolism [174]. The two major hormones produced by the pancreas are secreted by different cell types located in cell clusters named islets of Langerhans: insulin is produced by β-cells and glucagon by α-cells.

Insulin. High levels of blood glucose concentration (after a meal or an intravascular glucose administration) stimulate β-cells to secrete insulin, which is released in two phases. In the first phase, the majority of insulin is secreted at a high rate, which reaches its maximum around five minutes after the glucose stimulus. In the second phase, the remaining insulin is secreted at a much lower rate. Measuring endogenous production of insulin is practically impossible since most of the insulin is removed by liver before reaching peripheral circulation (see Sec. 6.1.2). For this reason C-peptide is measured as a marker of insulin production [49]. C-peptide is a short amino-acid polypeptide produced during insulin synthesis in a ratio 1:1 with insulin molecule [176].

When blood glucose concentration increases, glucose molecules are taken up by the transmembrane carrier protein glucose transporter 2 (GLUT2) and undergo glycolysis, eventually generating ATP. The increased ATP/ADP ratio stimulates the closure of ATP-sensitive K^+ channels. The consequent decrease of the outgoing K^+ current causes membrane depolarisation that is followed by the opening of voltage-dependent Ca^{2+} channels. The increase of intracellular concentration of calcium eventually triggers the fusion of granules containing insulin with the membrane cell and the subsequent release of insulin [157].

Pancreas does not release insulin at a continuous rate but in series of bursts with an interval of about 4–15 min [142]. The mechanism at the origin of such a pulsatile release resides in single cells as proven by in vitro studies showing that individual β cells are able to secrete in pulse. This periodicity is linked with the cycle of glycolysis, ATP production, and membrane depolarisation. However, in vivo studies show that all pancreas cells secrete insulin in common bursts. Thus, β cells must be electrophysiologically coupled to ensure macroscopic coordination. Several microscopic models have been proposed to explain these features of insulin release [104].

The rate of insulin production oscillates also on longer ultradian time scales, with a period of 50–120 min [170]. These insulin oscillations are correlated with and anticipated by blood glucose oscillations and their amplitude depends on the level of blood glucose. Their origin stems

from the complex hormone-mediated interactions between organs involved in maintaining glucose homoeostasis [177]. Thus, a proper model of glucose dynamics should be able to describe this phenomenon and predict its evolution (see Sec. 6.3).

Glucagon. Glucagon is produced by pancreatic α-cells when blood glucose concentration is lower than about 80 mg/dl and is inhibited above 90 dl/l. Whereas the biochemical mechanisms governing insulin secretion are well known, it is still unclear how glucagon secretion is regulated. Both intrinsic and paracrine mechanisms have been proposed and investigated but their importance in determining the rate of secreted glucagon is still controversial [36].

Among paracrine mechanisms, it seems that some factor secreted by β-cells can inhibit glucagon production. However it is a matter of debate whether the inhibitory action is provided by insulin, GABA, or Zn^{2+} [131, 159, 214, 149]. For instance, the contribution of insulin is not clear since glucagon release is inhibited at a glucose concentration of 90 mg/dl, where insulin is not yet secreted. An important role in inhibiting glucagon production may be played by somatostatin [175], which is secreted at lower glucose concentrations compared to insulin. However, it has been experimentally shown that the secretion of glucagon at high glucose concentration is inhibited even if the somatostatin signalling process is blocked [197, 47].

These studies suggest that other inhibitory mechanisms exist, independently of somatostatin and possibly intrinsic in α cells. Alternative mechanisms have been proposed based on electrophysiological arguments. Analogously to insulin release in β-cells, glucagon is secreted by α-cells when a high intracellular concentration of Ca^{2+} stimulates exocytosis of granules containing glucagon. Calcium concentration increases when voltage-dependent P/Q channels open as a result of high-voltage action potentials sustained by the activation of voltage-dependent Na^+ channels [73, 213].

When blood glucose increases, ATP-dependent K^+ channels close because of enhanced ATP production. This causes membrane depolarisation, which results in inactivation of Na^+ channels. Eventually, the voltage of action potential is no longer sufficient to open Ca^{2+} channels, inhibiting glucagon release. Membrane depolarisation may also be caused by a higher ingoing flux of positive Na^+ ions transported by sodium-glucose co-transporter 2 [31], a glucose transporter that carries one Na^+ ion inside the cell for each glucose molecule.

These considerations show that the complexity of the regulation mechanisms of glucagon secretion cannot be explained only through paracrine effects associated with insulin production. Hence, a proper dynamical model of glucose metabolism must include a variable, independent of insulin, which represents glucagon. Indeed a decrease of insulin concentration is neither physiologically nor mathematically equivalent to an increase of glucagon level.

6.1.2 Liver

Liver contributes to maintaining glucose homoeostasis by removing, accumulating, and releasing glucose in blood. Although glucose transfer across the membrane of hepatic cells is primarily guaranteed by an insulin-independent transporter, GLUT2, the flux of glucose from blood to liver is strongly controlled by hormones, through the regulation of the four processes at the basis of glucose storage and release: glycolysis, glycogenesis, gluconeogenesis, and glycogenolysis. The former two processes convert glucose into pyruvate ($CH3COCOO^-$) and glycogen (a multibranched polymeric carbohydrate molecule), respectively. Gluconeogenesis and glycogenolysis are almost the reverse processes (the respective pathways are not symmetrically reverted), converting pyruvate and glycogen into glucose.

When glucagon binds to its hepatic receptor a complex signalling cascade is activated, resulting in the promotion of gluconeogenesis and glycogenolysis and in the inhibition of the other two processes. Conversely, insulin stimulates glycolysis and the conversion of glucose into glycogen [157, 101, 145]. An amount of about 100 g of glycogen is stored in liver cells, ready to be converted into glucose and delivered to blood in fasting conditions.

Liver also plays an important indirect role in the control of glucose level by removing insulin from blood. After being released by pancreas, insulin reaches liver through the portal vein and about 50% is removed from circulation. Most of insulin uptake is receptor-mediated with the onset of saturation effects at concentrations of about 500–2000 μU/ml [57]. However, not all bound insulin is destroyed. A significant amount of receptor-bound insulin re-enters circulation, after spending a long time bound to liver receptors (about 1 h [90]). The fraction of insulin that is not released is internalised by the cell, where it can be processed and destroyed through multiple complex pathways.

Glucagon undergoes similar hepatic removal. Experimental studies in animals show indeed that a significant fraction of portal glucagon is removed by liver [99, 70]. However the biochemical mechanisms at the basis of this process have been less investigated especially in humans.

6.1.3 Kidneys

Kidneys provide an important contribution in maintaining glucose homoeostasis. Indeed, they release glucose in blood through gluconeogenesis, remove it by glomerular filtration, reabsorb it in proximal tubules [186], and remove insulin and glucagon from peripheral circulation.

At normal concentration, all glucose removed by glomerular filtration is actively reabsorbed through sodium-coupled glucose cotransporters (SGLT) [208, 209]. SGLT molecules exploit energy associated with sodium electrochemical potential, to transport glucose against its concentration

gradient. Indeed SGLT1 and SGLT2 cotransport two or one Na^+ ions, respectively, with one-molecule of glucose across the proximal-tubule membrane down the sodium concentration gradient. This gradient is actively maintained by the sodium/potassium pump using energy from ATP, which transports Na^+ and K^+ ions in a 3:2 ratio across the membrane against their concentration gradients. Above plasma glucose concentration of 180 mg/dl, SGLT binding sites start to saturate, glucose is not completely reabsorbed and is consequently found in urine. Eventually, when plasma glucose reaches a concentration of 350 mg/dl, cotransporters are fully saturated and glucose cannot be reabsorbed.

Kidneys remove about 50% of peripheral insulin [57] by the combined action of glomerular filtration and proximal-tubule reabsorption. After being eliminated by filtration insulin is reabsorbed by proximal-tubule cell by endocytosis. Here insulin is degraded through multiple pathways as in liver. Eventually, almost no insulin is excreted in urine. Because of the important contribution of kidneys to the clearance of this molecule, renal function may strongly affect glucose homoeostasis. For instance renal failure may cause hypoglycaemia, due to reduced clearance.

Kidneys are recognised also as one of the major sites of glucagon elimination, since a decrease in glucagon clearance was observed in patients with renal failure [70]. However, their contribution has not been precisely quantified yet.

6.1.4 Muscles and adipose tissue

Transport of glucose into muscle, cardiac, and adipose tissue is mainly due to glucose transporter 4 (GLUT4), an insulin-regulated transporter, that facilitates diffusion of glucose down its concentration gradient [186]. At low insulin levels, GLUT4 is stored in vesicles in the cytoplasm. When insulin binds to its receptors on the cell membrane, it stimulates the production of GLUT4 molecules and triggers insertion of stored GLUT4 in the cell membrane by exocytosis [201].

Thus, when glucose level increases, pancreas starts producing insulin and the rate at which muscle and adipose tissue uptake glucose increases. Glucose is either used for energy production or transformed into glycogen that is stored in muscles. Differently from liver, muscles cannot release glucose in blood. Thus, the glycogen accumulated in this tissue (about 400 g) is an energy reserve accessible only by muscles themselves.

Since muscle cells have insulin receptors, they are also responsible for insulin removal by internalisation and degradation, as in liver and kidney cells.

6.1.5 Central nervous system

Glucose represents the primary energy source of the central nervous system, which consumes about 60% of the blood glucose during fasting. The rate at which brain uptakes glucose (about 72 mg/min) is constant, insulin-independent, and almost independent from glucose concentration. Neurons are particularly sensitive to hypoglycaemia since they do not store glycogen. Consequently, in such condition their consumption of glucose rapidly drops [174].

Glucose is transported into neurons mainly by glucose transporter 3 (GLUT3), an insulin-independent transporter [195]. GLUT3 has a higher affinity with glucose and five-fold greater transport capacity than other glucose transporters [172]. This guarantees efficient glucose supply to neurons in an environment, the cerebrospinal fluid, where glucose concentration is about two-thirds than in blood [174].

6.2 Intravenous glucose-tolerance test

The first models describing the dynamics of blood glucose were developed to estimate insulin sensitivity through the intravenous glucose-tolerance test (IVGTT). This test involves frequent sampling of peripheral plasma after an intravenous glucose injection. By measuring the time course of plasma insulin and glucose concentration it is possible to derive a quantitative estimate of insulin tissue sensitivity. First investigations showed that blood glucose concentration approximately undergoes exponential decay with time [58]. A rough index of glucose tolerance was proposed as the constant K, simply computed as

$$K = \frac{\log(C_1/C_2)}{t_2 - t_1}, \tag{6.1}$$

using only two values C_1 and C_2 of blood glucose concentrations, measured at times t_1 and t_2.

More advanced models of IVGTT must be able to reproduce the full glycaemic curve resulting from the coupled evolution of glucose and insulin in a short period of time (a few hours) and are fitted on a dataset with frequent sampling. For these reasons they are quite simple and cannot be generalised to describe situations where glucose and insulin are administered with complex schemes. Furthermore they cannot be adopted to describe the physiological reaction to hypoglycaemic conditions, that is their approximations fail when the blood glucose levels drop below a certain level.

Bolie's model. The simplest model by Bolie [29] is based on a system of two linear differential equations describing the interaction between glucose and insulin

$$\frac{\mathrm{d}G}{\mathrm{d}t} = -a_1 G - a_2 I + p, \tag{6.2}$$

$$\frac{\mathrm{d}I}{\mathrm{d}t} = a_3 G - a_4 I, \tag{6.3}$$

where G and I represent glucose and insulin amount in blood. This model is affected by several drawbacks. First, it is not based on experimental evidence. The relationship between insulin secretion rate and glucose is not linear and requires many parameters [23, 72]. Second, this model does not properly consider the complex glucose control through hepatic production and uptake [22].

Minimal model. Starting from a few essential criteria Bergman et al. and Toffolo et al. [25, 24, 184] developed a *minimal model* that:

(a) is physiologically based,

(b) is identifiable from a single glycaemic curve,

(c) is parsimonious in terms of number of parameters,

(d) the estimated parameters must have a physiological interpretation.

In addition to insulin I and glucose G, the standard formulation of the minimal model includes an auxiliary function X representing insulin in a *distant* compartment, stimulating glucose uptake by tissues [53]:

$$\frac{\mathrm{d}G}{\mathrm{d}t} = -\left[p_1 + X\right] G + p_1 G_b, \qquad G(0) = p_0, \tag{6.4}$$

$$\frac{\mathrm{d}X}{\mathrm{d}t} = -p_2 X + p_3 \left[I - I_b\right], \qquad X(0) = 0, \tag{6.5}$$

$$\frac{\mathrm{d}I}{\mathrm{d}t} = p_4 \left[G - p_5\right]^+ t - p_6 \left[I - I_b\right], \qquad I(0) = p_7 + I_b, \tag{6.6}$$

where $[a]^+ = \max(a, 0)$ is the positive part of a, G_p and I_p are subject specific glucose and insulin basal levels, and p_i are:

p_0 theoretical glucose concentration after glucose bolus,

p_1 insulin-independent rate of glucose uptake,

p_2 insulin decay rate in the *distant* compartment,

p_3 rate of insulin increase in the *distant* compartment,

p_4 rate of pancreatic release of insulin after the bolus,

p_5 pancreatic *target glycaemia*,

p_6 decay rate of insulin in plasma,

p_7 theoretical plasma insulin concentration above basal insulinaemia, after glucose bolus.

Although this model can reproduce the short-time dynamics of an IVGTT, it is not suitable for a general description of the complex physiology at the basis of the full dynamics of blood glucose level.

First, the presence of the term t in Eq. (6.6) expresses the fact that after a sudden glucose bolus the amount of insulin released by pancreas increases with time. Although this approximation holds in the first tens of minutes after the bolus, it explicitly breaks the invariance of the equations for time translations, since it arbitrarily fixes a time origin with respect to which all biochemical events take place. Furthermore, if G was kept larger than p_5, by continuous glucose administration, this term would yield a linearly growing rate of insulin production and make the system unstable. This

clearly shows that this model cannot be applied to reproduce scenarios that differ from the settings of an IVGTT.

Second, in a proper physiological model, the basal values G_b and I_b of glucose and insulin levels should be stationary solutions of the system (based on parameters describing production, exchanges, uptake, and clearance of molecules) and must not be forced as external parameters. Conversely, all the terms of Eqs. (6.4), (6.5), and (6.6) containing G and I are expressed as deviations around the basal values G_b and I_b. Such an expansion is expected to be valid for values of G and I not too far from G_b and I_b. In particular, this approximation fails to describe the physiological reaction to hypoglycaemic conditions.

Dynamical model. To remove the auxiliary function X and the explicit time dependence from the equations, De Gaetano and Arino [53] proposed a model based on a couple of integro-differential equations

$$\frac{\mathrm{d}G}{\mathrm{d}t} = -p_1 G - b_4 I\, G + b_7, \qquad G(0) = G_b + b_0, \quad G(t) = G_b \quad \forall t \in [-b_5, 0), \tag{6.7}$$

$$\frac{\mathrm{d}I}{\mathrm{d}t} = -b_2 I + \frac{b_6}{b_5} \int_{t-b_5}^{t} G(s)\mathrm{d}s, \qquad I(0) = I_b + b_3 b_0, \tag{6.8}$$

where G_b and I_b are the basal pre-bolus glucose and insulin concentrations and b_i are:

b_0 theoretical increase of glucose concentration after glucose bolus,

b_1 insulin-independent rate of glucose elimination,

b_2 insulin decay rate,

b_3 first-phase increase of insulin concentration per unit of glucose increase after glucose bolus,

b_4 insulin-dependent rate of glucose elimination,

b_5 length of past period whose glucose concentration can influence pancreatic insulin secretion,

p_6 second-phase of insulin release dependent on the average of plasma glucose concentration in the previous b_5 period of time,

p_7 constant glucose release by liver.

Even if this model removes the ugly time-dependent feature of the minimal model, it does not provide a satisfactory solution to the presence of an auxiliary variable. The choice of introducing an effective delay between glucose increase and insulin production through the time average of G is as arbitrary as the introduction of an auxiliary variable and cannot be justified with simple

physiological arguments. By taking the time derivative of Eq. (6.8)

$$\frac{\mathrm{d}^2 I(t)}{\mathrm{d}t^2} = -b_2 \frac{\mathrm{d}I(t)}{\mathrm{d}t} + \frac{b_6}{b_5}\left[G(t) - G(t-b_5)\right] \tag{6.9}$$

which, introducing the new variable $Y = \mathrm{d}I/\mathrm{d}t$, can be written as a system of differential equations

$$\frac{\mathrm{d}Y}{\mathrm{d}t} = -b_2 Y + \frac{b_6}{b_5}\left[G(t) - G(t-b_5)\right], \tag{6.10}$$

$$\frac{\mathrm{d}I}{\mathrm{d}t} = Y. \tag{6.11}$$

It is now apparent that also De Gaetano and Arino's dynamical model contains an auxiliary variable Y, which in Eq. (6.8) is just masked through the trick of writing the equations in integro-differential form. Furthermore the formulation of Eq. 6.10 explicitly indicates the presence of an arbitrary time delay b_5 in the production of Y with respect to an increase of G. Interestingly, Eq. (6.8) has been extended to general non-negative square integrable normalised kernels [128]:

$$\frac{\mathrm{d}I}{\mathrm{d}t} = -b_2 I + b_6 \int_0^\infty \omega(s) G(t-s)\mathrm{d}s. \tag{6.12}$$

By varying $\omega(s)$ one can reproduce almost all the possible causal relationships between G and I. This formal definition of the link between G and I allows one to derive general theoretical results on the existence and the convergence of the solutions of the system. The choice of the functional form of $\omega(s)$ must be based on physiological considerations and should be constructed as a solution of differential equations describing fundamental physiological interactions.

Kernel estimation. To clarify with an example how to determine the kernel in an integro-differential equation like Eq. (6.12), I step back to the minimal model defined in the system of Eqs. (6.4), (6.5), and (6.6). The auxiliary variable X can be eliminated from this system by integrating Eq. (6.5) through the method of variation of parameters

$$X(t) = \int_{-\infty}^{t} \mathcal{G}(t-t')\left[I(t') - I_b\right]\mathrm{d}t', \tag{6.13}$$

where the interstitial insulin level X depends on past values of the plasma insulin level I, weighted by the Green function

$$\mathcal{G}(t) = p_3\, e^{-p_2 t}. \tag{6.14}$$

I have chosen the lower integration limit as $-\infty$. In practice, given the exponentially decaying behaviour of $\mathcal{G}$, it is enough to know the value of the insulin level I in the past of t back to a few $\tau = p_2^{-1}$.

As a last step, I eliminate X from Eq. (6.4):

$$\frac{\mathrm{d}G}{\mathrm{d}t} = -\left[p_1 + \int_{-\infty}^{t} \mathcal{G}(t-t')\,[I(t') - I_b]\,\mathrm{d}t'\right] G + p_1 G_b. \tag{6.15}$$

Though at first glance this equation looks more complicated than Eq. (6.8), the minimal model is based on much clearer and simpler physiological assumptions. The term $p_3\,[I - I_b]$ in Eq. (6.5) parametrises a diffusive process through which insulin I moves from plasma to a distant compartment (e.g., interstitial fluid). Furthermore, in Eq. (6.13) there is no explicit arbitrary time delay. The delay between I and X appears through the average of I with the smooth kernel $\mathcal{G}$ and the time scale τ of the corresponding delay is naturally fixed by the elimination rate p_2.

6.3 Ultradian oscillations of insulin and glucose

Glucose and insulin dynamics show ultradian oscillations on a time scale of 50–120 minutes with the following intriguing features [185, 171, 169, 177]:

- Oscillations are self-sustained during glucose infusion at a constant rate.
- The increase of the glucose infusion rate results in oscillations with larger amplitudes, but does not affect their frequency [40];
- The time evolution of glucose and insulin concentrations are highly correlated and glucose peaks precede insulin peaks by a few minutes [171, 140, 169, 40].
- Oscillations after meal or oral glucose ingestion are damped.

Several models have been proposed to explain this phenomenon [105], starting from the same heuristic argument: the release of insulin when blood concentration of glucose increases is not instantaneous. Analogously, there is a delay of a few minutes between the release of insulin by pancreas and the uptake of glucose by liver, muscle, and adipose tissues, stimulated by an increase of insulin concentration. The combination of these two delays produces a cyclic effect in the time evolution of glucose and insulin, even in a stationary scenario when all the parameters remain constants and there is no intake of glucose.

Starting from an initial condition where both the concentration of insulin and glucose are low, liver starts producing glucose. When blood glucose exceeds a certain threshold, pancreas releases insulin in the blood stream. However, the reaction of liver, muscles, and adipose tissues to a higher concentration of insulin is not instantaneous. Thus blood glucose concentration keeps increasing for a few minutes. Meanwhile pancreas continues to produce insulin. When the uptake of glucose

starts, the insulin level is already very high. After glucose levels go below the pancreatic threshold concentration, pancreas stops producing insulin. However, it will take a few minutes to completely clear insulin from blood. During this period, glucose concentration further decreases and goes down to a relatively low level. The system has returned to the initial state and an other cycle can start.

These delays can be modelled in two ways. One possibility is to write a couple of delayed differential equations (DDE) by explicitly introducing two constant delays in the two equations describing the variation of insulin and glucose [60, 112]. Another possibility consists in increasing the number of compartments in which insulin and/or glucose move (e.g. blood, interstitial flow, etc...), and, accordingly, the number of variables [177, 185]. The differential equations remain ordinary and of first order, but the number of equations increases. The first approach leads to a more compact set of equations and allows a more straightforward analysis of the mathematical properties of their solutions [60, 21, 112, 107].

6.3.1 Multicompartmental ODE system

In the model developed by Sturis et al [177], the delay between insulin production and the stimulation of glucose uptake implicitly appears through a complex system of six ordinary differential equations. In this work, the structure of the equations is based on an accurate theoretical description of the physiological processes.

This model contains three main variables: the total amount of glucose in plasma and intercellular space G, the amount of insulin in plasma I_p, and the amount of insulin in the intercellular space I_i. Furthermore, there are three auxiliary variables x_1, x_2, and x_3 representing the delay between insulin release in plasma and its effect on hepatic glucose production.

The three main equations, for G, I_p, and I_i are

$$\frac{\mathrm{d}I_p}{\mathrm{d}t} = f_1(G) - E\left(\frac{I_p}{V_p} - \frac{I_i}{V_i}\right) - \frac{I_p}{t_p}, \tag{6.16}$$

$$\frac{\mathrm{d}I_i}{\mathrm{d}t} = E\left(\frac{I_p}{V_p} - \frac{I_i}{V_i}\right) - \frac{I_i}{t_i}, \tag{6.17}$$

$$\frac{\mathrm{d}G}{\mathrm{d}t} = G_{\mathrm{in}} - f_2(G) - f_3(G)f_4(I_i) + f_5(x_3). \tag{6.18}$$

The auxiliary variable x_3 is related to the amount of insulin in plasma I_p, through a cascade of

Parameter	Value	Units
V_p	3	l
V_i	11	l
V_g	10	l
E	0.2	l/min
t_p	6	min
t_i	100	min
t_d	36	min
R_m	210	mU/min
a_1	300	mg/l
C_1	2000	mg/l
U_b	72	mg/min
C_2	144	mg/l
C_3	1000	mg/l
U_0	40	mg/min
U_m	940	mg/min
β	1.77	
C_4	80	mU/l
R_g	180	mg/min
α	0.29	l/mU
C_5	26	mU/l

Table 6.1: Parameters of the model presented in Eqs. (6.16)–(6.21) [177].

three simple differential equations

$$\frac{\mathrm{d}x_1}{\mathrm{d}t} = \frac{3}{t_d}\left(I_p - x_1\right), \tag{6.19}$$

$$\frac{\mathrm{d}x_2}{\mathrm{d}t} = \frac{3}{t_d}\left(x_1 - x_2\right), \tag{6.20}$$

$$\frac{\mathrm{d}x_3}{\mathrm{d}t} = \frac{3}{t_d}\left(x_2 - x_3\right). \tag{6.21}$$

The functional form of each term f_i was determined through a careful review of the experimental results. The value of all the parameters, reported in Table 6.1 were fitted to experimental results.

Equations (6.16) and (6.17) express the variation of the total amount of insulin in plasma and in the intercellular space, whose volumes are V_p and V_i, respectively. Insulin is degraded in plasma and in the intercellular space with two different time constants t_p and t_i. The transport between the two insulin compartments is modelled as a diffusive process driven by the difference in insulin concentration, with transfer rate E [139]. The pancreatic insulin production controlled by glucose concentration is

$$f_1(G) = \frac{R_m}{1 + e^{-(G/V_g - C_1)/a_1}}, \tag{6.22}$$

where unknown parameters were fitted to experimental results involving the measure of C-peptide concentration [140, 169].

Equation (6.18) describes the variation of the total amount of glucose, distributed in a volume V_g. The first term G_{in} represents the exogenous supply of glucose, either from food or intravenous

infusion. The other terms represent glucose removal and endogenous glucose production. Glucose is removed from plasma by several organs in different ways. Glucose utilisation by the central nervous system (CNS) does not depend on the concentration of insulin and is almost constant (approximately 72 mg/min). The consumption of glucose by the CNS drops to zero only in conditions of severe hypoglycaemia. This behaviour is described by

$$f_2(G) = U_b \left(1 - e^{-G/C_2 V_g}\right), \tag{6.23}$$

which was fitted to experimental data from Verdonk et al [196]. Glucose utilisation by muscle and adipose tissues depends instead on the concentration of both glucose and insulin. This dependence has been decoupled through the product of the two functions f_3 and f_4. The dependence on G is assumed to be linear

$$f_3(G) = \frac{G}{C_3 V_g}, \tag{6.24}$$

in agreement with experimental results [152, 196]. The insulin dependent term is modelled as

$$f_4(I_i) = U_0 + \frac{U_m - U_0}{1 + \left[I_i \left(1/V_i + 1/Et_i\right)/C_4\right]^{-\beta}}, \tag{6.25}$$

which is expressed in terms of the experimental relation between plasma insulin concentration and cellular glucose uptake [152]. The last term of the glucose equation represents hepatic glucose production. In this model endogenous glucose production is controlled only by insulin and involves a time delay, implemented through the three auxiliary variables x_1, x_2, and x_3:

$$f_5(x_3) = \frac{R_g}{1 + e^{\alpha(x_3/V_p - C_5)}}. \tag{6.26}$$

Indeed, Eqs. (6.19), (6.20), and (6.21) generate an effective total delay of t_d [144]. By integrating these equations one at a time, as shown in Appendix A, one finds that

$$x_3(t) = \int_{-\infty}^{t} \mathcal{G}_3\left(t - t_1\right) I(t_1) \mathrm{d}t_1, \quad \mathcal{G}_3(\tau) = \frac{1}{2}\kappa^3 \tau^2 \, e^{-\kappa\tau}. \tag{6.27}$$

The value of x_3 computed at time t is the weighted average of the insulin concentrations $I(t')$ measured at times $t' < t$, with weight $\mathcal{G}_3(t - t')$, where the function $\mathcal{G}_3$ is normalised to 1, with average $\bar{\tau} = t_d$, and standard deviation $t_d/\sqrt{3}$.

Sturis' model has self-sustained oscillatory solutions in a wide range of parameters [177] and accounts for the experimental findings summarised at the beginning of this section (see page 169).

6.3.2 DDE systems with explicit delays

Bennett and Gourley's model. The delay between the production of insulin and its effect on liver or other organs can be implemented by introducing an explicit time delay in the system of differential equation [21]. Equations (6.19), (6.20), and (6.21) are removed from the system and Eq. (6.18) is modified as

$$\frac{\mathrm{d}G}{\mathrm{d}t} = G_{\mathrm{in}} - f_2(G) - f_3(G)f_4(I_i) + f_5(I_p(t-\tau)), \tag{6.28}$$

with initial conditions

$$I_p(t) = I_p^0(t) \geq 0, \quad -\tau \leq s \leq 0, \text{ and } I_p^0(0) > 0, \tag{6.29}$$

$$I_i(0) = I_i^0 > 0, \tag{6.30}$$

$$G(0) = G^0 > 0. \tag{6.31}$$

With respect to Sturis' model, this system does not introduce unobserved auxiliary variables x_i. Several fundamental properties of its solutions can be derived analytically [21] by assuming that f_3 is linear and f_i satisfies very weak conditions

$$f_i > 0, \quad i = 1, 2, 4, 5, \tag{6.32}$$

$$f_i' > 0, \quad i = 1, 2, 4, \qquad f_5' < 0, \tag{6.33}$$

$$f_i(0) = 0, \quad i = 2, 3, \qquad f_i(x) \to a_i > 0, \text{ as } x \to 0, \quad i = 4, 5, \tag{6.34}$$

$$f_i(x) \to b_i > 0, \text{ as } x \to +\infty, \quad i = 1, 2, 4, \qquad f_5(x) \to 0, \text{ as } x \to +\infty. \tag{6.35}$$

Under these conditions the solutions of this model exist for any $t > 0$, are strictly positive, and uniformly bounded from above and below. Furthermore, there is only one equilibrium point (I_p^*, I_i^*, G^*), solution of

$$\frac{\mathrm{d}G}{\mathrm{d}t} = \frac{\mathrm{d}I_i}{\mathrm{d}t} = \frac{\mathrm{d}I_p}{\mathrm{d}t} = 0. \tag{6.36}$$

Using Lyapunov functions, Bennett and Gourley [21] identified a set of sufficient conditions under which the solutions converge to the equilibrium (I_p^*, I_i^*, G^*). They found quite complex conditions involving the time scale t_i and t_p on which interstitial and plasma insulin degrades and the delay τ between the production of insulin and the appearance of its effect. Qualitatively, if t_i, t_p, and τ are all sufficiently small, then the solutions globally converge to the equilibrium solutions (I_p^*, I_i^*, G^*). For larger delay τ, and slow degradation rates (large t_i and t_p) solutions with self-sustained oscillations become possible.

It was also proved that the solution does not converge to equilibrium if the rate G_{in} is large. Furthermore, in order to sustain oscillations, the rate of plasma insulin production must be large enough and sensitive to variation of glucose concentrations (i.e., large $f_1'(C_1V_g) = R_m/4a_1V_g$). Analogously, oscillations are more likely to occur if the rate of liver glucose production stimulated by insulin is large and sensitive to variations of insulin concentrations (i.e., large $f_5'(C_5V_p) = R_g\alpha/4V_p$).

Engelborghs, Lemaire, Bélari, and Roose's model. The model by Sturis et al was generalised in Ref. [60] to describe glucose dynamics in patients affected by type-I diabetes undergoing insulin infusion. Sturis' model was initially simplified by removing the interstitial compartment for insulin, and introducing a term τ_2 to mimic the time delay between insulin production and hepatic glucose release.

$$\frac{\mathrm{d}I}{\mathrm{d}t} = f_1(G) - \frac{I}{t_1}, \tag{6.37}$$

$$\frac{\mathrm{d}G}{\mathrm{d}t} = G_{\text{in}} - f_2(G) - f_3(G)f_4(I) + f_5(I(t-\tau_2)). \tag{6.38}$$

Although simpler, this model is still able to capture the fundamental features of glucose dynamics in healthy subjects, assuming a degradation time $t_1 = 6$ min and a delay $\tau_2 = 50$ min.

The pathophysiology of diabetes is modelled by decreasing the internal insulin production and replacing $f_1(G)$ by $\gamma f_1(G)$, with $0 \leq \gamma \leq 1$. The lower the γ, the worse the patient conditions. External insulin infusion is assumed to compensate the decrease of pancreatic insulin production (it is proportional to $[1-\gamma]$) and to depend on plasma glucose concentration in much the same way as insulin is produced by pancreas (proportional to $f_1(G)$). Namely, the rate of insulin infusion is adjusted according to variations in glucose concentration, with a certain delay τ_1, which parametrises the time required to measure the glucose concentration and change the rate of infusion of the insulin pump. By modifying Eq. (6.37) according to these criteria, the system assumes the following form, with two time delays τ_1 and τ_2:

$$\frac{\mathrm{d}I}{\mathrm{d}t} = \gamma\, f_1(G) - \frac{I}{t_1} + (1-\gamma) f_1(G(t-\tau_1)), \tag{6.39}$$

$$\frac{\mathrm{d}G}{\mathrm{d}t} = G_{\text{in}} - f_2(G) - f_3(G)f_4(I) + f_5(I(t-\tau_2)). \tag{6.40}$$

This system is simple enough to allow for a semi-analytical study of its solutions. The properties of its steady-state solutions can be determined by applying the techniques illustrated in Appendix B.

The steady state (I^*, G^*) is the solution of

$$f_1(G^*) - \frac{I^*}{t_1} = 0. \tag{6.41}$$

$$G_{\text{in}} - f_2(G^*) - f_3(G^*)f_4(I^*) + f_5(I^*) = 0. \tag{6.42}$$

The solution exists and is unique. From the first equation I can compute $I^* = t_1 f_1(G^*)$ and replace it in the second equation, which becomes

$$g(G^*) = 0, \tag{6.43}$$

where

$$g(x) = G_{\text{in}} - f_2(x) - f_3(x)f_4(t_1 f_1(x)) + f_5(t_1 f_1(x)). \tag{6.44}$$

For $x = 0$,

$$g(0) = G_{\text{in}} + f_5(t_1 f_1(0)) > 0, \tag{6.45}$$

since f_5 is always positive. For $x \to +\infty$

$$\lim_{x\to+\infty} g(x) = -\infty, \tag{6.46}$$

since $f_2(x) \to U_b$, $f_5(t_1 f_1(x)) \to f_5(t_1 R_m)$, $f_4(t_1 f_1(x)) \to f_4(t_1 R_m) > 0$, and $f_3(x) \to +\infty$. Since g is continuous there must exist at least one solution of $g(x) = 0$ in $(0, \infty)$. Furthermore, the solution is unique because g is strictly monotonic and decreasing. Indeed,

$$g'(x) = -f_2'(x) - f_3'(x)f_4(t_1 f_1(x)) - f_3(x)f_4'(t_1 f_1(x))t_1 f_1'(x) + f_5'(t_1 f_1(x))t_1 f_1'(x) \tag{6.47}$$

is negative for any $x > 0$, because $t_i > 0$, $f_i > 0$, $f_i' > 0$ for $i = 1, 2, 3, 4$, and $f_5' < 0$ [see Eqs. (6.22), (6.23), (6.24), (6.25) and (6.26)].

Following Appendix B, I linearise Eqs. (6.39) and (6.40) around (I^*, G^*). Defining $y(t) = (i(t), g(t))$, with $i(t) = I(t) - I^*$ and $g(t) = G(t) - G^*$:

$$\dot{y}(t) = \sum_{i=0}^{2} A_i\, y(t - \tau_i), \tag{6.48}$$

where $\tau_0 = 0$ and

$$A_0 = \begin{pmatrix} -1/t_1 & \gamma f_1'(G^*) \\ -f_3(G^*)f_4'(I^*) & -f_2'(G^*) - f_3'(G^*)f_4(I^*) \end{pmatrix}, \tag{6.49}$$

$$A_1 = \begin{pmatrix} 0 & (1-\gamma)f_1'(G^*) \\ 0 & 0 \end{pmatrix}, \tag{6.50}$$

$$A_2 = \begin{pmatrix} 0 & 0 \\ f_5'(I^*) & 0 \end{pmatrix}. \tag{6.51}$$

The corresponding characteristic equation [see Eq. (B.10)] is

$$\lambda^2 + A\lambda + B + C\,e^{-\lambda(\tau_1+\tau_2)} + D\,e^{-\lambda\tau_1} + E\,e^{-\lambda\tau_2} = 0, \tag{6.52}$$

where

$$A = 1/t_1 + f_2'(G^*) + f_3'(G^*)f_4(I^*), \tag{6.53}$$

$$B = f_2'(G^*)/t_1 + f_3'(G^*)f_4(I^*)/t_1 + \gamma f_1'(G^*)f_3(G^*)f_4'(I^*), \tag{6.54}$$

$$C = -(1-\gamma)f_1'(G^*)f_5'(I^*), \tag{6.55}$$

$$D = f_3(G^*)f_4'(I^*)(1-\gamma)f_1'(G^*), \tag{6.56}$$

$$E = -\gamma f_1'(G^*)f_5'(I^*). \tag{6.57}$$

All these parameters are positive since $f_i' > 0$ for $i = 1, 2, 3, 4$, and $f_5' < 0$. The fixed point is unstable when the real part of the complex frequency λ becomes positive. The boundary between the stable and unstable region is therefore defined by $\lambda = i\omega$, with $\omega \in \mathbb{R}$. For healthy people $C = D = 0$ and the boundary condition reduces to

$$\omega^2 - iA\omega - B = Ee^{-i\omega\tau_2}. \tag{6.58}$$

This is a complex equation for the two real variables ω and τ_2. In the complex plane the solution of this equation corresponds to the intersection of the curve expressed by the left-hand side with a circle of radius E on the right-hand side. Taking the modulus squared of the equation one obtains an equation for ω:

$$\left(\omega^2 - B^2\right)^2 + A^2\omega^2 = E^2. \tag{6.59}$$

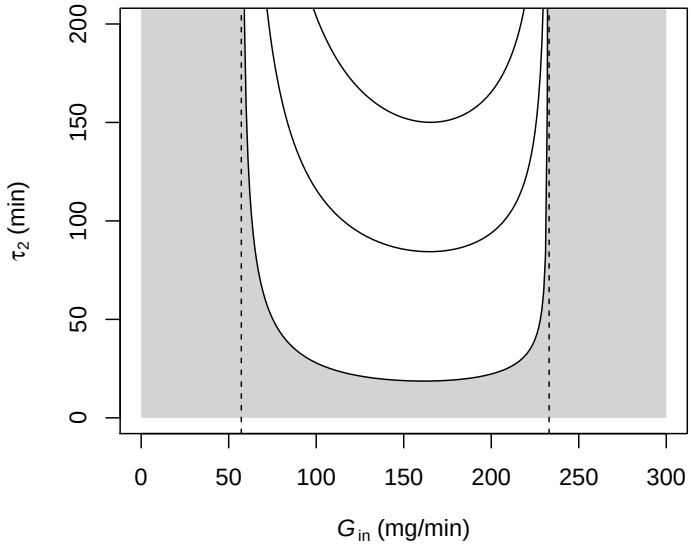

Figure 6.2: Phase-space representation in the plane (G_{in}, τ_2) of the solution of Eq. (6.52) for a healthy individual with $\lambda = 1$. Solid lines represent the couples G_{in}, τ_2 for which there are purely imaginary eigenvalues $\lambda = i\omega$. The lowest curve separates the region where the stationary solution (G^*, I^*) is stable ($\Re(\lambda) > 0$). The region outside the dashed lines ($G_{\text{in}} = 57.2\,\text{mg/min}$ and $G_{\text{in}} = 233.1\,\text{mg/min}$) is stable for any value of τ_2. This plot has been constructed by reproducing the calculations outlined in Ref. [60], using the values of Table 6.1.

Once ω is determined, the other unknown τ_2 is obtained by solving

$$\begin{cases} \cos(\omega\tau_2) = \dfrac{\omega^2 - B}{E}, \\ \sin(\omega\tau_2) = \dfrac{A}{E}\omega. \end{cases} \tag{6.60}$$

In Fig. 6.2 the solid lines represent the couples of parameters G_{in}, τ_2 for which Eq. (6.52) admits a pure imaginary solution $\lambda = i\omega$. In the phase-space region below the lowest curve (grey area), the stationary solution (G^*, I^*) is stable since all the eigenvalues λ have a negative real part. Above this curve there are unstable solutions with a positive real part of λ. For $G_{\text{in}} < 57.2\,\text{mg/min}$ and $G_{\text{in}} > 233.1\,\text{mg/min}$ all the stationary solutions are stable. When stationary solutions of the form (G^*, I^*) are not stable, the solution of a system of delayed differential equations may show a periodic behaviour, rotating around (G^*, I^*). The appearance of such solutions was discussed in Ref. [60], using more sophisticated techniques.

Refinement of Sturis' model The version of Sturis' model simplified by Engelborghs *et al* [see Eqs. (6.37) and (6.38)] was taken as the basis for further refinements. Li, Kuang, and Mason [112] modified that system by explicitly introducing a time delay in Eq. (6.37) in the term describing

Parameter	Value	Units
s	0.072	min^{-1}
m_b	60	min
d_i	0.065	min^{-1}
C_6	2300	mU/l

Table 6.2: Values of additional parameters in the model by Kissler *et al* [107] compared to Sturis' model [177] (see Table 6.1).

pancreatic insulin production, partially mimicking Eq. (6.39):

$$\frac{\mathrm{d}I}{\mathrm{d}t} = f_1(G(t-\tau_1)) - d_i I, \tag{6.61}$$

$$\frac{\mathrm{d}G}{\mathrm{d}t} = G_{\text{in}} - f_2(G) - f_3(G)f_4(I) + f_5(I(t-\tau_2)), \tag{6.62}$$

where d_i is the insulin degradation constant. Wang, Li, and Kuang [199] further improved the insulin equation by accounting for insulin administration and saturation effect in insulin degradation:

$$\frac{\mathrm{d}I}{\mathrm{d}t} = I_{\text{in}} + \beta f_1(G(t-\tau_1)) - f_6(I), \tag{6.63}$$

where $I_{\text{in}}(t)$ is the rate of insulin administration and β pancreas efficiency (with $0 \leq \beta \leq 1$). Insulin degradation is described by the new function f_8,

$$f_6(I) = \frac{d_i C_6}{I/V_p + C_6}\, I. \tag{6.64}$$

When the insulin concentration is much less than the half-saturation concentration C_6 ($I/V_p \ll C_6$), the insulin elimination term becomes proportional to the insulin concentration ($d_i I$), as in Eq. (6.61). At high insulin concentrations $I/V_p \gg C_6$, the elimination rate becomes insulin independent saturating at $d_i C_6 V_p$.

Finally, Kissler, Cichowitz, Sankaranarayanan, and Bortz [107] adapted this model by modifying the glucose equation (6.62) taking into account variations in muscle glucose uptake according to physical activity

$$\frac{\mathrm{d}G}{\mathrm{d}t} = G_{\text{in}} - f_2(G) - \gamma\left[1 + s\left(m - m_b\right)\right] f_3(G)f_4(I) + f_5(I(t-\tau_2)), \tag{6.65}$$

where γ parametrises insulin tissue sensitivity, s the rate of increase of insulin sensitivity per minute of exercise, m the daily minutes of physical activity, and m_b the baseline minutes of physical activity. In this analysis, the parameters values were chosen as in Table 6.1. Values of additional parameters are reported in Table 6.2.

6.4 Models for critically ill patients

In this section I briefly present some of the most interesting models proposed to describe the kinetics of glucose and insulin in critically ill patients. However, some of these models, which provide a good physiological description, are very complex and their mathematical and statistical treatment is not simple. This makes it almost impossible to derive analytical results. Conversely, other models, which offer a much easier and stable application (e.g., to data fitting), do not properly reproduce the relevant physiological mechanisms.

For these reasons, in Chap. 7, I construct my model starting from the one illustrated in Sec. 6.3.2. Although much simpler from a mathematical point of view, that model allows a faithful and detailed physiological description of glucose regulation.

6.4.1 Glucose and insulin subsystems

In a series of papers, Hovorka *et al*, proposed [88], applied, and tested, also on a population of critically ill patients [89, 14] a very complex model describing the coupled dynamics of glucose and insulin through a set of eight differential equations: two represent the dynamics of the glucose subsystem, three of the insulin one [90], and three the action of insulin on glucose. The equations for the glucose subsystem are

$$\frac{\mathrm{d}Q_1(t)}{\mathrm{d}} = -\left[\frac{F_{01}^c}{V_G G(t)} + x_1(t)\right] Q_1(t) + k_{12} Q_2(t) - F_R + U_G(t) + \mathrm{EGP}_0\left[1 - x_3(t)\right] \tag{6.66}$$

$$\frac{\mathrm{d}Q_2(t)}{\mathrm{d}t} = x_1(t) Q_1(t) - \left[k_{12} + x_2(t)\right] Q_2(t) y(t), \tag{6.67}$$

where Q_1 and Q_2 are the masses of glucose in the accessible and non-accessible compartments, V_G the volume of the first compartment, $G = Q_1/V_G$ the glucose concentration, EGP_0 the endogenous glucose production at zero insulin concentration, F_{01}^c the insulin-independent glucose flux

$$F_{01}^c = F_{01} \times \begin{cases} 1 & \text{if } G \geq 4.5\,\mathrm{mmol/l}, \\ G/(4.5\,\mathrm{mmol/l}) & \text{otherwise}, \end{cases} \tag{6.68}$$

and F_R is the renal glucose clearance above $G = 9\,\mathrm{mmol/l}$

$$F_R = F_{01} \times \begin{cases} 0.003\,(G - 9\,\mathrm{mmol/l})\,V_G & \text{if } G \geq 9\,\mathrm{mmol/l}, \\ 0 & \text{otherwise}. \end{cases} \tag{6.69}$$

U_G is glucose intake, expressed as

$$U_G(t) = \frac{D_G A_G t e^{-t/t_{\max,G}}}{t^2_{\max,G}}, \tag{6.70}$$

to model the gut absorption rate of glucose after meals.

The insulin subsystem is based on the three following equations:

$$\frac{\mathrm{d}I(t)}{\mathrm{d}t} = \frac{U_I(t)}{V_I} - k_e\, I(t), \tag{6.71}$$

$$\frac{\mathrm{d}S_1(t)}{\mathrm{d}t} = u(t) - \frac{S_1(t)}{t_{\max,I}}, \tag{6.72}$$

$$\frac{\mathrm{d}S_2(t)}{\mathrm{d}t} = \frac{S_1(t)}{t_{\max,I}} - \frac{S_2(t)}{t_{\max,I}}. \tag{6.73}$$

The first equation expresses the variation of plasma insulin concentration I, where V_I is its distribution volume, and k_e the elimination rate. The form of U_I, the insulin intake rate, is obtained as the solution of Eqs. (6.72) and (6.73). S_1 and S_2 are two-compartment insulin concentrations modelling absorption of fast insulin, $u(t)$ represent intravenous infusion of insulin. Eventually, the insulin absorption rate is obtained as $U_I(t) = S_2(t)/t_{\max,I}$. The insulin-mediated glucose production and the removal terms in Eqs. (6.66) and (6.67) are derived by solving a further series of differential equations

$$\frac{\mathrm{d}x_1(t)}{\mathrm{d}t} = -k_{a1}x_1(t) + k_{b1}I(t), \tag{6.74}$$

$$\frac{\mathrm{d}x_2(t)}{\mathrm{d}t} = -k_{a2}x_2(t) + k_{b2}I(t), \tag{6.75}$$

$$\frac{\mathrm{d}x_3(t)}{\mathrm{d}t} = -k_{a3}x_3(t) + k_{b3}I(t), \tag{6.76}$$

where x_1, x_2, and x_3 represent the effect of insulin on glucose distribution between compartments, disposal, and endogenous production.

This model provides a very detailed description of some microscopic physiological mechanisms and implements delay effects with a cascade of coupled differential equations (see Appendix A). However, it does not model saturation effects as well as the models illustrated in Sec. 6.3 and it contains a huge number of parameters. From a mathematical perspective, it is extremely complex and contains non-differentiable functions (F^c_{01}, F_R). As a consequence, an analytical treatment is more difficult in this model than, for instance, the one proposed in Ref. [177] and subsequently refined by several authors (Sec. 6.3.2).

6.4.2 Model for estimation of time-dependent parameters

Based on the minimal model [25, 24, 184] (see Sec. 6.2), Chase *et al* proposed a simple model with the aim of estimating the fractional clearance of plasma glucose p_G at basal insulin and the insulin sensitivity S_I, in an adaptive, time-dependent way [44, 79, 116, 43, 45, 42]. The model consists of three differential equations

$$\frac{\mathrm{d}G}{\mathrm{d}t} = -p_G G - S_I \left(G + G_E\right) \frac{Q}{1 + \alpha_G Q} + P(t), \tag{6.77}$$

$$\frac{\mathrm{d}Q}{\mathrm{d}t} = kI - kQ, \tag{6.78}$$

$$\frac{\mathrm{d}I}{\mathrm{d}t} = -n\frac{I}{1 + \alpha_I I} + \frac{u_{\mathrm{ex}}(t)}{V}, \tag{6.79}$$

where G is the difference between the concentration of plasma glucose and its equilibrium level G_E, I is the concentration of insulin resulting from exogenous administration u_{ex}, and Q is the concentration of insulin bounded to interstitial sites. The Authors also implement a very interesting method to fit the parameters in a time-dependent way. The model is very robust when fitted to data and it was also implemented in an automatic controller to adjust insulin and nutrition input in critically ill patients [207, 136, 98]. However it does not provide a good description of the physiological processes at the basis of glucose dynamics. The first equation is indeed a sort of linearisation around the equilibrium value G_E, which must be estimated from data. Furthermore, the endogenous production of insulin is not modelled.

6.4.3 Adaptive model with endogenous insulin production

Starting from the minimal model (Sec. 6.2), Van Herpe *et al.* developed a new simple model, which, differently from the model illustrated in Sec. 6.4.2, includes a term representing endogenous insulin production:

$$\frac{\mathrm{d}G}{\mathrm{d}t} = \left(P_1 - X\right) G - P_1 G_b + \frac{F_G}{V_G}, \tag{6.80}$$

$$\frac{\mathrm{d}X}{\mathrm{d}t} = P_2 X + P_3 \left(I_1 - I_b\right), \tag{6.81}$$

$$\frac{\mathrm{d}I_1}{\mathrm{d}t} = \alpha \max\left(0, I_2\right) - n\left(I_1 - I_b\right) + \frac{F_I}{V_I}, \tag{6.82}$$

$$\frac{\mathrm{d}I_2}{\mathrm{d}t} = \beta\gamma\left(G - h\right) - nI_2, \tag{6.83}$$

where G and I_1 are the glucose and insulin concentrations in plasma and X describes the effect of insulin on glucose uptake. The variable I_2 was introduced only for mathematical reasons and interpreted *a posteriori* as the fraction of the available insulin from the endogenous insulin secretion.

Thanks to its simplicity this model was implemented in an automatic control system [80, 192]. A single-centre randomised clinical trial showed that, compared with expert nursing, this automatic system improved the efficacy of a tight glycaemic control without increasing the risk of hypoglycaemia [194].

Although this model was able to produce important results, its formulation is not satisfactory from a physiological and mathematical point of view. Equation (6.83) was introduced without a clear physiological motivation. Furthermore, because of the presence of the term $G - h$ in Eq. (6.83), I_2 can assume non-physical negative values. Eventually, a max function was introduced in Eq. (6.82) to fix this issue. This, in turn, generates annoying mathematical complications in the analytical treatment of the equations since the max function is not differentiable.

Chapter 7

GLUCOSE–INSULIN–GLUCAGON DYNAMICS

A reliable mathematical model must be able, first of all, to reproduce realistic glucose dynamics in healthy individuals. One expects that pathological dynamics can be described by adjusting the system of equations introducing modifiers as β and γ in Eqs. (6.63) and (6.65), which parametrise the efficiency of pancreatic insulin production and insulin tissue sensitivity, respectively. For instance, a patient with type I diabetes will have $\beta < 0$, not being able to produce insulin as a healthy subject. On the other hand, patients with type II diabetes are characterised by the inability to respond to normal insulin levels. Hence, they are modelled by taking $\gamma < 1$. Similarly, one expects to be able to reproduce the glucose dynamics in critically ill patients under severe stress condition by just adapting the parameters of the system, once all the physiological mechanisms underlying glucose regulation are properly taken into account by the model.

In this Chapter I shall test the models presented in Sec. 6.3 by performing a numerical analysis on simulated healthy individuals. Then, I shall introduce a new model describing the coupled dynamics of glucose, insulin, and glucagon and test its performance with analytical investigations, simulations, and on measured data at single-patient level. The objective of this investigation is to study the mathematical properties of this new model, to produce a phase-space analysis of the stability of its solution and to discuss at a qualitative level the patho-physiological interpretation of those results. No population model will be constructed because of the lack of frequent and robust data, as explained in Sec. 7.5.

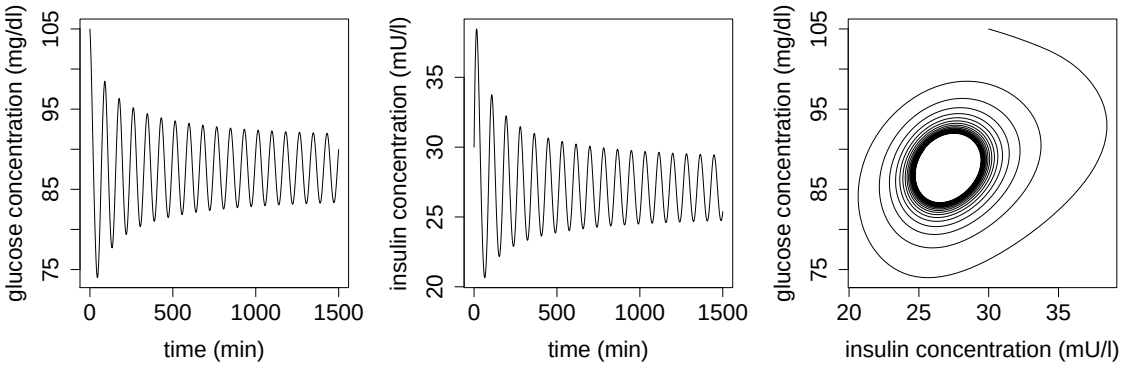

Figure 7.1: Evolution of plasma glucose (left panel) and insulin (central panel) concentrations and glucose-insulin phase-space plot (right panel) for a subject with $\tau_1 = 5\,\text{min}$, $\tau_2 = 4.5\,\text{min}$, $G_{\text{in}} = 54\,\text{mg/min}$, $d_i = 0.06\,\text{min}^{-1}$, with initial glucose and insulin concentrations of $105\,\text{mg/dl}$ and $30\,\text{mU/l}$, respectively. Values of other parameters as in Table 6.1. The results were obtained integrating Eqs. (6.61) and (6.62) as in Fig. 4, left panel, of Ref. [112].

7.1 Glucose–insulin dynamics

I perform my test adopting the last model presented in Sec. 6.3.2. This model is compact, it properly describes the interactions between the most important organs involved in the regulation of the glucose level, and implements saturation and delay effects in explicit forms. Finally, all its functions are analytical. This makes it possible to derive analytical results on the existence, uniqueness, and stability of the solutions, which ensure the robustness of the model and the possibility of performing numerical simulations and fitting.

I start from Eqs. (6.63) and (6.65), without accounting for physical exercise, namely,

$$\frac{\mathrm{d}I}{\mathrm{d}t} = I_{\text{in}} + \beta f_1(G(t-\tau_1)) - f_6(I), \tag{7.1}$$

$$\frac{\mathrm{d}G}{\mathrm{d}t} = G_{\text{in}} - f_2(G) - \gamma f_3(G) f_4(I) + f_5(I(t-\tau_2)), \tag{7.2}$$

First, I tested my code by reproducing the plots of Fig. 4 in Ref. [112], using a linear insulin elimination rate $d_i\, I$ and $\beta = \gamma = 1$, $G_{\text{in}} = I_{\text{in}} = 0$, and the plots of Fig. 11 in Ref. [107]. The results of this preliminary analyses are reported in Figs 7.1 and 7.2, respectively. These results correctly show ultradian oscillations with a period of about two hours, with insulin that follows glucose after a few minutes. Accordingly, in the phase-space picture the solution is attracted to a limit cycle.

To test the robustness of the two-compartment model of Eqs. (7.1) and (7.2), I simulated the evolution of glucose concentration for a healthy subject (parameters in Tables 6.1 and 6.2) receiving enteral nutrition.

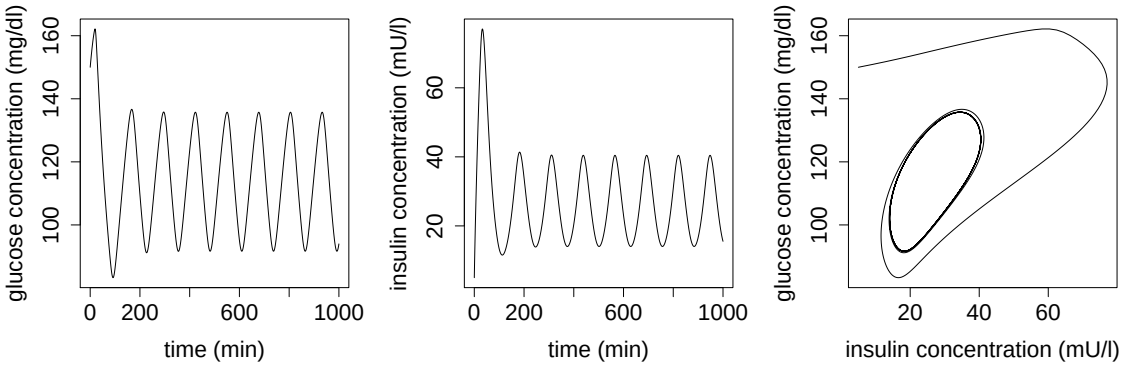

Figure 7.2: Evolution of plasma glucose (left panel) and insulin (central panel) concentrations and glucose-insulin phase-space plot (right panel) for a subject with $\tau_1 = 5\,\text{min}$, $\tau_2 = 15\,\text{min}$, $G_{\text{in}} = 0$, $\beta = 0.4$, $\gamma = 0.55$, with initial glucose and insulin concentrations of $150\,\text{mg/dl}$ and $5\,\text{mU/l}$. Values of other parameters as in Tables 6.1 and 6.2. The results were obtained integrating Eqs. (7.1) and (7.2) as in Fig. 11 of Ref. [107].

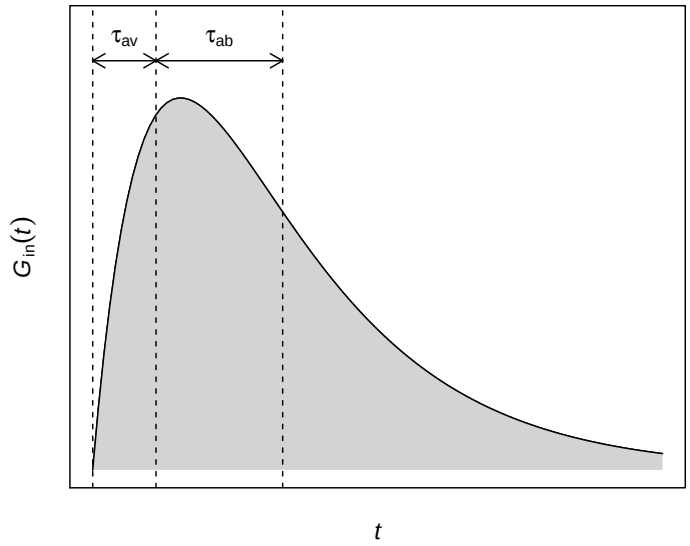

Figure 7.3: Rate of glucose intake for a meal. τ_{av} is the time needed to make the meal available for absorption and τ_{ab} is the time taken to absorb glucose.

The rate of glucose absorption is modelled with a standard absorption curve

$$G_{\text{in}}(t) = \frac{G_{\text{meal}}}{\tau_{\text{ab}} - \tau_{\text{av}}} \left[e^{-(t-t_{\text{meal}})/\tau_{\text{ab}}} - e^{-(t-t_{\text{meal}})/\tau_{\text{av}}} \right], \tag{7.3}$$

where t_{meal} is the time at which the meal starts, τ_{av} is the time-scale needed to make the meal available for absorption, and τ_{ab} the time taken to absorb glucose (see Fig. 7.3). Thus, a total time of the order $\tau_{\text{av}} + \tau_{\text{ab}}$ is needed by the whole process.

First I simulated a fasting healthy patient with parameters as in Tables 6.1 and 6.2, normal pancreas efficiency ($\beta = 1$) and no insulin resistance ($\gamma = 1$). I started from initial glucose level of $90\,\text{mg/dl}$ and insulin level of $20\,\text{mU/l}$ and prolonged the simulation until the stationary oscillating

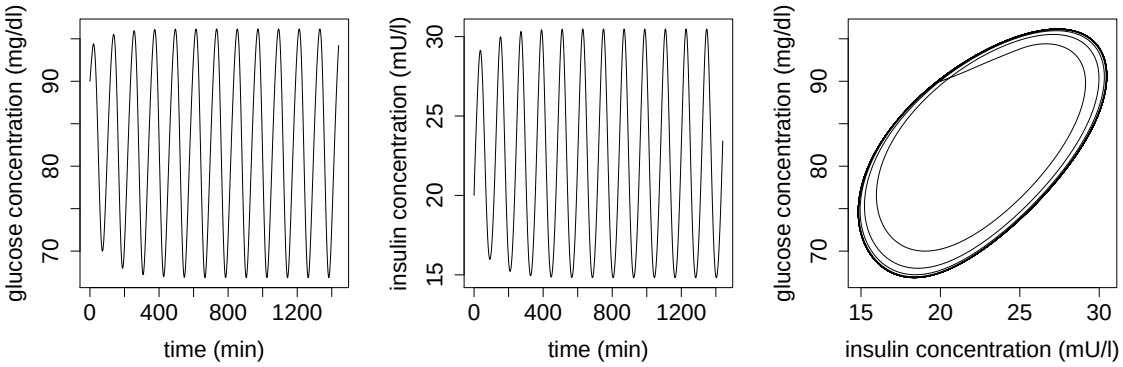

Figure 7.4: Evolution of plasma glucose (left panel) and insulin (central panel) concentrations and glucose-insulin phase-space plot (right panel) for a subject with $\tau_1 = 5\,\text{min}$, $\tau_2 = 15\,\text{min}$, $G_{\text{in}} = 0$, $\beta = \gamma = 1$, with initial glucose and insulin concentrations of 90 mg/dl and 20 mU/l. Values of other parameters as in Tables 6.1 and 6.2. The results were obtained integrating Eqs. (7.1) and (7.2) until the long-time oscillating state was attained.

state is eventually attained (see Fig. 7.4).

I then simulated the glucose dynamics for a subject receiving enteral nutrition, starting from this stationary oscillating state to guarantee that the result of the simulation is not affected by the choice of the initial condition. In Fig. 7.5, I plot the results of this simulation for a subject receiving three meals at $t_{\text{meal}} = 8\,\text{h}$, 13 h, 20 h. For each meal I assumed an intake of glucose of 20 g, 80 g, and 80 g, respectively, with absorption parameters $\tau_{\text{ab}} = 60\,\text{min}$, while $\tau_{\text{av}} = 30\,\text{min}$ for lunch and dinner and $\tau_{\text{av}} = 15\,\text{min}$ and for breakfast. The resulting rate of glucose administration throughout a whole day is plotted in the top left panel. In the top right panel I represent the phase-space co-evolution of glucose and insulin, while their time evolutions are pictured in the bottom panels. This simulation still shows self-sustained oscillation during fasting. After meals there are high peaks in glucose concentration, reaching values about 250 mg/dl, followed by peaks in insulin concentration. The delay between insulin production, insulin-stimulated glucose uptake, and the consequent decrease in insulin concentration causes the appearance of mild hypoglycaemic levels just after the hyperglycaemic peaks following glucose administration. After meals the glucose concentration increases and stimulates insulin production. This causes the removal of glucose from blood. However the insulin level remains quite high even after glucose has returned to a normal value. As a consequence, the glucose level keeps decreasing eventually reaching a value just above 60 mg/dl.

To test the robustness of this model for different types of meals, parametrised by different absorption rates, I repeated the same simulation using $\tau_{\text{ab}} = 36\,\text{min}$, and $\tau_{\text{av}} = 18\,\text{min}$ for lunch and dinner and $\tau_{\text{av}} = 7\,\text{min}$ for breakfast. This corresponds to a meal with less lipids and proteins and more sugars and carbohydrates. The results are shown in Fig. 7.6. Comparing these plots with Fig. 7.5, one notes that the glucose peaks increased from 180 mg/dl to about 230 mg/dl, remaining

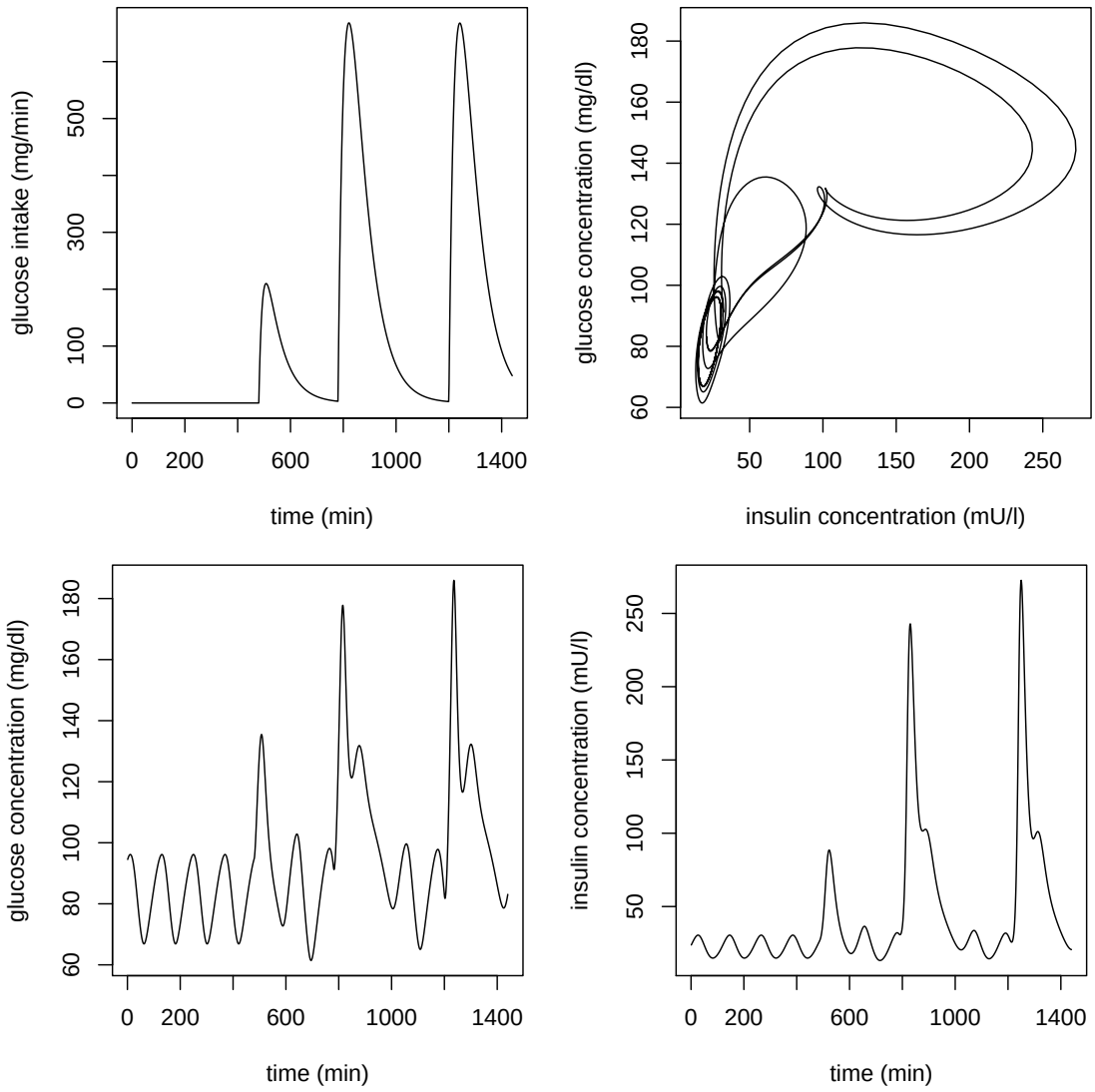

Figure 7.5: Simulation of glucose dynamics for a healthy subject receiving three meals at time $t_{\text{meal}} = 8\,\text{h}$, 13 h, and 20 h, with an intake of glucose of 20 g, 80 g, and 80 g, respectively. Absorption parameters $\tau_{\text{ab}} = 60\,\text{min}$, while $\tau_{\text{av}} = 30\,\text{min}$ for lunch and dinner and $\tau_{\text{av}} = 15\,\text{min}$ and for breakfast Upper left panel: glucose intake $G_{\text{in}}(t)$ over time. Upper right panel: phase-space solution. Lower panels: glucose and insulin time evolution.

quite well controlled by a relatively prompt insulin release. Indeed, insulin levels are more than doubled with respect to Fig. 7.6. This yields the appearance of a deeper hypoglycaemic trough.

To further test the model, I simulated the scenario of an intravenous infusion of 20 g of glucose in 60 s, the dose administered in a typical intravenous glucose tolerance test for a subject of about 70 kg [77]. This dose was administered at $t = 7\,\text{h}$, starting from the stationary oscillating state represented in Fig. 7.4. This simulation confirms the hypothesis formulated above. Although the rate of glucose administration (20 000 mg/min) is twenty times as high as in Fig. 7.6, the peak glucose concentration is still around 250 mg/dl and glucose levels go back to normal values very rapidly. This proves that the physiological mechanisms that prevent hyperglycaemic states are correctly modelled. However, insulin reaches a concentration of 500 mU/l and its effects last for

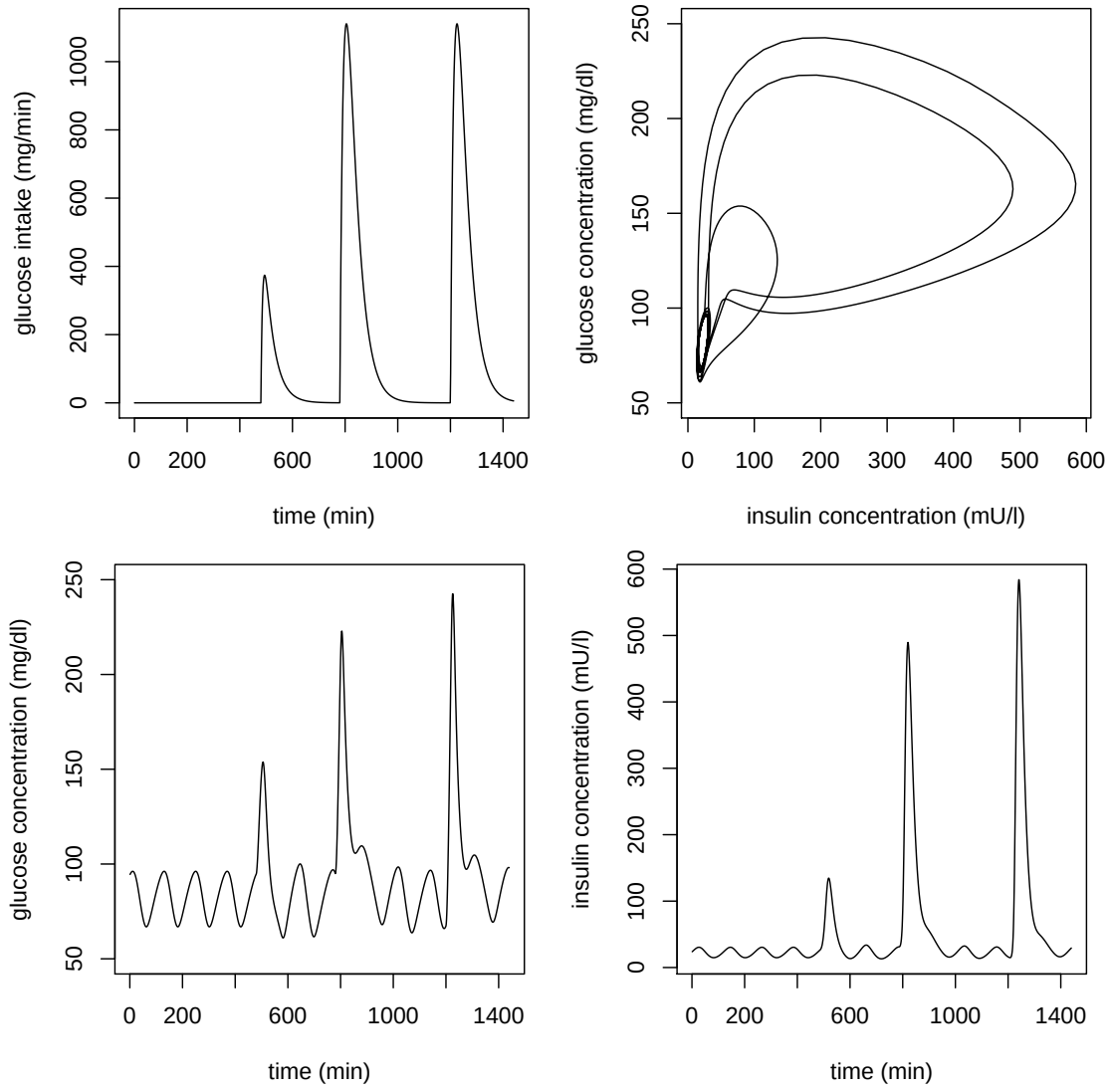

Figure 7.6: Simulation of glucose dynamics for a healthy subject receiving three meals as in Fig. 7.5. Absorption parameters $\tau_{\rm ab} = 36\,\text{min}$, while $\tau_{\rm av} = 18\,\text{min}$ for lunch and dinner and $\tau_{\rm av} = 7\,\text{min}$ and for breakfast Upper left panel: glucose intake $G_{\rm in}(t)$ over time. Upper right panel: phase-space solution. Lower panels: glucose and insulin time evolution.

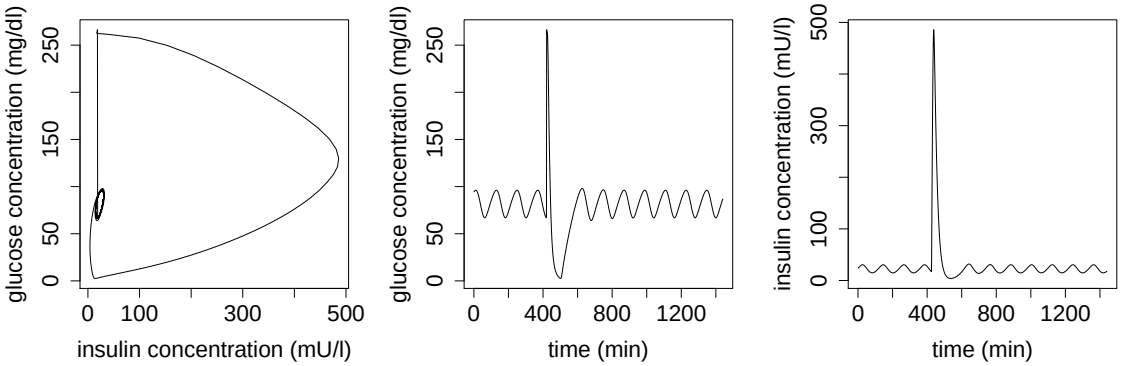

Figure 7.7: Glucose (left panel) and insulin (central panel) time evolutions and phase-space picture (right panel) for a healthy subject receiving an intravenous glucose bolus of 20 g at time $t = 7\,\text{h}$. Parameters as in Tables 6.1 and 6.2.

several minutes after the glucose bolus. This causes glucose concentration to drop to zero. This result is completely unrealistic and makes it apparent that this two-compartment model lacks a mechanism preventing serious hypoglycaemia.

7.2 The glucose-insulin-glucagon model

In the previous section I tested the performance of the system of Eqs. (7.1) and (7.2) in reproducing the coupled glucose-insulin dynamics in realistic simulated scenarios. I observed that this model is able to reproduce the physiological mechanisms preventing hyperglycaemic states, but not hypoglycaemia. In the case of a rapid intravascular glucose infusion, the glucose peak was followed by a deep non-physiological hypoglycaemic trough.

This model must be completed by adding a third compartment that implements the action of counter-regulatory hormones, primarily glucagon. Such hormones stimulate endogenous glucose production in response to a decrease of glucose concentration below physiological values. I propose the following system of equations

$$\frac{\mathrm{d}I}{\mathrm{d}t} = I_{\mathrm{in}} + \beta_I f_1(G(t-\tau_1)) - f_6(I), \tag{7.4}$$

$$\frac{\mathrm{d}L}{\mathrm{d}t} = \beta_L f_7(G) - d_l\, L, \tag{7.5}$$

$$\frac{\mathrm{d}G}{\mathrm{d}t} = G_{\mathrm{in}} - f_2(G) - \gamma_I f_3(G) f_4(I) + f_5(I(t-\tau_2)) + \gamma_L f_8(L). \tag{7.6}$$

With respect to Eqs. (7.1) and (7.2), I have introduced the variable L, representing the amount of glucagon in plasma and the term $\gamma_L f_8(L)$ in the glucose equation. The new functions

$$f_7(G) = \frac{R_l}{1 + e^{(G/V_g - C_7)/a_2}} \tag{7.7}$$

and

$$f_8(L) = \frac{R_{gl}}{1 + e^{-\alpha_L (L/V_p - C_8)}} \tag{7.8}$$

describe the rate of glucagon production by pancreas and the rate of glucagon-stimulated glucose production. To model pathological situations I have introduced β_L and γ_L, which parametrise the efficiency of pancreas glucagon production and the efficiency of liver glucagon-stimulated glucose release. Both parameters vary from 0 to 1 and are equal to 1 in healthy subjects.

Thanks to this new formulation of the glucose-insulin-glucagon dynamics, the endogenous glucose production depends on plasma concentrations of both insulin and counter-regulatory hormones (mainly glucagon, see Secs. 6.1), with two very different time scales. The old $f_5(I)$ term represents

Parameter	Value	Units
R_l	120	ng/min
C_7	920	mg/l
a_2	100	mg/l
d_l	0.2	min^{-1}
R_{gl}	750	mg/min
C_8	180	ng/l
α_L	0.1	ng/l

Table 7.1: Values of additional parameters introduced in the glucose-insulin-glucagon model of Eqs. (7.4), (7.5), and (7.6).

slow and delayed glucose release, which contributes to maintaining glucose homoeostasis during fasting periods (in the following simulations I have used $\tau_1 = 5\,\text{min}$ and $\tau_2 = 15\,\text{min}$ as in Secs. 7.1). The new term $f_8(L)$ represents instead fast and high-rate glucose release (mainly by liver, but also by kidneys) stimulated by counter-regulatory hormones. This terms provides the necessary glucose supply in situations of intense physical activity or to counteract hypoglycaemia. The term $f_3(G)f_4(I)$ still represents in a very general way all the processes that remove glucose from blood in a hormone-dependent way (e.g., liver or muscle insulin-stimulated uptake).

Finally, in Eq. (7.5) I have introduced a term to model glucagon removal proportional to the amount of glucagon. This term is simplified with respect to the expression for insulin degradation in Eq. (7.4). Although the two hormones are degraded similarly, the knowledge of the mechanisms at the basis of glucagon elimination is less precise (see Sec. 6.1.2 and 6.1.3). For this reason I have chosen a rougher approximation with respect to insulin.

The shapes of the new functions f_7 and f_8 and the values of their parameters (see Table 7.1) were chosen to mimic the observed behaviour for pancreas glucagon release and liver glucose production [148, 70, 145, 114]. The values of the other parameters have been maintained as in Tables 6.1 and 6.2.

7.3 Stability analysis

I investigated the stability analysis of the solutions of the system of Eqs. (7.4), (7.5), and (7.6) following the semi-analytical approach illustrated in Sec. 6.3.2 [60]. First, I have proven that the system always admits one unique steady-state solution (I^*, L^*, G^*), satisfying

$$I_{\text{in}} + \beta_I f_1(G^*) - f_6(I^*) = 0, \tag{7.9}$$

$$\beta_L f_7(G^*) - d_l\, L^* = 0, \tag{7.10}$$

$$G_{\text{in}} - f_2(G^*) - \gamma_I f_3(G^*) f_4(I^*) + f_5(I^*) + \gamma_L f_8(L^*) = 0. \tag{7.11}$$

Since the function f_6 is monotonically increasing [see Eq. (6.64)], one can write

$$I^* = h(\beta_I\, f_1(G^*)), \tag{7.12}$$

with

$$h(x) = \frac{C_6 V_p}{d_i C_6 V_p / (I_{\text{in}} + x) - 1}. \tag{7.13}$$

Thus, Eq. (7.9) admits a positive solution of I^* only if h is positive, that is if $d_i C_6 V_p > I_{\text{in}} + x$. Since $\beta_I\, f_1$ is always smaller than R_m [see Eq. (6.22)] h is positive for patients not receiving insulin administration ($I_{\text{in}} = 0$), for realistic values of the parameters d_i, C_6, and V_p (see Tables 6.1 and 6.2). Furthermore, using the chosen values of the system parameters, h is positive also if

$$I_{\text{in}} < d_i C_6 V_p - R_m \approx 240\,\text{mU/min}. \tag{7.14}$$

When these conditions are satisfied, one can proceed to solve the system. Equation (7.10) gives

$$L^* = \frac{\beta_L}{d_l} f_7(G^*). \tag{7.15}$$

Replacing those values of I^* and L^* in Eq. (7.11) reads

$$g(G^*) = 0, \tag{7.16}$$

with

$$g(x) = G_{\text{in}} - f_2(x) - \gamma_I f_3(x) f_4(h(\beta_I\, f_1(x))) + f_5(h(\beta_I\, f_1(x))) + \gamma_L f_8(\beta_L\, f_7(x)/d_l). \tag{7.17}$$

Following the same steps as in Sec. 6.3.2, it is easy to prove that Eq. (7.16) always admits a solution, if Eq. (7.14) is satisfied.

First, I note that

$$g(0) = G_{\text{in}} + f_5(h(\beta_I\, f_1(0))) + \gamma_L f_8(\beta_L\, f_7(0)/d_l) > 0, \tag{7.18}$$

since, $f_2(0) = f_3(0) = 0$, while f_5 and f_8 are always positive for any values of their arguments. Moreover

$$\lim_{x \to +\infty} g(x) = -\infty, \tag{7.19}$$

because, for $x \to +\infty$, $f_3 \to +\infty$ all the other functions f_i, $i \neq 3$, are bound and, in particular,

$$\lim_{x\to+\infty} f_4(h(\beta_I\, f_1(x))) = f_4(h(\beta_I\, R_g)) > 0, \tag{7.20}$$

under condition (7.14).

Hence, g admits a solution for $x > 0$ because all the involved functions are continuous for $x > 0$. The solution is also unique because g is monotonically decreasing. Indeed,

$$\begin{aligned} g'(x) = &-f_2'(x) - \gamma_I f_3'(x) f_4(h(\beta_I\, f_1(x))) - \gamma_I f_3(x) f_4'(h(\beta_I f_1(x))) h'(\beta_I f_1(x)) \beta_I f_1'(x) \\ &+ f_5'(h(\beta_I f_1(x))) h'(\beta_I f_1(x)) \beta_I f_1'(x) + \gamma_L f_8'(\beta_L f_7(x)/d_l) \beta_L f_7'(x)/d_l \end{aligned} \tag{7.21}$$

is negative for any $x > 0$ since $f_i > 0$, $h' > 0$, $f_i' < 0$ for $i = 5, 7$ and $f_i' > 0$ otherwise.

I then linearise Eqs. (7.4), (7.5), and (7.6) around the stationary solution $x^* = (I^*, L^*, G^*)$, using the method presented in Appendix B. Defining $y(t) = (i(t), l(t), g(t))$, with $i(t) = I(t) - I^*$, $l(t) = L(t) - L^*$, and $g(t) = G(t) - G^*$,

$$\dot{y}(t) = \sum_{i=0}^{2} A_i\, y(t - \tau_i), \tag{7.22}$$

where I have defined $\tau_0 = 0$, and

$$A_0 = \begin{pmatrix} -f_6'(I^*) & 0 & 0 \\ 0 & -d_l & \beta_L f_7'(G^*) \\ -\gamma_I f_3(G^*) f_4'(I^*) & \gamma_L f_8'(L^*) & -f_2'(G^*) - \gamma_I f_3'(G^*) f_4(I^*) \end{pmatrix}, \tag{7.23}$$

$$A_1 = \begin{pmatrix} 0 & 0 & \beta_I f_1'(G^*) \\ 0 & 0 & 0 \\ 0 & 0 & 0 \end{pmatrix}, \tag{7.24}$$

$$A_2 = \begin{pmatrix} 0 & 0 & 0 \\ 0 & 0 & 0 \\ f_5'(I^*) & 0 & 0 \end{pmatrix}. \tag{7.25}$$

Equation (7.22) admits solutions of the form $y = \Re\left(e^{\lambda t} v\right)$, with $v \in \mathbb{C}$ and $v \in \mathbb{C}^3$. These solutions are non-trivial if

$$\det\left[\lambda I - \sum_{i=0}^{2} A_i e^{-\lambda \tau_i}\right] = 0. \tag{7.26}$$

The corresponding characteristic equation is

$$\lambda^3 + A\lambda^2 + B\lambda + C + D\lambda e^{-\lambda\tau_1} + E e^{-\lambda\tau_1} + F\lambda e^{-\lambda(\tau_1+\tau_2)} + G e^{-\lambda(\tau_1+\tau_2)}, \tag{7.27}$$

with

$$A = f_6'(I^*) + d_l + f_2'(G^*) + \gamma_I f_3'(G^*) f_4(I^*) + \beta_L f_7'(G^*), \tag{7.28}$$

$$\begin{aligned} B = {} & f_6'(I^*)\left[d_l + f_2'(G^*) + \gamma_I f_3'(G^*) f_4(I^*) + \beta_L f_7'(G^*)\right] \\ & + d_l\left[f_2'(G^*) + \gamma_I f_3'(G^*) f_4(I^*)\right] - \beta_L \gamma_L f_7'(G^*) f_8'(L^*), \end{aligned} \tag{7.29}$$

$$C = f_6'(I^*)\left[d_l f_2'(G^*) + d_l \gamma_I f_3'(G^*) f_4(I^*) - \beta_L \gamma_L f_7'(G^*) f_8'(L^*)\right], \tag{7.30}$$

$$D = \beta_I \gamma_I f_1'(G^*) f_3(G^*) f_4'(I^*), \tag{7.31}$$

$$E = \beta_I \gamma_I f_1'(G^*) f_3(G^*) f_4'(I^*) d_l, \tag{7.32}$$

$$F = -\beta_I f_1'(G^*) f_5'(I^*), \tag{7.33}$$

$$G = -\beta_I f_1'(G^*) f_5'(I^*) d_l. \tag{7.34}$$

All the above coefficients are positive since all the terms f_i and f_i' are positive, except f_5' and f_7' which are negative. The fixed point x^* is stable when the perturbation y exponentially decreases with time, that is when $\Re(\lambda) < 0$, and is unstable otherwise. Thus, the boundary of the stability region is given by the configurations that admit solutions with $\Re(\lambda) = 0$, namely $\lambda = i\omega$, with $\omega \in \mathbb{R}$. One must then solve the complex equation

$$-i\omega^3 - A\omega^2 + iB\omega + C + iD\omega e^{-i\omega\tau_1} + Ee^{-i\omega\tau_1} + iF\omega e^{-i\omega(\tau_1+\tau_2)} + Ge^{-i\omega(\tau_1+\tau_2)} = 0. \tag{7.35}$$

This system is equivalent to two real equations that fix the solution ω and describe an $(n-1)$-dimensional manifold in the n-dimensional parameter space.

It is convenient to isolate the $e^{-i\omega\tau_1}$ term as

$$\frac{i\omega^3 + A\omega^2 - iB\omega - C}{iD\omega + E + (iF\omega + G)e^{-i\omega\tau_2}} = e^{-i\omega\tau_1}. \tag{7.36}$$

The right-hand side describes a unit circle in the complex plane (see, dashed circle in Fig. 7.8) that is covered infinite times as ω runs from 0 to ∞. The left-hand side is instead a spiral (solid curve) starting at $\omega = 0$ at the real point $-C/(E+G)$ (open dot), whose shape and speed of covering by varying ω depends on the values of the parameters of the system. Let me define η as the vector of the system parameters excluding τ_1. The left-hand side is a complex function $R(\omega, \eta)$ of ω and η, which does not depend on τ_1. Thus, for any values of η, I can take the squared modulus of Eq. (7.36), which gives a real equation for ω, given the values of η:

$$|R(\omega, \eta)|^2 = 1. \tag{7.37}$$

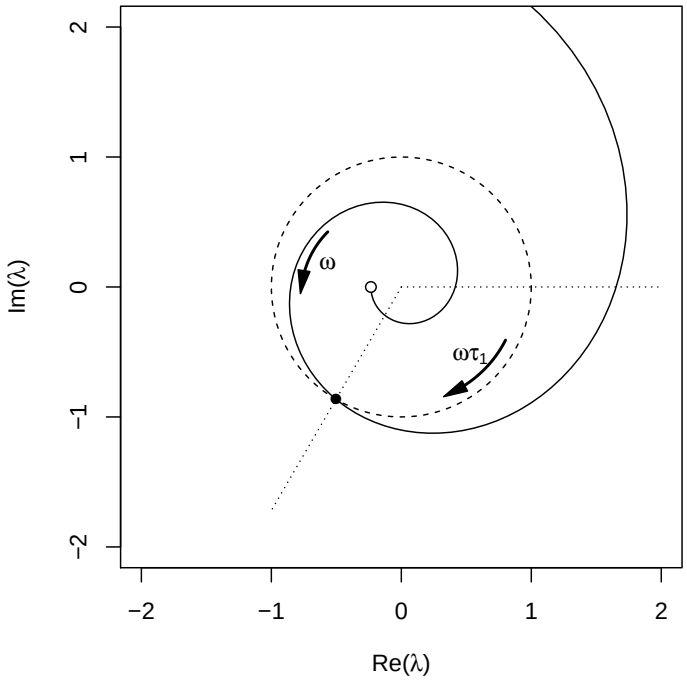

Figure 7.8: Graphical representation of Eq. (7.36) in the complex plane λ. The solid curve is the left-hand side, covered by the real parameter ω from 0 to $+\infty$. The dashed circle represents the right-hand side of the equation. The angle is the product $\omega\tau_1$.

Once all the m solutions ω_j, with $j = 1, \ldots, m$ of this equation are determined (closed dot in Fig. 7.8, there $m = 1$), one may find the corresponding values of τ_{1j} that solve Eq. (7.36).

$$\begin{cases} \cos(\omega_j \tau_{1j}) = \Re(R(\omega, \eta)), \\ \sin(\omega_j \tau_{1j}) = -\Im(R(\omega, \eta)). \end{cases} \tag{7.38}$$

Defining $\tau_{1j}^{(0)}$, the smallest τ_{1j} that solves the above system, there is a countable set of solutions

$$\tau_{1j}^{(k)} = \tau_{1j}^{(0)} + \frac{2\pi}{\omega_j}, \qquad k \in \mathbb{N}, \tag{7.39}$$

for each ω_j. Varying the values of η, the solutions $\left(\eta, \tau_{1j}^{(k)}\right)$ describe a countable set (for $j = 1, \ldots, m$ and $k \in \mathbb{N}$) of $(n-1)$-dimensional manifolds in the n-dimensional space of parameters over which there are oscillating, non-damped, and non-growing solutions of Eq. (7.22).

Following the value of an eigenvalue $\lambda_j(\eta)$ of Eq. (7.22) along a curve $\mathcal{C}_\eta$ in the parameter space, by varying η, the real part of λ_j changes sign whenever one crosses a surface $\left(\eta, \tau_{1j}^{(k)}\right)$. Accordingly, the solution y switches from stable to unstable or *vice versa*. A steady-state solution x^* is stable in the parameter region $\mathcal{S}$ where all λ_j have a negative real part. The boundary of $\mathcal{S}$ is then built by pieces of manifolds $\left(\eta, \tau_{1j}^{(k)}\right)$.

I investigated the stability of the solution x^* in a cross-section of the parameter space (τ_1, τ_2),

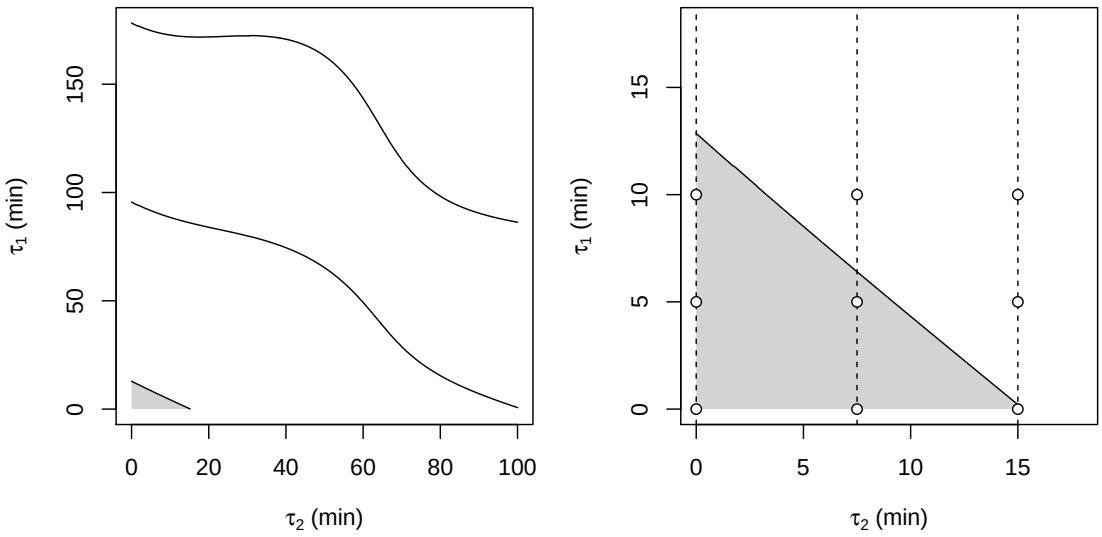

Figure 7.9: Stability diagram of the steady-state solution of the system of Eqs. (7.4), (7.5), and (7.6) in the plane τ_1 and τ_2 for $G_{\text{in}} = I_{\text{in}} = 0$ and $\beta_I = \beta_L = \gamma_I = \gamma_L = 1$. Solid lines represent the parameter surfaces where the real part of an eigenvalue of the linear equation Eq. (7.22) is zero. The grey area represents the region where the steady-state solution is stable, that is where every eigenvalue λ_j has a negative real part. Left panel: zoom on the region $\tau_1 < 18\,\text{min}$, $\tau_2 < 18\,\text{min}$. The evolution of (I, L, G) for the parameters represented by dots $\tau_1 = 0$, 5, and 10 min, and $\tau_2 = 0$, 7.5, and 15 min has been numerically integrated and the results are shown in Figs. 7.16 and 7.17.

by fixing the values of all the other parameters as in Tables 6.1, 6.2, and 7.1, and for a fasting healthy subject with $G_{\text{in}} = I_{\text{in}} = 0$ and $\beta_I = \beta_L = \gamma_I = \gamma_L = 1$. I solved Eq. (7.37) for ω_j by varying τ_2. Then, I derived the corresponding values of $\tau_{1j}^{(0)}$ from Eq. (7.38) and eventually plot the corresponding curves in the plane (τ_1, τ_2) in Fig. 7.9 (left panel: plane region $\tau_1 < 100\,\text{min}$ and $\tau_1 < 180\,\text{min}$; right panel: zoom on region $\tau_1 < 18\,\text{min}$ and $\tau_1 < 18\,\text{min}$). These curves divide the plane in several regions. By passing from one region to another, the sign of the real part of at least one eigenvalue λ_j changes sign. Conversely, if one moves inside a region, the real parts of all eigenvalue maintains their own signs. Thus, it is enough to compute the sign of the real parts of all λ_j in one point per region to know their signs in all the phase space. The regions where the solutions are stable are those where all the real parts of λ_j are negative (grey area). For the adopted parameter values, the steady-state solution (I^*, L^*, G^*) is stable only in an approximately triangular region with $\tau_1 + \tau_2 \lesssim 15\,\text{min}$. Outside the solution is expected to converge to a limit circle, as observed in Sec. 7.1 for the glucose-insulin system, corresponding to physiological ultradian oscillations (see Sec. 7.4).

I analysed several phase-space sections by varying different parameters (G_{in}, I_{in}, β_I, γ_I, β_L and γ_L). For each parameter p I plotted the stability diagram in the plane (p, τ_1) for three sections corresponding to $\tau_2 = 0$, 7.5, and 15 min (dashed lines, right panel, Fig. 7.9). The results of this investigation are reported in Figs. 7.10–7.15. In each figure, the left, central, and right panels refer to the three values of $\tau_2 = 0$, 7.5, and 15 min. The lower panels are a zoom of the diagrams on

the physiologically-relevant region $\tau_1 < 40\,\text{min}$. As in Fig. 7.9, the real part of λ vanishes on the solid curves and the grey area is the region where the solution is stable. The dashed line, where present, indicates the boundary of the region where the solution is always stable independently of the value of τ_1.

Following Ref. [60], I first considered how the rate of glucose intake G_{in} affects the stability of the solution (Fig. 7.10). For values $G_{\text{in}} > 1646\,\text{mg/min}$, the solution is always stable. For lower values of G_{in}, the stability region has quite a peculiar shape. There is a narrow region, around $G_{\text{in}} = 250\,\text{mg/min}$ where the solution is always stable up to very high values of τ_1 ($\tau_1 \lesssim 35\,\text{mg/min}$). On the left and on the right of this strip, I can find unstable solutions at lower values of τ_1, down to $\tau_1 \approx 12\,\text{mg/min}$ around $G_{\text{in}} = 600\,\text{mg/min}$. On the left side (corresponding to a quasi-fasting condition), the boundary of the stability region strongly depends on τ_2, becoming deeper for higher vales of τ_2.

In Fig. 7.11, the solution becomes stable as soon as a patient receives insulin administration. Indeed, a continuous infusion rate $I_{\text{in}} \gtrsim 0.91\,\text{mU/min}$, corresponding to $1.3\,\text{U/day}$ is sufficient to make the solution stable and halt oscillations. To maintain the physiological ultradian oscillations, it would be necessary to make intermittent insulin administrations with a suitable frequency.

In Figs. 7.12 and 7.13 I investigated how pathological conditions correlated to the insulin-regulatory mechanisms affect the stability of the system. The solution becomes stable when either the pancreas is not able to react to increased glucose concentrations ($\beta_I \ll 1$, Fig. 7.12), as in patients affected by type-I diabetes, or tissues become resistant to insulin ($\gamma_I \ll 1$, Fig. 7.13). The latter scenario is typical of type-II-diabetic patients or of critically ill patients developing acute insulin resistance. A relatively small reduction of tissue insulin sensitivity ($\gamma_I \lesssim 0.77$) suffices to make the solution stable.

Finally, the stability diagrams in the planes (β_L, τ_1) and (γ_L, τ_1) are reported in Figs. 7.14 and 7.15, respectively. These plots show that the stability of the system is almost independent of pathological conditions associated with dysfunctions in the release of glucagon by the pancreas (β_L) or in the endogenous glucagon-stimulated glucose production (γ_L). This result is coherent with my choice of introducing Eq. (7.5) and the last term in Eq. (7.6) to model the prompt physiological reaction to very low glucose concentrations. Accordingly, the behaviour of the stationary state in fasting conditions mildly depends on glucagon dynamics.

The results of this stability analysis show that the solution tends to be stable when the system is forced by the presence of the administration of either glucose or insulin. From a physiological point of view, when there is a significant and constant intake of glucose, the pancreas stops producing glucagon and keeps releasing insulin to stimulate liver and other tissues to uptake glucose from the bloodstream. In this scenario, the system does not oscillate. Similarly, when there is a significant

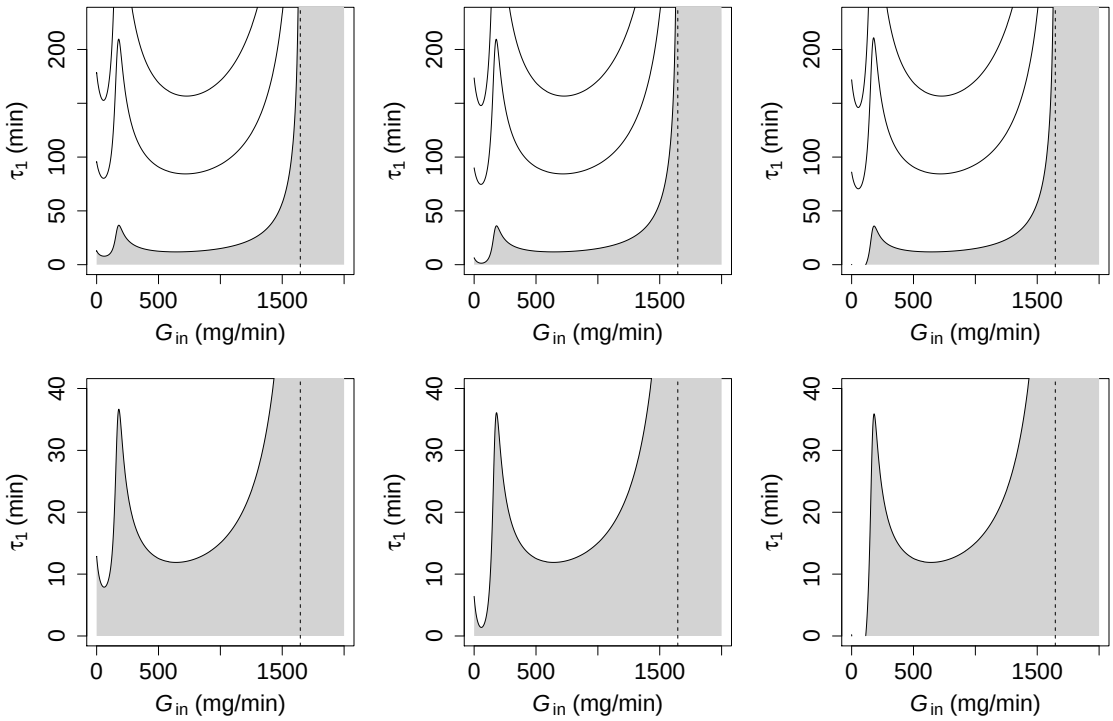

Figure 7.10: Stability diagrams of the steady-state solution of the system of Eqs. (7.4), (7.5), and (7.6) in the plane τ_1 and G_{in} for $\tau_2 = 0$, 7.5, 15 min (left, central, and right panels, respectively) for $I_{\text{in}} = 0$ and $\beta_I = \beta_L = \gamma_I = \gamma_L = 1$. The bottom panels are a zoom for $\tau_1 < 40$ min. Solid lines represent the surfaces where an eigenvalue of Eq. (7.22) is imaginary. The grey area represents the region where the steady-state solution is stable. The dashed line corresponds to the value of G_{in} ($G_{\text{in}} \approx 1646$ mg/min) above which the steady-state solution is stable for any value of τ_1.

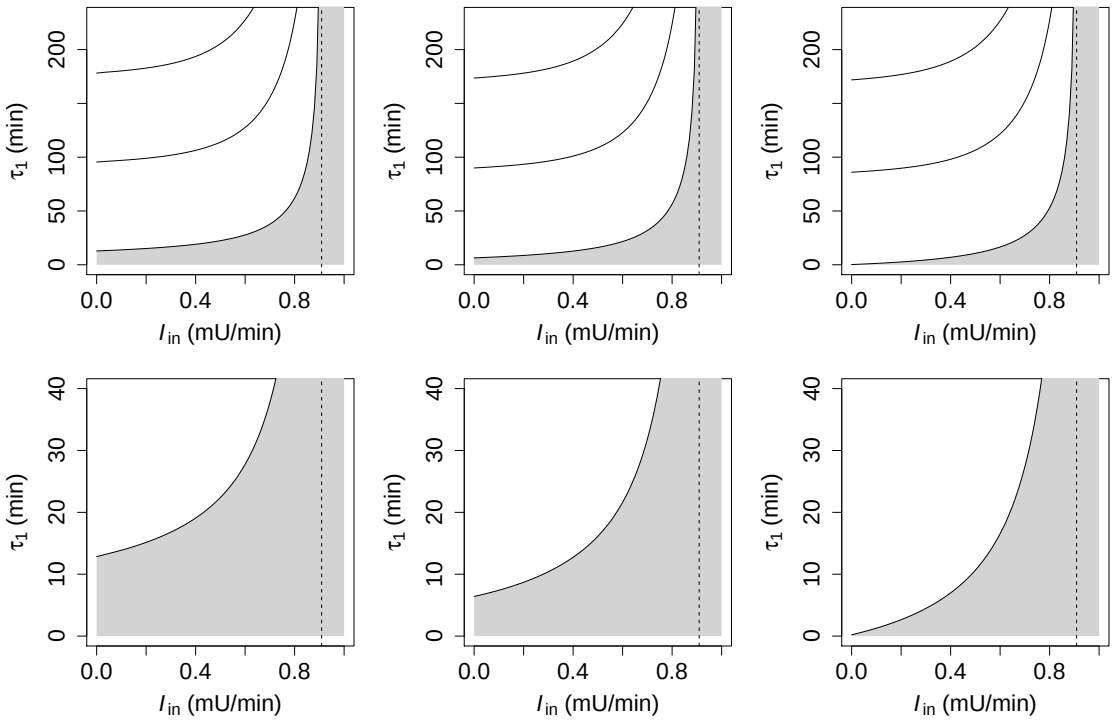

Figure 7.11: Stability diagrams of the steady-state solution of the system of Eqs. (7.4), (7.5), and (7.6) in the plane τ_1 and I_{in} for $\tau_2 = 0$, 7.5, 15 min (left, central, and right panels, respectively) for a subject with $G_{\text{in}} = 0$ and $\beta_I = \beta_L = \gamma_I = \gamma_L = 1$. The bottom panels are a zoom for $\tau_1 < 40$ min. When $I_{\text{in}} \gtrsim 0.91$ mU/min, the steady-state solution is stable for any value of τ_1.

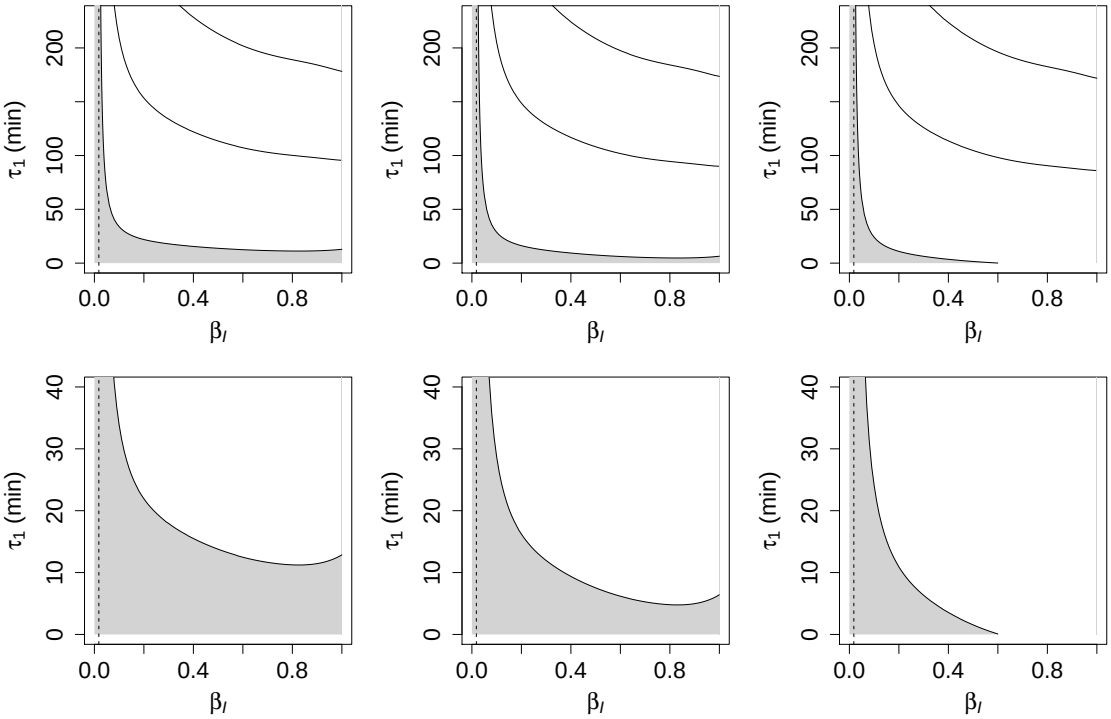

Figure 7.12: Stability diagrams of the steady-state solution of the system of Eqs. (7.4), (7.5), and (7.6) in the plane τ_1 and β_I for $\tau_2 = 0$, 7.5, 15 min (left, central, and right panels, respectively) for a subject with $G_{\text{in}} = I_{\text{in}} = 0$ and $\beta_L = \gamma_I = \gamma_L = 1$. The bottom panels are a zoom on the region $\tau_1 < 40$ min. When $\beta_I \lesssim 0.18$, the steady-state solution is stable for any value of τ_1.

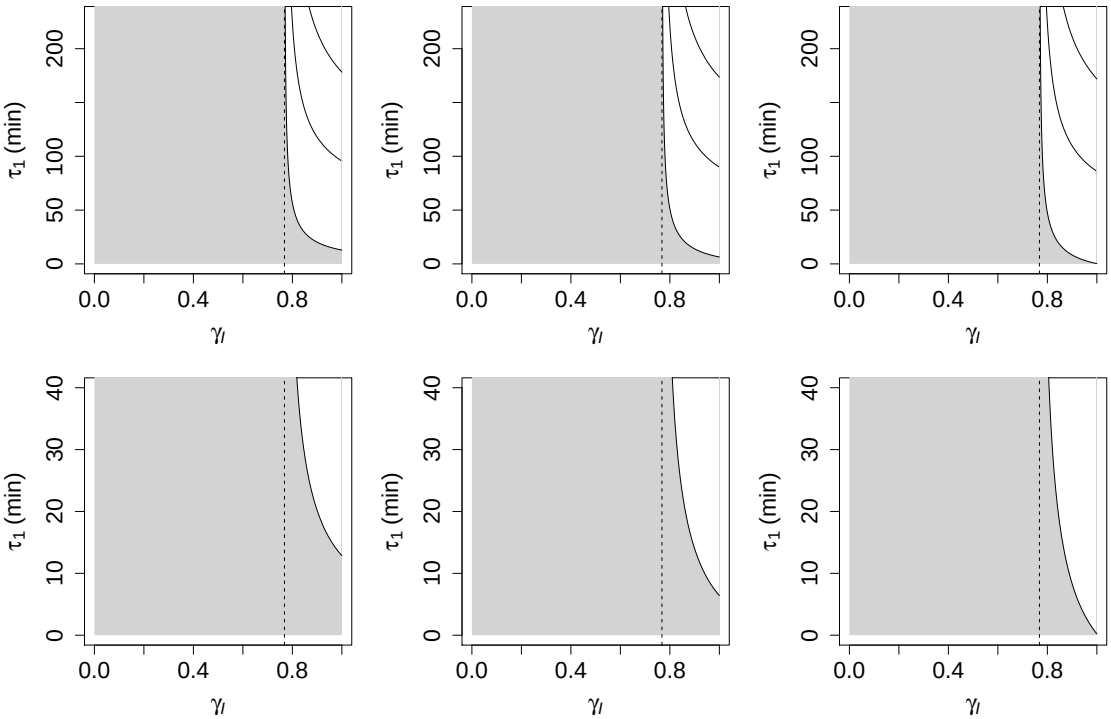

Figure 7.13: Stability diagrams of the steady-state solution of the system of Eqs. (7.4), (7.5), and (7.6) in the plane τ_1 and γ_I for $\tau_2 = 0$, 7.5, 15 min (left, central, and right panels, respectively) for a subject with $G_{\text{in}} = I_{\text{in}} = 0$ and $\beta_I = \beta_L = \gamma_L = 1$. The bottom panels are a zoom on the region $\tau_1 < 40$ min. When $\gamma_I \lesssim 0.77$, the steady-state solution is stable for any value of τ_1.

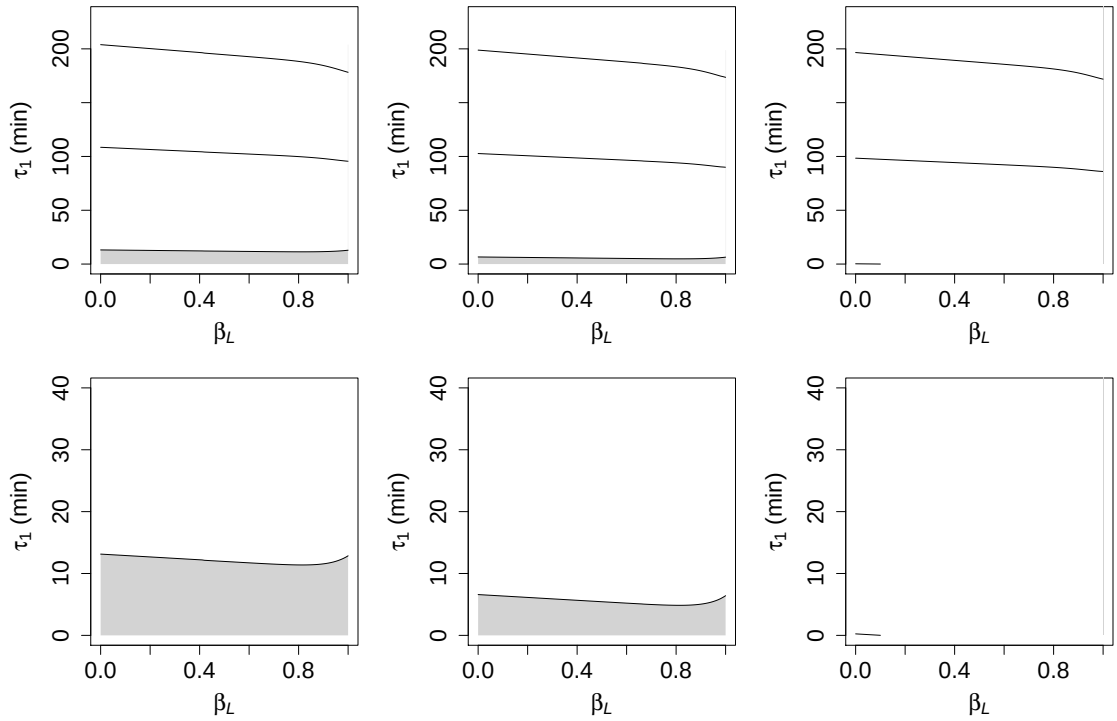

Figure 7.14: Stability diagrams of the steady-state solution of the system of Eqs. (7.4), (7.5), and (7.6) in the plane τ_1 and β_L for $\tau_2 = 0$, 7.5, 15 min (left, central, and right panels, respectively) for a subject with $G_{\text{in}} = I_{\text{in}} = 0$ and $\beta_I = \gamma_I = \gamma_L = 1$. The bottom panels are a zoom on the region $\tau_1 < 40$ min.

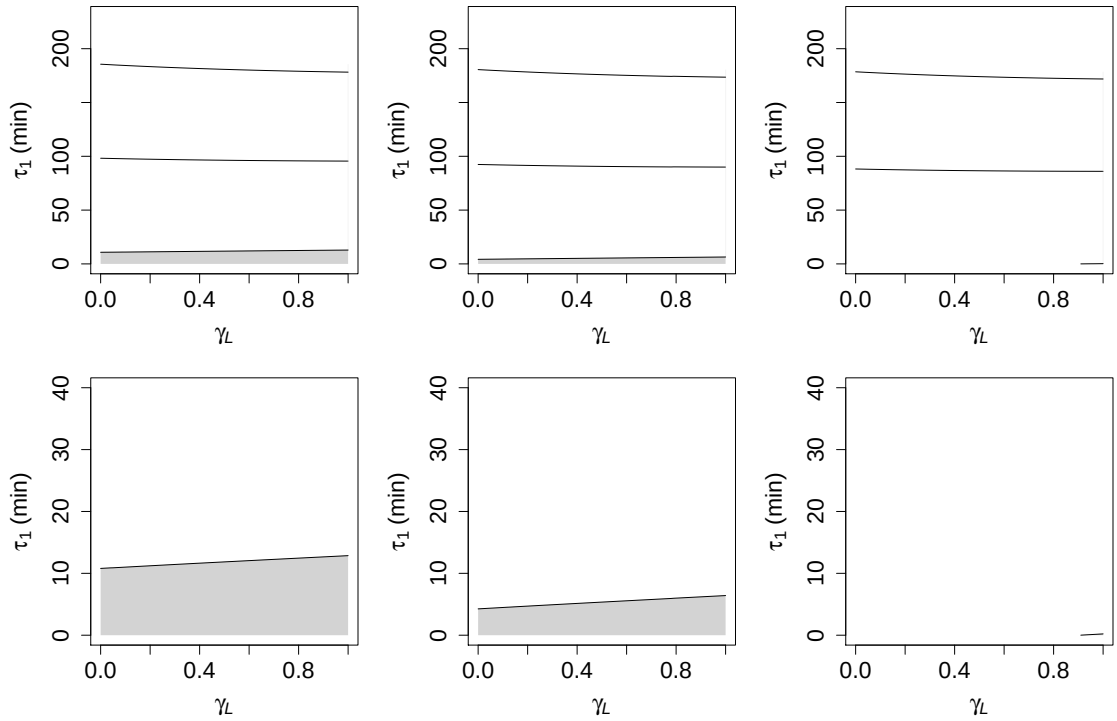

Figure 7.15: Stability diagrams of the steady-state solution of the system of Eqs. (7.4), (7.5), and (7.6) in the plane τ_1 and γ_L for $\tau_2 = 0$, 7.5, 15 min (left, central, and right panels, respectively) for a subject with $G_{\text{in}} = I_{\text{in}} = 0$ and $\beta_I = \beta_L = \gamma_I = 1$. The bottom panels are a zoom on the region $\tau_1 < 40$ min.

infusion of insulin, organs all cooperate to remove glucose and no oscillation is present.

Oscillations also disappear when either the pancreas efficiency in producing insulin (β_I) or the liver efficiency in releasing glucose (γ_I) is reduced. The reduction of time variability of physiological parameters is a typical signature of pathological condition [38].

7.4 Numerical simulations

I tested the new model introduced in Sec. 7.2 by simulating the dynamics of glucose, insulin, and glucagon in a subject with $\beta_I = \beta_L = \gamma_I = \gamma_L = 1$ for all the values of (τ_1, τ_2) represented by dots in Fig. 7.9 and in the scenarios studied in Sec. 7.1: fasting (Fig. 7.4), three daily meals with either long- or short- absorption time (Figs. 7.5 and 7.6), and IVGTT (Fig. 7.7). The former set of simulations allows one to investigate the model from a mathematical perspective and confirms the results of the stability analysis performed in Sec. 7.3. The latter simulations show that my model overcomes the limitations of glucose-insulin models illustrated in Sec. 7.1.

In Figs. 7.16 and 7.17 I report the results of the integration of Eqs. (7.4), (7.5) and (7.6) in the planes (G, I) and (L, I), respectively, for $\tau_1 = 0$, 5, and 10 min (lower, central, and upper panels) and $\tau_2 = 0$, 7.5, and 15 min (left, central, and right panels). All the trajectories with $\tau_2 = 0$ (left panels) or $\tau_1 = 0$ (lower panels) plus the trajectory with $\tau_1 = 5$ min and $\tau_2 = 15$ min converge to a steady-state point. Those solutions correspond indeed to phase-space points in the grey area of Fig. 7.9. The other three solutions, corresponding to points outside the grey area, are attracted to a limit circle.

The results of the simulations of a subject in a fasting condition or receiving different meals are reported in Fig. 7.18, 7.19, 7.20, and 7.21. In each figure I plot the time evolution of glucose, insulin, and glucagon concentrations (top panels) and the corresponding phase-space pictures in the glucose-insulin and glucose-glucagon planes (bottom left and central panels) and in the three-dimensional glucose-insulin-glucagon space (bottom right panel).

The simulation in the fasting condition (Fig. 7.18) shows that the model still reproduces ultradian oscillations on a time scale of about 100 min and the solution orbits on a three-dimensional limit-cycle in phase space. In this regime the endogenous glucose production is dominated by fluctuations in insulin concentration and glucagon release oscillates around the basal level.

The organism reaction to enteral glucose intake is reported in Figs. 7.19 and 7.19, starting from the stationary limit-cycle of the fasting condition. The phase-space path is quite complex. After glucose absorption, the pancreas starts to produce insulin while glucagon release is inhibited. Endogenous glucose production is halted and insulin-stimulated glucose uptake is maximum.

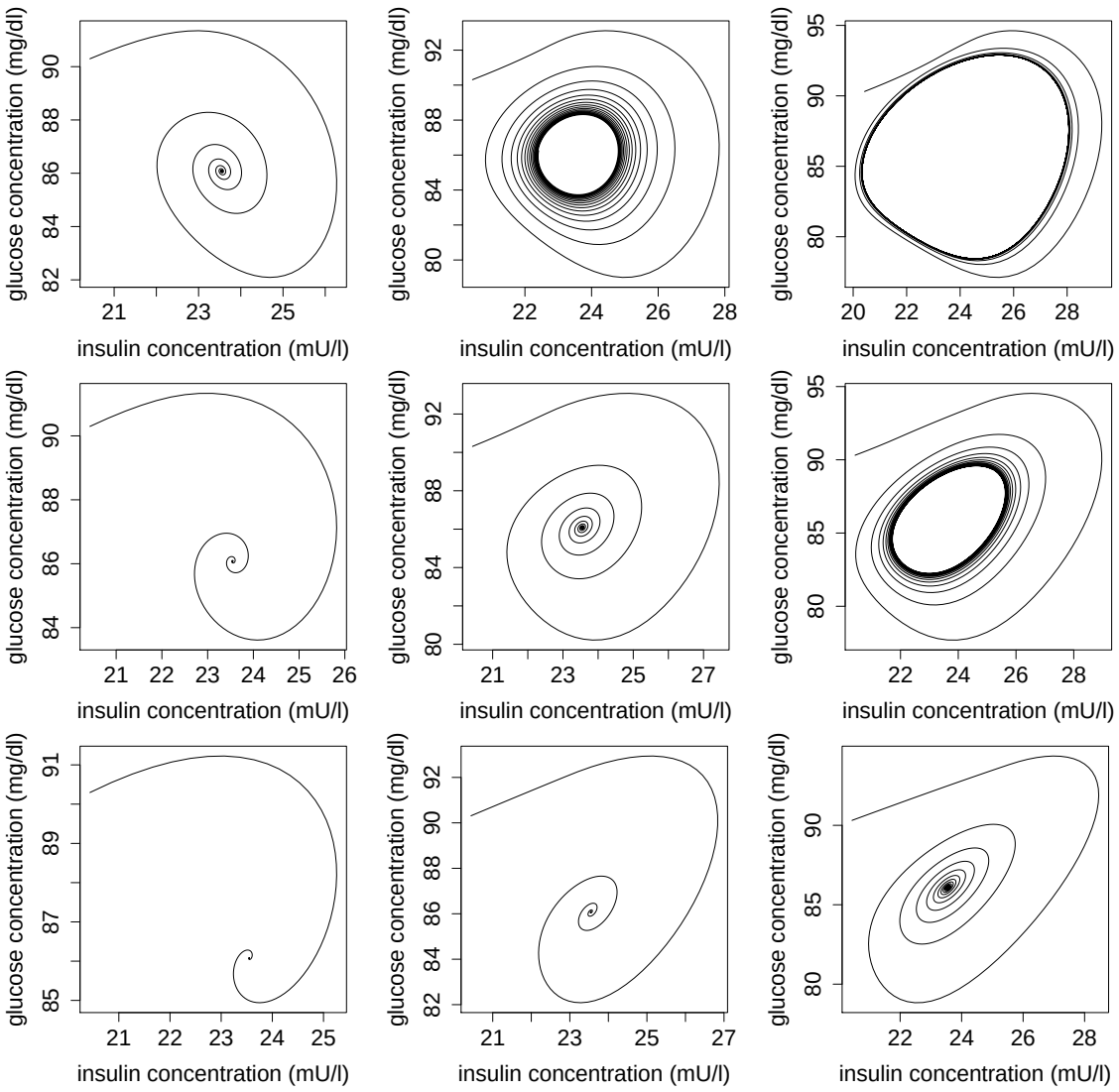

Figure 7.16: Trajectories in the plane (G, I) for $\tau_1 = 0$, 5, and 10 min (lower, central, and upper panels) and $\tau_2 = 0$, 7.5, and 15 min (left, central, and right panels), corresponding to the dots in Fig. 7.9. In all panels $\beta_I = \beta_L = \gamma_I = \gamma_L = 1$ and the system parameters were chosen as in Tables 6.1, 6.2, and 7.1.

Glucose concentration never reaches hypoglycaemic level. Indeed, when glucose concentration goes below the normal level, a prompt release of glucagon stimulates endogenous glucose release. Insulin excess is eventually eliminated and a normal oscillatory state is restored.

This mechanism protecting against hypoglycaemia is even more active after a sudden intravenous administration of 20 g of glucose, as shown in Fig. 7.18. In this scenario, the insulin release is huge to counteract hyperglycaemia. As a consequence glucose goes down to a hypoglycaemic level. However, this state lasts for a very short time, since the glucagon release stimulates a strong endogenous production of glucose, which reaches its maximum rate (as in a regime of intense physical activity) and promptly restores the normal state. Using the full model of Eqs. (7.4), (7.5), and (7.6) the glucose concentration never approaches zero as in the simulation of Fig. 7.7, based on Eqs. (7.1) and (7.2).

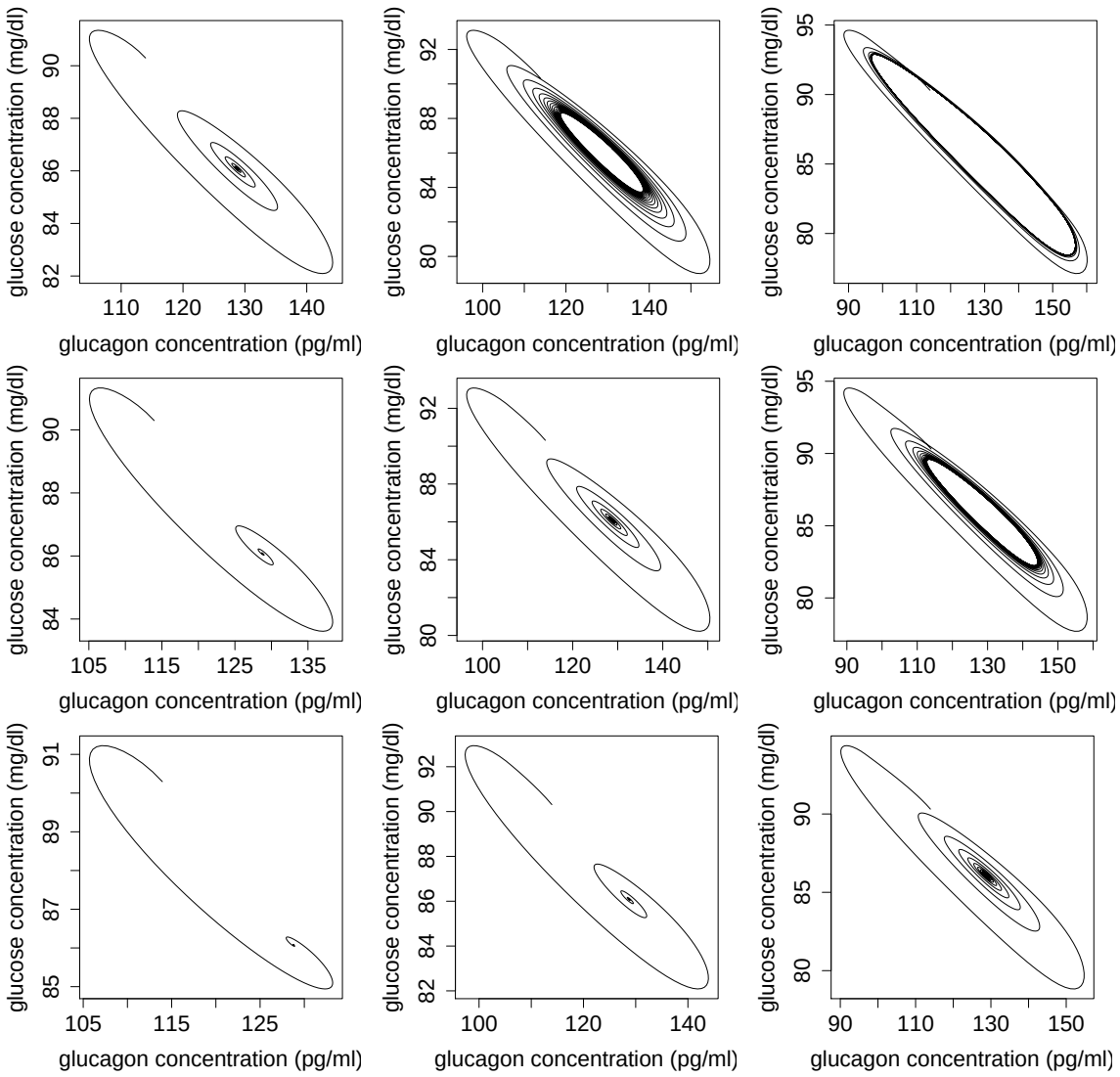

Figure 7.17: Trajectories in the plane (G, L) for $\tau_1 = 0$, 5, and 10 min (lower, central, and upper panels) and $\tau_2 = 0$, 7.5, and 15 min (left, central, and right panels), corresponding to the dots in Fig. 7.9. In all panels $\beta_I = \beta_L = \gamma_I = \gamma_L = 1$ and the system parameters were chosen as in Tables 6.1, 6.2, and 7.1.

7.5 Model fitting

The aim of the analysis presented in this Section is to study whether data available in the electronic health record *MargheritaTre* are informative enough to estimate the parameters of the model developed in this Chapter and to appreciate differences with previous models. Only two examples are reported for illustrative purposes and no population models will be constructed.

Diabetic patient

First, I tested my model on a diabetic patient for whom measurements of glucose concentrations were available with higher frequency (one measure every 5 min) with respect to data collected with

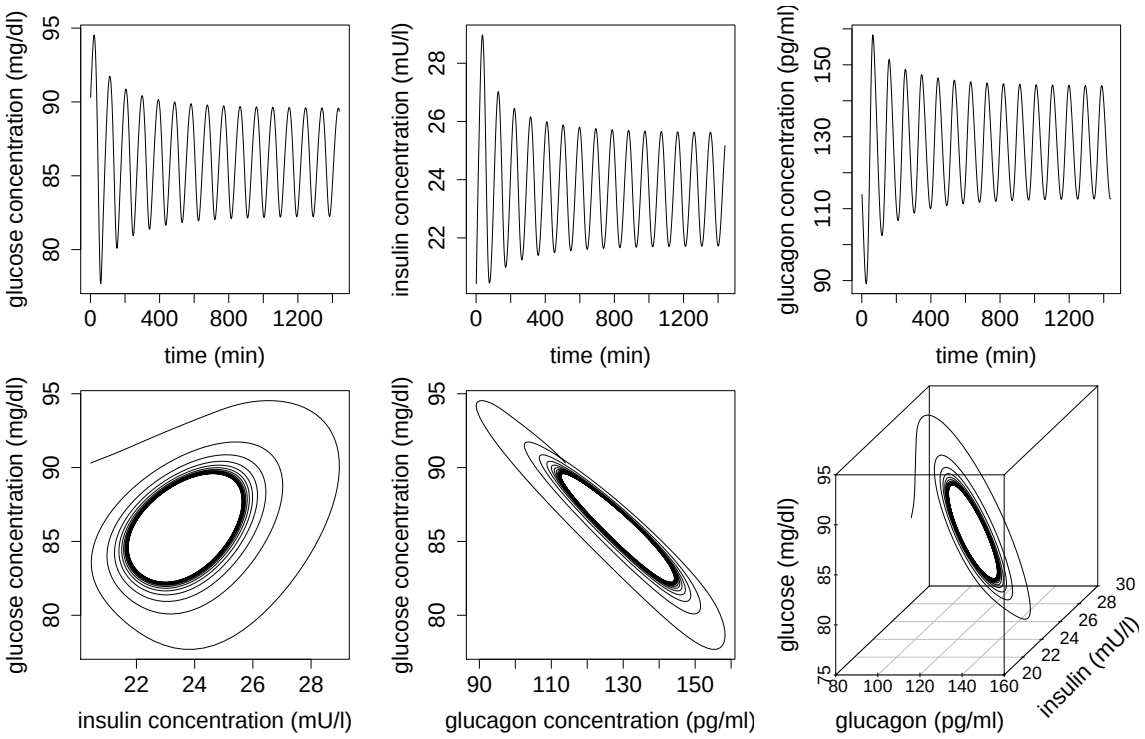

Figure 7.18: Evolution of plasma glucose, insulin, and glucagon concentrations (top panels) and phase-space plots in glucose-insulin and glucose-glucagon planes (bottom left and central panels) and three-dimensional glucose-insulin-glucagon space (bottom right panel) for a subject with $\tau_1 = 5\,\text{min}$, $\tau_2 = 15\,\text{min}$, $G_{\text{in}} = 0$, $\beta_I = \gamma_I = \beta_L = \gamma_L = 1$, with initial glucose, insulin, and glucagon concentrations of 90 mg/dl, 20 mU/l, and 115 pg/ml. Values of other parameters as in Tables 6.1, 6.2, and 7.1. The results were obtained integrating Eqs. (7.4), (7.5), and (7.2) until the long-time oscillating time was attained.

Margherita Tre. The patient received four meals a day, whose carbohydrate content is recorded and converted into amount of intaken glucose: 50 g for breakfast, 80 g for lunch and dinner, and 20 g for mid-afternoon snack. The absorption curve is modelled as in Eq. (7.3) (see also Fig. 7.3), with different time scales for main meals (longer for lunch and dinner) and small meals (shorter for breakfast and mid-afternoon snack).

The patient also received two types of insulin administrations: regular short-acting human insulin (Actrapid®) and long-acting insulin glargine (Lantus®). Regular human insulin has an onset of action at 30 to 60 minutes from administration, a peak at between 1 and 2 hours, and a duration of action of more or less 3 to 5 hours [65]. Insulin glargine has instead a duration of about 24 h without a marked peak [141]. The former is administered about 30 min before meals, the latter once a day. I modelled the rate of absorption of insulin adapting Eq. (7.3) to reproduce the measured absorption curves of both insulin types. The resulting curves are plotted in Fig. 7.22, where I have chosen $\tau_{\text{av}} = 60\,\text{min}$ and $\tau_{\text{ab}} = 120\,\text{min}$ as the values of availability and absorption times for regular insulin (solid line) and $\tau_{\text{av}} = 6\,\text{h}$ and $\tau_{\text{ab}} = 12\,\text{h}$ for insulin glargine (dashed line).

In Fig. 7.23 the values of measured glucose concentration are plotted in a time window of

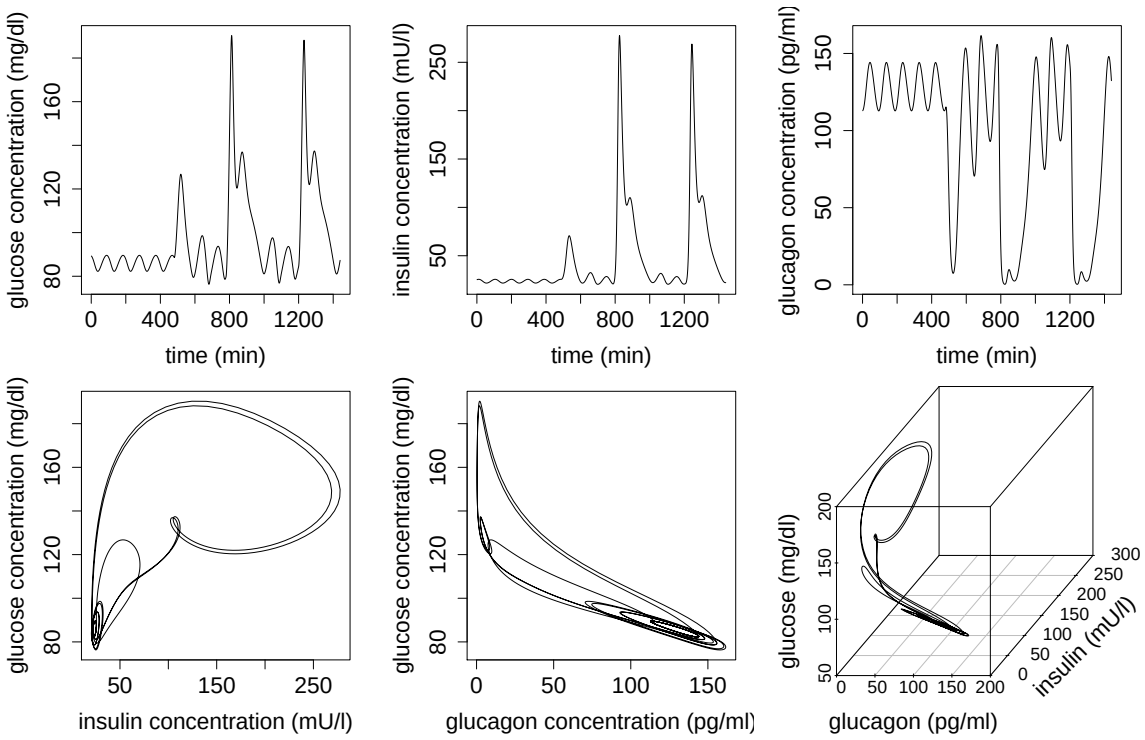

Figure 7.19: Simulation of glucose dynamics for a healthy subject receiving three meals in one day with long absorption time as in Fig. 7.5. See captions of Fig. 7.18 for the panel description.

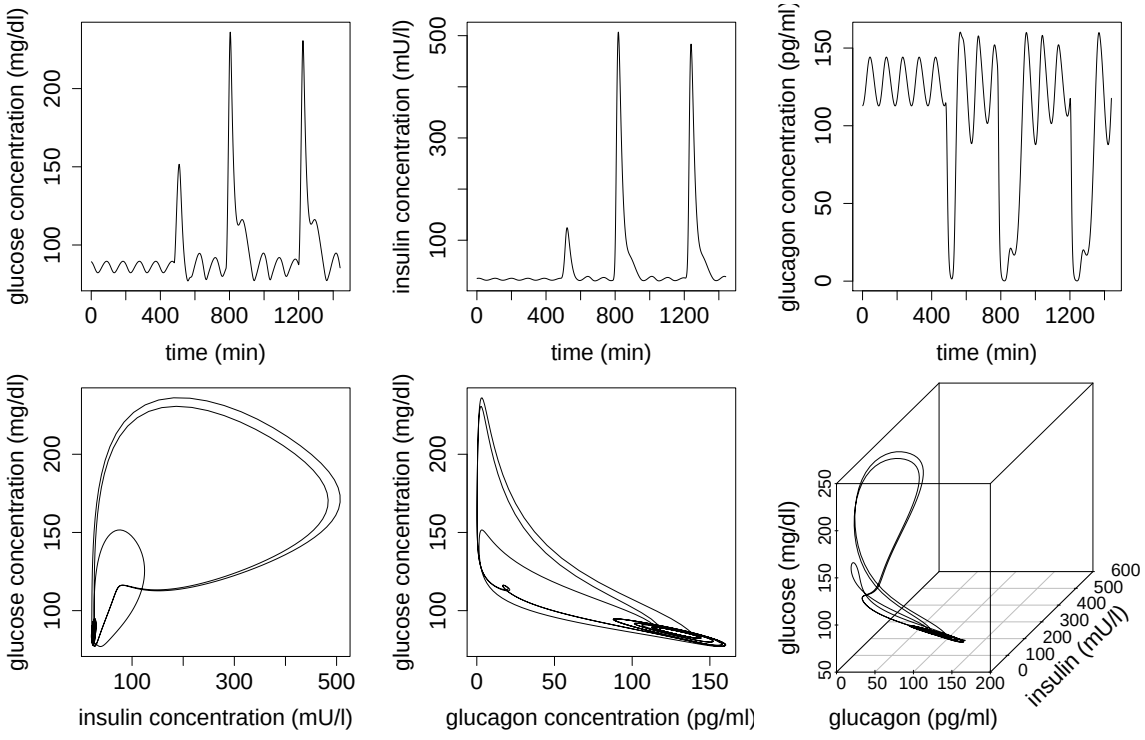

Figure 7.20: Simulation of glucose dynamics for a healthy subject receiving three meals in one day with short absorption time as in Fig. 7.6. See captions of Fig. 7.18 for panel description.

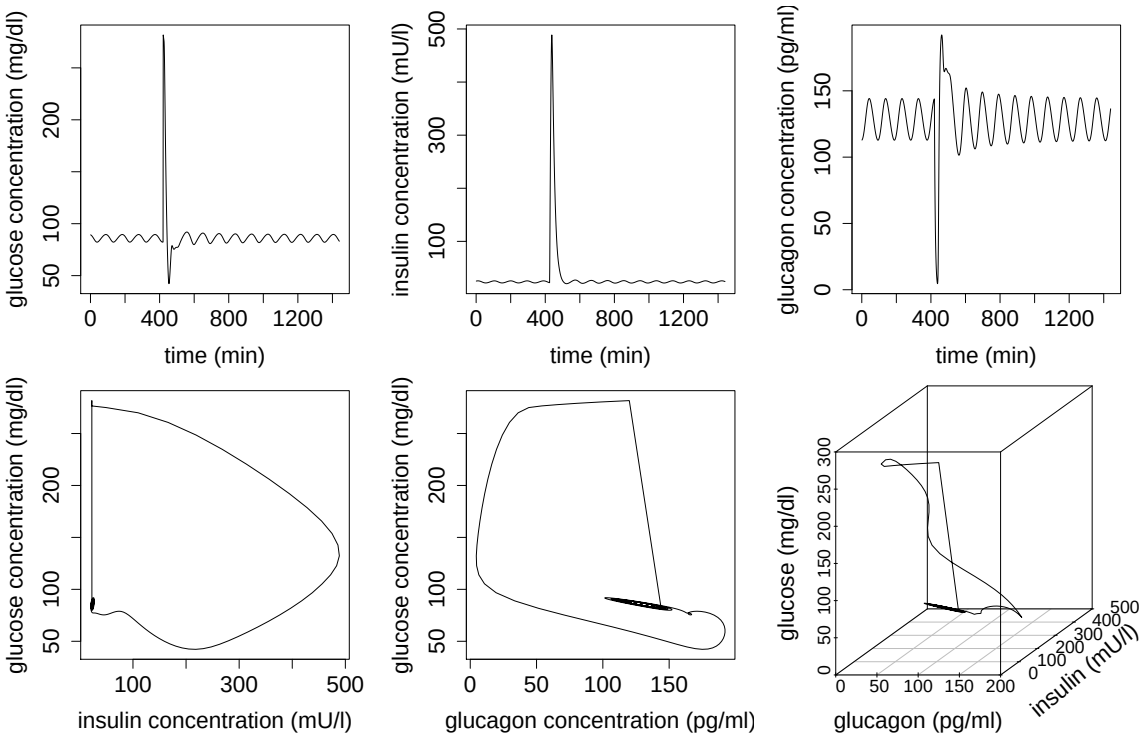

Figure 7.21: Simulation of glucose dynamics for a healthy subject undergoing an intravenous glucose bolus of 20 g as in Fig. 7.7. See captions of Fig. 7.18 for panel description.

2000 min (dots). Solid vertical lines represent meals whose glucose intake, measured in grams, is reported below each line. Dashed and dotted lines represent regular insulin and insulin glargine, respectively. The amount of insulin administered in international units is reported above each line. In spite of regular intakes of glucose and administrations of insulin, the amplitude of fluctuations of glucose concentrations is extremely variable. For $t < 500$ min glucose concentrations vary from 150 mg/dl to less than 250 mg/dl. From $t = 500$ min to 1200 min variations are wider ($100 - 350$ mg/dl) and, eventually, glucose concentration peaks beyond the maximum measurable concentration (400 mg/dl). This suggests that the patient's condition was not stable during the observation window. I thus expect that a dynamical model with constant coefficients will be able to fit the data only when applied to a narrow window $t < 500$ min, where all the parameters remain reasonably constant. For larger windows the quality of the fit becomes worse.

This is exactly what I observed using either the glucose-insulin model [Eqs. 7.1 and (7.2)] or the complete glucose-insulin-glucagon model [Eqs. (7.4), (7.5), and (7.6)]. The results of this analysis are reported in Figs. 7.24 and 7.25, respectively, where I fitted the two models to data of Fig. 7.23 in three different time-windows, from $t = 0$ to $t_{\max} = 500$, 1000, and 2000 min (left, central, and right panels). Dots indicate measured concentrations. The solid line is the result of the fit. In Fig. 7.24 and in the top row of Fig. 7.25, I have estimated, as free parameters, the initial conditions I_0, G_0 (and L_0 in Fig. 7.25), the patient parameters β, γ, R_g (mg/min), plus the time scales of

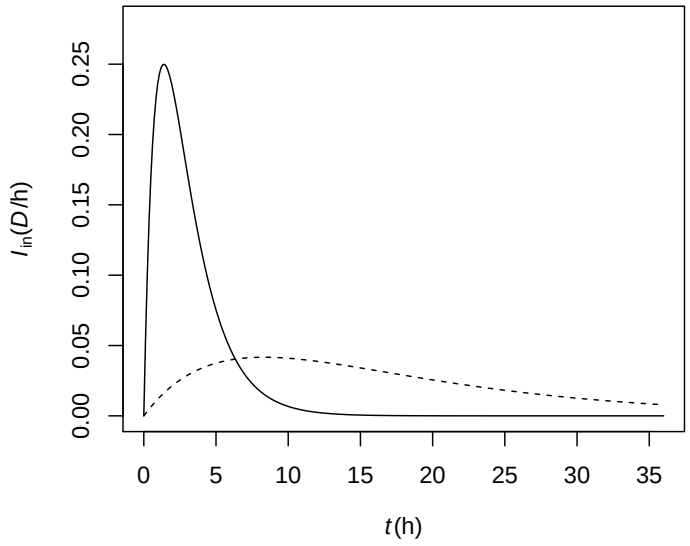

Figure 7.22: Absorption curve of regular insulin (solid line) and insulin glargine (dashed line) insulin for a single dose of insulin D modelled through Eq. (7.3) with $\tau_{\rm av} = 60\,{\rm min}$, $\tau_{\rm ab} = 120\,{\rm min}$ and $\tau_{\rm av} = 6\,{\rm h}$, $\tau_{\rm ab} = 12\,{\rm h}$, respectively. The rate of insulin absorption $I_{\rm in}$ is measured in units $D/{\rm h}$.

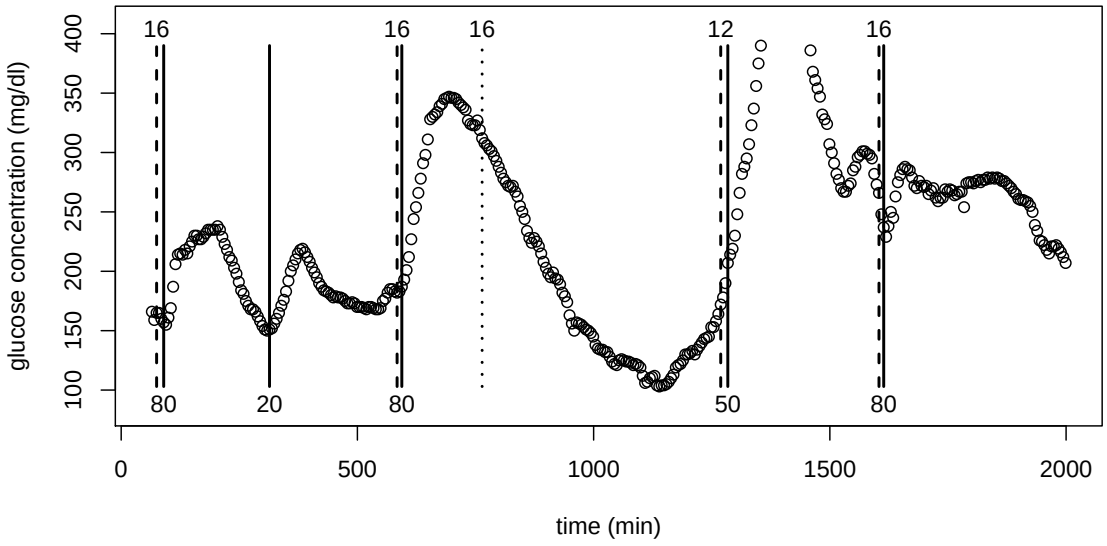

Figure 7.23: Values of measured values of glucose concentrations (dot), meals (solid lines) with glucose content in grams reported below, and administration of regular insulin (dashed lines) and insulin glargine (dotted lines), with amount of administered insulin in international units reported above.

the meal absorption curves $\tau_{\rm av}^{\rm slow}$, $\tau_{\rm ab}^{\rm slow}$, $\tau_{\rm av}^{\rm fast}$, and $\tau_{\rm ab}^{\rm fast}$, for main meals and snacks, respectively. In the bottom row of Fig. 7.25 I also left as a free parameter the value of β_L which parametrises pancreas efficiency in releasing glucagon. The final values of the fitted parameters are reported in Tables 7.2 and 7.3 for glucose-insulin and glucose-insulin-glucagon models, respectively.

I have highlighted the estimates obtained by fitting the model on the narrowest time window (500 min). Those values are similar for all fits (glucose-insulin model, glucose-insulin-glucagon model without or with free parameter γ_I), indicating that for such time windows all the models

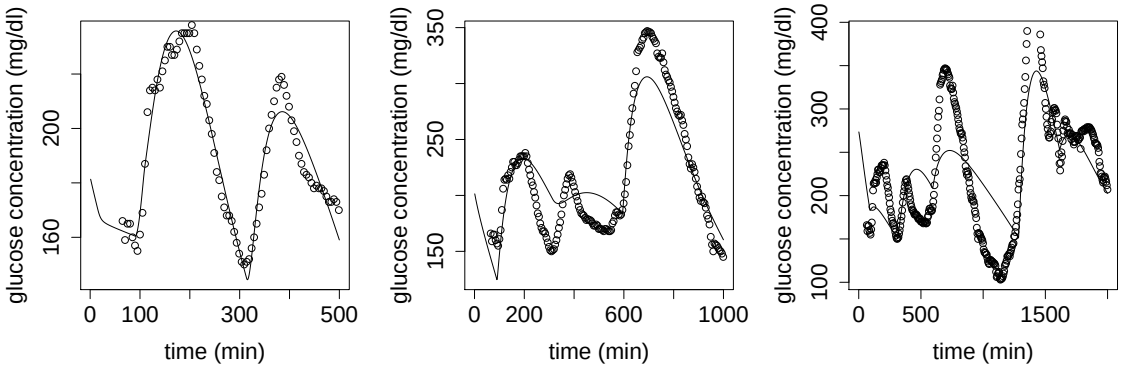

Figure 7.24: Measured glucose concentrations (dots) and fitted glucose-insulin model [solid line, Eqs. (7.1) and (7.2)] for a diabetic patient receiving meals and insulin administrations (see Fig. 7.23). The fit was performed on three different time windows, from $t = 0$ min to $t_{\max} = 500$, 1000, and 2000 min (left, central, and right panels). Values of fitted parameters are reported in Table 7.2.

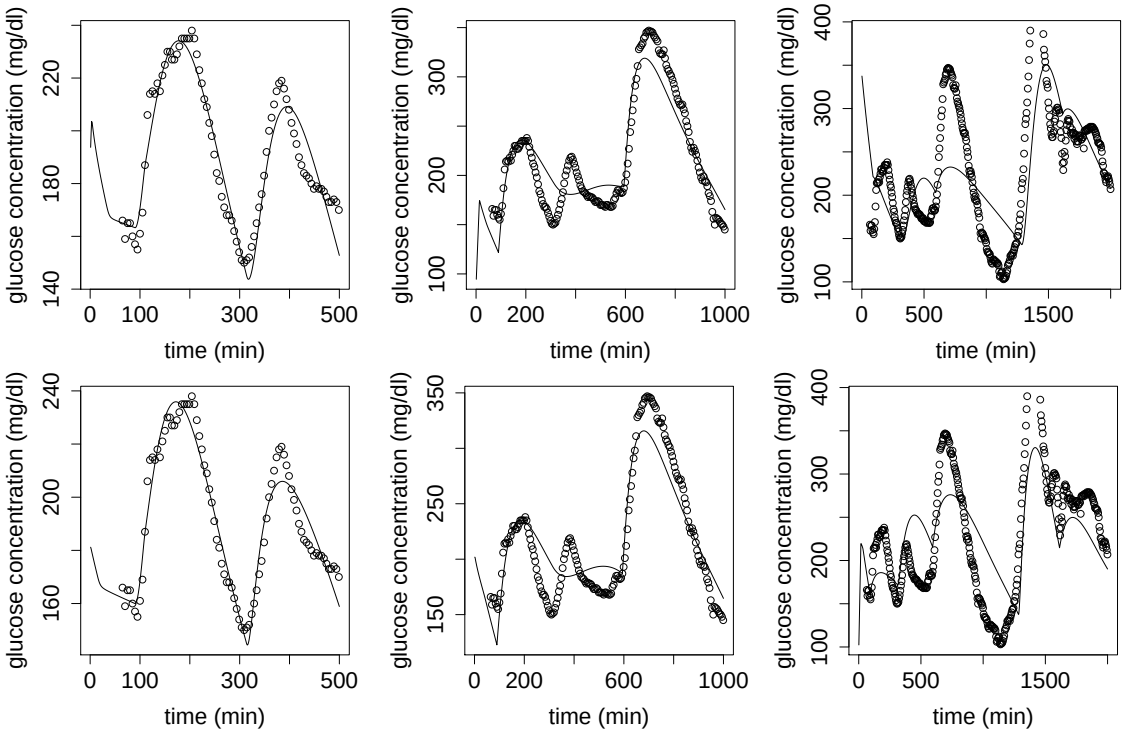

Figure 7.25: Measured glucose concentrations (dots) and fitted glucose-glucagon-insulin model [solid line, Eqs. (7.4), (7.5), and (7.6)] for the same patient of Fig. 7.25 in the same time windows. The fits of the first row were performed leaving the same free parameters as in Fig. 7.25. In the second row also β_L was let free. Values of fitted parameters are reported in Table 7.3.

provide similar results. Conversely, in the other columns, corresponding to time windows of 1000 and 2000 min, the fitted values of the parameters are much more variable and assume very large non-physiological values. This confirms the observation that the patient's condition varies too much to fit a model with constant coefficients on such long time windows.

Focusing on the grey columns ($t_{\max} = 500$ min), the addition of the glucagon term to the dynamical system does not significantly improve the model. In this patient the effect of the

$t_{\max}$ (min)	500	1000	2000
$\tau_{\rm av}^{\rm slow}$	24	1	1
$\tau_{\rm ab}^{\rm slow}$	137	229	663
$\tau_{\rm av}^{\rm fast}$	7	29	1
$\tau_{\rm ab}^{\rm fast}$	58	253	130
I_0 (mU/l)	32	113	67
G_0 (mg/dl)	182	203	274
β	0.02	0.08	0.17
γ	0.17	0.08	0.04
R_g (mg/min)	76	0	6

Table 7.2: Values of the fitted parameters for the glucose-insulin model [Eqs. (7.1) and (7.2)], corresponding to the curves plotted in Fig. 7.24.

	fixed $\beta_L = 1$			free β_L		
$t_{\max}$ (min)	500	1000	2000	500	1000	2000
$\tau_{\rm av}^{\rm slow}$	34	0	0	25	0.00	0.00
$\tau_{\rm ab}^{\rm slow}$	112	211	815	131	211	504
$\tau_{\rm av}^{\rm fast}$	30	98	53	6	70	7
$\tau_{\rm ab}^{\rm fast}$	30	229	95	58	259	113
I_0 (mU/l)	114	167	309	32	116	10
L_0 (pg/ml)	322	263	153	189	216	5522
G_0 (mg/dl)	188	9	34	180	197	95
β_I	0.00	0.00	0.20	0.01	0.01	0.19
γ_I	0.20	0.10	0.03	0.18	0.10	0.04
R_g (mg/min)	78	18	228	76	0	50
β_L	–	–	–	0.95	0.93	2.

Table 7.3: Values of the fitted parameters for the glucose-glucagon-insulin model [Eqs. (7.4), (7.5), and (7.6)], corresponding to the curve plotted in Fig. 7.25.

glucagon equation cannot be appreciated since glucagon release is negligible as a consequence of the high glycaemic level. Furthermore, pancreas is almost unable to produce insulin ($\beta_I \lesssim 0.02$) and tissue insulin resistance is high ($\gamma_I \approx 0.2$), coherently with the condition of severe diabetes.

The values of the initial conditions I_0, L_0, and G_0 are somehow irrelevant when fitting delay differential equations. To integrate the equations I must impose initial conditions on a whole segment $t \in [-\max(\tau_1, \tau_2), 0]$, by making very arbitrary assumptions. I decided to impose constant conditions, namely

$$I(t<0) = I_0, \qquad L(t<0) = L_0, \qquad G(t<0) = G_0. \tag{7.40}$$

In order to compensate for this choice, the initial condition may prove non-physical at $t = 0$. However, the solution soon becomes independent of the assumptions made for $t < 0$. Thus, one can safely rely on the quality of the model as long as the predicted values agree with the first measured concentrations, as observed in the left panels of Figs. 7.24 and 7.25.

The parameters $\tau_{\rm av/ab}^{\rm slow/fast}$ were fitted as free parameters because it is practically impossible

to determine *a priori* how fast a meal is absorbed and glucose enters the systemic circulation. I just observe that the estimated values $\tau_{\mathrm{av/ab}}^{\mathrm{slow/fast}}$ are realistic and compatible, from a physiological perspective, with the time needed to absorb full meals and snacks, respectively.

Critically ill patient

Blood glucose levels are commonly measured in ICUs through blood gas analysis. This test is usually performed about three or four times a day, but, for very few patients, the sampling frequency may be increased up to once every two hours. I have shown above that a good fit is possible only if measurements are performed very frequently and for a time period in which the patient's condition is almost stable, so that model coefficients can be reasonably assumed to be constant.

Furthermore, to avoid complications associated with the estimate of absorption time-scales I decided to first test my model on a patient receiving only parenteral nutrition. In this case, it is quite simple to compute the precise rate of glucose intake as a function of time.

Thus, I selected from the database of *MargheritaTre* a patient who satisfied the following requirements:

1. a long ICU stay with purely parenteral nutrition;
2. slowly evolving conditions;
3. relatively frequent measures of blood glucose concentrations;
4. no insulin administration.

I tested the performance of the model on a few patients satisfying the above conditions. However, for the sake of simplicity, here I present in detail the results relating to a single patient. The results obtained for the other patients are qualitatively analogous.

I identified a 29-year-old epileptic patient affected by bowel obstruction, that prevented enteral nutritions for about 7 days. The last condition was required to appreciate the physiological hormone-mediated interactions between the pancreas and the other organs in the absence of spurious exogenous effects. Blood glucose concentration was measured 49 times, with an average frequency of about once every 3.5 h.

Measured concentrations (dots) and the results of the fits (solid curve) are compared in Fig. 7.26 for the glucose-insulin model over the full observation period (upper panel, see Table 7.4, for the estimated values of the fitted parameters). In the fit procedure I_0, G_0, β, γ, R_g (mg/min) were estimated as free parameters. The predicted curve shows ultradian oscillations and is able to recognise the difference in the average glucose level before and after $t = 2000$ min, when the amount of administered glucose was increased. However, it is not able to faithfully follow the measured

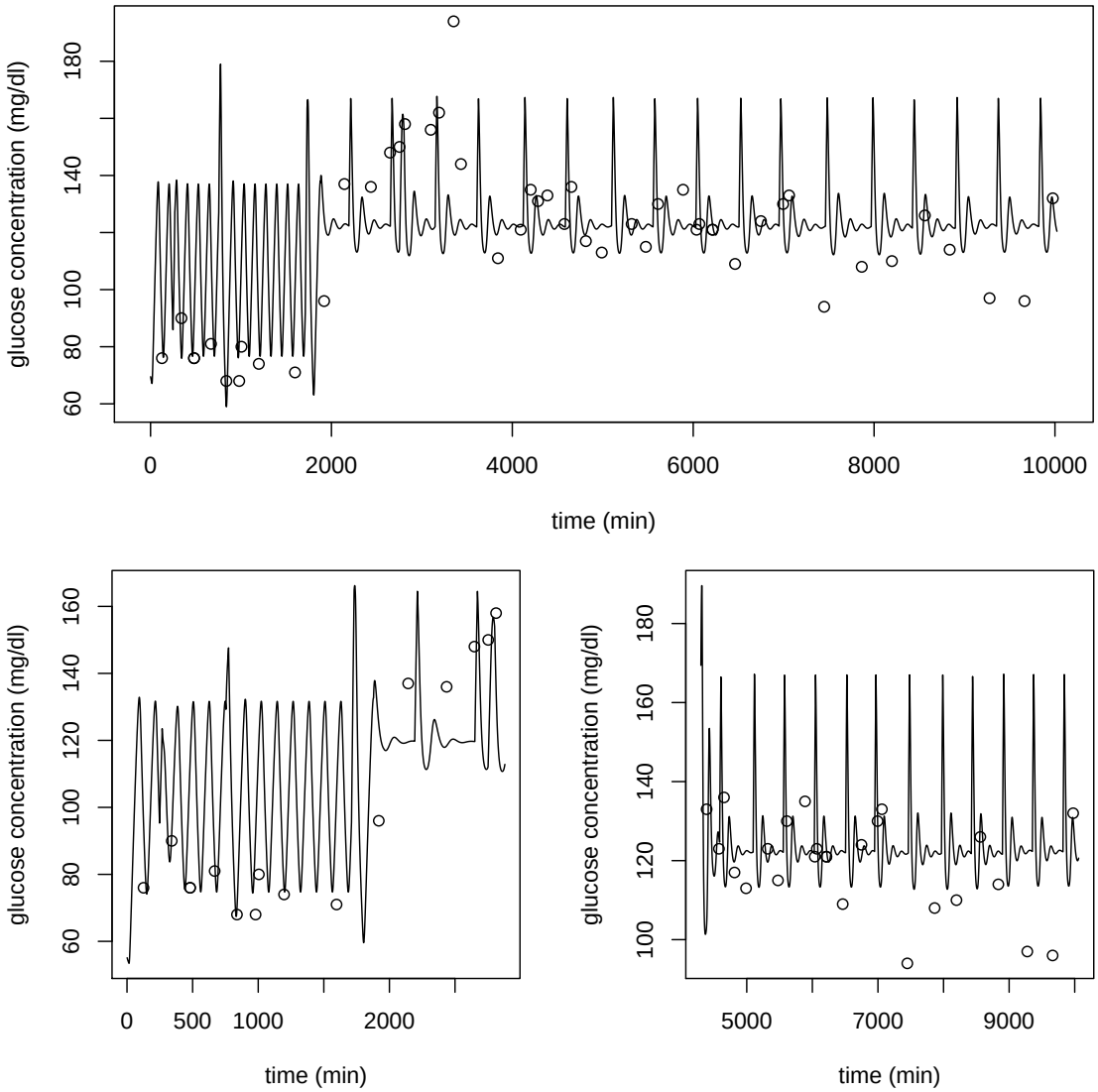

Figure 7.26: Measured concentrations (dots) and predictions of the glucose-insulin model (solid curve) for a 29-year-old epileptic patient affected by bowel obstruction. The fit was performed with parameters I_0, G_0, β, γ, R_g (mg/min) on three different time-windows: full observation time (upper panel), from $t = 0$ to $t = 2880$ min (two days, left panel), and from $t = 4300$ min to $t = 10\,060$ min (four days, right panel). The values of the fitted parameters are reported in Table 7.4.

$t_{\min}$ (min)	0	0	4300
$t_{\max}$ (min)	10722	2440	10 060
time-window (days)	7.4	2	4
I_0 (mU/l)	28	28	1.4
G_0 (mg/dl)	70	55	168
β	0.48	0.54	0.49
γ	0.64	0.61	0.62
R_g (mg/min)	230	220	253

Table 7.4: Values of the fitted parameters for the glucose-insulin model, corresponding to the curve plotted in Fig. 7.26.

$t_{\min}$ (min)	0	0	4300
$t_{\max}$ (min)	10722	2440	10 060
time-window (days)	7.4	2	4
I_0 (mU/l)	36	31	40
L_0 (pg/ml)	407	1424	570
G_0 (mg/dl)	4	55	166
β_I	0.87	0.98	0.65
γ_I	0.29	0.19	0.51
R_g (mg/min)	228	184	233
β_L	0.83	0.87	0

Table 7.5: Values of the fitted parameters for the glucose-glucagon-insulin model, corresponding to the curve plotted in Fig. 7.27.

observations. The period of the oscillations is indeed shorter than the average temporal distance between two consecutive observations. It is thus impossible for the model to reproduce the shape of the oscillations. Furthermore, for $t > 2000$, the average blood glucose level decreases, although the nutritional regime remains constant and the patient does not receive insulin administrations. This means that the patient's condition evolved during this period (about 5.5 days) and the model, whose parameters are constant, should not be fitted on such a wide time-window.

In the lower panels of Fig. 7.26 the model was fitted on shorter time-windows, from $t = 0$ to $t = 2880$ min (two days, left panel), and from $t = 4300$ min to $t = 10\,060$ min (four days, right panel) on 15 and 24 observations, respectively. The results are qualitatively similar to the upper panel. In both plots, the agreement between observations and predictions has only slightly improved with respect to the upper panel. This confirms my interpretation and proves that even reducing the time-windows to 2 or 4 days is not enough to ensure a good fit, since the patient's condition evolves on shorter time scales. However, because of the lack of frequent data in *MargheritaTre*, it is impossible to perform a fit on shorter time windows.

As a last test, I fitted my model to the data of this patient, including the glucagon term and leaving as a free parameter β_L, which parametrises pancreas efficiency in releasing glucagon. The results are shown in Fig. 7.27 and the final estimated values of the fitted parameters are reported in Table 7.5. When applied to the full observation period, the quality of the fit is quantitatively as poor as for the simpler glucose-insulin model, because of the very low frequency of available data. However, this fit shows interestingly qualitative features.

First, ultradian oscillations are present only for $t < 2000$ min. When the rate of glucose administration is higher, they disappear ($t < 2000$ min). This result is coherent with the result of my theoretical investigation of Sec. 7.3, where it was shown that oscillations are suppressed when the system is dominated by intense glucose administrations.

Second, the fit on the smallest initial time-window (lower left plot) is qualitatively better than in Fig. 7.26. Compared to the model without glucagon, the average predicted values of glucose con-

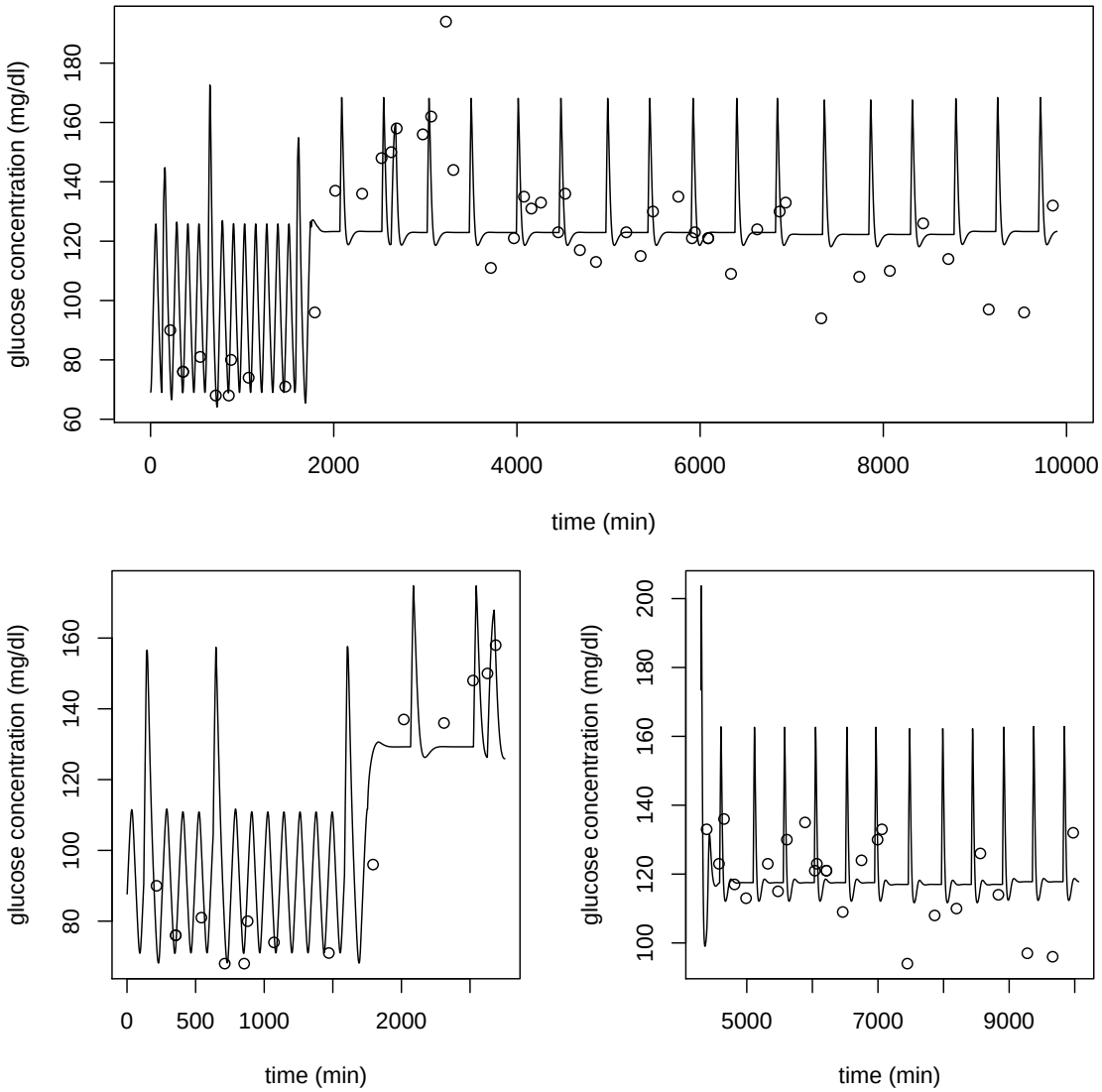

Figure 7.27: Measured concentrations (dots) and predictions of the complete glucose-insulin-glucagon model (solid curve) for the same patient as Fig. 7.26. The fit was performed with parameters I_0, G_0, L_0, β_I, γ_I, β_L R_g (mg/min) on three different time-windows: full observation time (upper panel), from $t = 0$ to $t = 2880$ min (two days, left panel), and from $t = 4300$ min to $t = 10\,060$ min (four days, right panel). Fitted values in Table 7.5.

centration in the first region $t < 2000$ min are much smaller than in the second region $t < 2000$ min, and the amplitude of oscillations for $t < 2000$ min is also reduced. This suggests that the complete model discriminates better between the two dosage regimens of parenteral nutrition. Indeed for $t < 2000$ min, glucose concentration reaches quite low values (about 70 mg/dl), where glucagon starts to play an important role in the maintenance of glucose homoeostasis. Interestingly, the estimated value of parameter β_L, corresponding to the efficiency of pancreas glucagon production, vanishes when the fit is performed on the third time-window (third column of Table 7.5). With this nutritional regimen, the concentration of glucose remains so high (above 100 mg/dl) that the effect of glucagon cannot be appreciated.

The low frequency of available data is not sufficient to properly estimate model parameters and to appreciate differences between models at a quantitative level.

7.6 Conclusions and future perspectives

In this second Part I reviewed several mathematical models of glucose metabolism. Starting from a critical analysis of their features I selected one model that best described glucose-insulin dynamics. By means of numerical simulations I revealed that the model was not robust against too rapid variations of glucose concentrations. In particular, non-physiological hypoglycaemic levels were reached soon after rapid and abundant glucose administrations because of consequent intense insulin release. Such models would not be able to reliably predict the evolution of the glucose level in critically ill patients whose conditions often vary very rapidly and in very wide ranges.

To overcome these limitations I proposed a more complete model involving the contribution of counter-regulatory hormones. This model explicitly accounts for the prompt release of glucagon when a hypoglycaemic condition is approached, counteracting the effect of insulin. Using semi-analytical techniques I investigated the stability of the steady-state solutions by varying the system parameters. This analysis revealed important features of my equations, suggesting that the glucose dynamics were properly modelled. The main results, derived in Secs. 7.3 and 7.4, prove that the proposed model provides a good physiological description of glucose metabolism and has a robust mathematical structure, that allows one to derive semi-analytical solutions.

First, this model preserves the appearance of ultradian oscillations during fasting periods, an important prediction of glucose-insulin models. I also observed that the system converges to stable-steady states in three interesting scenarios:

- The system is driven by intense glucose administrations. The body reacts with an almost continuous release of insulin and oscillations are halted.
- The system is driven by insulin administrations. Even small amounts of exogenous insulin, administered at a constant rate, are sufficient to stop self-sustained oscillations.
- In patients with low pancreas efficiency or insulin resistance. Time variability is a typical condition of healthy subjects and is maintained by the cooperation among several organs. If one element contributing to this fragile equilibrium is damaged, oscillations are halted and the solution of the system converges to a constant value.

I also showed with numerical simulations that both hyperglycaemia and hypoglycaemia are avoided by this new model thanks to the introduction of the double feedback mechanism based on

insulin and glucagon. This allows finer, more stable control of the glycaemic level.

Finally I tested the performance of both the glucose-insulin model and the glucose-insulin-glucagon model on real data from a patient affected by severe diabetes and a critically-ill patient. In the first case, measured concentrations were available with very high frequency (once every five minutes). Both models were able to fit the data well, provided that the patient's condition did not vary in the considered time-window. On this patient, the model including glucagon did not give any apparent advantage over the simpler glucose-insulin model because blood glucose always remained at very high levels, above which glucagon is not significantly released.

Data from *MargheritaTre* had a much lower frequency (once every 3.5 hours). Consequently, I had to extend the time-window to several days. The quality of the fit was very poor for two reasons: the time-separation of observed data was too wide to describe the evolution of a phenomenon that varies on time scales of a few minutes. The patient's condition was not stable in the considered time-window. Analyses of data from other patients yield analogous results. With available data in *MargheritaTre* it is not possible to test the model and to estimate model parameters as functions of patient covariates in a population model as done in the previous part of the Thesis for vancomycin pharmacockinetics (see Chap. 5).

At a theoretical physiological level, my model properly describes the dynamics of glucose in very extreme conditions, as those faced by critically ill patients. However current *MargheritaTre* data are not suitable to develop models describing glucose metabolism. The long-term objective of this project is to realise a bedside simulator of glucose dynamics starting from the model developed and analytically studied in this Thesis. However the experience acquired during this Thesis work showed that *ad hoc* data should be prospectively collected to test the model and fit its parameters. Thus, I have designed a new pilot study GluDyPS (Glucose Dynamics: a Pilot Study) on 20 patients in a single ICU, at San Giovanni Bosco Hospital, Turin. The study protocol has been just finalised and will be submitted for Ethical Review.

In this study we shall measure:

- subcutaneous glucose concentration once every 5 min;
- blood glucose concentration through blood gas analysis four times a day;
- concentration of C-peptide (see Sec. 6.1.1) twice a day.

By measuring blood glucose concentration a few times a day through standard techniques, I shall calibrate the subcutaneous concentration measured in the interstitial fluid on the corresponding blood concentration. Furthermore, the measurement of C-peptide will allow us to calibrate the endogenous production of insulin on each patient. In this way, the power of the fit procedure will be increased, since information will be collected not only on glucose variations [Eq. (7.6)] but also

on insulin variations due to endogenous production [Eq. (7.4)], whereas exogenous insulin is known from *MargheritaTre* data.

With this project I shall be able to test my model, compare its performance against other models, and, if needed, improve its structure. With the acquired data it will be possible to construct stochastic simulations to test the predictive performance of the model [116, 136, 98]. Indeed, to provide realistic results, those simulations needs to be fed with observation-based probability distributions that cannot be currently constructed out of available data.

Furthermore, I shall estimate the feasibility of a larger observational study with the aim of constructing a population model, similar to the one built to describe antimicrobial kinetics in Chap. 5. With such a model, glucose dynamics would be simulated as a function of patient conditions since the parameters of Eqs. (7.4), (7.5), and (7.6) would become functions of patient covariates. Hence, it would be possible to reproduce glucose variations even with evolving patient conditions.

CONCLUSIONS

Electronic health records are invaluable mines of data that can be exploited to conduct epidemiological analyses, pathophysiological investigations, analyses of decision processes, and clinical studies. Since 2008, GiViTI has been developing *MargheritaTre* (M3), an EHR designed to collect data for research purposes and to support clinical practice in ICUs. It is currently installed in about 40 ICUs and its database contains about 65 000 patient records. Unlike standard EHRs for general hospital wards, M3 is highly specialised software designed in collaboration with clinicians and researchers to describe the complexity of critically ill patients, ease the effort of data input and, at the same time, guarantee a high-quality standardised data collection. Thus, only a few features of M3 are customisable by the users and most of the information is collected in structured form. For instance, clinical notes contain both free text and keywords chosen from a dictionary. This makes data extraction simpler and reduces the need for preprocessing.

The ultimate aim of these research projects is to support clinical practice, improve the quality of care and patient outcomes. The results of the projects will be delivered to clinicians directly through M3. Indeed, this EHR offers the possibility to implement expert systems to support clinical decisions, for instance, in the diagnosis of diseases or in the design of therapeutic treatments.

For this Thesis, I implemented the informatics tools required to extract data from the M3 database, preprocess and analyse them. I then investigated two clinical aspects associated with the treatment of critically ill patients: the administration of antimicrobial drugs and the control of the glycaemic level. For both topics I reviewed the most relevant physiological mechanisms and the literature of some among the most important existing models. On the basis of these preliminary analyses, I have formulated new mathematical models to describe antibiotic kinetics and glucose dynamics. However, for the latter project I had to adopt much more complex techniques. For this reason, with available data, I was able to push the development of those models to two different

levels.

For the former project, I built one- and two-compartment linear models of vancomycin pharmacokinetics and, for both models, I estimated the pharmacokinetic parameters as functions of patient covariates using multilevel regression on a set of 141 patients from a single unit participating in the M3 project. The predictive performance of the two models is similar. Furthermore I simulated single-patient dynamics, showing that concentration curves can be used, on the one hand, to predict future vancomycin concentrations and, on the other hand, to critically review administration strategies. The result of the fit revealed that drug clearance was well characterised in terms of patient conditions, whereas the correlation of the distribution volume with patient variables was poorer. Thanks to large amount of clinical data available in M3, the model presented in this Thesis is richer than previous models [54, 117, 150, 156, 27] in terms of patient covariates. Thus, it is able to better follow the evolution of the patient's condition. Its predictive performance is fair but the uncertainty of the predictions is still too wide for implementation in a bedside simulator of pharmacokinetics.

To collect high-quality data in order to build pharmacokinetic models of four molecules among the most used in ICUs, we have started a new multicentric observational study, AbioKin. Sample collection for one of the four molecules (piperacillin-tazobactam) has concluded. In the following months we shall proceed with the measurement of drug concentration and the building of pharmacokinetic models. The models constructed with AbioKin will serve to develop a simulator of drug kinetics which will be implemented in M3 to support clinicians in the design of personalised dosage regimens.

Regarding the project on glycaemic control, the main objective of this Thesis was to identify a new model providing good physiological description, with a robust mathematical structure, and whose solutions where realistic also in extreme conditions of critically ill patients. We also required that the structure of the equations ensured an analytical treatment. I improved the physiological accuracy of existing models, by taking into account the role played by glucagon in maintaining glucose homoeostasis. This new model is based on a system of three delayed differential equations and includes sophisticated non-linear effects.

The main results of this Thesis are the mathematical proofs of the existence and uniqueness of stationary solutions and the study of their stability properties with an analytical approach. Such a theoretical analysis, which is often overlooked, is important to ensure that all the solutions are well-behaved and to prevent unexpected features when the model is implemented in automatic predictive algorithms.

Furthermore, I performed numerical simulations to test the behaviour of the model in realistic scenarios. Finally, I tested its performance in fitting real data. I showed that the model is able

to reproduce observed dynamics for a time-window as large as a few hours and for a sampling frequency of once every five minutes. Accordingly, I was not able to obtain reliable results when the model was fitted to data of critically ill patients collected with M3. Indeed, in ICUs glucose plasma concentration is typically measured by blood gas analysis, with a sampling frequency of about once every three or four hours.

Although this analysis has shown that my dynamical model provides a good physiological description, including in extreme conditions, it also suggests that data currently available in M3 are not sufficient to estimate the model parameters as functions of the patient's condition, as done, for instance, in the construction of the pharmacokinetic model. To collect the required data, I am starting a new pilot study to measure glucose concentrations in critically ill patients, combining subcutaneous measurements and blood gas analysis.

On the one hand, the results obtained in this Thesis indicate that M3 is a promising tool to conduct advanced research projects and that mathematical modelling and simulations based on ICU data may provide new insight in clinical research. On the other hand, they also show some limitations in the projects that can be pursued with purely retrospective data. Although the amount of information is huge, the frequency and the quality of data collected mainly for clinical purposes is not always adequate for the construction of sophisticated mathematical models. Both studies have shown indeed similar limitations, connected with the low number and frequency of measurements of plasma vancomycin concentration and of blood glucose concentration, respectively.

These limitations may be overcome only through the integration of data recorded in everyday clinical practice with new *ad-hoc* data collected for specific projects. EHRs facilitate the realisation of such prospective observational studies. The additional effort required to clinicians to input extra-data or to perform additional laboratory tests is minimised since the majority of the required information is already present in the EHR.

The findings of this Thesis have stimulated the modification of M3, whose interface and data structure have been adapted to the requirements of our research projects. A specific module has been developed to guide clinicians in the protocol of the AbioKin study. Furthermore, data recorded with M3 still have relatively low sample frequencies, allowing one to study phenomena with time scales of hours, but no shorter. To fill this gap we have been considering the possibility of importing more frequent data.

New analytical techniques should also be implemented to deal with a source of data collected with the primary aim of clinical documentation. In this Thesis I analysed only structured data, such as drug administration, vital signs and laboratory tests. However a large amount of information is present in non-structured form, for instance as free text in clinical notes. More advanced techniques should be adopted to extract and analyse both unstructured information [68, 180] and the newly

acquired quasi-continuous data in the form of complex time series [210, 181].

Finally, M3 data are still available for analysis only to the GiViTI coordinating centre. To fully exploit the potential of an EHR, its data must be available to external groups interested in exploring new research lines and strategies of analysis. The experience of MIMIC-III [103] shows, for instance, that a collaborative approach may boost both clinical and methodological research. Furthermore, the availability of databases such as MIMIC and M3 sharing similar structures and containing analogous information allows one to test reproducibility of research analyses on different data. It would be interesting, for instance, to reproduce the analyses performed in this Thesis with other databases.

Appendix A

EFFECTIVE DELAY FROM ORDINARY LINEAR EQUATIONS

To implement an effective time delay t_d between a time-dependent variable $s(t)$ and output variable x_n, it is enough to link s and x_n through a cascade of linear ordinary equations

$$\dot{x}_1 = \kappa(s - x_1), \tag{A.1}$$

$$\dot{x}_2 = \kappa(x_1 - x_2), \tag{A.2}$$

$$\dots$$

$$\dot{x}_n = \kappa(x_{n-1} - x_n), \tag{A.3}$$

where the dot denotes time derivative.

The solution of a single equation of the form

$$\dot{x} = \kappa(y - x) \tag{A.4}$$

is

$$x(t) = \int_{-\infty}^{t} \mathrm{d}t_1 \, \mathcal{G}_1(t - t_1) y(t_1), \tag{A.5}$$

where the Green function $\mathcal{G}_1$ is

$$\mathcal{G}_1(\tau) = \kappa \, e^{-\kappa\tau}. \tag{A.6}$$

Therefore, the solution for x_1 is

$$x_1(t) = \int_{-\infty}^{t} \mathrm{d}t_1 \, \mathcal{G}_1(t - t_1) s(t_1) \tag{A.7}$$

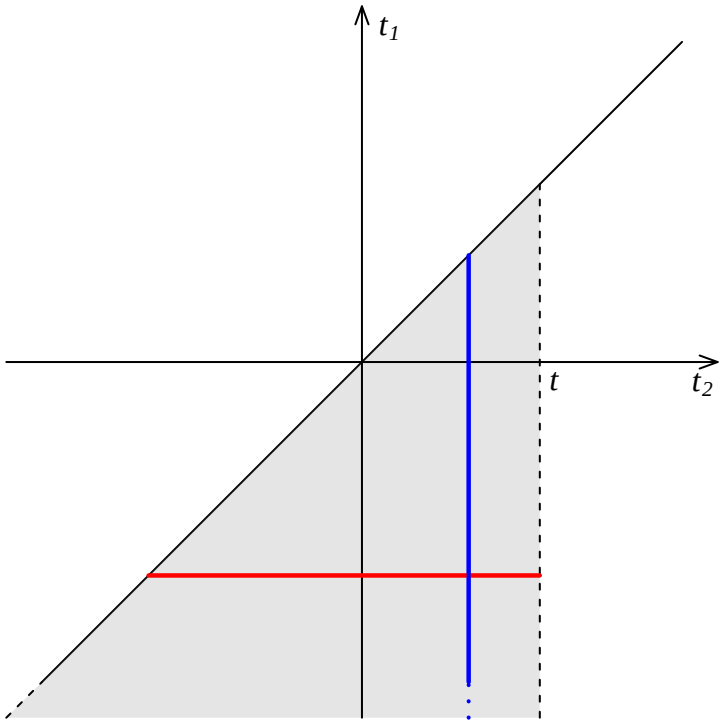

Figure A.1: Domain of integration of the double integral of Eq. (A.9) Fixing t_2 the integral with respect to t_1 is performed along the blue integration path. If the order of the integrals is exchanged, the integral with respect to t_2 is performed along the red path at fixed t_1.

and for x_2 is

$$x_2(t) = \int_{-\infty}^{t} \mathrm{d}t_2\, \mathcal{G}_1(t-t_2) \int_{-\infty}^{t_2} \mathrm{d}t_1\, \mathcal{G}_1(t_2-t_1) s(t_1). \tag{A.8}$$

By replacing $\mathcal{G}_1$ with its explicit form of Eq. (A.6):

$$x_2(t) = \kappa^2 \int_{-\infty}^{t} \mathrm{d}t_2 \int_{-\infty}^{t_2} \mathrm{d}t_1\, e^{-\kappa(t-t_1)} s(t_1). \tag{A.9}$$

The integral in t_2 can be worked out after exchanging the integration order as illustrated in Fig. A.1:

$$x_2(t) = \kappa^2 \int_{-\infty}^{t} \mathrm{d}t_1 \int_{t_1}^{t} \mathrm{d}t_2\, e^{-\kappa(t-t_1)} s(t_1), \tag{A.10}$$

which gives

$$x_2(t) = \int_{-\infty}^{t} \mathcal{G}_2\left(t-t_1\right) s(t_1) \mathrm{d}t_1, \quad \mathcal{G}_2(\tau) = \kappa^2 \tau\, e^{-\kappa\tau}. \tag{A.11}$$

Analogously,

$$x_3(t) = \int_{-\infty}^{t} \mathrm{d}t_2\, \mathcal{G}_1(t-t_2) \int_{-\infty}^{t_2} \mathrm{d}t_1\, \mathcal{G}_2(t_2-t_1) s(t_1). \tag{A.12}$$

Integration with respect to t_2 is performed after switching the integration order:

$$x_3(t) = \int_{-\infty}^{t} \mathcal{G}_3\left(t-t_1\right) s(t_1) \mathrm{d}t_1, \quad \mathcal{G}_3(\tau) = \frac{1}{2}\kappa^3\tau^2\, e^{-\kappa\tau}. \tag{A.13}$$

By inspection of the solutions for x_1, x_2, and x_3, Eqs (A.7), (A.11), and (A.13), and of the definition of the respective Green functions $\mathcal{G}_1$, $\mathcal{G}_2$, and $\mathcal{G}_3$, one may argue that the general solution for x_n is

$$x_n(t) = \int_{-\infty}^{t} \mathcal{G}_n\left(t - t_1\right) s(t_1) \mathrm{d}t_1, \tag{A.14}$$

with

$$\mathcal{G}_n(\tau) = \frac{\kappa^n}{(n-1)!}\, \tau^{n-1}\, e^{-\kappa\tau}. \tag{A.15}$$

For $n = 1$ these equations reduce to Eqs. (A.7) and (A.6). The proof for a generic $n > 1$ is given by induction, assuming that Eqs. (A.14) and (A.15) are valid for $n-1$ and verifying that x_n satisfies the recurrence relation Eq. (A.3). Differentiating Eq. (A.14) with respect to time,

$$\dot{x}_n(t) = \mathcal{G}_n(0) s(t) + \int_{-\infty}^{t} \mathcal{G}_n'\left(t - t_1\right) s(t_1) \mathrm{d}t_1. \tag{A.16}$$

From Eq. (A.15), $\mathcal{G}_n(0) = 0$ for $n > 1$ and

$$\mathcal{G}_n'(\tau) = \frac{\kappa^n}{(n-2)!}\, \tau^{n-2}\, e^{-\kappa\tau} - \frac{\kappa^{n+1}}{(n-1)!}\, \tau^{n-1}\, e^{-\kappa\tau} = \kappa\left[\mathcal{G}_{n-1}(\tau) - \mathcal{G}_n(\tau)\right]. \tag{A.17}$$

Inserting this in Eq. A.16, I obtain

$$\dot{x}_n(t) = \kappa\left[\int_{-\infty}^{t} \mathcal{G}_{n-1}\left(t - t_1\right) s(t_1) \mathrm{d}t_1 - \int_{-\infty}^{t} \mathcal{G}_n\left(t - t_1\right) s(t_1) \mathrm{d}t_1\right] = \kappa\left(x_{n-1}(t) - x_n(t)\right), \tag{A.18}$$

which coincides with the recurrence relation Eq. (A.3).

Normalisation and moments of the Green function The value of the variable $x_n(t)$ at time t is the weighted-average of the past of the signal s at time $t_1 < t$ with weight $\mathcal{G}_n(t - t_1)$. The Green function $\mathcal{G}_n$ is indeed a probability density, being always non-negative and normalized to 1. The generic moment of order m of $\mathcal{G}_n$ is

$$\begin{aligned}\mu_m = \int_0^\infty \mathrm{d}\tau\, \tau^m\, \mathcal{G}_n(\tau) = \int_0^\infty \mathrm{d}\tau\, \frac{\kappa^n}{(n-1)!}\, \tau^{m+n-1}\, e^{-\kappa\tau} = \frac{\kappa^{-m}}{(n-1)!} \int_0^\infty \mathrm{d}y\, y^{m+n-1}\, e^{-y} \\ = \frac{\kappa^{-m}}{(n-1)!}\Gamma(m+n) = \frac{(m+n-1)!}{(n-1)!}\, \kappa^{-m}.\end{aligned} \tag{A.19}$$

The normalisation of $\mathcal{G}_n$ is given by the moment of order 0, $\mu_0 = 1$. The average time $\bar{\tau}$ over which the average of s is performed is the first order moment

$$\bar{\tau} = \mu_1 = \frac{n}{\kappa} \tag{A.20}$$

The variance σ_τ^2 of τ is given by

$$\sigma_\tau^2 = \mu_2 - \mu_1^2 = \frac{(n+1)n}{\kappa^2} - \frac{n^2}{\kappa^2} = \frac{n}{\kappa^2}. \tag{A.21}$$

In terms of the average time $\bar{\tau}$ the standard deviation is

$$\sigma_\tau = \frac{\bar{\tau}}{\sqrt{n}}. \tag{A.22}$$

The higher the number n of auxiliary variables, the narrower the width of the kernel $\mathcal{G}_n$, around its mean value $\bar{\tau} = \kappa/n$.

Appendix B

DELAY DIFFERENTIAL EQUATIONS

A delay differential equation (DDE) is a differential equation of the form [60]

$$\dot{x}(t) = f\left(x(t), x(t-\tau_1), \ldots, x(t-\tau_m), \eta\right), \tag{B.1}$$

where $x(t) \in \mathbb{R}^n$, $f : \mathbb{R}^{n\times(m+1)+k} \to \mathbb{R}^n$, and $\eta \in \mathbb{R}^k$.

Due to the explicit dependence on the past of t ($x(t-\tau_i)$), a solution is not defined by an initial condition $x(t_0)$ at some time t_0. Instead, an initial solution segment x_0 must be specified over an interval of length $\tau = \max_{i=1,\ldots,m}\{\tau_i\}$, where $x_0 \in C = C\left([-\tau, 0], \mathbb{R}^n\right)$, the infinite-dimensional function space of continuous function segments from $[-\tau, 0]$ to $\mathbb{R}^n$. Similarly, for all t, the function segment $x_t \in C$, with $x_t(\theta) = x(t+\theta)$, $\theta \in [-\tau, 0]$, identifies the state of the systems which uniquely determines the solution x in the future of t. This implies that the set of solutions of Eq. (B.1) is infinite-dimensional, unlike ordinary differential equations, whose set of solutions is n-dimensional. As a consequence, a DDE can exhibit periodic, quasi-periodic and even-chaotic solutions.

Functional analysis formulation Equation (B.1) can be written in a more formal fashion by introducing the nonlinear operator $\mathcal{S}_f(t; x_0) : \mathbb{R} \times C \to C$, which maps the initial function segment x_0 onto its image under the time evolution defined by Eq. (B.1):

$$\dot{\phi} = \mathcal{A}\phi, \quad \phi \in \mathcal{D}(\mathcal{A}), \tag{B.2}$$

where $\mathcal{A}$ is the infinitesimal generator of the semigroup of the operators $\mathcal{S}_f$, defined by

$$(\mathcal{A}\phi)(\theta) = \frac{\mathrm{d}\phi(\theta)}{\mathrm{d}\theta}, \quad -\tau \leq \theta \leq 0. \tag{B.3}$$

The domain $\mathcal{D}(\mathcal{A})$ of $\mathcal{A}$ is the set of continuous and differentiable segment functions, with initial conditions satisfying Eq. (B.1):

$$\mathcal{D}(\mathcal{A}) = \left\{\phi \in C : \dot{\phi} \in C, \dot{\phi}(0) = f\left(\phi(0), \phi(-\tau_1), \ldots, \phi(-\tau_m), \eta\right)\right\}. \tag{B.4}$$

By working in a functional analysis setting, this abstract formulation allows to apply techniques developed for non-delayed differential equations to study the properties of DDE.

Steady state The steady state solution x^* of Eq. (B.1) can be found by solving

$$f(x^*, x^*, \ldots, x^*, \eta) = 0. \tag{B.5}$$

Its stability can be investigated by linearising Eq. (B.1), around $x(t)$ around x^*

$$\dot{y}(t) = \sum_{i=0}^{m} A_i(x^*, \eta) y(t - \tau_i), \tag{B.6}$$

where $\tau_0 = 0$,

$$x(t) = x^* + y(t), \tag{B.7}$$

and $A_i(x^*, \eta)$ is the matrix of derivatives of f with respect to all the n components of its i-th argument

$$A_i(x^*, \eta) = \left.\frac{\partial f(z^0, z^1, \ldots, z^m, \eta)}{\partial z^i}\right|_{z_i = x^*} \tag{B.8}$$

evaluated in $z^i = x^*$.

As usual, it is convenient to write the real solutions of a linear system with real coefficients, $\Im\left(A_i(\xi^*, \eta)\right) = 0$, as the real part of its complex solutions. With this notation, Eq. (B.6) exhibits exponential complex solutions of the form $e^{\lambda t} v$, where $v \in \mathbb{C}^n$ and $\lambda \in \mathbb{C}$, satisfying

$$\left[\lambda I - \sum_{i=0}^{n} A_i(x^*, \eta) e^{-\lambda \tau_i}\right] v = 0, \tag{B.9}$$

where I is the $n \times n$ identity matrix. Non-trivial solutions appear when λ satisfies the non linear eigenvalue equation

$$\det\left[\lambda I - \sum_{i=0}^{m} A_i(x^*, \eta) e^{-\lambda \tau_i}\right] = 0. \tag{B.10}$$

The steady state solution x^* is stable if the real part of all the roots of Eq. (B.10) are negative. It is unstable if at least one root has a positive real part. A branch of periodic solutions appears at a Hopf bifurcation when one root acquires a non-negative imaginary part.

Appendix C

CODE STRUCTURE

C.1 Database synchronisation and restoring

The class structure of the daemon that imports and restores *MargheritaTre* databases is pictured in Fig. C.1.

`daemon` takes care of interacting with the operative system to properly forking the process, decoupling it from the parent environment, creating a PID file, and running the script. It declares an abstract `run` method that has to be implemented by the class defining the script.

`lockManager` provides the methods to check, create, and delete locks in a database to prevent the daemon from interfering with the script that creates views.

`importManager` is the core class of the daemon. It inherits from `daemon` and `lockManager` and defines the `run` method. This method creates an instance of `downloadManager` and `creationManager`, by means of which it checks for new updated database dumps, downloads and restores them.

`downloadManager` implements the methods to communicate with the web service that manages the synchronisation of databases from ICU servers. It provides methods to check if new databases are available, to download them, and to notify the web service of the success/failure of the download and restoration.

`creationManager` implements the methods to create a new database on the local PostgreSQL server, to unzip and restore database dumps. Furthermore, the method `createViews` calls some bash scripts to re-create some basic views in the newly restored database.

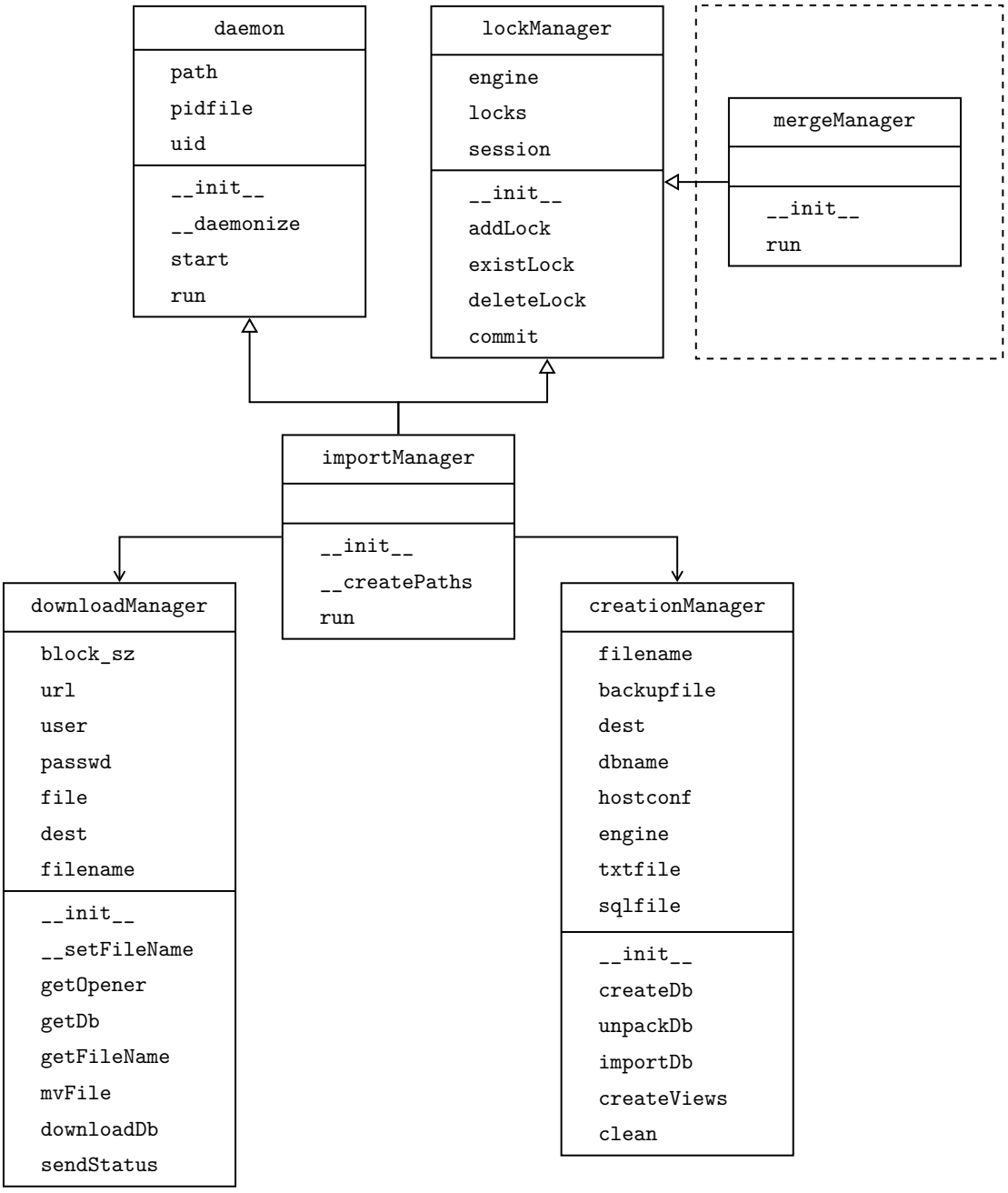

Figure C.1: Class structure of the Python daemon importing and restoring databases from ICU servers. The class `mergeManager` in the dashed box is not used by the daemon, but by a script that merges all *MargheritaTre* tables in a single database.

C.2 Creation of views

After databases are restored, data are cast in a more convenient form for analysis by joining several tables from the original dataset. Furthermore data from all centres are copied in a single database. Every night crontab run a Python script which contains the class `mergeManager`, that inherits from `lockManager` and implements a single `run` method (see Fig. C.1). After getting a

lock from ensuring that databases are no longer restored, this method executes a series of bash scripts that recreate views and merge them together.

The merge scripts are executed in the following order.

`db_replacement` fixes isolated errors.

`configcode` checks the list of ICU databases present on the server and creates a list in a configuration database with their centre ID.

`updatetablesprontfar` normalises the format of string variables in the database of drugs.

`createviewsprontvar` creates a view in the database of drugs by joining the tables containing commercial names, active ingredients, and other details.

`updatetables` normalises the format of string variables in the M3 database of every ICU.

`createftables` creates in every ICU database a series of foreign tables pointing to configuration tables in common external databases (e.g. codification of drug names, laboratory tests, vital signs, etc...)

`createviews` creates a series of views in every ICU database. Each view contains information on a specific aspect, such as demographic details, pathologies, infections, comorbidities, reason for admission, drug administrations, laboratory tests, vital signs, clinical notes.

`createallftables` creates in a unique database a series of foreign tables pointing to each view in each ICU database.

`createallviews` creates union views by pasting together the view of all ICUs through the foreign tables created by the previous script. These views are *materialised* to speed up query execution.

Appendix D

LIST OF ABBREVIATIONS AND SYMBOLS

List of abbreviations and symbols by chapter where they are defined and used for the first time.

Introduction

ICU Intensive Care Unit

M3 MargheritaTre – Electronic Health Record

GiViTI Italian Group for the Evaluation of Intervention in Intensive Care Medicine

MIC minimum inhibitory concentration

$C_{\max}$ maximum plasma drug concentration

T_{MIC} time above MIC

TDM Therapeutic Drug Monitoring

Chapter 1

EHR Electronic Health Record

MIMIC Medical Information Mart for Intensive Care

GICU General ICU

SICU Surgical ICU

CICU Cardiosurgical ICU

NICU Neurosurgical ICU

HDU High Dependency Unit

WBC White blood cell count

PCT Procalcitonin

Chapter 2

PK	Pharmacokinetics
PD	Pharmacodynamics
F	flux of molecules crossing a membrane
C_i	molecule concentration in region i
d	diffusion coefficient
S	membrane surface
K_a	acid drug dissociation constant
K_b	basis drug dissociation constant
f_{ua}	non-ionised fraction of acids
f_{ub}	non-ionised fraction of bases
K_w	water dissociation constant
Q	total drug amount
V_p	plasma volume
C_p	plasma drug concentration
$V_{t,i}$	volume of tissue i
$C_{t,i}$	drug concentration in tissue i
V_{tot}	total volume
r_c	ratio between tissue and plasma concentrations
f_u	fraction on unbound drug
f_b	fraction drug bound to plasma proteins
C_u	plasma concentration of unbound drug
C_b	plasma concentration of drug bound to proteins
K	association constant
P_u	unbound protein concentration
P_b	bound protein concentration

P_p	total plasma protein concentration
f_{tu}	fraction of unbound drug in tissues
P_t	protein concentration in tissues
K_t	association constant in tissue
C_{tu}	un bound drug concentration in tissue
V_a	apparent distribution volume
F_B	blood flow
C_A	arterial drug concentration
C_V	venous drug concentration
Q_t	amount of drug in tissues
κ_e^{perf}	perfusion-limited exit rate
κ_p	perfusion rate
τ_{perf}	perfusion-limited filling half-time
κ_e^{perm}	permeability-limited exit rate
τ_{perm}	permeability-limited filling half-time
k	clearance
k_{drug}	drug clearance
r_e	drug extraction ration
k_{liver}	hepatic drug clearance
k_{kidneys}	renal drug clearance
k_u	clearance for unbound drug
C_s	saturation concentration
k_{bile}	biliary clearance
C_{bile}	bile drug concentration
F_{bile}	bile flow
GFR	glomerular filtration rate

k_{GFR}	glomerular filtration rate – mathematical symbol
$k_{\mathrm{filtration}}$	clearance associated with renal filtration
$f_{ua,p}$	non-ionised fraction of acid drug in plasma
$f_{ua,U}$	non-ionised fraction of acid drug in urine
C_U	drug concentration in urine
$\mathrm{pH_B}$	urine pH
$\mathrm{pH_B}$	blood pH
F_U	urine flow
RRT	Renal Replacement Therapy
C_B	blood drug concentration
C_D	dialysate drug concentration
v_B	blood flow
v_D	dialysate flow
γ	blood-dialysate diffusion coefficient
C_{Bi}	initial blood drug concentration
C_{Bf}	final blood drug concentration
κ	decay constant
L	filter length
k_{HD}	haemodialysis clearance
C_{pre}	pre-filter drug concentration
F_{pre}	flow of pre-dilution fluid
S_c	filter sieving coefficient
h	haematocrit
C_{UF}	ultrafiltrate drug concentration
k_{HF}	haemofiltration clearance
F_{post}	flow of post-dilution fluid

Δ	fluid balance
f_{pre}	fraction of pre-dilution fluid
$C_{\min}$	minimum therapeutic concentration
$T_{>C_{\min}}$	time for which drug
AUC	Area Under the Concentration-time curve
$\mathbf{AUC}_{0--24}$	Area Under the Concentration-time curve in 24 h
A_C	AUC – mathematical symbol
$\bar{C}_T$	mean concentration in the time interval T
D	drug dosage
I	infusion rate
Q_i	drug amount in compartment i
C_i	drug concentration in compartment i
V_i	volume of compartment i
κ_e	elimination rate
κ_{12}	diffusion rate from the first to the second compartment
κ_{21}	diffusion rate from the second to the first compartment
κ_{crea}	creatinine clearance
d_{dial}	dialysis dose
θ_i	parameters in compartmental models

Chapter 3

a	age
C_{alb}	albumin concentration
s	Apache II Score
k^L_{crea}	creatine clearance estimated with Levey's formula [111]
w	body weight

k_{vanco}	vancomycin clearance
V_c	volume of central compartment
V_p	volume of peripheral compartment
$k_{\text{crea}}^{\text{CG}}$	creatinine clearance estimated with Cockroft–Gault formula [50]
k_{int}	intercompartmental clearance
η_i	random effect on pharmacokinetic parameters ($i = k, V$, clearance, distribution volume, respectively)
ε	residual variability
S	body surface area

Chapter 4

κ	elimination rate
D_{opt}	optimal loading dose
C_{opt}	target optimal concentration
I_{opt}	optimal infusion rate
λ_i	decay rates in two-compartment model $i = 1, 2$
t_{min}	time at which the central-compartment concentration reaches its minimum
Q_{min}	minimum drug amount
t_{flex}	time at which the central-compartment concentration has an inflection point
Q_{flex}	drug amount at inflection point
D_{cons}	loading dose in conservative administration strategy
D_{agg}	loading dose in aggressive administration strategy
θ	vector of structural model parameters
Ω	covariance matrix of η_i
σ	standard deviation of ε
ψ	full vector of model parameters

L	likelihood function
$\mathcal{L}$	logarithm of likelihood function
$S(\psi)$	sum of squared residuals
Γ	gradient of $S(\psi)$
Δ	Hessian of $S(\psi)$
$\hat{x}$	best-fit estimated value of x
$\mathbb{E}(x)$	expected value of x

Chapter 5

LIS	Laboratory Information System
VIS	Vasoactive Inotropic Score
EVID	Event type
DV	Measured value of the dependent variable
AMT	Amount of administered drug
EBE	Empirical Bayes Estimate
NPDE	Normalised predicted distribution error
CWRES	Conditional Weighted Residuals
VPC	Visual Predictive Checks
OFV	Objective Function Value
δ_{CRRT}	CRRT treatment – binary variable
Q_c	drug amount in the central compartment
Q_p	drug amount in the peripheral compartment
C_{ALT}	concentration of alanine transaminase
δ_{SEX}	sex – binary variable
W	Wilcoxon test
KS	Kolmogorov–Smirnov test

SW	Shapiro–Wilk test

Chapter 6

GLUT	Glucose transporter
SGLT	Sodium-coupled glucose cotransporters
CNS	Central Nervous System
K	glucose tolerance index
G	blood glucose amount
I	blood insulin amount
X	auxiliary function – insulin in a distant compartment
I_b	baseline insulin level
G_b	baseline glucose level
$\mathcal{G}$	Green function
I_p	insulin amount in plasma
I_i	insulin amount in intercellular space
V_p	plasma volume
V_i	intercellular space volume
t_p	insulin degradation time constant in plasma
V_i	insulin degradation time constant in intercellular space
E	insulin transfer rate
V_g	glucose distribution volume
G_{in}	rate of glucose intake
t_d	implicit response delay
R_m	scale factor of pancreatic insulin production rate
C_1	threshold glucose concentration for pancreatic insulin production
C_2	threshold glucose concentration for CNS glucose uptake

U_b	maximum rate of CNS glucose uptake
C_3	scale factor of glucose concentration in glucose utilisation by muscle and adipose tissue
U_0	minimum rate of insulin dependent glucose uptake
U_m	maximum rate of insulin dependent glucose uptake
R_g	scale factor of rate of hepatic glucose production
C_5	threshold insulin concentration for hepatic glucose production
f_1	pancreatic insulin production rate
f_2	CNS glucose uptake
$f_3 \cdot f_4$	Muscle- and adipose-tissue glucose uptake
f_5	hepatic glucose production
f_6	insulin degradation rate
d_i	insulin-degradation scale factor
C_6	half-saturation insulin concentration in insulin concentration rate
τ	explicit response delay
τ_1	pancreatic response delay to glucose stimulus
τ_2	hepatic response delay to insulin stimulus
x^*	steady state solution of variable x
EGP_0	endogenous glucose production at zero insulin concentration
F_{01}^c	insulin-dependent glucose flux
F_R	renal glucose clearance

Chapter 7

G_{meal}	meal glucose amount
t_{meal}	meal initial time
τ_{ab}	glucose absorption time

τ_{av}	glucose availability time
L	amount of glucagon in plasma
f_7	pancreatic glucagon production rate
f_8	hepatic glucagon production rate stimulated by glucagon
d_l	glucagon elimination constant
R_l	scale factor of glucagon production
C_7	glucose concentration threshold in pancreatic glucose production
R_{gl}	scale factor of glucagon-stimulated glucose production rate
C_8	glucagon concentration threshold in glucagon-stimulated glucose production
β_I	pancreatic efficacy of insulin production
β_L	pancreatic efficacy of glucagon production
γ_I	efficacy of insulin dependent glucose uptake
γ_L	efficacy of glucagon dependent glucose release
I_{in}	insulin intake

BIBLIOGRAPHY

[1] AbioKin, ClinicalTrial.gov. https://clinicaltrials.gov/ct2/show/NCT02609646.

[2] EUCAST website. http://www.eucast.org.

[3] GiViTI. https://http://giviti.marionegri.it/.

[4] MargheritaTre Project. http://www.giviti.marionegri.it/MargheritaTre.asp.

[5] NONMEM guide. https://nonmem.iconplc.com/nonmem720/guides/v.pdf.

[6] Perl-speaks-NONMEM (PsN). https://uupharmacometrics.github.io/PsN/.

[7] PostgreSQL. https://www.postgresql.org/.

[8] PROSAFE. https://http://prosafe.marionegri.it/.

[9] Xpose4 manual. https://cran.r-project.org/web/packages/xpose4/xpose4.pdf.

[10] A. Ahmed, S. Chandra, V. Herasevich, O. Gajic, and B. W. Pickering. The effect of two different electronic health record user interfaces on intensive care provider task load, errors of cognition, and performance. *Critical care medicine* **39**, 1626 (2011).

[11] S. Ajami and T. Bagheri-Tadi. Barriers for adopting electronic health records (ehrs) by physicians. *Acta Informatica Medica* **21**, 129 (2013).

[12] J. Allyn, D. Vandroux, J. Jabot, C. Brulliard, R. Galliot, X. Tabatchnik, P. Combe, O. Martinet, and N. Allou. Prognosis of patients presenting extreme acidosis (ph$<$ 7) on admission to intensive care unit. *Journal of critical care* **31**, 243 (2016).

[13] F. Álvarez-Lerma and S. Grau. Management of antimicrobial use in the intensive care unit. *Drugs* **72**, 447 (2012).

[14] K. Amrein, M. Ellmerer, R. Hovorka, N. Kachel, D. Parcz, S. Korsatko, K. Smolle, S. Perl, G. Bock, W. Doll, *et al.* Hospital glucose control: safe and reliable glycemic control using enhanced model predictive control algorithm in medical intensive care unit patients. *Diabetes technology & therapeutics* **12**, 405 (2010).

[15] T. Asada, Y. Aoki, T. Sugiyama, M. Yamamoto, T. Ishii, Y. Kitsuta, S. Nakajima, N. Yahagi, and K. Doi. Organ system network disruption in nonsurvivors of critically ill patients. *Critical care medicine* **44**, 83 (2016).

[16] M. Baker. 1,500 scientists lift the lid on reproducibility. *Nature News* **533**, 452 (2016).

[17] A. Balasubramanyam. Intensive glycemic control in the intensive care unit: promises and pitfalls. *The Journal of clinical endocrinology and metabolism* **94**, 416 (2009).

[18] R. P. Bartsch, K. K. Liu, A. Bashan, and P. C. Ivanov. Network physiology: how organ systems dynamically interact. *PloS one* **10**, e0142143 (2015).

[19] A. Bashan, R. P. Bartsch, J. W. Kantelhardt, S. Havlin, and P. C. Ivanov. Network physiology reveals relations between network topology and physiological function. *Nature communications* **3**, 702 (2012).

[20] H. Bence Jones. On the variations of the acidity of the urine in the state of health on the influence of medicines on the acidity of the urine. *Proceedings of the Royal Society of London Series I* **5**, 825 (1843).

[21] D. L. Bennett and S. A. Gourley. Asymptotic properties of a delay differential equation model for the interaction of glucose with plasma and interstitial insulin. *Applied Mathematics and Computation* **151**, 189 (2004).

[22] R. Bergman. Integrated control of hepatic glucose metabolism. In *Federation proceedings*, volume 36, pp. 265–270 (1977).

[23] R. Bergman and R. Bucolo. Nonlinear metabolic dynamics of the pancreas and liver. *Journal of Dynamic Systems Measurement and Control* **95**, 296 (1973).

[24] R. N. Bergman and C. Cobelli. Minimal modeling, partition analysis, and the estimation of insulin sensitivity. In *Federation proceedings*, volume 39, p. 110 (1980).

[25] R. N. Bergman, Y. Z. Ider, C. R. Bowden, and C. Cobelli. Quantitative estimation of insulin sensitivity. *American Journal of Physiology-Endocrinology And Metabolism* **236**, E667 (1979).

[26] M. Bergstrand, A. C. Hooker, J. E. Wallin, and M. O. Karlsson. Prediction-corrected visual predictive checks for diagnosing nonlinear mixed-effects models. *The AAPS journal* **13**, 143 (2011).

[27] M. Beumier, J. A. Roberts, H. Kabtouri, M. Hites, F. Cotton, F. Wolff, J. Lipman, F. Jacobs, J.-L. Vincent, and F. S. Taccone. A new regimen for continuous infusion of vancomycin during continuous renal replacement therapy. *Journal of antimicrobial chemotherapy* **68**, 2859 (2013).

[28] C. Blixt, O. Rooyackers, B. Isaksson, and J. Wernerman. Continuous on-line glucose measurement by microdialysis in a central vein. a pilot study. *Critical Care* **17**, R87 (2013).

[29] V. W. Bolie. Coefficients of normal blood glucose regulation. *Journal of Applied Physiology* **16**, 783 (1961).

[30] P. L. Bonate. The effect of collinearity on parameter estimates in nonlinear mixed effect models. *Pharmaceutical research* **16**, 709 (1999).

[31] C. Bonner, J. Kerr-Conte, V. Gmyr, G. Queniat, E. Moerman, J. Thévenet, C. Beaucamps, N. Delalleau, I. Popescu, W. J. Malaisse, *et al.* Inhibition of the glucose transporter sglt2 with dapagliflozin in pancreatic alpha cells triggers glucagon secretion. *Nature medicine* **21**, 512 (2015).

[32] B. A. Boucher, G. C. Wood, and J. M. Swanson. Pharmacokinetic changes in critical illness. *Critical care clinics* **22**, 255 (2006).

[33] D. W. Bratzler, E. P. Dellinger, K. M. Olsen, T. M. Perl, P. G. Auwaerter, M. K. Bolon, D. N. Fish, L. M. Napolitano, R. G. Sawyer, D. Slain, *et al.* Clinical practice guidelines for antimicrobial prophylaxis in surgery. *Surgical infections* **14**, 73 (2013).

[34] D. Brealey and M. Singer. Hyperglycemia in critical illness: a review. *Journal of diabetes science and technology* **3**, 1250 (2009).

[35] K. Brendel, E. Comets, C. Laffont, C. Laveille, and F. Mentré. Metrics for external model evaluation with an application to the population pharmacokinetics of gliclazide. *Pharmaceutical research* **23**, 2036 (2006).

[36] L. Briant, A. Salehi, E. Vergari, Q. Zhang, and P. Rorsman. Glucagon secretion from pancreatic α-cells. *Upsala journal of medical sciences* **121**, 113 (2016).

[37] N. Brown, D. Ho, K. Fong, L. Bogerd, A. Maksymiuk, R. Bolivar, V. Fainstein, and G. Bodey. Effects of hepatic function on vancomycin clinical pharmacology. *Antimicrobial agents and chemotherapy* **23**, 603 (1983).

[38] T. G. Buchman. Physiologic failure: multiple organ dysfunction syndrome. In *Complex Systems Science in BioMedicine*, pp. 631–640 (Springer, 2006).

[39] P. Campanella, E. Lovato, C. Marone, L. Fallacara, A. Mancuso, W. Ricciardi, and M. L. Specchia. The impact of electronic health records on healthcare quality: a systematic review and meta-analysis. *The European Journal of Public Health* **26**, 60 (2015).

[40] E. V. Cauter, D. Desir, C. Decoster, F. Fery, and E. O. Balasse. Nocturnal decrease in glucose tolerance during constant glucose infusion. *The Journal of Clinical Endocrinology & Metabolism* **69**, 604 (1989).

[41] K. S. Chan, J. B. Fowles, and J. P. Weiner. Electronic health records and the reliability and validity of quality measures: a review of the literature. *Medical Care Research and Review* **67**, 503 (2010).

[42] J. G. Chase, A. J. Le Compte, F. Suhaimi, G. M. Shaw, A. Lynn, J. Lin, C. G. Pretty, N. Razak, J. D. Parente, C. E. Hann, *et al.* Tight glycemic control in critical care–the leading role of insulin sensitivity and patient variability: a review and model-based analysis. *Computer methods and programs in biomedicine* **102**, 156 (2011).

[43] J. G. Chase, A. J. LeCompte, G. M. Shaw, J. Lin, C. G. Pretty, N. Razak, J. Parente, A. Lynn, C. E. Hann, and F. Suhaimi. Tight glycemic control-the leading role of insulin sensitivity in determining efficacy and thus outcome (2009).

[44] J. G. Chase, G. M. Shaw, J. Lin, C. V. Doran, C. Hann, M. B. Robertson, P. M. Browne, T. Lotz, G. C. Wake, and B. Broughton. Adaptive bolus-based targeted glucose regulation of hyperglycaemia in critical care. *Medical engineering & physics* **27**, 1 (2005).

[45] J. G. Chase, F. Suhaimi, S. Penning, J.-C. Preiser, A. J. Le Compte, J. Lin, C. G. Pretty, G. M. Shaw, K. T. Moorhead, and T. Desaive. Validation of a model-based virtual trials method for tight glycemic control in intensive care. *Biomedical engineering online* **9**, 84 (2010).

[46] B. Chaudhry, J. Wang, S. Wu, M. Maglione, W. Mojica, E. Roth, S. C. Morton, and P. G. Shekelle. Systematic review: impact of health information technology on quality, efficiency, and costs of medical care. *Annals of internal medicine* **144**, 742 (2006).

[47] R. Cheng-Xue, A. Gómez-Ruiz, N. Antoine, L. A. Noël, H.-Y. Chae, M. A. Ravier, F. Chimienti, F. C. Schuit, and P. Gilon. Tolbutamide controls glucagon release from mouse islets differently than glucose: involvement of katp channels from both α-cells and δ-cells. *Diabetes* p. DB_120347 (2013).

[48] G. Choi, C. D. Gomersall, Q. Tian, G. M. Joynt, R. Freebairn, and J. Lipman. Principles of antibacterial dosing in continuous renal replacement therapy. *Critical care medicine* **37**, 2268 (2009).

[49] P. Clark. Assays for insulin, proinsulin (s) and c-peptide. *Annals of clinical biochemistry* **36**, 541 (1999).

[50] D. W. Cockcroft and H. Gault. Prediction of creatinine clearance from serum creatinine. *Nephron* **16**, 31 (1976).

[51] E. Comets, K. Brendel, and F. Mentré. Computing normalised prediction distribution errors to evaluate nonlinear mixed-effect models: the npde add-on package for r. *Computer methods and programs in biomedicine* **90**, 154 (2008).

[52] D. Czock and F. Keller. Mechanism-based pharmacokinetic–pharmacodynamic modeling of antimicrobial drug effects. *Journal of pharmacokinetics and pharmacodynamics* **34**, 727 (2007).

[53] A. De Gaetano and O. Arino. Mathematical modelling of the intravenous glucose tolerance test. *Journal of mathematical biology* **40**, 136 (2000).

[54] M. d. M. F. de Gatta Garcia, N. Revilla, M. V. Calvo, A. Domínguez-Gil, A. S. Navarro, *et al.* Pharmacokinetic/pharmacodynamic analysis of vancomycin in icu patients. *Intensive care medicine* **33**, 279 (2007).

[55] P. De Paepe, F. M. Belpaire, and W. A. Buylaert. Pharmacokinetic and pharmacodynamic considerations when treating patients with sepsis and septic shock. *Clinical pharmacokinetics* **41**, 1135 (2002).

[56] A. Di Paolo, P. Malacarne, E. Guidotti, R. Danesi, and M. Del Tacca. Pharmacological issues of linezolid. *Clinical pharmacokinetics* **49**, 439 (2010).

[57] W. C. Duckworth, R. G. Bennett, and F. G. Hamel. Insulin degradation: progress and potential. *Endocrine reviews* **19**, 608 (1998).

[58] L. Duncan. The intravenous glucose tolerance test. *Quarterly Journal of Experimental Physiology and Cognate Medical Sciences: Translation and Integration* **41**, 85 (1956).

[59] K. Dungan, J. Chapman, S. S. Braithwaite, and J. Buse. Glucose measurement: confounding issues in setting targets for inpatient management. *Diabetes care* **30**, 403 (2007).

[60] K. Engelborghs, V. Lemaire, J. Belair, and D. Roose. Numerical bifurcation analysis of delay differential equations arising from physiological modeling. *Journal of mathematical biology* **42**, 361 (2001).

[61] L. Escobar, M. Andresen, P. Downey, M. N. Gai, T. Regueira, T. Bórquez, J. Lipman, and J. A. Roberts. Population pharmacokinetics and dose simulation of vancomycin in critically ill patients during high-volume haemofiltration. *International journal of antimicrobial agents* **44**, 163 (2014).

[62] A. C. Faust, R. L. Attridge, and L. Ryan. How low should you go? the limbo of glycemic control in intensive care units. *Critical care nurse* **31**, e9 (2011).

[63] S. Finazzi, G. Mandelli, E. Garbero, M. Mondini, G. Trussardi, M. Giardino, M. Tavola, and G. Bertolini. Data collection and research with margheritatre. *Physiological measurement* **39**, 084004 (2018).

[64] S. Finfer, D. Chittock, S. Su, D. Blair, D. Foster, V. Dhingra, R. Bellomo, D. Cook, P. Dodek, W. Henderson, *et al.* Intensive versus conventional glucose control in critically ill patients. *The New England journal of medicine* **360**, 1283 (2009).

[65] J. S. Freeman. Insulin analog therapy: improving the match with physiologic insulin secretion. *The Journal of the American Osteopathic Association* **109**, 26 (2009).

[66] C. R. Frei, N. P. Wiederhold, and D. S. Burgess. Antimicrobial breakpoints for gram-negative aerobic bacteria based on pharmacokinetic–pharmacodynamic models with monte carlo simulation. *Journal of antimicrobial chemotherapy* **61**, 621 (2008).

[67] G. G. Gallo, G. Lancini, and F. Parenti. *Antibiotics: a multidisciplinary approach* (Springer Science & Business Media, 2013).

[68] M. Ghassemi, T. Naumann, F. Doshi-Velez, N. Brimmer, R. Joshi, A. Rumshisky, and P. Szolovits. Unfolding physiological state: Mortality modelling in intensive care units. In *Proceedings of the 20th ACM SIGKDD international conference on Knowledge discovery and data mining*, pp. 75–84 (ACM, 2014).

[69] M. Gibaldi. *Biopharmaceutics and clinical pharmacokinetics* (Lea & Febiger, 1977).

[70] N. R. Gosmanov, A. R. Gosmanov, and J. E. Gerich. Glucagon physiology (2011).

[71] C. R. Greyson. Pathophysiology of right ventricular failure. *Critical care medicine* **36**, S57 (2008).

[72] G. M. Grodsky. A threshold distribution hypothesis for packet storage of insulin and its mathematical modeling. *Journal of Clinical Investigation* **51**, 2047 (1972).

[73] J. Gromada, X. Ma, M. Høy, K. Bokvist, A. Salehi, P.-O. Berggren, and P. Rorsman. Atp-sensitive k+ channel–dependent regulation of glucagon release and electrical activity by glucose in wild-type and sur1-/- mouse α-cells. *Diabetes* **53**, S181 (2004).

[74] C. O. Gualerzi, L. Brandi, A. Fabbretti, and C. L. Pon. *Antibiotics: Targets, mechanisms and resistance* (John Wiley & Sons, 2013).

[75] J. Gunst and G. Van den Berghe. Blood glucose control in the icu: don't throw out the baby with the bathwater! *Intensive care medicine* **42**, 1478 (2016).

[76] I. Gustafsson, E. Löwdin, I. Odenholt, and O. Cars. Pharmacokinetic and pharmacodynamic parameters for antimicrobial effects of cefotaxime and amoxicillin in an in vitro kinetic model. *Antimicrobial agents and chemotherapy* **45**, 2436 (2001).

[77] R. G. Hahn, S. Ljunggren, F. Larsen, and T. Nyström. A simple intravenous glucose tolerance test for assessment of insulin sensitivity. *Theoretical Biology and Medical Modelling* **8**, 12 (2011).

[78] J. A. Hammes, F. Pfuetzenreiter, F. d. Silveira, Á. Koenig, and G. A. Westphal. Potential drug interactions prevalence in intensive care units. *Rev Bras Ter Intensiva* **20**, 349 (2008).

[79] C. E. Hann, J. G. Chase, J. Lin, T. Lotz, C. V. Doran, and G. M. Shaw. Integral-based parameter identification for long-term dynamic verification of a glucose–insulin system model. *Computer methods and programs in biomedicine* **77**, 259 (2005).

[80] N. Haverbeke, T. Van Herpe, M. Diehl, G. Van den Berghe, and B. De Moor. Nonlinear model predictive control with moving horizon state and disturbance estimation-application to the normalization of blood glucose in the critically ill. *IFAC Proceedings Volumes* **41**, 9069 (2008).

[81] J. Henry, Y. Pylypchuk, T. Searcy, and V. Patel. Adoption of electronic health record systems among us non-federal acute care hospitals: 2008-2015. *The Office of National Coordinator for Health Information Technology* (2016).

[82] T. V. Herpe, M. Espinoza, N. Haverbeke, B. De Moor, and G. Van den Berghe. Glycemia prediction in critically ill patients using an adaptive modeling approach (2007).

[83] R. Hillestad, J. Bigelow, A. Bower, F. Girosi, R. Meili, R. Scoville, and R. Taylor. Can electronic medical record systems transform health care? potential health benefits, savings, and costs. *Health affairs* **24**, 1103 (2005).

[84] M. Hilscher and W. Sanchez. Congestive hepatopathy. *Clinical Liver Disease* **8**, 68 (2016).

[85] A. C. Hooker, M. Foracchia, M. G. Dodds, and P. Vicini. An evaluation of population d-optimal designs via pharmacokinetic simulations. *Annals of biomedical engineering* **31**, 98 (2003).

[86] A. C. Hooker, C. E. Staatz, and M. O. Karlsson. Conditional weighted residuals (cwres): a model diagnostic for the foce method. *Pharmaceutical research* **24**, 2187 (2007).

[87] E. A. Hoste, J. Damen, R. C. Vanholder, N. H. Lameire, J. R. Delanghe, K. Van den Hauwe, and F. A. Colardyn. Assessment of renal function in recently admitted critically ill patients with normal serum creatinine. *Nephrology Dialysis Transplantation* **20**, 747 (2005).

[88] R. Hovorka, V. Canonico, L. J. Chassin, U. Haueter, M. Massi-Benedetti, M. O. Federici, T. R. Pieber, H. C. Schaller, L. Schaupp, T. Vering, *et al.* Nonlinear model predictive control of glucose concentration in subjects with type 1 diabetes. *Physiological measurement* **25**, 905 (2004).

[89] R. Hovorka, L. J. Chassin, M. Ellmerer, J. Plank, and M. E. Wilinska. A simulation model of glucose regulation in the critically ill. *Physiological measurement* **29**, 959 (2008).

[90] R. Hovorka, J. Powrie, G. Smith, P. Sonksen, E. Carson, and R. Jones. Five-compartment model of insulin kinetics and its use to investigate action of chloroquine in niddm. *American Journal of Physiology-Endocrinology And Metabolism* **265**, E162 (1993).

[91] Y.-L. Huang, T. Badrick, and Z.-D. Hu. Using freely accessible databases for laboratory medicine research: experience with mimic database. *Journal of Laboratory and Precision Medicine* **2** (2017).

[92] A. Hurst, M. Yoshinaga, G. Mitani, K. Foo, R. Jelliffe, and E. Harrison. Application of a bayesian method to monitor and adjust vancomycin dosage regimens. *Antimicrobial agents and chemotherapy* **34**, 1165 (1990).

[93] J. M. Hyatt, P. S. McKinnon, G. S. Zimmer, and J. J. Schentag. The importance of pharmacokinetic/pharmacodynamic surrogate markers to outcome. *Clinical pharmacokinetics* **28**, 143 (1995).

[94] E. H. Ibrahim, G. Sherman, S. Ward, V. J. Fraser, and M. H. Kollef. The influence of inadequate antimicrobial treatment of bloodstream infections on patient outcomes in the icu setting. *Chest Journal* **118**, 146 (2000).

[95] P. C. Ivanov and R. P. Bartsch. Network physiology: mapping interactions between networks of physiologic networks. In *Networks of Networks: the last Frontier of Complexity*, pp. 203–222 (Springer, 2014).

[96] P. C. Ivanov, K. K. Liu, and R. P. Bartsch. Focus on the emerging new fields of network physiology and network medicine. *New Journal of Physics* **18**, 100201 (2016).

[97] M. Jacobs. Optimisation of antimicrobial therapy using pharmacokinetic and pharmacodynamic parameters. *Clinical microbiology and Infection* **7**, 589 (2001).

[98] U. K. Jamaludin, F. M. Suhaimi, N. N. A. Razak, A. M. Ralib, M. B. M. Nor, C. G. Pretty, and L. Humaidi. Performance of stochastic targeted blood glucose control protocol by virtual trials in the malaysian intensive care unit. *Computer methods and programs in biomedicine* **162**, 149 (2018).

[99] J. B. Jaspan, A. H. Huen, C. G. Morley, A. R. Moossa, and A. H. Rubenstein. The role of the liver in glucagon metabolism. *The Journal of clinical investigation* **60**, 421 (1977).

[100] P. B. Jensen, L. J. Jensen, and S. Brunak. Mining electronic health records: towards better research applications and clinical care. *Nature Reviews Genetics* **13**, 395 (2012).

[101] G. Jiang and B. B. Zhang. Glucagon and regulation of glucose metabolism. *American Journal of Physiology-Endocrinology And Metabolism* **284**, E671 (2003).

[102] A. E. Johnson, T. J. Pollard, and R. G. Mark. Reproducibility in critical care: a mortality prediction case study. In *Machine Learning for Healthcare Conference*, pp. 361–376 (2017).

[103] A. E. Johnson, T. J. Pollard, L. Shen, H. L. Li-wei, M. Feng, M. Ghassemi, B. Moody, P. Szolovits, L. A. Celi, and R. G. Mark. Mimic-iii, a freely accessible critical care database. *Scientific data* **3**, 160035 (2016).

[104] J. P. Keener and J. Sneyd. *Mathematical physiology, 2nd Edition*, volume 1 (Springer, 2009).

[105] J. P. Keener and J. Sneyd. *Mathematical physiology, 2nd Edition*, volume 2 (Springer, 2009).

[106] R. Keizer, K. Harling, and M. Karlsson. Extended npde diagnostics for the between subjectvariability and residual error models. In *PAGE. Abstracts of the Annual Meeting of the Population Approach Group in Europe*, volume 21 (2012).

[107] S. Kissler, C. Cichowitz, S. Sankaranarayanan, and D. Bortz. Determination of personalized diabetes treatment plans using a two-delay model. *Journal of theoretical biology* **359**, 101 (2014).

[108] M. A. Kovalaske and G. Y. Gandhi. Glycemic control in the medical intensive care unit. *Journal of diabetes science and technology* **3**, 1330 (2009).

[109] M. H. Kutner, C. J. Nachtsheim, J. Neter, and W. Li. *Applied linear statistical models, Fifth Edition* (McGraw-Hill Irwin Boston, 2005).

[110] L. Lalande, B. Charpiat, G. Leboucher, and M. Tod. Consequences of renal failure on non-renal clearance of drugs. *Clinical pharmacokinetics* **53**, 521 (2014).

[111] A. S. Levey, J. P. Bosch, J. B. Lewis, T. Greene, N. Rogers, and D. Roth. A more accurate method to estimate glomerular filtration rate from serum creatinine: a new prediction equation. *Annals of internal medicine* **130**, 461 (1999).

[112] J. Li, Y. Kuang, and C. C. Mason. Modeling the glucose–insulin regulatory system and ultradian insulin secretory oscillations with two explicit time delays. *Journal of Theoretical Biology* **242**, 722 (2006).

[113] L. Li and W. Zheng. Global stability of a delay model of glucose–insulin interaction. *Mathematical and Computer Modelling* **52**, 472 (2010).

[114] M. Lieberman and A. D. Marks. *Marks' basic medical biochemistry: a clinical approach* (Lippincott Williams & Wilkins, 2009).

[115] T.-P. Lim, K. W. Garey, and V. H. Tam. Pharmacokinetic/pharmacodynamic antimicrobial individualization and optimization strategies. *Current infectious disease reports* **10**, 9 (2008).

[116] J. Lin, D. Lee, J. G. Chase, G. M. Shaw, A. Le Compte, T. Lotz, J. Wong, T. Lonergan, and C. E. Hann. Stochastic modelling of insulin sensitivity and adaptive glycemic control for critical care. *Computer methods and programs in biomedicine* **89**, 141 (2008).

[117] P. Llopis-Salvia and N. Jiménez-Torres. Population pharmacokinetic parameters of vancomycin in critically ill patients. *Journal of clinical pharmacy and therapeutics* **31**, 447 (2006).

[118] A. Makroglou, J. Li, and Y. Kuang. Mathematical models and software tools for the glucose-insulin regulatory system and diabetes: an overview. *Applied numerical mathematics* **56**, 559 (2006).

[119] M. A. Malesker, P. A. Foral, A. C. McPhillips, K. J. Christensen, J. A. Chang, and D. E. Hilleman. An efficiency evaluation of protocols for tight glycemic control in intensive care units. *American Journal of Critical Care* **16**, 589 (2007).

[120] E. A. Mann, J. A. Jones, S. E. Wolf, and C. E. Wade. Computer decision support software safely improves glycemic control in the burn intensive care unit: a randomized controlled clinical study. *Journal of burn care & research: official publication of the American Burn Association* **32**, 246 (2011).

[121] Q. Mao, M. Jay, J. Hoffman, J. Calvert, C. Barton, D. Shimabukuro, L. Shieh, U. Chettipally, G. Fletcher, Y. Kerem, *et al.* Multicenter validation of a sepsis prediction algorithm using only vital sign data in the emergency department, general ward and icu. *bioRxiv* p. 243964 (2018).

[122] R. W. McLawhon. Guidelines for the monitoring of vancomycin, aminoglycosides and certain antibiotics. In *Therapeutic Drug Monitoring*, pp. 197–218 (Elsevier, 2012).

[123] M. M. McMahon and J. M. Miles. Glycemic control and nutrition in the intensive care unit. *Current Opinion in Clinical Nutrition & Metabolic Care* **9**, 120 (2006).

[124] A. Merril and S. Jones. Effectiveness of tight glycemic control in the medical intensive care unit: a systematic review. JBI Databases of Systematic Reviews and Implementation Reports. http://www.joannabriggslibrary.org/jbilibrary/index.php/jbisrir/article/view/122.

[125] P. A. Moise-Broder, A. Forrest, M. C. Birmingham, and J. J. Schentag. Pharmacodynamics of vancomycin and other antimicrobials in patients with staphylococcus aureus lower respiratory tract infections. *Clinical pharmacokinetics* **43**, 925 (2004).

[126] V. M. Montori, B. R. Bistrian, and M. M. McMahon. Hyperglycemia in acutely ill patients. *Jama* **288**, 2167 (2002).

[127] J. R. Moorman, D. E. Lake, and P. C. Ivanov. Early detection of sepsis—a role for network physiology? *Critical care medicine* **44**, e312 (2016).

[128] A. Mukhopadhyay, A. De Gaetano, and O. Arino. Modeling the intra-venous glucose tolerance test: a global study for a single-distributed-delay model. *Discrete and Continuous Dynamical Systems Series B* **4**, 407 (2004).

[129] D. Nicolau. Predicting antibacterial response from pharmacodynamic and pharmacokinetic profiles. *Infection* **29**, 11 (2001).

[130] Y. K. Oh. Acid-base disorders in icu patients. *Electrolytes & Blood Pressure* **8**, 66 (2010).

[131] C.-G. Östenson. Regulation of glucagon release: effects of insulin on the pancreatic a2-cell of the guinea pig. *Diabetologia* **17**, 325 (1979).

[132] J. Papadopoulos and P. L. Smithburger. Common drug interactions leading to adverse drug events in the intensive care unit: Management and pharmacokinetic considerations. *Critical care medicine* **38**, S126 (2010).

[133] J. E. Parrillo, M. M. Parker, C. Natanson, A. F. Suffredini, R. L. Danner, R. E. Cunnion, and F. P. Ognibene. Septic shock in humans: advances in the understanding of pathogenesis, cardiovascular dysfunction, and therapy. *Annals of internal medicine* **113**, 227 (1990).

[134] F. Pea, P. Viale, F. Pavan, and M. Furlanut. Pharmacokinetic considerations for antimicrobial therapy in patients receiving renal replacement therapy. *Clinical pharmacokinetics* **46**, 997 (2007).

[135] N. Penfold and G. Park. Effects of organ failure and therapy on drug metabolism. *Current Opinion in Anesthesiology* **3**, 235 (1990).

[136] U. Pielmeier, S. Andreassen, B. S. Nielsen, J. G. Chase, and P. Haure. A simulation model of insulin saturation and glucose balance for glycemic control in icu patients. *Computer methods and programs in biomedicine* **97**, 211 (2010).

[137] M. Plantier, N. Havet, T. Durand, N. Caquot, C. Amaz, P. Biron, I. Philip, and L. Perrier. Does adoption of electronic health records improve the quality of care management in france? results from the french e-si (preps-sips) study. *International journal of medical informatics* **102**, 156 (2017).

[138] E. Polard, V. Le Bouquin, P. Le Corre, C. Kérebel, H. Trout, A. Feuillu, R. Le Verge, and Y. Mallédant. Non steady state and steady state pks bayesian forecasting and vancomycin pharmacokinetics in icu adult patients. *Therapeutic drug monitoring* **21**, 395 (1999).

[139] K. Polonsky, B. Given, W. Pugh, J. Licinio-Paixao, J. Thompson, T. Karrison, and A. Rubenstein. Calculation of the systemic delivery rate of insulin in normal man. *The Journal of Clinical Endocrinology & Metabolism* **63**, 113 (1986).

[140] K. Polonsky, B. Given, and E. Van Cauter. Twenty-four-hour profiles and pulsatile patterns of insulin secretion in normal and obese subjects. *Journal of Clinical Investigation* **81**, 442 (1988).

[141] F. Porcellati, P. Rossetti, N. B. Ricci, S. Pampanelli, E. Torlone, S. H. Campos, A. M. Andreoli, G. B. Bolli, and C. G. Fanelli. Pharmacokinetics and pharmacodynamics of the long-acting insulin analog glargine after 1 week of use compared with its first administration in subjects with type 1 diabetes. *Diabetes care* **30**, 1261 (2007).

[142] N. Pørksen, M. Hollingdal, C. Juhl, P. Butler, J. D. Veldhuis, and O. Schmitz. Pulsatile insulin secretion: detection, regulation, and role in diabetes. *Diabetes* **51**, S245 (2002).

[143] B. M. Power, A. M. Forbes, P. V. van Heerden, and K. F. Ilett. Pharmacokinetics of drugs used in critically ill adults. *Clinical pharmacokinetics* **34**, 25 (1998).

[144] R. Prager, P. Wallace, and J. M. Olefsky. In vivo kinetics of insulin action on peripheral glucose disposal and hepatic glucose output in normal and obese subjects. *Journal of Clinical Investigation* **78**, 472 (1986).

[145] I. Quesada, E. Tudurí, C. Ripoll, and Á. Nadal. Physiology of the pancreatic α-cell and glucagon secretion: role in glucose homeostasis and diabetes. *Journal of Endocrinology* **199**, 5 (2008).

[146] C. Radke, D. Horn, C. Lanckohr, B. Ellger, M. Meyer, T. Eissing, and G. Hempel. Development of a physiologically based pharmacokinetic modelling approach to predict the pharmacokinetics of vancomycin in critically ill septic patients. *Clinical pharmacokinetics* **56**, 759 (2017).

[147] H. Rafieii, M. Arab, H. Ranjbar, N. Arab, G. Sepehri, and M. Amiri. The prevalence of potential drug interactions in intensive care units. *Journal of Critical Care Nursing* **4**, 191 (2012).

[148] C. Ramnanan, D. Edgerton, G. Kraft, and A. Cherrington. Physiologic action of glucagon on liver glucose metabolism. *Diabetes, Obesity and Metabolism* **13**, 118 (2011).

[149] M. A. Ravier and G. A. Rutter. Glucose or insulin, but not zinc ions, inhibit glucagon secretion from mouse pancreatic α-cells. *Diabetes* **54**, 1789 (2005).

[150] N. Revilla, A. Martín-Suárez, M. P. Pérez, F. M. González, and M. d. M. Fernández de Gatta. Vancomycin dosing assessment in intensive care unit patients based on a population pharmacokinetic/pharmacodynamic simulation. *British journal of clinical pharmacology* **70**, 201 (2010).

[151] A. Rhodes, L. E. Evans, W. Alhazzani, M. M. Levy, M. Antonelli, R. Ferrer, A. Kumar, J. E. Sevransky, C. L. Sprung, M. E. Nunnally, *et al.* Surviving sepsis campaign: international guidelines for management of sepsis and septic shock: 2016. *Intensive care medicine* **43**, 304 (2017).

[152] R. A. Rizza, L. J. Mandarino, and J. E. Gerich. Dose-response characteristics for effects of insulin on production and utilization of glucose in man. *American Journal of Physiology-Endocrinology And Metabolism* **240**, E630 (1981).

[153] D. M. Roberts, J. A. Roberts, M. S. Roberts, X. Liu, P. Nair, L. Cole, J. Lipman, and R. Bellomo. Variability of antibiotic concentrations in critically ill patients receiving continuous renal replacement therapy: a multicentre pharmacokinetic study. *Critical care medicine* **40**, 1523 (2012).

[154] J. A. Roberts, C. M. Kirkpatrick, and J. Lipman. Monte carlo simulations: maximizing antibiotic pharmacokinetic data to optimize clinical practice for critically ill patients. *Journal of Antimicrobial Chemotherapy* **66**, 227 (2010).

[155] J. A. Roberts and J. Lipman. Pharmacokinetic issues for antibiotics in the critically ill patient. *Critical care medicine* **37**, 840 (2009).

[156] J. A. Roberts, F. S. Taccone, A. A. Udy, J.-L. Vincent, F. Jacobs, and J. Lipman. Vancomycin dosing in critically ill patients: robust methods for improved continuous-infusion regimens. *Antimicrobial agents and chemotherapy* **55**, 2704 (2011).

[157] P. V. Röder, B. Wu, Y. Liu, and W. Han. Pancreatic regulation of glucose homeostasis. *Experimental & molecular medicine* **48**, e219 (2016).

[158] A. Rodríguez-Molinero, L. Narvaiza, J. Ruiz, and C. Gálvez-Barrón. Normal respiratory rate and peripheral blood oxygen saturation in the elderly population. *Journal of the American Geriatrics Society* **61**, 2238 (2013).

[159] P. Rorsman, P.-O. Berggren, K. Bokvist, H. Ericson, H. Möhler, C.-G. Östenson, and P. A. Smith. Glucose-inhibition of glucagon secretion involves activation of gabaa-receptor chloride channels. *Nature* **341**, 233 (1989).

[160] C. Rose, A. Parker, B. Jefferson, and E. Cartmell. The characterization of feces and urine: a review of the literature to inform advanced treatment technology. *Critical reviews in environmental science and technology* **45**, 1827 (2015).

[161] J. Rotschafer, K. Crossley, D. Zaske, K. Mead, R. Sawchuk, and L. Solem. Pharmacokinetics of vancomycin: observations in 28 patients and dosage recommendations. *Antimicrobial Agents and Chemotherapy* **22**, 391 (1982).

[162] M. Rowland, T. N. Tozer, H. Derendorf, and G. Hochhaus. *Clinical pharmacokinetics and pharmacodynamics: concepts and applications* (Wolters Kluwer Health/Lippincott William & Wilkins Philadelphia, PA, 2011).

[163] M. Rybak, B. Lomaestro, J. C. Rotschafer, R. Moellering, W. Craig, M. Billeter, J. R. Dalovisio, and D. P. Levine. Therapeutic monitoring of vancomycin in adult patients: a consensus review of the american society of health-system pharmacists, the infectious diseases society of america, and the society of infectious diseases pharmacists. *American Journal of Health-System Pharmacy* **66**, 82 (2009).

[164] M. J. Rybak. The pharmacokinetic and pharmacodynamic properties of vancomycin. *Clinical Infectious Diseases* **42**, S35 (2006).

[165] L. D. Saravolatz, F. Pea, and P. Viale. The antimicrobial therapy puzzle: could pharmacokinetic-pharmacodynamic relationships be helpful in addressing the issue of appropriate pneumonia treatment in critically ill patients? *Clinical infectious diseases* **42**, 1764 (2006).

[166] F. Scaglione and L. Paraboni. Pharmacokinetics/pharmacodynamics of antibacterials in the intensive care unit: setting appropriate dosing regimens. *International journal of antimicrobial agents* **32**, 294 (2008).

[167] W. Schregel, H.-D. Kuntz, and M. Vitt. Hepatic drug metabolism in multiple organ failure. In *Innovations in Physiological Anaesthesia and Monitoring*, pp. 171–179 (Springer, 1989).

[168] G. Seller-Pérez, M. Herrera-Gutiérrez, E. Banderas-Bravo, R. Olalla-Sánchez, R. Lozano-Sáez, and G. Quesada-García. Concordance in critical patients between the equations designed for the calculation of glomerular filtration rate and 24-hour creatinine clearance. *Medicina intensiva* **34**, 294 (2010).

[169] E. T. Shapiro, H. Tillil, K. S. Polonsky, K., V. S. Fang, A. H. Rubenstein, and E. V. Cauter. Oscillations in insulin secretion during constant glucose infusion in normal man: relationship to changes in plasma glucose. *The Journal of Clinical Endocrinology & Metabolism* **67**, 307 (1988).

[170] C. Simon and G. Brandenberger. Ultradian oscillations of insulin secretion in humans. *Diabetes* **51**, S258 (2002).

[171] C. Simon, G. Brandenberger, and M. Follenius. Ultradian oscillations of plasma glucose, insulin, and c peptide in man during continuous enteral nutrition. *The Journal of Clinical Endocrinology & Metabolism* **64**, 669 (1987).

[172] I. A. Simpson, D. Dwyer, D. Malide, K. H. Moley, A. Travis, and S. J. Vannucci. The facilitative glucose transporter glut3: 20 years of distinction. *American Journal of Physiology-Endocrinology and Metabolism* **295**, E242 (2008).

[173] B. S. Smith, D. Yogaratnam, K. E. Levasseur-Franklin, A. Forni, and J. Fong. Introduction to drug pharmacokinetics in the critically iii patient. *Chest* **141**, 1327 (2012).

[174] C. L. Stanfield. *Principles of Human Physiology, 5th Edition* (Pearson Education, 2013).

[175] A. Starke, T. Imamura, and R. Unger. Relationship of glucagon suppression by insulin and somatostatin to the ambient glucose concentration. *The Journal of clinical investigation* **79**, 20 (1987).

[176] D. F. Steiner, D. Cunningham, L. Spigelman, and B. Aten. Insulin biosynthesis: evidence for a precursor. *Science* **157**, 697 (1967).

[177] J. Sturis, K. S. Polonsky, E. Mosekilde, and E. Van Cauter. Computer model for mechanisms underlying ultradian oscillations of insulin and glucose. *American Journal of Physiology-Endocrinology And Metabolism* **260**, E801 (1991).

[178] D.-Q. Sun, C.-F. Zheng, W.-Y. Liu, S. Van Poucke, Z. Mao, K.-Q. Shi, X.-D. Wang, J.-D. Wang, and M.-H. Zheng. Aki-clif-sofa: a novel prognostic score for critically ill cirrhotic patients with acute kidney injury. *Aging (Albany NY)* **9**, 286 (2017).

[179] H. Sun, E. Maderazo, and A. Krusell. Serum protein-binding characteristics of vancomycin. *Antimicrobial agents and chemotherapy* **37**, 1132 (1993).

[180] H. Suresh, N. Hunt, A. Johnson, L. A. Celi, P. Szolovits, and M. Ghassemi. Clinical intervention prediction and understanding using deep networks. *arXiv preprint arXiv:1705.08498* (2017).

[181] H. Suresh, P. Szolovits, and M. Ghassemi. The use of autoencoders for discovering patient phenotypes. *arXiv preprint arXiv:1703.07004* (2017).

[182] S. D. Taylor and M. Palmer. The action mechanism of daptomycin. *Bioorganic & medicinal chemistry* **24**, 6253 (2016).

[183] M. Tod and J.-M. Rocchisani. Comparison of ed, eid, and api criteria for the robust optimization of sampling times in pharmacokinetics. *Journal of pharmacokinetics and biopharmaceutics* **25**, 515 (1997).

[184] G. Toffolo, R. N. Bergman, D. T. Finegood, C. R. Bowden, and C. Cobelli. Quantitative estimation of beta cell sensitivity to glucose in the intact organism: a minimal model of insulin kinetics in the dog. *Diabetes* **29**, 979 (1980).

[185] I. M. Tolić, E. Mosekilde, and J. Sturis. Modeling the insulin–glucose feedback system: the significance of pulsatile insulin secretion. *Journal of theoretical biology* **207**, 361 (2000).

[186] C. L. Triplitt. Examining the mechanisms of glucose regulation. *American Journal of Managed Care* **18**, S4 (2012).

[187] A. Udy, J. Roberts, R. Boots, and J. Lipman. You only find what you look for: the importance of high creatinine clearance in the critically ill. *Anaesthesia and intensive care* **37**, 11 (2009).

[188] A. A. Udy, J. A. Roberts, J. J. De Waele, D. L. Paterson, and J. Lipman. What's behind the failure of emerging antibiotics in the critically ill? understanding the impact of altered pharmacokinetics and augmented renal clearance. *International journal of antimicrobial agents* **39**, 455 (2012).

[189] A. A. Udy, J. A. Roberts, and J. Lipman. Clinical implications of antibiotic pharmacokinetic principles in the critically ill. *Intensive care medicine* **39**, 2070 (2013).

[190] G. Van den Berghe, P. Wouters, F. Weekers, C. Verwaest, F. Bruyninckx, M. Schetz, D. Vlasselaers, P. Ferdinande, P. Lauwers, and R. Bouillon. Intensive insulin therapy in critically ill patients. *New England journal of medicine* **345**, 1359 (2001).

[191] I. van den Heuvel and B. Ellger. A sweet debate: Glycemic control in the intensive care unit*. *Critical care medicine* **36**, 3271 (2008).

[192] T. Van Herpe, N. Haverbeke, G. Van den Berghe, and B. De Moor. Prediction performance comparison between three intensive care unit glucose models. *IFAC Proceedings Volumes* **42**, 7 (2009).

[193] T. Van Herpe and D. Mesotten. Blood glucose measurements in critically ill patients (2012).

[194] T. Van Herpe, D. Mesotten, P. J. Wouters, J. Herbots, E. Voets, J. Buyens, B. De Moor, and G. Van den Berghe. Logic-insulin algorithm–guided versus nurse-directed blood glucose control during critical illness: The logic-1 single-center randomized, controlled clinical trial. *Diabetes Care* p. DC_120584 (2012).

[195] S. J. Vannucci, F. Maher, and I. A. Simpson. Glucose transporter proteins in brain: delivery of glucose to neurons and glia. *Glia* **21**, 2 (1997).

[196] C. A. Verdonk, R. A. Rizza, and J. E. Gerich. Effects of plasma glucose concentration on glucose utilization and glucose clearance in normal man. *Diabetes* **30**, 535 (1981).

[197] E. Vieira, A. Salehi, and E. Gylfe. Glucose inhibits glucagon secretion by a direct effect on mouse pancreatic alpha cells. *Diabetologia* **50**, 370 (2007).

[198] C. Wacker, A. Prkno, F. M. Brunkhorst, and P. Schlattmann. Procalcitonin as a diagnostic marker for sepsis: a systematic review and meta-analysis. *The Lancet infectious diseases* **13**, 426 (2013).

[199] H. Wang, J. Li, and Y. Kuang. Enhanced modelling of the glucose–insulin system and its applications in insulin therapies. *Journal of biological dynamics* **3**, 22 (2009).

[200] Y. Wang. Derivation of various nonmem estimation methods. *Journal of Pharmacokinetics and pharmacodynamics* **34**, 575 (2007).

[201] D. H. Wasserman. Four grams of glucose. *American Journal of Physiology-Endocrinology and Metabolism* **296**, E11 (2009).

[202] A. J. Weiss and J. I. Mechanick. Glycemic control: how tight in the intensive care unit? In *Seminars in thoracic and cardiovascular surgery*, volume 23, pp. 1–4 (Elsevier, 2011).

[203] M. Wells and J. Lipman. Measurements of glomerular filtration in the intensive care unit are only a rough guide to renal function. *South African journal of surgery. Suid-Afrikaanse tydskrif vir chirurgie* **35**, 20 (1997).

[204] J. Wernerman, T. Desaive, S. Finfer, L. Foubert, A. Furnary, U. Holzinger, R. Hovorka, J. Joseph, M. Kosiborod, J. Krinsley, *et al.* Continuous glucose control in the icu: report of a 2013 round table meeting. *Critical care* **18**, 226 (2014).

[205] G. Wernovsky, D. Wypij, R. A. Jonas, J. E. Mayer Jr, F. L. Hanley, P. R. Hickey, A. Z. Walsh, A. C. Chang, A. R. Castañeda, J. W. Newburger, *et al.* Postoperative course and hemodynamic profile after the arterial switch operation in neonates and infants: a comparison of low-flow cardiopulmonary bypass and circulatory arrest. *Circulation* **92**, 2226 (1995).

[206] Wikimedia Commons. Chemical structure of vancomycin (2008). https://en.wikipedia.org/wiki/Vancomycin#/media/File:Vancomycin.svg (31 July 2018).

[207] X. Wong, J. Chase, G. Shaw, C. Hann, T. Lotz, J. Lin, I. Singh-Levett, L. Hollingsworth, O. Wong, and S. Andreassen. Model predictive glycaemic regulation in critical illness using insulin and nutrition input: a pilot study. *Medical engineering & physics* **28**, 665 (2006).

[208] E. Wright, B. Hirayama, and D. Loo. Active sugar transport in health and disease. *Journal of internal medicine* **261**, 32 (2007).

[209] E. M. Wright. Renal na+-glucose cotransporters. *American Journal of Physiology-Renal Physiology* **280**, F10 (2001).

[210] W. Xiong, L. Faes, and P. C. Ivanov. Entropy measures, entropy estimators, and their performance in quantifying complex dynamics: Effects of artifacts, nonstationarity, and long-range correlations. *Physical Review E* **95**, 062114 (2017).

[211] X. S. Xu, M. Yuan, M. O. Karlsson, A. Dunne, P. Nandy, and A. Vermeulen. Shrinkage in nonlinear mixed-effects population models: quantification, influencing factors, and impact. *The AAPS journal* **14**, 927 (2012).

[212] M. Yasuhara, T. Iga, H. Zenda, K. Okumura, T. Oguma, Y. Yano, and R. Hori. Population pharmacokinetics of vancomycin in japanese adult patients. *Therapeutic drug monitoring* **20**, 139 (1998).

[213] Q. Zhang, R. Ramracheya, C. Lahmann, A. Tarasov, M. Bengtsson, O. Braha, M. Braun, M. Brereton, S. Collins, J. Galvanovskis, *et al.* Role of k atp channels in glucose-regulated glucagon secretion and impaired counterregulation in type 2 diabetes. *Cell metabolism* **18**, 871 (2013).

[214] H. Zhou, T. Zhang, J. S. Harmon, J. Bryan, and R. P. Robertson. Zinc, not insulin, regulates the rat α-cell response to hypoglycemia in vivo. *Diabetes* **56**, 1107 (2007).

[215] A. E. Zimmermann, B. G. Katona, and K. I. Plaisance. Association of vancomycin serum concentrations with outcomes in patients with gram-positive bacteremia. *Pharmacotherapy: The Journal of Human Pharmacology and Drug Therapy* **15**, 85 (1995).